Characterization and Preliminary Demonstration of

Microcantilever Array Integrated Sensors

Ryan R. Anderson

A dissertation submitted to the faculty of
Brigham Young University
in partial fulfillment of the requirements for the degree of

Doctor of Philosophy

Gregory P. Nordin, Chair
Aaron R. Hawkins
Stephen M. Schultz
Richard H. Selfridge
Adam T. Woolley

Department of Electrical and Computer Engineering

Brigham Young University

August 2012

ABSTRACT

Characterization and Preliminary Demonstration of
Microcantilever Array Integrated Sensors

Ryan R. Anderson
Department of Electrical and Computer Engineering, BYU
Doctor of Philosophy

I characterize the behavior of microcantilever arrays which utilize the in-plane photonic transduction that I've previously developed and evaluate the performance of the microcantilever arrays in simple sensing scenarios with integrated microfluidics. First the thermal responses of microcantilevers with a variety of patterns of deposited gold films are compared. Using a scanning electron microscope, I observe the deflection thermal sensitivities of 300 μm long microcantilevers to be -170.82 nm/K for a full gold coating and -1.93 nm/K for no gold coating. Using the photonic transduction method I measure a thermal sensitivity of -1.46 nm/K for a microcantilever array with no gold.

A microcantilever array integrated with microfluidics is exposed to a solution of bovine serum albumin (BSA) followed by solutions of various pH's. In all cases I observe a previously unreported transient deflection response. We find that the transient response is due to temporary nonuniform concentration distributions. In response to nonspecific binding of BSA, I observe a transient surface stress of -0.23 mN/m that agrees well with the -0.225 mN/m predicted by simulations. We hypothesize that the deflection response to pH changes is due to stress generated by conformational changes of bound BSA.

The deflection response of an integrated microcantilever array to different types of flow and different flow rates is observed. Simulations of the deflection response match well with experimental results but disagree at higher flow rates. For flow rates greater than 200 μL/min, the limitation of the differential signal's dynamic range becomes apparent. We then investigate flow driven by an on-chip reciprocating reservoir pump. We demonstrate that it is possible to use the reciprocating pump to achieve high flow rates while making deflection measurements in-between reservoir actuations.

Investigations of the microcantilever array noise show that flicker noise dominates below 10 Hz, while above 10 Hz, readout noise dominates. A minimum deflection noise density of 15 pW/$\sqrt{\text{Hz}}$ is achieved. To improve the signal-to-noise ratio I develop algorithms for a digital lock-in amplifier with a digital phase-lock loop. In simulation the lock-in amplifier is able to improve the SNR by up to a factor of 6000, and self-lock to a noisy carrier signal without an external reference signal.

Keywords: Ryan Anderson, lab-on-a-chip, microcantilever, microcantilever arrays, temperature sensitivity, lock-in amplifier, bovine serum albumin, pH, microfluidics

ACKNOWLEDGMENTS

I would certainly be remiss if I did not acknowledge my immense gratitude for my advisor, Dr. Gregory P. Nordin. He has been a mentor to me in the classroom, in the lab, and in life. Through the all too infrequent moments of unhindered progress and through the more usual stretches of frustrations and trials that are research, he has been a constant source of encouragement and guidance. In many ways, he gave me a second opportunity to pursue my dreams and help me get my feet back on a path that led forward.

I am also grateful to the large number of coworkers in our research group, those who have gone before and as well as those who I am leaving behind. I am especially grateful to Dr. Jong Noh and Dr. Weisheng Hu who took the time to involve me in their own projects when I was beginning my graduate career and taught me the ins and outs of research in general and microcantilevers in particular. I am also indebted to my fellow graduate students. Tim Gustafson, Danny Richards and Ben Tsai, along With Dr. Noh and Dr. Hu, spent long hours in the clean room to fabricate the numerous samples for the experiments I would run. Many late nights at the lab running experiments would have been duller and more frustrating without the company and assistance of others like Joseph Oxborrow, William Dahlquist, Stan Ness and Chad Rogers.

And of course my parents and my brothers and sisters have encouraged me throughout this process, especially during the moments of frustrations and pitfalls of research and life. I could not have reached this far without them, their support and loving encouragement.

CONTENTS

LIST OF TABLES

LIST OF FIGURES

CHAPTER 1. INTRODUCTION

1.1 Microcantilever

A microcantilever is a beam supported on only one end while the other end is free to move. Microcantilevers can be fabricated using a variety of materials, usually from silicon (Si), silicon nitride (SiN), or polymers. In some cases the fabricated microcantilever will consist of two or more layers of different materials The dimensions of the microcantilevers are on the scale of microns, typically 0.2-1 μm thick, 20-100 μm wide and 100-500 μm long. The material and dimensions determine the response of the microcantilever to external forces.

Stoney's formula has undoubtedly become the most important equation in understanding the microcantilever behavior. The formula relates the deflection, Δz, of the free end of the microcantilever to the differential stress, $\Delta\sigma$, between the microcantilever's upper and lower surfaces [1]:

$$\Delta z = \frac{3\Delta\sigma\,(1-\nu)\,L^2}{Et^2} \tag{1.1}$$

where ν is the Poisson's ratio of the material, E is the Young's modulus, L is the beam length and t is the beam thickness. Another important equation gives the spring constant of the microcantilever, which relates the deflection to an externally applied point force at the free end, in terms of the dimensions and material constants:

$$k = \frac{Ewt^3}{4L^3} \tag{1.2}$$

where w is the microcantilever width. The spring constant, k, is related to the fundamental resonant frequency, f_0, of the microcantilever by the usual harmonic oscillator equation:

$$f_0 = \frac{1}{2\pi}\sqrt{\frac{k}{m}} \tag{1.3}$$

where m is the effective mass of the microcantilever.

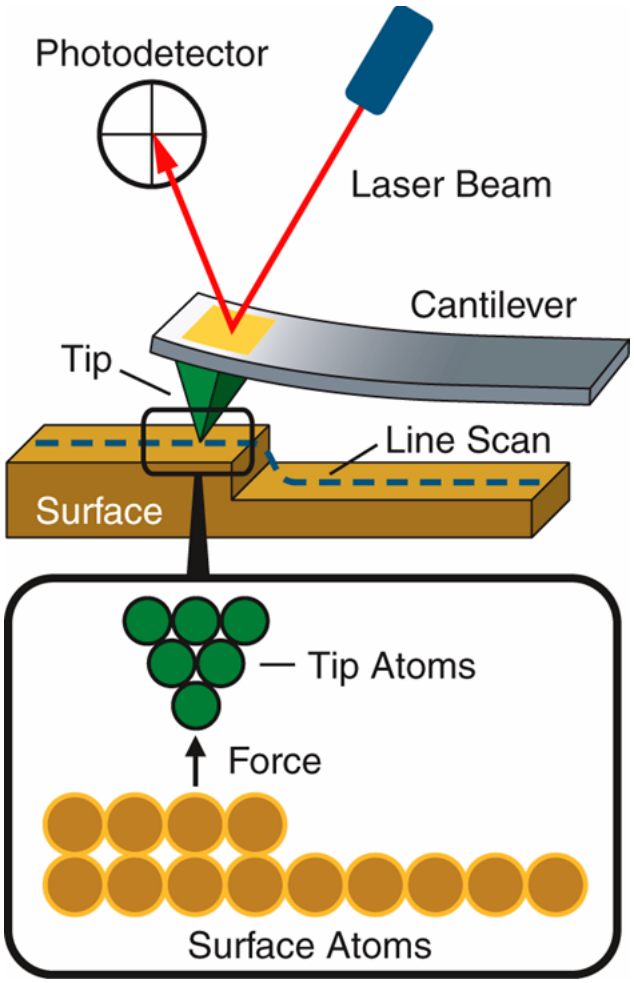

Figure 1.1: Schematic showing the general operation of AFM and the OBD method to measure the microcantilever deflection. From Agilent Inc. (http://nano.tm.agilent.com)

The first major application of microcantilever was as a probe in atomic force microscopes (AFM) in the 1980's [2]. The AFM consists of a microcantilever with an atomically sharp tip at its free end. The sharp tip is actual probe that is used to scan a sample surface. As the tip is brought near the sample surface, forces between the tip and the sample surface will affect the static deflection and the resonance of the microcantilever. In most AFMs the deflection of the microcantilever is determined using a method called optical beam deflection (OBD) as shown in Fig. 1.1. A laser is reflected from the top surface (the surface facing away from the sample) to a position sensitive photodetector (PSD). Either the sample or the microcantilever probe is mounted on a movable platform which allows the scanning tip to be rastered across the sample surface.

By observing the change in microcantilever deflection, the topography and other properties of the sample surface can be measured.

Beyond measuring surface topography, microcantilevers have been used in science and in industry for a variety of applications. The AFM is the most notable form in which the microcantilever serves as a sensor platform. More general microcantilever-based sensors rely on the ability to specially prepare the microcantilever surface, for example the probe tip for AFMs, to enable it to respond to external stimuli. Microcantilevers have been developed as sensing platform for a variety of sensors to detect physical [3–5], chemical [6–14], biological [15–25], and environmental [26–28] conditions.

1.2 Microcantilever Sensor

Microcantilevers are attractive as sensors because they provide a simple and ready platform for label-free sensing with high sensitivity [24, 28–31]. Using the microfabrication techniques and technology developed for the semiconductor industry, microcantilevers can be mass produced at low cost. As demonstrated in AFMs, the microscopic size of the microcantilever results in low spring constants and high sensitivities to applied forces and stresses. Moreover, because of the fine control of microfabrication process, microcantilevers can be produced with desired spring constants to allow access to specific force regimes. Integration of microcantilever sensor further extends the scope of applications to rapid, lab-on-a-chip detection systems [28, 32].

For biological and chemical sensing applications, one or both surfaces of the microcantilever are sensitized the target analyte by coating the surfaces with chemo-selective receptors [6, 17, 28]. Microcantilever sensors operate in either a static deflection mode [21, 28, 33] or a dynamic resonant mode [13,21,28]. In the static deflection, the selective adsorption of analyte to only one side generates an unbalanced differential surface stress resulting in a measurable change in the deflection state of the microcantilever, as illustrated in Fig. 1.2. In the dynamic resonant mode, illustrated in Fig. 1.3, adsorption of analyte to the microcantilever increases its mass resulting in a measurable shift of the resonant frequencies. The dynamic mode is advantageous because it does not require only one surface to be sensitized to the analyte, simplifying the sensor preparation process. However, the dynamic resonant mode operates best in air or vacuum, but performs poorly in liquid environments due to the large damping effects on oscillations from the viscosity of the

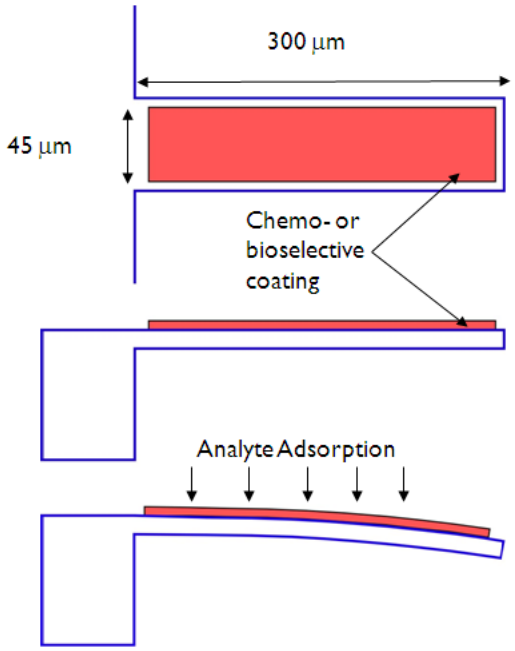

Figure 1.2: Illustration of a static deflection mode, microcantilever-based sensor with a selective coating on one surface. Analyte adsorption to the selective coating generates a differential surface stress which induces a deflection.

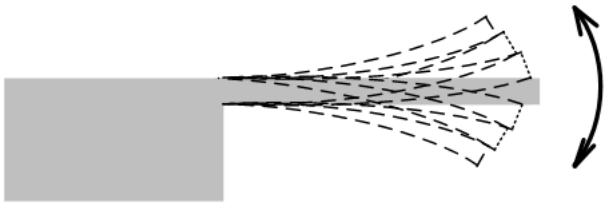

Figure 1.3: Illustration of the dynamic resonant mode of operation of a microcantilever sensor.

liquid. The static deflection mode, on the other hand, performs well in vacuum, gas, and liquid environments.

Microcantilever sensors can also be characterized by the readout method for transducing the deflection state of the microcantilever. The most common transduction method is OBD [2, 21, 22, 28, 34], largely because of the prevalence of AFMs. Other methods have developed based on other mechanisms such as piezoresistive [16, 19, 21, 22, 24], piezoelectric [10, 35], capacitive [14], and optical waveguides [36]. The type of transduction method can place limitations on the possible sensing environments, for example OBD does not work well with opaque or scattering liquid

solutions, and on the ability to scale up to sensing devices with large numbers of microcantilever sensors.

1.3 Microcantilever Sensor Array

Much effort has been placed in developing sensors consisting of large arrays of microcantilevers. Large array sensors provide the ability to perform simultaneous parallel assays which increases the efficiency of the use of sample volume, improves the sensor capability to distinguish effects from the target analyte and other environmental stimuli, increases the sensitivity of the overall sensor package [15, 25, 30, 37]. Each microcantilever in the array can be sensitized to a different target analyte, allowing the sensor to perform different assays simultaneously without the need for multiple sample volumes. Microcantilevers that are left unsensitized or passivated so that they will not respond to the target analyte act as reference cantilevers. The reference cantilevers will respond to the ambient sensing environment such as variations in temperature, pH, and flow rate, which are not due to the target analyte, that can then be removed from the sensing microcantilevers. Finally, overall sensitivity is increased when the array of microcantilevers is coated with the same receptor, increasing the redundancy of the assay and improving the sensor's signal-to-noise ratio (SNR).

1.4 Microfluidics

Microfluidics provide the ability to expose the sensors to small sample volumes and improve sensor response time. Combining microfluidics with an array of label-free sensors, such as microcantilevers, can lead to a versatile multiplexed sensor platform. In such a platform all sensor elements can be exposed to the same environment of interest and queried simultaneously to improve the overall sensor capability, efficiency, and sensitivity [15, 25, 30, 37]. As is often the case in traditional microcantilever sample containers, longer periods of observation or reduced overall device sensitivities result if transport of target analytes relies on diffusion alone, particularly as the dimensions of each sensor element shrink [38]. An advantage of properly implemented microfluidics is a much higher target analyte flux to the sensor surface through flow-induced advection [39], which reduces sensor response time. High target analyte flux is achieved with high flow rates to continually replenish the concentration depletion region due to binding to the sensor surface. The

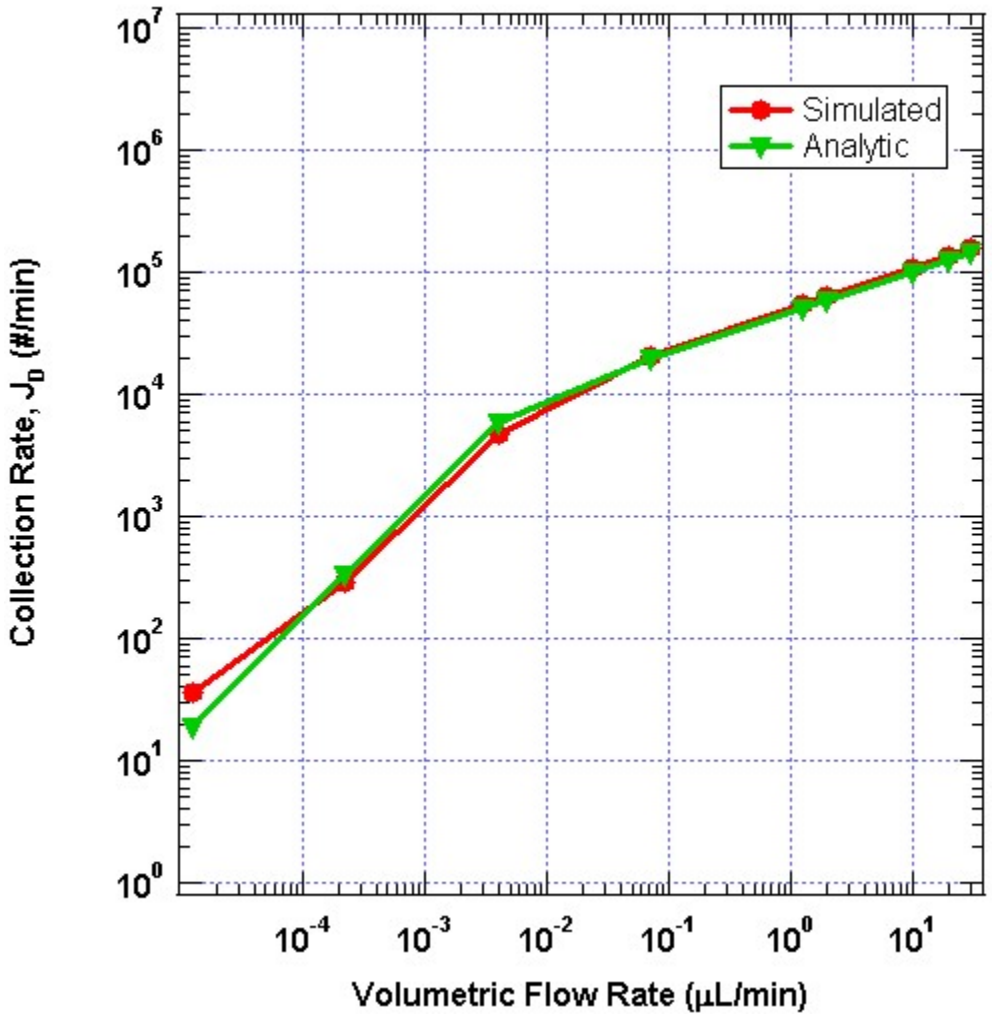

Figure 1.4: Collection rate, assuming 100% capture probability, for a 10 pM PSA concentration in a 200 μm wide, 24 μm tall channel and a sensor width of 35 μm.

effects of flow rate on the collection rate is shown in Fig. 1.4. The small channel cross-section of microfluidics allows such high flow rates to be achieved with the small sample volumes typical of lab-on-a-chip applications.

1.5 Contributions

My specific contributions to the development and demonstration of integrated sensors based on photonic microcantilever arrays are as follows:

1. Derived a more complete theoretical model for the temperature dependent deflection response of silicon microcantilevers with full and partial gold film coatings on one side. I demonstrated that the model agrees well with experimental solutions and that certain assumptions such as ignoring the effects of the Young's modulus and Poisson ratio of gold and orientation of the microcantilever relativeto the crystal axes of the silicon (as is often done in the literature) significantly increase the error of the model.

2. Discovered and demonstrated a previously unreported transient deflection of microcantilever sensors in a microfluidic channel related to the proximity of the microcantilevers to the bottom boundary of the channel. After initial observations of the transient response I hypothesized that the deflection was due to a temporary inhomogeneous concentration distribution above and below the microcantilever. For the case of non-specific binding of bovine serum albumin to the microcantilever surface, I developed a theoretical model based on Langmuir binding kinetics that also included a finite concentration gradient across a depletion region from the bulk solution to the microcantilever surface. The model was validated by combining it with 2D fluid simulations of concentration over time to produce theoretical predictions which matched closely with experimental observations.

3. Demonstrated the functioning of microcantilever array sensors in fluid with integrated PDMS microfluidics. The deflection of the microcantilevers in response to pressure driven flow both from an external source (syringe pump) and an on-chip source (reciprocating diaphragm pump). In the latter, I demonstrated that efficient use of a sample volume, the production of bursts of high flow rates in the fluid channel, and the ability to make static deflection measurements with the on-chip pump.

4. Measured the noise density as a function of frequency, signal power, and adjustable camera parameters. I identified the dominant noise sources in the different frequency ranges and in the different output power regimes, and derived and measured the resulting deflection noise densities from these sources.

5. Developed and demonstrated in simulation a unique digital lock-in amplifier with a digital phase-locked loop for use with our sensing apparatus. Because of the limitations of our

apparatus, the algorithm had to be self-locking to the carrier frequency and operate without an external reference. It also had to accommodate possible frequency mismatches between the carrier and the demodulation oscillator.

6. Provided design and processing inputs for the photonic microcantilever array and PDMS microfluidic layouts with respect to integration with other sensing apparatus and experimental apparatus.

My efforts and contributions to the development and demonstration of photonic microcantilever array sensors are included in the following refereed journals:

1. R. R. Anderson, W. Hu, J. W. Noh, W. C. Dahlquist, S. J. Ness, T. M. Gustafson, D. C. Richards, S. Kim, B. A. Mazzeo, A. T. Woolley, and G. P. Nordin, "Transient deflection response in microcantilever array integrated with polydimethylsiloxane (PDMS) microfluidics," *Lab on a Chip*, vol. 11, pp. 2088–2096, 2011.

2. J. W. Noh, R. R. Anderson, S. Kim, W. Hu, and G. P. Nordin, "Sensitivity enhancement microcantilever arrays," *Nanotechnology*, vol. 21, no. 15, p. 155501, 2010.

3. J. W. Noh, R. R. Anderson, S. Kim, W. Hu, and G. P. Nordin, "In-plane all-photonic transduction with differential splitter using double-step rib waveguide for photonic microcantilever arrays," *Opt. Express*, vol. 17, no. 22, pp. 20012–20020, 2009.

4. W. Hu, R. Anderson, Y. Qian, J. Song, J.W. Noh, S. Kim, and G. P. Nordin, "Demonstration of microcantilever array with simultaneous readout using an in-plane photonic transduction method," *Rev. Sci. Instrum.*, vol. 80, no. 8, p. 085101, 2009.

5. J. W. Noh, R. Anderson, S. Kim, J. Cardenas, and G. P. Nordin, "In-plane photonic transduction of silicon-on-insulator microcantilevers," *Opt. Express*, vol. 16, no. 16, pp. 12114–12123, 2008.

1.6 Overview of Dissertation

This dissertation is focused on discussing the characterization of the microcantilever sensor and the development of microcantilever array sensors integrated with microfluidics as a lab-on-a-chip sensing platform. The dissertation is organized as follows.

Chapter 2 introduces background information including the SOI rib waveguide and the in-plane all-photonic transduction method. The structure of the differential splitter and the transduction method is described.

Chapter 3 describes the integrated data acquisition system and the automation of experiments. The procedures I developed for alignment of the optics and protocol for calibrating the deflection responsivity of the microcantilever array are described.

Chapter 4 provides an in-depth analysis of the response of microcantilevers to temperature fluctuations and compares unimorph silicon microcantilevers to bimorph gold-on-silicon microcantilevers. The necessity of using the proper parameters and equations for temperature-induced deflection is demonstrated. It is also shown through experimental data the high temperature sensitivity of the gold-on-silicon microcantilevers compared to the low temperature sensitivity of the all-silicon microcantilevers.

Chapter 5 describes the response of an integrated microcantilever array sensor to bovine serum albumin (BSA) and solution pH changes. In particular, it reports a previously unreported transient deflection response of a microcantilever due to its position in the microfluidic channel. The responses agree with simulations of the concentration as a function of time and estimated stresses from non-specific binding of BSA.

Chapter 6 presents the deflection response of the integrated microcantilever array sensor to pressure driven flow rates. The measured responses are compared to the finite element method (FEM) simulations of a microcantilever in the fluidic channel with flow.

Chapter 7 discusses preliminary results from the successful integration of the microcantilever array with on-chip PDMS pumps. The microcantilevers respond strongly to the fast fluid flow during pump actuation ideal for quick response times, but return quickly to a steady state at which point the deflection can be measured. This investigation is meant to be prerequisite to sensing a target analyte with limited sample volume and flow driven by the on-chip pumps.

In chapter 8, the noise of the system used to measure the signal from the microcantilever array is analyzed and its effect on the deflection detection limit calculated. I identify the presence of flicker noise near DC, readout noise as the dominant noise above ~10 Hz, and the onset of shot noise as the output power increases. The readout noise from the InGaAs camera is the main limiting factor of the deflection noise density.

Chapter 9 discusses the development of a digital lock-in algorithm as a tool to overcome certain noise sources. The digital lock-in amplifier is designed for implementation with the current equipment. In simulations, it is shown that the algorithm is capable of recovering signals from noise with signal-to-noise ratios less than 0.001, has the ability to self-phase lock without an external reference signal, and can overcome a frequency mismatch between the carrier and demodulation frequencies.

Finally, in chapter 10 the dissertation is summarized and future work discussed.

CHAPTER 2. BACKGROUND

2.1 SOI Rib Waveguide

Silicon-on-insulator (SOI) wafers are often used in the semiconductor industry as well in the development of silicon photonics [40]. The top single-crystal silicon layer, often termed the device layer, can be used to create optical waveguides and passive optical elements for integrated optics. The silicon device layer sits between the two media, the buried insulator (silicon dioxide) on the bottom and typically air on top, with lower indices of refraction, which allows electromagnetic waves to propagate in guided modes of waveguides due to total internal reflection.

The SOI device layer in which the waveguides are fabricated is 0.75 μm thick. Regions of the device layer are etched down 0.1 μm to form rib waveguides with rib widths of 1.6 μm. Beneath the device layer, the under cladding for the waveguides is a SiO_2 layer. Initially SOI wafers with an insulator thickness of 3 μm were used. After development of the deep silicon etch process, I now use SOI wafers with an insulator thickness of 1 μm. The dimensions of the rib waveguide are such that it only supports the fundamental TE polarization mode at a wavelength of 1550 nm based on a refractive index of 3.477 for silicon, an index of 1.444 for the SiO_2, and an index of 1 for the upper cladding of air.

2.2 Differential Splitter Network

The microcantilevers are defined in the device layer using optical photolithography followed by a silicon etch. The microcantilevers are patterned such that a rib waveguide is embedded in the middle of each microcantilever. To use the waveguide as a transduction method, a capture waveguide has to be fabricated opposite what will be the free end of the microcantilever. Several groups have proposed using a static single mode capture waveguide for light to couple into after exiting at the free end from the embedded waveguide [36, 40, 41]. In this case, the the mi-

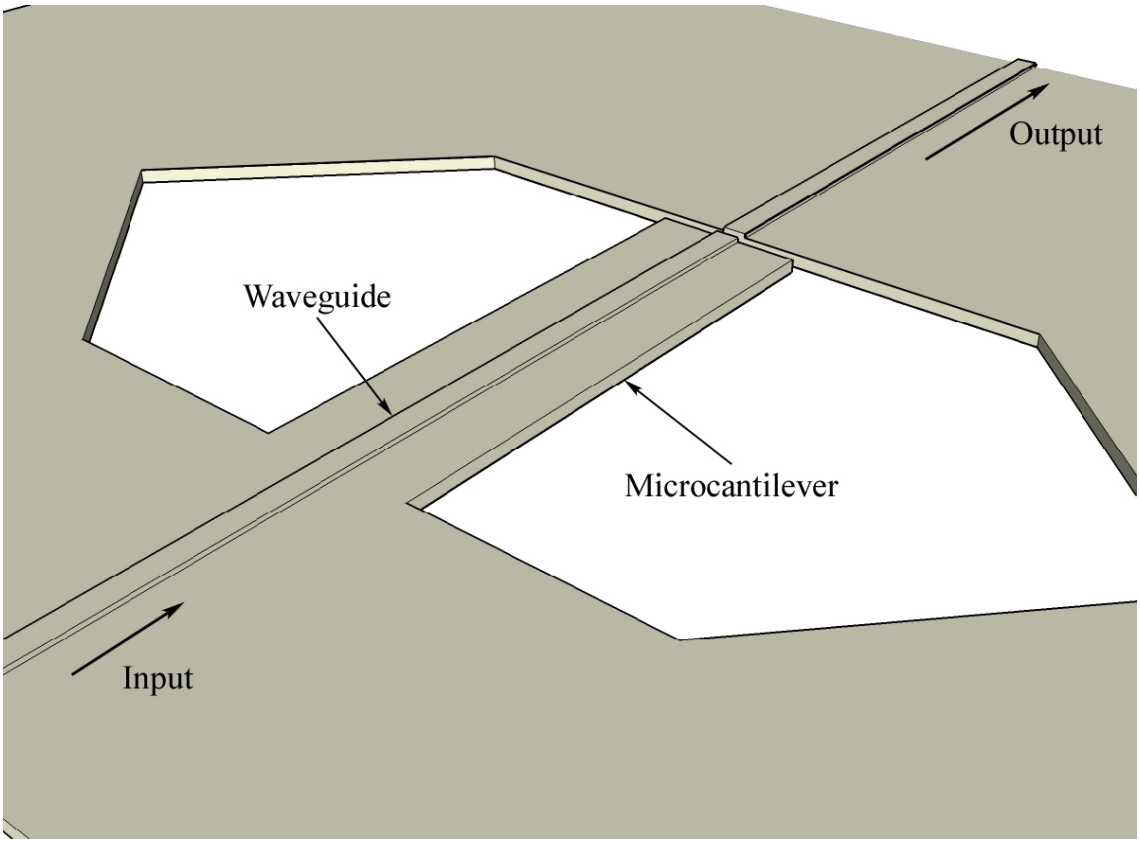

Figure 2.1: Schematic of photonic microcantilever with an embedded waveguide and a single mode capture waveguide.

crocantilever structure with the embedded and capture waveguides appears like the structure seen in Fig. 2.1. The output power of the capture waveguide as a function of deflection is shown in Fig. 2.2. The single mode capture waveguide has little to no sensitivity near zero deflection where the slope of the output power curve is zero, making this an unattractive design for a photonic microcantilever-based sensor.

As an alternative solution for the photonic microcantilever, my group has developed and demonstrated a new in-plane photonic waveguide microcantilever transduction method which uses an asymmetric multimode capture waveguide with two optical outputs [42–45]. The two outputs are used to form a differential signal that is a monotonic function of deflection over a range of $\pm$500 nm centered about zero deflection. Fig. 2.3 shows an overhead close-up of the photonic microcantilever and the capture waveguide geometry. The capture waveguide consists of a 3.0 μm wide multimode rib waveguide in the silicon device layer that has the same ridge height, 0.1 μm,

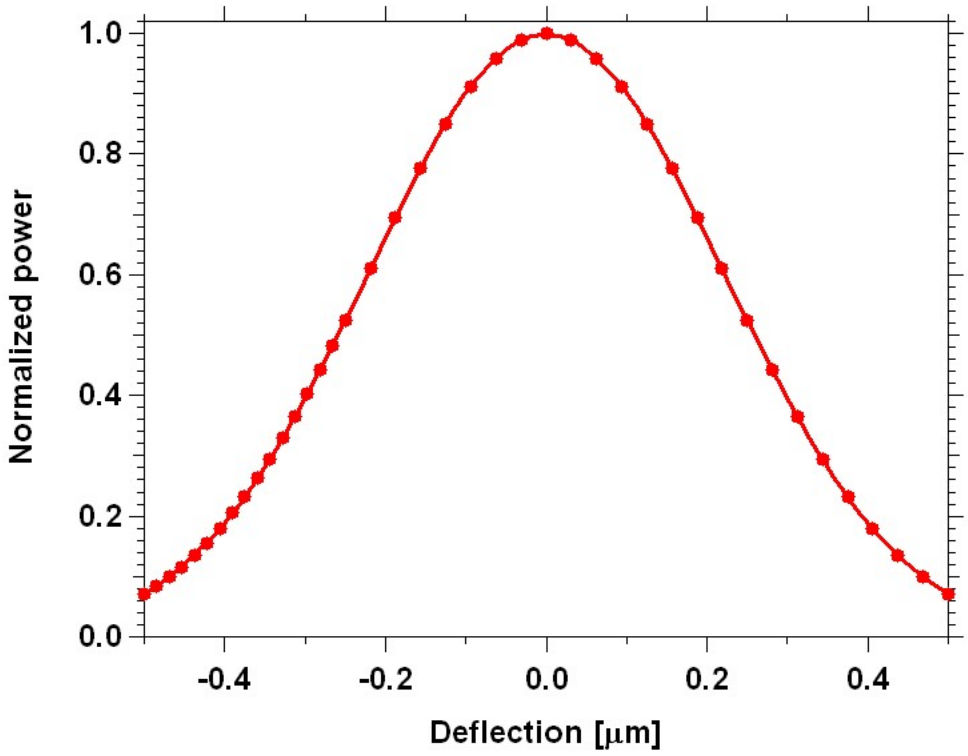

Figure 2.2: Simulation results for the output power as a function of microcantilever deflection for a single mode capture waveguide.

as the single mode rib waveguide. The asymmetry is produced by etching half of the multimode waveguide down a further 0.2 μm, as seen in Fig. 2.4(a), to form a double step rib waveguide along the first 4 μm of the waveguide. The asymmetric multimode waveguide supports two TE guided modes and terminates in a Y-branch 1×2 waveguide splitter. The combination of the double-step rib waveguide and Y-branch splitter is called a differential splitter.

The Y-branch is placed such that each of the two guided modes couple into a separate output, as shown in Fig. 2.4(b). As the centroid of the main lobe for the first excited mode is lower than that of the fundamental mode, optimum coupling from the microcantilever into that mode occurs at a deflection below zero-deflection. In this way, the asymmetric structure causes a slight offset, Δ, between the peaks of the output power profiles as a function of deflection of the two outputs as seen in Fig. 2.5(a). Because of the offset, it is possible to use the two output signal,

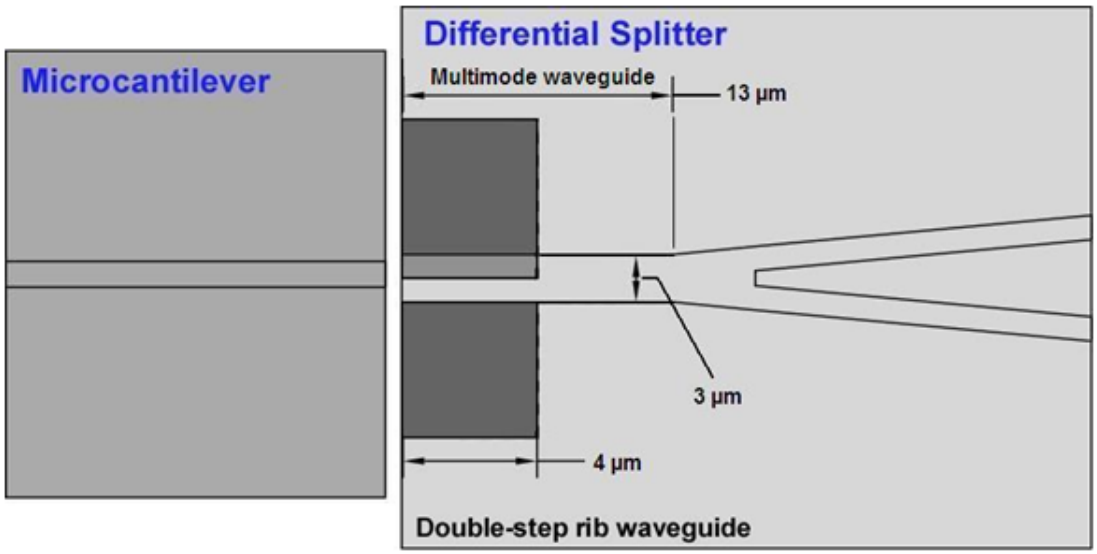

Figure 2.3: Schematic showing an overhead view of the microcantilever and differential splitter.

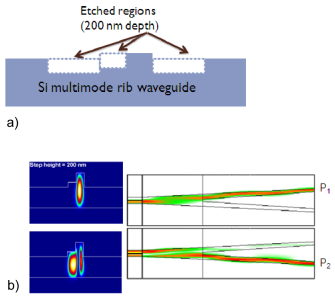

Figure 2.4: (a) Cross-section of the silicon layer at the asymmetric multimode capture waveguide. (b) Fundamental and first harmonic modes and the outputs into which they couple.

P_1 and P_2, to form a scaled differential signal, η, defined as

$$\eta = \frac{P_2 - \alpha P_1}{P_2 + \alpha P_1} \tag{2.1}$$

where α is the ratio of P_2 to P_1 at zero deflection. The scaling factor compensates for uneven losses in the Y-branch splitter waveguides and effectively forces the differential signal to be zero at zero-deflection (Fig. 2.5(b)). The differential signal is monotonic and nearly linear over the measurement range of interest, avoiding the low sensitivity region previously seen in Fig. 2.2.

Jong Wook Noh and I have worked together to demonstrate and optimize the performance of the double-step rib waveguide differential splitter [43, 44]. Fig. 2.6 shows an example of a

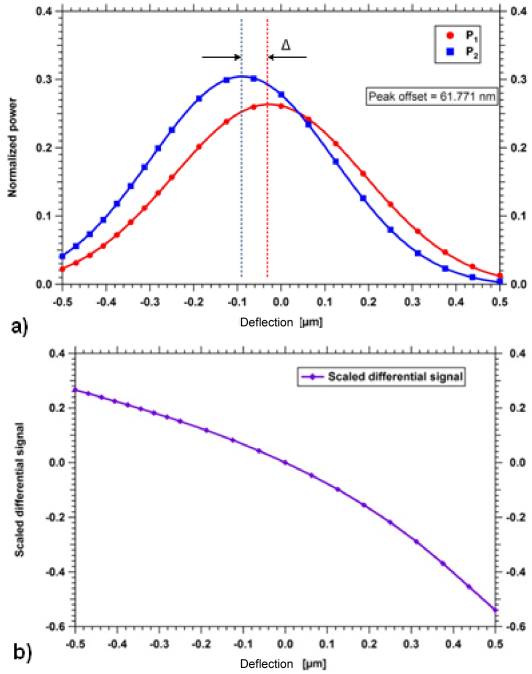

Figure 2.5: (a) Simulation of the two output powers from the differential splitter as a function of deflection. (b) Scaled differential signal formed from the outputs as a function of deflection.

measured scaled differential signal as a function of deflection for a microcantilever array. The slope of the differential signal is the deflection responsivity of the microcantilever. I have demonstrated the ability to consistently fabricate microcantilever arrays with average responsivities of ~1 μm^{-1}, comparable to the responsivity of the OBD method with AFM microcantilevers.

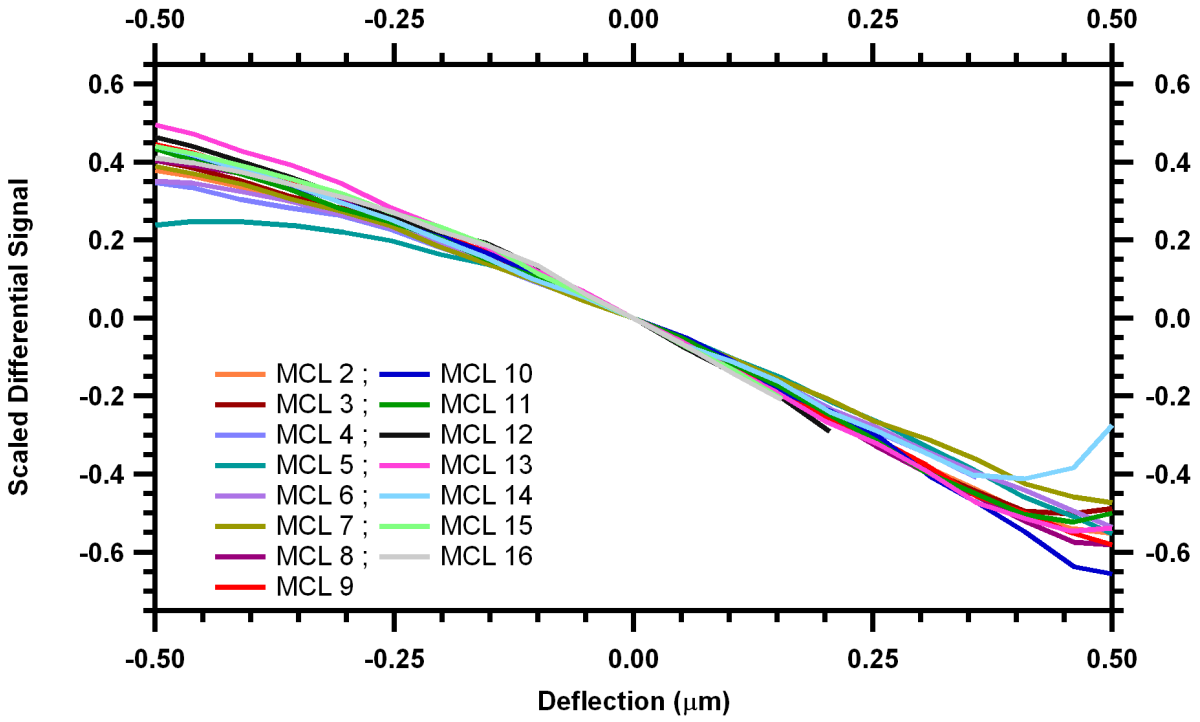

Figure 2.6: Scaled differential signals as a function of deflection obtained from a microcantilever array. The average responsivity (slope) is 1.01 μm^{-1}.

CHAPTER 3. MEASUREMENT SETUP DESIGN

3.1 Motivation

Creating a full package total analysis system using the microcantilever arrays requires a significant amount of systems integration. Initially, when the in-plane photonic transduction method was first being demonstrated [42], each silicon chip contained a small number of microcantilevers and the layout and experimental apparatus was such that only one microcantilever at a time could be sourced with light, physically actuated, and read out. Scaling up the device to large arrays necessitated the advancement of means to be able to source all microcantilevers and observe all outputs simultaneously. Additionally, as preliminary demonstrations progressed to measuring deflection response to environmental stimuli and the complexity of the experiments increased, the whole system would need to be automated and the data acquisition method would need to be synchronized with a variety of other control apparatus. To that end I developed a number of virtual control systems using LabVIEW (National Instruments) to quickly prototype experimental designs and control as much of an experiment as possible within a single user interface environment.

The basic schematic of the experimental apparatus is shown in Fig 3.1. Included in the schematic are all the devices for which virtual instruments (VIs) were created. In this chapter I will describe the main basic elements of the experimental apparatus and my contributions to integrating them into the measurement system both in terms of software as well as in terms of experimental procedures. Two additional computers are used, though not shown, which control the auto-align system and the 2D IR camera using commercial proprietary software. These two systems are mainly used for the alignment of the optics but are used very little during actual data acquisition and so are not included in my automation software. Their use in the alignment process will be described shortly.

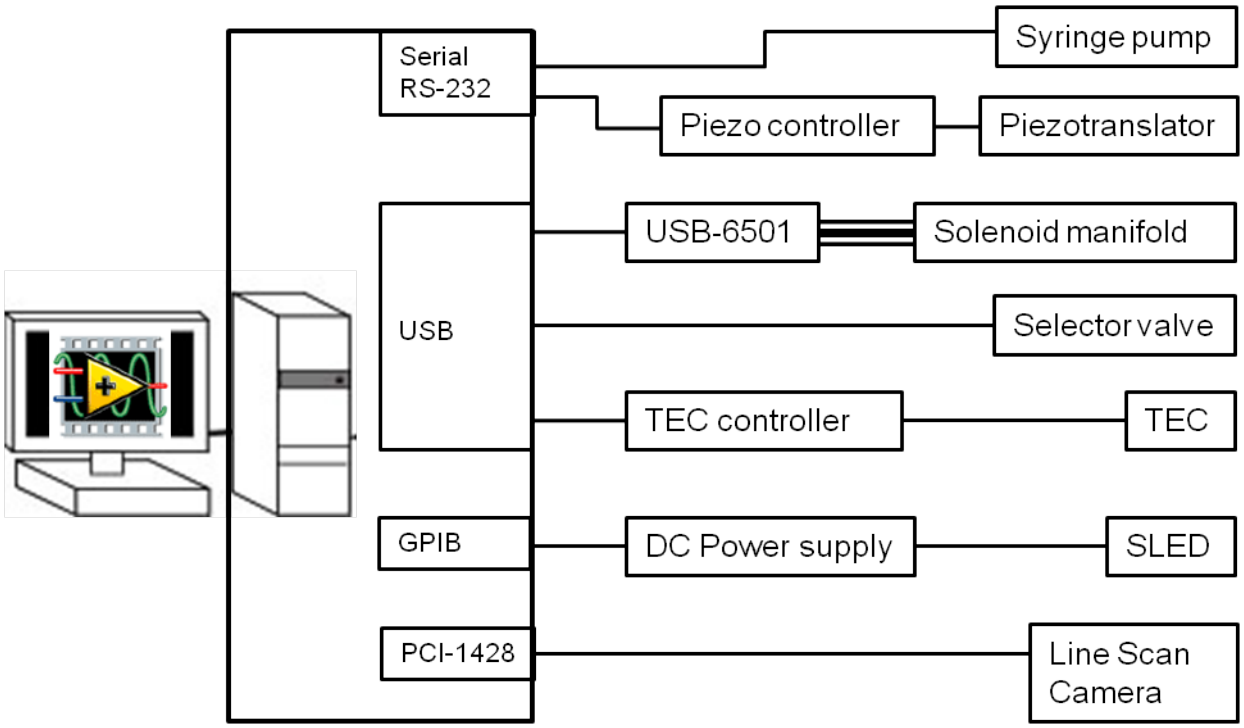

Figure 3.1: Schematic of overall data acquisition system.

3.2 Optics

The light source for the embedded waveguides is provided by a superluminescent light emitting diode, or SLED (DL-BZ1-CS5403A-FP-00; Denselight Semiconductors). The SLED emits polarized light with a central wavelength of 1550 nm, the wavelength at which the embedded waveguides have been designed to support only a single TE mode, and a bandwidth of 35 nm. The output power of the SLED is also dependent on an applied control voltage. The measured relationship between the control voltage and the SLED output power is shown in Fig. 3.2. The maximum input control voltage is 2.5 V, resulting in a maximum output power of 48 mW. Typical operation during experimental runs use a control voltage in the range of 1-2 V depending on the optical losses and the initial deflection of the microcantilevers. A SLED with a variable output power was also chosen to allow for the option of implementing a lock-in amplifier, which would require the ability to directly modulate the light source.

The outputs of the microcantilever array die are imaged with optics (Zoom 70XL NIR Optical System; Optem) onto the focal plane array of an InGaAs line scan camera (SU512LDV; Goodrich). The focal plane array consists of 512 pixels with a pixel pitch of 50 μm. The readout

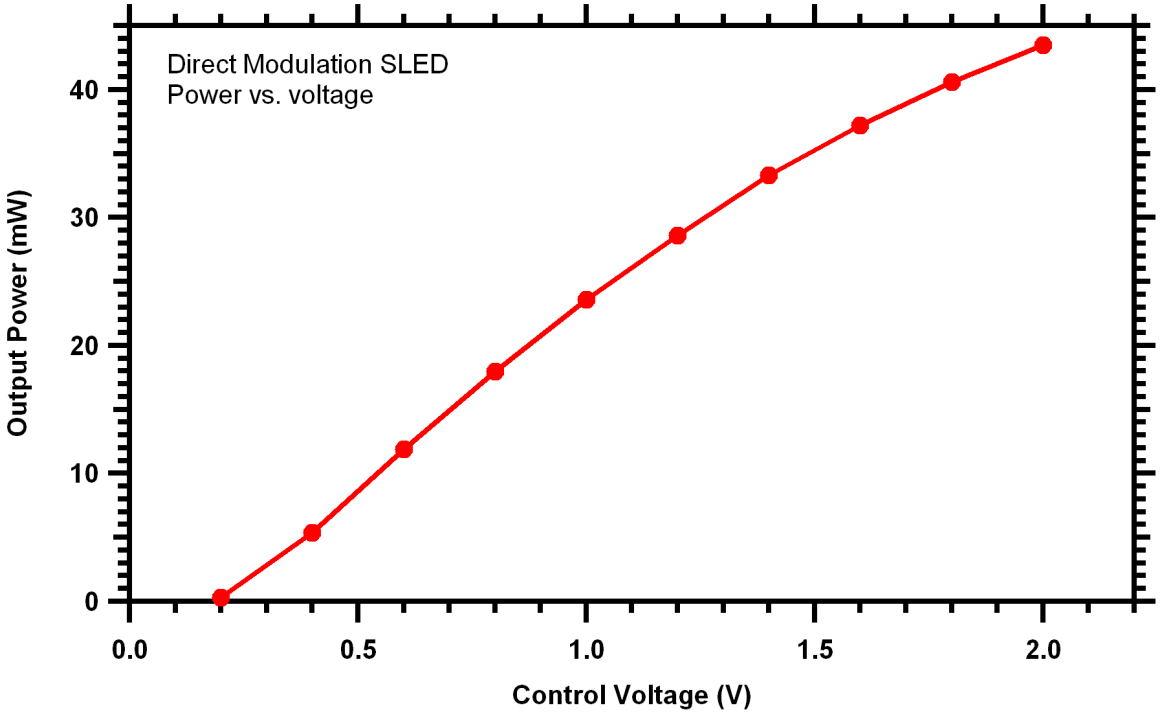

Figure 3.2: SLED output power as a function of control voltage.

of the focal plane array is acquired and converted to a digital signal by the integrated circuitry in the main body of the camera. Software for the line scan camera provided by the manufacturers included both high and low level VIs, simplifying the integration of the camera with the whole experimental system. It should be noted that the preprogrammed exposure times and line scan rates are not directly inversely related due to the computational and communications tasks that also must be performed during frame grabs. Each frame grab, or image, consists of a user-defined number of line scans with each column in the image corresponding to a pixel and each row to an individual line scan. While the camera does have internal memory for storing images to be retrieved at a later time, I found that, for the higher scan rates, images need to consist of at least 400 line scans for continuous data acquisition. When the images consist of only a few line scans, the additional communication between the computer and the camera for each frame grab inevitable causes the retrieval of images to fall behind until the camera's internal memory is full and images start to be overwritten.

For all experimental measurements, the alignment of the optics are the same. The micro-cantilever array die sits between the two adjustable vertical auto-align stages (15-1000-0400-21

M-PM500-1V.50 MINI Z; Kensington Labs). The stage on the output side is lowered so that the outputs from the die can be imaged with a 2D infrared camera. The stage on the input side holds the cleaved end of a standard polarization maintaining (PM) fiber connected to the SLED. The input stage is moved up in the *y*-direction until the fiber is about 1 cm above the die. The input stage is then translated in the *z*-direction until the fiber is near, but not over, the die as seen with an overhead camera. The fiber is then aligned in the *x*-direction so that it lines up with the input waveguide. The PM fiber is connected to a red laser and moved down in *z*-direction in 100 μm steps; when the fiber is in-plane with the die, the scatter from the red laser light can easily be seen in the overhead camera. With the fiber in the plane of the die, the fiber is aligned with the waveguide using 2 μm steps in the *x* and *y* directions with the stage. The PM fiber is then connected with the SLED and the SLED is powered on. The outputs are then imaged with the 2D infrared camera, and again the PM fiber is more finely aligned with the waveguide using 0.05 μm steps until the outputs are optimized. Once the *x* and *y* positions are aligned, the fiber is moved in the *z* direction until it comes into contact with the die.

The 2D infrared camera is replaced with the InGaAs line scan camera. The mounts for the two cameras are such that their object planes occur roughly at the same position relative to the die. Translation stages allow for adjustments along all three axes until the outputs appear in the line scan camera read out. The focus is adjusted using the translation in the *z*-direction, while the magnification is adjusted by the appropriate knob on the upper core of the NIR optical system. Because of the divergence of the outputs and the limitations of the 1 inch diameter aperture optics, one output cannot be imaged to a single pixel with 1:1 magnification. Using a 1:2 magnification, the output is imaged mostly to a single pixel with the adjacent pixels about 4% of the main signal. Because of the 1:2 magnification, these adjacent pixels do not overlap with the signal from the next output, preventing crosstalk between output readouts. I have found that a simple way to test the quality of the magnification of the optics is to translate the camera back and forth in the *x* direction. If the magnification is off, a Moirï¿œ-type pattern is produced and the outputs appear to grow and shrink at different instances as each transitions from one pixel to the next. When the magnification is correct, the outputs appear to grow and shrink in unison across the entire array.

3.3 Microfluidics

3.3.1 Valve Control

As will be described in later chapters, microcantilevers arrays are integrated with microfluidics fabricated in polydimethylsiloxane (PDMS). The microfluidic structure consists of two layers bonded together, a lower containing the fluidic channels for analyte solution and an upper layer containing valve chambers used to actively control the direction of flow through the microfluidics. For external connections for both the fluid channels and valve chambers, holes are punched in the PDMS layers (through both layers for fluid channels and only the top layer for the PDMS valves). Short metal pins (0.394" New England Small Tube Corp.) are inserted into the punched holes and attached to external tubing (Microbore PTFE #24; Cole-Palmer). The PDMS valve chambers are connected via the external tubing to a pneumatic manifold (LFMX0510438BF; The Lee Company) with eight solenoid valves (LHDA1211111H; The Lee Company). The solenoid valves allow the air pressure in the PDMS valves to be switched being atmospheric pressure and compressed air.

In order to achieve computer control of the solenoid valves, I use a 24-channel digital I/O controller (USB-6501; National Instruments) connected to the computer via USB. However, the digital I/O controller outputs typical TTL voltage levels, 0 and 5 V for logic low and high respectively, with a maximum single channel current of 8.5 mA and a maximum combined current of 65 mA. However, the digital outputs are insufficient to directly operate the solenoid valves which require 12 V to switch and draw 46 mA each. The digital I/O can control a transistor circuit, shown in Fig. 3.3(a), to switch the current through the solenoid valves on and off. The choice of base resistor and transistor needs to match the specifications of both the digital I/O controller and the solenoid valves. A transistor acting as a switch operates in a saturated mode such that the voltage drop from the collector to the emitter, V_{CE}, is almost zero with negligible power dissipation in the transistor itself. In the saturated mode, the current into the transistor collector, I_{C}, is determined entirely by the load, in this case the solenoid valve, so that $I_{\mathrm{C}} = I_{\mathrm{L}}$ when the switch is on. To ensure that the transistor is saturated, the minimum current gain, $h_{\mathrm{FE}}(min)$, should be five times larger than the ratio of the collector current to the maximum base current:

$$h_{\mathrm{FE}}(min) > 5\frac{I_{\mathrm{C}}}{I_{\mathrm{B}}(max)} \tag{3.1}$$

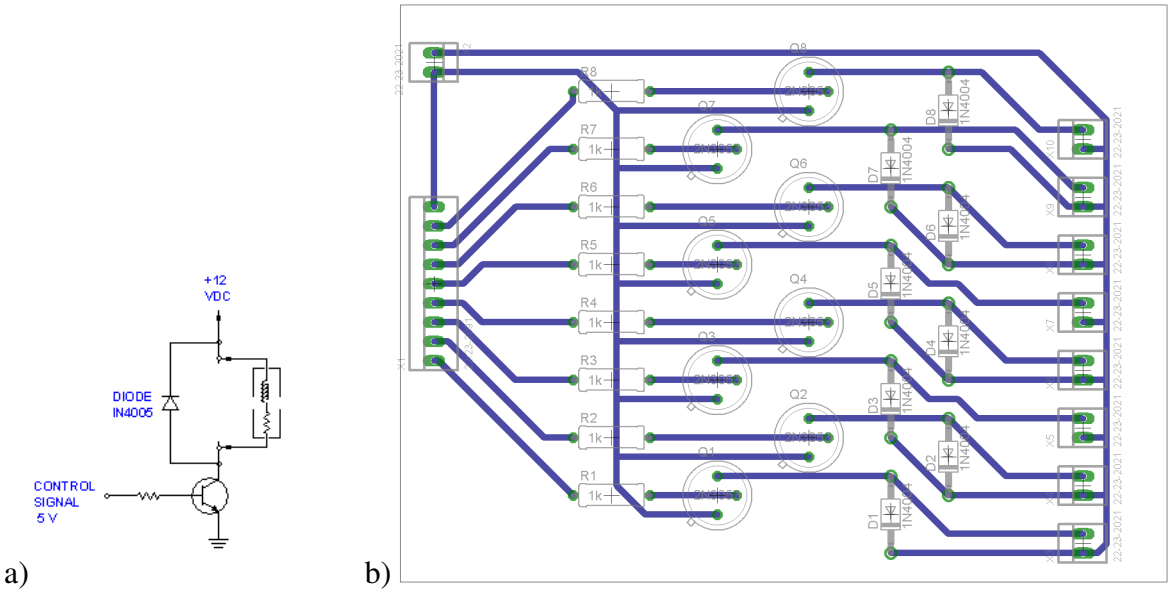

Figure 3.3: (a) Circuit diagram of a basic transistor switch for a solenoid valve. (b) Schematic of first generation printed circuit board with transistor switches for controlling eight solenoid valves.

where $I_{\mathrm{B}}(max)$ is the maximum current into the transistor base from the digital I/O controller, in this case 8.5 mA. Once a transistor is chosen, the values for $h_{\mathrm{FE}}(min)$ and the load current, I_{L}, can be used to determine an approximate base resistor value, R_{B}:

$$R_{\mathrm{B}} = \frac{V_{\mathrm{DIO}}}{I_{\mathrm{DIO}}} = \frac{V_{\mathrm{DIO}} h_{\mathrm{FE}}}{5 I_{\mathrm{L}}} \tag{3.2}$$

where V_{DIO} and I_{DIO} are the maximum voltage and current of the digital I/O controller. Using these equation to calculate the appropriate transistor parameters and base resistors, I built a first-generation printed circuit board (PCB), shown in Fig. 3.3(b), which uses the 2N3053 NPN transistor ($h_{\mathrm{FE}}(min) = 50$) and a 1 kΩ base resistor and is capable of controlling the eight solenoid valves in the manifold.

Since the fabrication of the first generation PCB, the circuit has undergone a few significant changes. The most notable is the use of inverters (also known as NOT gates) between the digital I/O controller and the transistor circuit. This is advantageous because the controller's digital outputs revert to logic high states when the controller's power is cycled, for example when it is reconnected to the computer or when the computer is restarted, which previously caused the solenoids switch and compressed air to be sent to the PDMS valves inadvertently. In some instances pressures

greater than 20 psi are required (the limit of the Lee solenoid valves). For these situations, two more robust solenoid valve manifolds (H010E1; Humphrey Valves, and EVO-3M-24; Clippard) are employed which use 24 VDC, can handle up to 100 and 105 psi, and draw 70 and 28 mA respectively. Based on the similar calculations, appropriate transistors and base resistors are a 2N4124 transistor and 1.8 kΩ for the first manifold and the 2N3904 and 3.9 kΩ for the second.

3.3.2 Fluid Control

For introducing solutions into the microfluidics and driving flow, fluid handling control is accomplished using a syringe pump (Pump 33; Harvard Apparatus) and an 11-port selector valve (MX-II; Rheodyne). The syringe pump is controlled via serial commands sent from the RS-232 port on the back panel of the main computer. The selector valve also is controlled via serial commands but uses a USB connection to the computer. Along with the basic commands to start and stop the syringe pumps, the data acquisition software also sends commands to set the values for the diameter of the mounted syringe, the desired flow rate, and the direction (infuse or refill) of flow. Tubing from the mounted syringe connects to the common port of the selector valve. The principal command for the selector valve controls which one of ten ports is connected to the common port. A single output port is connected to the input of the chip microfluidics. Other output ports can be used to expel waste fluid from the tubing between the valve and pump or to load small volumes of test solution into the fluid line close to the chip.

3.4 Responsivity Calibration

A critical component to interpreting the microcantilever array response to environmental stimuli is the ability to convert the scaled differential signal into microcantilever deflection. The change in scaled differential signal per unit deflection is the deflection responsivity. The deflection responsivity is measured by physically actuating the microcantilever arrays, as shown in the schematic in Fig. 3.4, and observing the corresponding scaled differential signal. Actuation of the microcantilevers is accomplished with a glass piece attached to a piezotranslator (P-841.30; Physik Instrumente). The glass is 500 μm thick and cut in a tapered shape ~4 cm in length and end widths

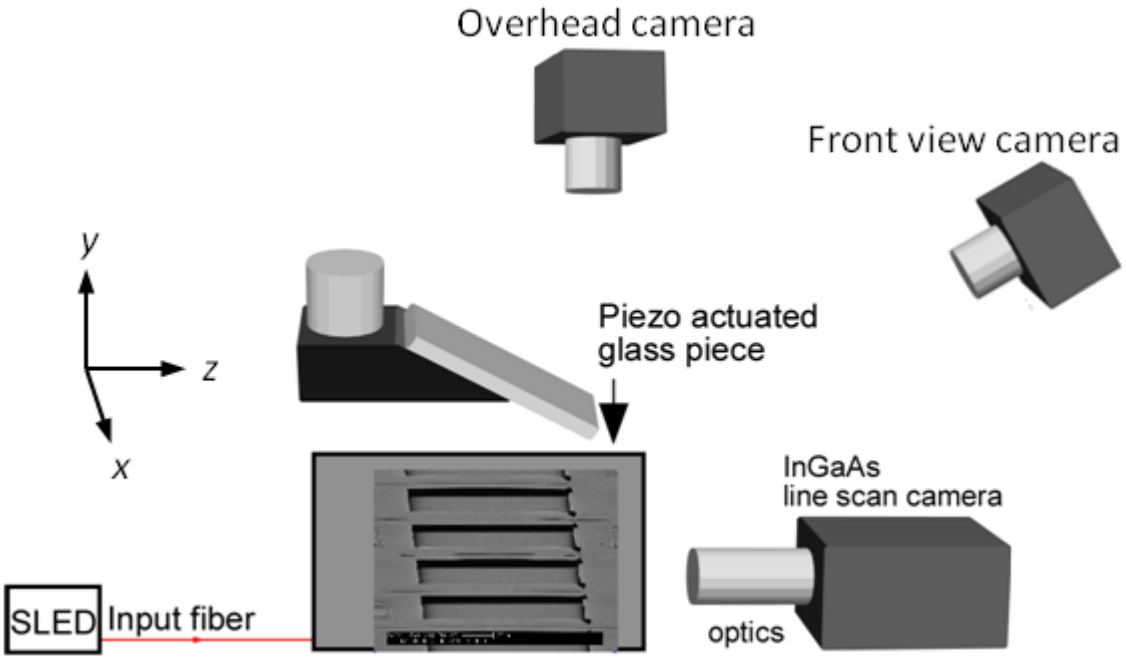

Figure 3.4: General schematic of deflection responsivity calibration measurements.

of 10 and 2 mm. The 2 mm wide end physically contacts the microcantilever array and is polished to remove any defects so that the deflection from cantilever to cantilever is as uniform as possible.

Positioning of the glass piece and the piezotranslator is controlled using a series of stepper motors and rotation stages. When describing the positioning, I define the axes as such (shown in Fig. 3.4): the x and z axes are in the plane of the microcantilever array die, with the z-axis parallel to the microcantilever beam and x-axis transverse to the beam, and the y-axis is normal to the plane of the microcantilever array die. Coarse adjustment along the axes is controlled by three stepper motors (07EAS503 and 07EAS504; Melles Griot). The motors along the x and y axes are controlled using a microcontroller (APT17BSC002; Melles Griot) connected to the main computer; the z-axis motor is controlled manually as the microcontroller can only control two motors. The mount holding the piezotranslator is also mounted on a rotation stage (481-A; Newport) that allows adjustment of the rotation about the y-axis. Finally, rotation about the z-axis is adjusted using a goniometer stage (GNL18; Thorlabs). The motors and rotation stages allow the polished edge of the glass piece to be positioned so that it is parallel to the xz-plane and to the line defined by the free ends of the microcantilevers in the array.

Aligning the glass piece to the microcantilever array in preparation for the measurement of the deflection responsivity is a multistep process. Two cameras with adjustable magnification optics assist in positioning the glass piece relative to the microcantilever array. One camera provides an overhead view while the second looks at the microcantilever array from in front and above the die. Initially, the coarse y-axis motor is adjusted so that the glass piece is a few centimeters above the the plane of the die. The z-axis motor is manually adjusted until the glass piece is above the microcantilever array, as seen from the overhead camera. The y-axis rotation stage is then used to align the edge of the glass piece with the free ends of the microcantilevers. With the overhead camera at low magnification and the glass piece still centimeters above the die, this alignment can only be done coarsely. Finer adjustment of the rotation is done at a later stage in the alignment procedure. Because the radial distance from the glass piece edge to the axis of rotation is ~15 cm, adjusting the rotation also requires compensating lateral displacements using the x-axis. The y-axis motor then lowers the glass piece in 100 μm steps until it is approximately 100 μm above the array, as seen from the front view camera. At this stage the magnification of the overhead camera is maximized at which point only a two or three microcantilevers are visible in the camera's view. Now the rotation about the y-axis can be adjusted more finely and the rotation stage locked, and position in the xz-plane adjusted so that the edge is just above the free end of the microcantilevers. The glass piece is lowered using the y-axis stepper motor in 10 μm steps until it is several 10s of microns above the microcantilever array. Some adjustment of the rotation of the glass piece about the z-axis can be made using the goniometer stage based on the image from the front view camera.

After the coarse positioning described above, a final finer adjustment is performed prior to the calibration measurement. For the finer adjustment, the overhead and front view cameras do not have sufficient resolution, and so the quality of the alignment is taken from the optical outputs of the microcantilever array. The glass piece is lowered in initially 2 μm steps towards the array with the piezotranslator until the optical outputs, as seen from the line scan camera, disappear from view. If the rotation about the z-axis is off, the outputs from one end of the array will respond before the other end. This may require the use of smaller step sizes, usually down to 0.5 μm, to more precisely observe any difference in response across the array. In this case, the piezotranslator returns to its zero position raising the glass piece up and the rotation adjusted using the goniometer stage. The process of lowering the glass piece, observing the repose of the optical outputs, and

adjusting the goniometer stage is repeated until the edge is parallel to the plane of the die. Finally, the piezotranslator is moved about 1.5 μm above the position at which it makes contact with the microcantilevers.

For the measurement of the deflection responsivity the piezotranslator is set to step through a 3 μm range in 0.05 μm steps. This range is usually sufficient to push the microcantilevers completely through the expected 1 μm dynamic range, although a larger range can be used if needed. I find that the 0.05 μm step size is the minimum repeatable step size which the piezotranslator can achieve. Additionally, the piezotranslator goes through the range twice, going down and coming back up. As the piezotranslator comes back up, a number of the microcantilevers adhere to the glass piece allowing the scaled differential signal to be measured for deflection states above their original deflection state. The attraction between the glass piece and the microcantilevers and the glass piece can be enhanced by blowing compressed air across the edge of the glass piece prior to the initiation of the alignment procedure, which I believe generates a static charge on the glass piece and results in electrostatic attraction between the glass and microcantilevers. The data acquisition computer records the piezotranslator position and takes several scans from the line scan camera of the outputs from the microcantilever array. To assist in converting the piezotranslator position to actual microcantilever deflection, two images are recorded using the overhead camera with its highest magnification, one image of the glass piece edge at the beginning of the calibration process (nearly making contact with the microcantilevers) and a second image at the same magnification of the same region with the glass piece moved for an unobstructed view of the full length of the microcantilever. I then measure the distances from the base of the microcantilever to the edge of the glass piece, from the first image, and to the free end of the microcantilever, from the second image. For small deflections, the ratio of the second distance to the first distance provides the conversion factor for converting the piezotranslator position to microcantilever deflection.

3.5 Other Equipment

A number of other devices are connected to the data acquisition computer, some of which are only connected for a specific type of experiments. Connected to the computer via GPIB is a function generator (33250; Agilent) whose output provides the control voltage for SLED. The function generator is included mainly with the intent of developing a lock-in amplifier which re-

quires a modulated source. However, in normal operation the function generator provides an adjustable DC control voltage. Being able to adjust the DC output power of the SLED gives the experimental setup more degrees of freedom to accomodate a variety of array designs and, when combined with the variable exposure time of the line scan camera, the means to achieve low-noise measurements. Another device is a Peltier thermoelectric cooler (1MC06-030-05.TB103; RMT Ltd.) and its commercial microcontroller (DX5100; RMT Ltd.). While the microcontroller uses a slightly uncommon RS-422 data communication protocol, fortunately the microcontroller is sold with a USB to RS-422 converter. A thermistor attached to the thermoelectric cooler (TEC) provides temperature feedback to the microcontroller. The main commands for the microcontroller set the target temperature, retrieve the current temperature according to the thermistor, and define the parameters of the PID algorithm for matching the target temperature. An advantage of the TEC microcontroller is that a series of target temperatures and durations can be programmed into the microcontroller to be executed in series later, reducing the need for multiple commands from the main computer to change the target temperature over the course of an experiment.

3.6 Control and Acquisition Software

As mentioned previously, the whole data acquisition system is brought together in a LabVIEW environment. Each experiment required slightly different variations, but each had a common basic structure illustrated in Fig. 3.5. The basic structure consists of three main panels in a LabVIEW sequenced structure. The first panel initializes the equipment, such as defining the internal buffer size of the line scan camera, switching all the solenoid valves to the off position, opening and creating files for the data acquisition, and other such tasks. The second panel consists of a main while-loop which contains the body of the data acquisition software and terminates when the user elects to exit the experiment. The final panel includes all the necessary commands for shutting down the system. The main while-loop contains an event structure that watches for specific changes (button presses or control value changes) from the graphical user interface (GUI) and performs the appropriate actions in repose. Additionally, the while-loop contains a case structure that determines whether or not an image is retrieved from the camera. Commercial driver VIs have been provided for some equipment, such as the line scan camera and piezotranslator, however

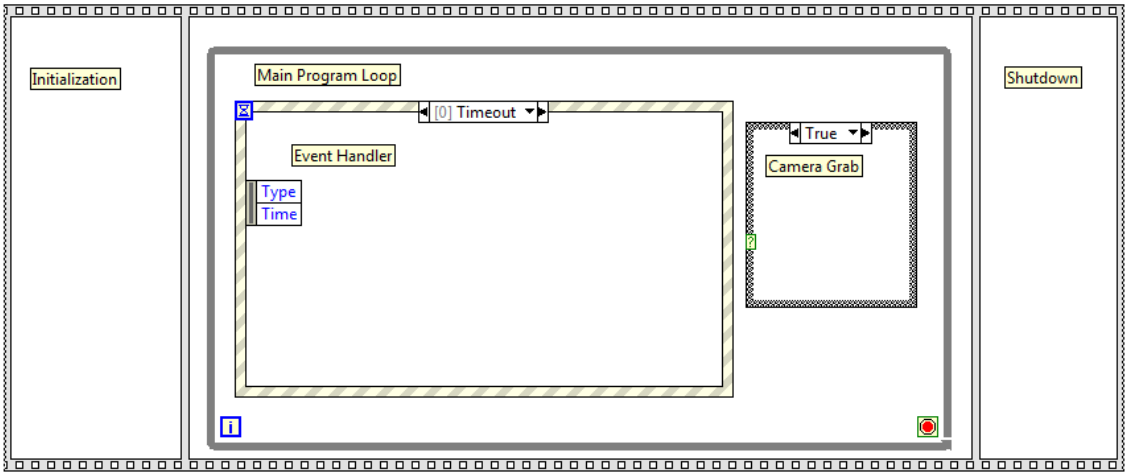

Figure 3.5: General LabVIEW block diagram for data acquisition control.

other equipment, such as the selector valve and syringe pump, required that I write my own driver VIs based on the serial commands found in the equipment documentation.

The VI for each experiment differs principally in the event structure in main while-loop. For the calibration measurements, the event structure watches for four main events: a switch for continuously retrieving images from the camera, a set of controls for the camera settings, a numeric control for the position of the piezotranslator, and a button to initiate a calibration measurement. Continuous retrieval of images does not save the images, but merely displays in the GUI the average of all line scans in an image to assist in the alignment of the optics and camera. The event structure only contains the commands to tell the camera to begin or stop acquiring and storing images. The case structure outside of the event handler contains the actual commands to retrieve the images from the camera, so that other events can be handled while the images are continuously acquired and displayed. The commands for this event and for the event of changing the camera settings are common to all experiment. The numeric control for the position of the piezotranslator should be used with caution. Instead of manually setting the number, I prefer to use the increment/decrement buttons adjacent to the numeric control field. Doing so ensures that I will not accidentally enter the wrong number and cause the glass piece push the microcantilevers into underlying surface. When the value of the numeric control is changed, a command is sent to the piezotranslator's microcontroller with the new position to which it should move. Finally, the button

for initiating a calibration measurement takes the entered values for the upper and lower positions and the number of steps to determine the series of positions for each step and creates an array with correspond series of commands to the piezotranslator. At each step, the piezotranslator the next element in the command array is sent, telling it to the new position, and the piezotranslator is queried several times for its position after it has moved. Also at each step an image is acquired from the camera. The rows of the images are averaged together and the columns corresponding to the pixels where the outputs are imaged are extracted and saved to a file. The format of the saved file matches with the data processing software (IGOR; Wavemetrics) which I use so that the scaled differential signal and relevant graphs are automatically created when the file is loaded.

Other experiments replace the piezotranslator commands with a variety of other sets of commands corresponding to the equipment and the experimental setup. For example, a similar approach is used for the experiments looking at the thermal deflection response of the microcantilever array. Instead of the piezotranslator microcontroller, commands and queries are sent to the TEC microcontroller. The user defines the start and stop temperatures, how many steps in between, and the time spent at each step, which should be sufficient to allow the PID feedback to lock to the target temperature. Similarly, at each step the temperature is queried and an image is captured from the camera. Rather than averaging the multiple line scans of an image, all line scans are kept to improve the temporal resolution of the microcantilever response.

Experiments involving microfluidics are the most complicated since the software includes events and commands for controlling the syringe pump the selector valve, and the solenoid valve manifold. As previously mentioned, the syringe pump and the selector valve are controlled using serial commands and the solenoid valves are controller with a the digital I/O interface. The VI in this case is capable of initiating a number of automated experiments. Most of these automated experiments involve data acquisition from the line scan camera over an extended period of time (>500 s). To prevent a memory overflow in LabVIEW, the pixel values from the acquired images are written to a temporary text file. Once the data acquisition terminates, the temporary file is then read line by line (reading the whole file at once also often results in a memory overflow), and the relevant columns extracted and written to the final data file. For experiments involving the sensing of a target analyte, initiation of the experiment begins a state machine that controls the automation. These experiments require preparing the microfluidics by loading the solution to be analyzed into

the microfluidic bypass channel on chip. The user defines the time when certain events will happen as well as which solenoid valves correspond to which PDMS valves in the microfluidics. When the experiment is initiated, the state machine sends a command setting the volumetric flow rate of the syringe pump but not starting the pump. After a user-defined period, the command to start pumping is sent, and again after a period, sends a command to the digital I/O controller to open the PDMS valves to the microcantilever array channel. After an extended period of time, the commands to stop the syringe pump and close the PDMS valve are sent. Finally, after another short period, the camera stops acquiring images and the experiment terminates.

CHAPTER 4. COMPARISONS AND MEASUREMENTS OF MICROCANTILEVER THERMAL STABILITY

4.1 Motivation

A common practice in functionalizing the microcantilever is to deposit a thin layer of gold on one surface. The gold layer also can provide a highly reflective surface for the incident laser beam used in the optical beam deflection method [46–48], the most common means of detecting microcantilever deflection. It has previously shown that the gold layer itself can act as a selective coating, as demonstrated by the detection of mercury vapor [6, 35, 49] and alkanethiols [4, 50]. For chemical sensors, the gold layer provides a surface that readily reacts with thiolated molecules, a technique that is widely used to attach selective coatings to the microcantilever surface. The gold layer also is likely to play a significant role in the generation of surface stress for static deflection measurements [51]. However, the dissimilar coefficients of thermal expansion between gold and the microcantilever material (usually silicon or silicon nitride) result in differential surface stresses in response to thermal fluctuations, which cause a temperature induced deflection of the microcantilever. The temperature sensitivity of the structure has been used to remotely sense infrared radiation [52], to detect the heat transfer for chemical reactions [3], and to calibrate the signal-to-deflection responsivity of microcantilever sensors [25, 37, 53, 54]. In order to distinguish thermal fluctuations from other environmental stimuli, microcantilever chemical sensors that use a gold-based attachment chemistry must implement measures to reduce the temperature-dependent effects. Such measures include precise temperature control of the environment [29, 30, 33, 48], non-functionalized reference cantilevers [29, 30, 33, 46, 48, 55, 56] and an additional gold coating on the non-functionalized surface of the microcantilever.

4.2 Design

4.2.1 Equipment and Sample Preparation

To investigate the thermal response of silicon microcantilevers, I fabricated silicon microcantilever arrays and differential splitter structures for in-plane all-photonic transduction with silicon-on-insulator (SOI) wafers having a 1 μm buried oxide layer and a 750 nm silicon device layer [43, 44]. Prior to patterning the waveguide and microcantilever structures, the SOI wafers undergo a boron ion doping implantation in the areas around the waveguides. The boron doping increases the opacity of the exposed regions and diminished the scatter and unguided light at the output face. The microcantilevers themselves are 45 μm wide and 650 nm thick; devices were made with both 300 μm and 200 μm long microcantilevers to demonstrate the effect of the length of the microcantilever on the thermal response. An embedded rib waveguide with a rib height of 100 nm and width of 1.6 μm extends down the center of each microcantilever to form a single mode waveguide at a wavelength of 1550 nm. All other waveguides within the device, with the exception of the differential splitter, have the same dimensions. As shown in Fig. 4.1(a), a fabricated sensor die has three microcantilever arrays, two with 8 microcantilevers and one with 16 microcantilevers. A Y-branch waveguide network directs light from a single input to all microcantilevers in an array. For the sample which is used in the photonic transduction measurements, the responsivities of the microcantilevers are measured, shown in Fig. 4.2, using the process described in Refs. [43, 45].

On select samples, thin film gold coatings are deposited via e-beam evaporation on some of the microcantilever using photolithography. Each array of microcantilevers consisted of three types of coating, as shown in Fig. 4.1(b): full, partial, and no coating. For the microcantilevers with a full coating, gold was deposited along the entire width and length of the microcantilever. A gold film on the surface of the waveguide completely extinguishes the guided mode by coupling it into a radiative external mode, making the full gold coating incompatible with the in-plane photonic transduction. Therefore on some of the microcantilevers I deposited a partial gold coating by exposing 15 μm wide strips along each outside edge of the microcantilever, leaving a 15 μm wide strip centered on the waveguide and running the entire length of the microcantilever protected by photoresist. In this way microcantilever structure with a high thermal sensitivity could be observed

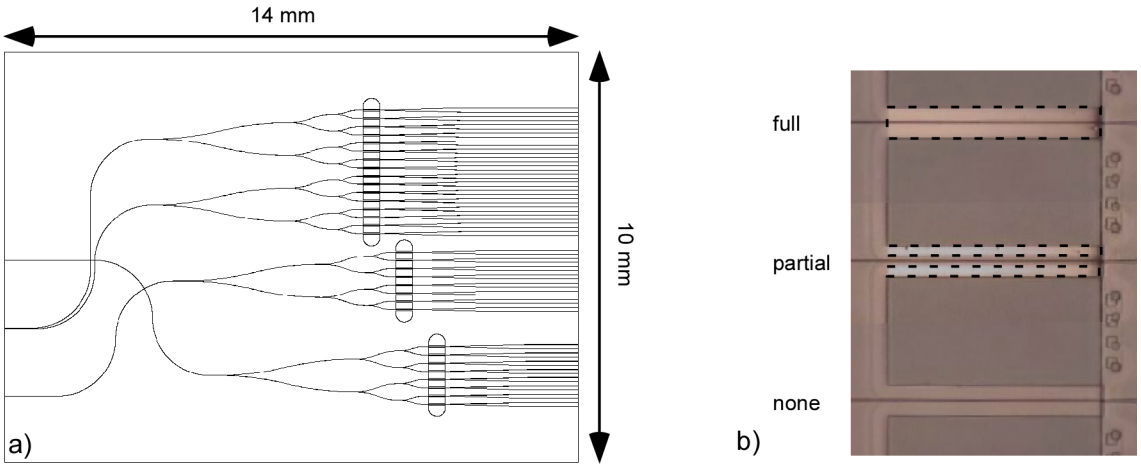

Figure 4.1: (a) Schematic diagram of waveguides and microcantilever array layout on die. (b) Images of the three types of gold coating used for thermomechanical response measurement. In the images, the gold is the more reflective surface and the boundaries of the regions where it is deposited are shown by the dashed lines.

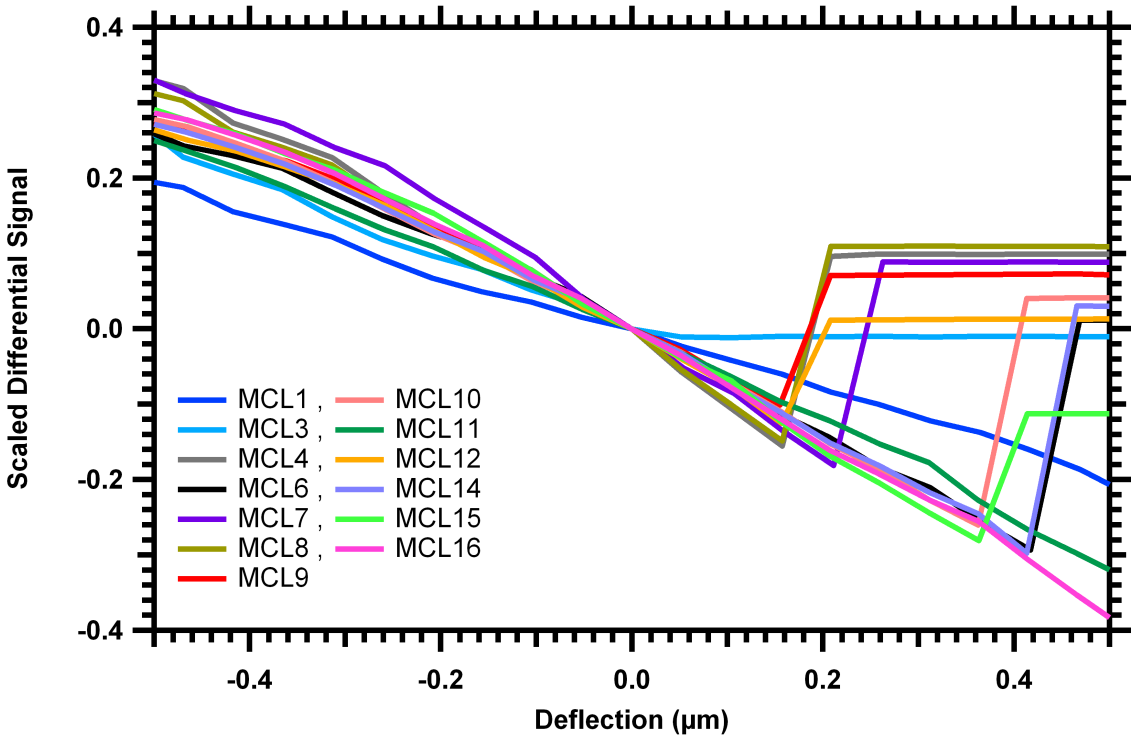

Figure 4.2: Responsivities of microcantilever array used for thermal sensitivity. No output signals are shown for microcantilevers that are broken or stuck down (MCLs #2, 5, 13).

with the in-plane photonic transduction. It was expected that the deposited gold and chromium films would have some amount of residual surface stress [57]. However, despite testing other gold deposition methods, all deposited gold layers, both full and partial, had sufficient residual surface stress to deflect the microcantilevers out of the range measurable by photonic transduction.

Sample temperature was monitored and controlled by mounting the SOI chip on a Peltier thermoelectric cooler (1MC06-030-05.TB103, RMT Ltd.). A thermistor attached to the top surface of the thermoelectric cooler provided feedback to a commercial microcontroller (DX5100, RMT Ltd.) which implemented a PID algorithm to keep the sample at a set temperature. In addition to the provided commercial control software, additional drivers were developed for the microcontroller in LabVIEW (National Instruments) to integrate temperature control with previously written data acquisition LabVIEW software.

4.3 Measurements

4.3.1 SEM Measurements

As microcantilevers with the full or partial coating are deflected more than 0.5 μm due to residual stress, the in-plane photonic transduction is only used to measure the microcantilever thermal deflection response for an array of uncoated microcantilevers. A scanning electron microscope (SEM) is used to measure the thermal deflection responses for microcantilevers with the full and partial gold coatings, as well as for microcantilevers with no gold coating. As shown in Fig. 4.3, the samples are mounted on the thermoelectric cooler (TEC). The mount is also rotated so the sample plane is 10° from vertical and from the incident electron beam so that the deflection of the microcantilever can be measured (see Fig. 4.4).

The samples fabricated for the SEM measurements include microcantilevers that are 200 μm and 300 μm in length, with the three coating patterns (full, partial, and none) for each length. The temperature is increased from 299 K up to 319 K in 2 K steps using the TEC microcontroller and its commercial software. At each step, a SEM image is captured once the the temperature has stabilized to the set temperature, usually a duration of 30-60 s. From the images, the microcantilever deflection is measured from the bottom of the microcantilever to the top of the substrate layer at the differential splitter, taking into account the 10° deviation from vertical orientation of the sample.

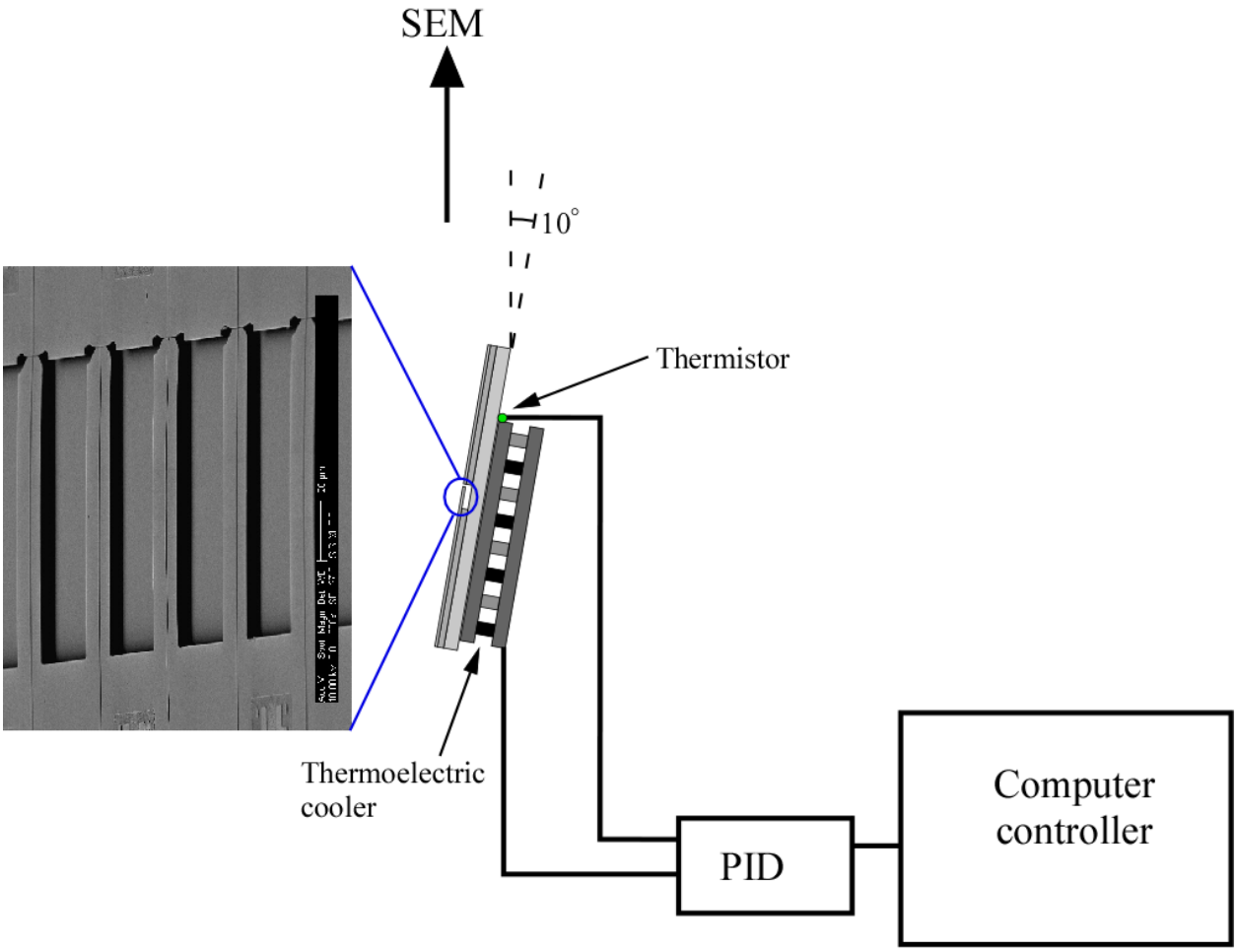

Figure 4.3: Schematic of SEM testing setup.

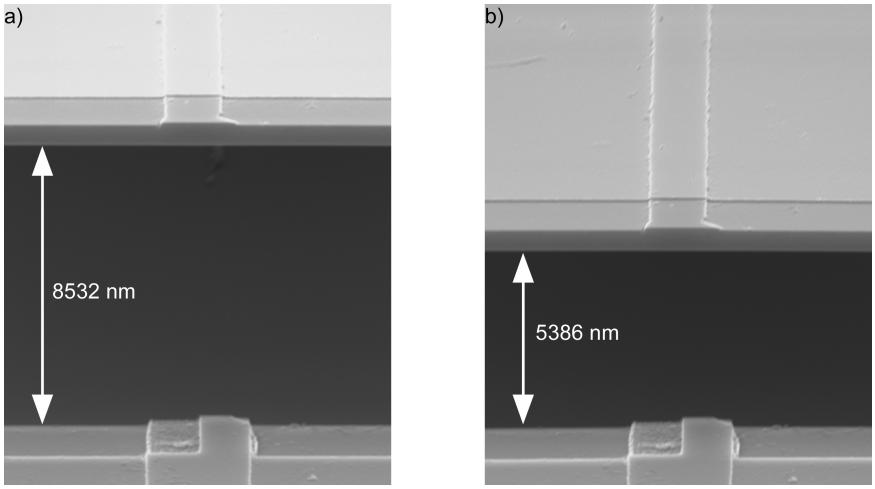

Figure 4.4: SEM images for gold coated microcantilever at (a) 301 K and (b) 319 K.

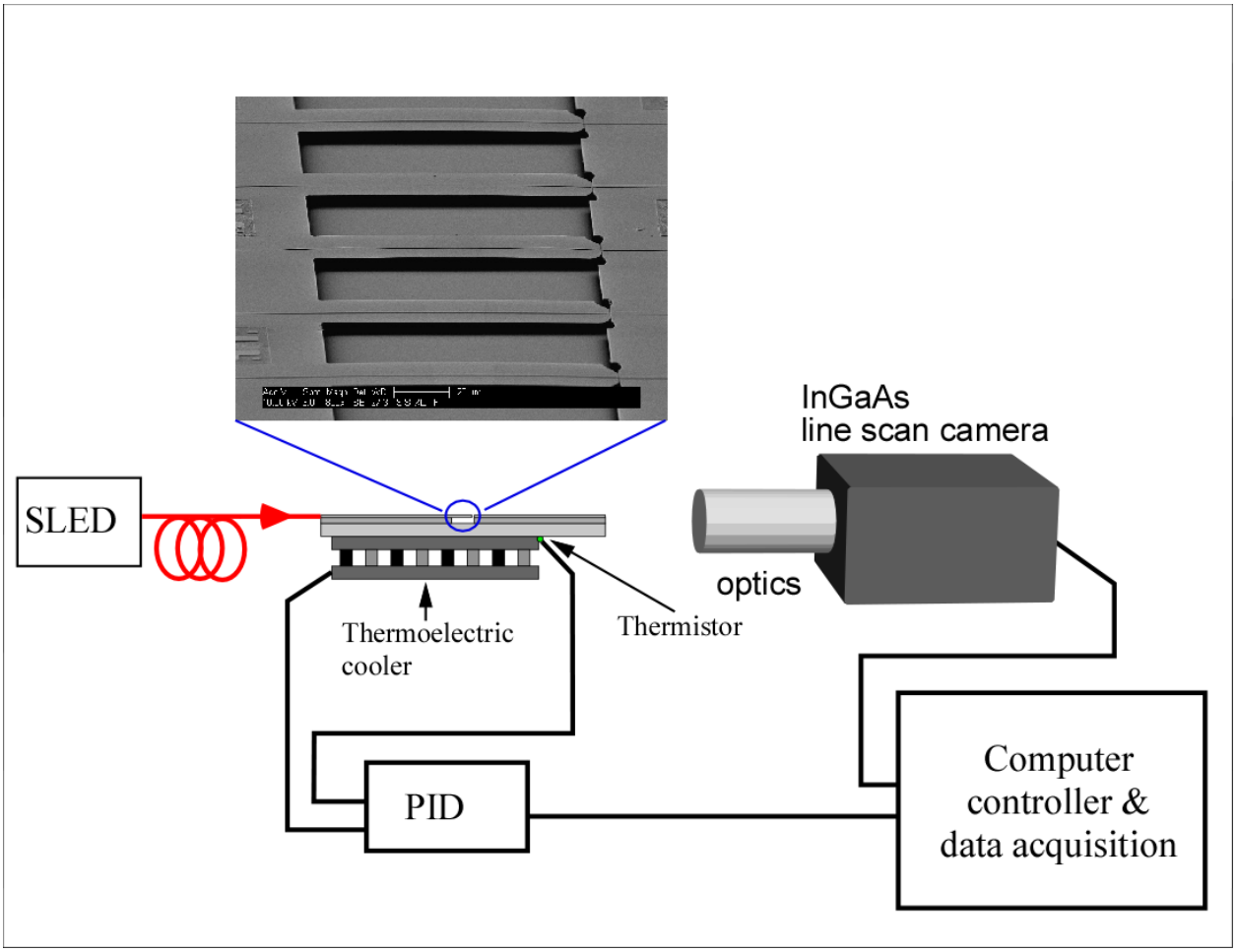

Figure 4.5: Schematic of experimental setup for measuring thermally induced deflection of microcantilevers using in-plane photonic transduction.

4.3.2 Photonic Transduction of Uncoated MCLs

The schematic shown in Fig. 4.5 shows the layout of the experimental setup for measurement of the thermal deflection response of an array of uncoated microcantilever. As in the SEM images, the sample is placed on TEC which is controlled with a commercial microcontroller. Unlike the SEM measurements, none of the microcantilevers have been coated with gold for reasons discussed previously. In addition, for the photonic transduction measurements the deflection of the entire array of microcantilevers, as opposed to a single microcantilever, is acquired simultaneously. Data acquisition also is continuous at a rate ~4 kHz as the set temperature of the TEC changes. The set temperature is increased in 2 K steps from 299 K to 319 K, each step having a duration of 30 s.

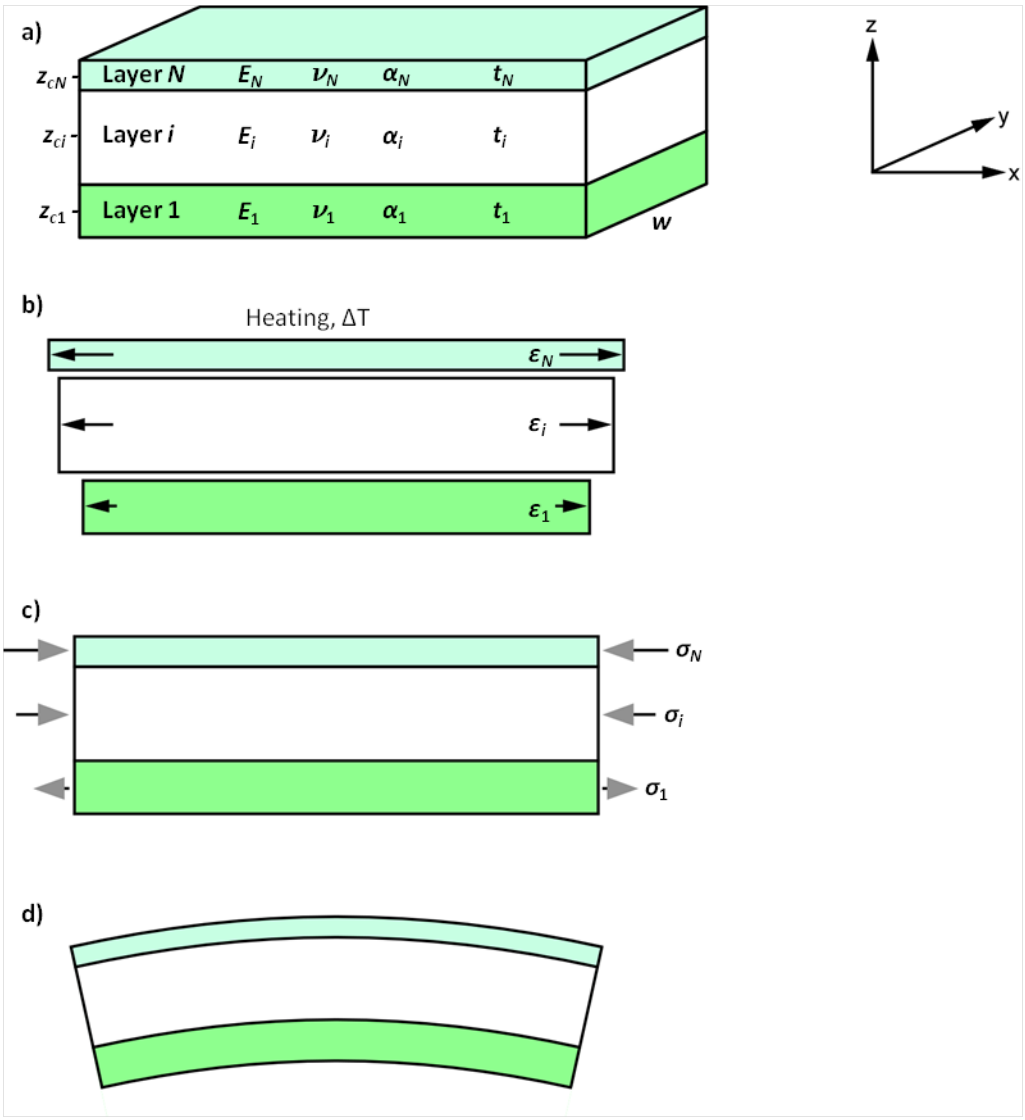

Figure 4.6: Analysis of the bending of a multilayer beam due to thermal expansion. (a) The beam consists of N layers with different material properties (E, ν, α) and thicknesses (t). (b) The layers are allowed to expand due to a temperature change as if they were not connected. (c) External stresses are applied to remove strain discontinuities and the layers are reconnected. (d) The unbalanced moment results in beam curvature.

4.4 Results and Analysis

4.4.1 Theory

Multilayer Beam Bending

One of the common methods to analyze the bending of the composite beam structure under these conditions is illustrated in Fig. 4.6 [58–60]. As shown in Fig. 4.6, the coordinate axes are defined such that the length of the beam extends in the x-direction, the width in the y-direction, and the thickness in the z-direction. To find the solution for the strain distribution throughout the the composite beam and to ensure that the distribution satisfies the necessary boundary conditions, the total strain of the beam is decomposed into a constant uniform component, c, and a bending component. The bending strain component is inversely proportional to the radius of curvature and varies linearly with distance from the neutral axis of the beam, so that the total strain can be formulated as [60]

$$\varepsilon = c - \frac{z-\delta}{R}. \tag{4.1}$$

The strain distribution solution is therefore characterized by three parameters: the uniform strain component c, the position of the neutral axis δ, and the radius of curvature R, which can all be found from the material properties of the layers and by applying the necessary boundary conditions.

In the analysis, each material layer of the beam is treated as a separate structure unconnected to the other layers as seen in Fig.4.6(b). When the i-th layer undergoes a temperature change ΔT, the thermally-induced change in length causes a strain

$$\varepsilon_i = \alpha_i \Delta T \tag{4.2}$$

where α_i is the thermal expansion coefficient. The thermally-induced strain in each layer is then constrained by compression/tensile forces so the layer lengths are compatible for bonding (Fig. 4.6(c)). The compressive and tensile stresses that are applied for displacement compatibility must satisfy two boundary conditions. These conditions are that the resultant strain cannot be discontinuous at the interface between layers and that the net force on all layers must sum to zero.

These two conditions can be expressed as

$$\varepsilon_i + \frac{\sigma_i}{E_i} = c \tag{4.3}$$

and

$$\sum_{i=1}^{N} w_i t_i \sigma_i = 0 \tag{4.4}$$

where σ_i is the applied stress to the i-th layer, w_i and t_i are the width and thickness of the layer, E_i is the Young's modulus of the material, and N is the number of layers. Solving the two equations for the uniform strain component c gives the formula

$$c = \frac{\sum E_i t_i w_i \varepsilon_i}{\sum E_i t_i w_i}. \tag{4.5}$$

When the layers are bonded together the beam will bend due to the unbalanced moment of the asymmetric external forces (Fig. 4.6(d)). The bending strain induced by this will vary linearly with distance from the neutral axis. Just as the net force due to the external stresses summed to zero, likewise the sum of the forces due to the bending strain should sum to zero. This is expressed as

$$\sum \int_{z_{ci}-t_i/2}^{z_{ci}+t_i/2} w_i E_i \frac{z-\delta}{R}\, \mathrm{d}z = 0 \tag{4.6}$$

where z_{ci} is the z-coordinate of the center of the i-th layer. From this equation can be found the position of the neutral axis, defined as the axis along which the normal bending stress is zero,

$$\delta = \frac{\sum z_{ci} E_i t_i w_i}{\sum E_i t_i w_i}. \tag{4.7}$$

The other boundary condition which must be satisfied when the beam is allowed to bend is that the moments with respect to the neutral axis sum to zero. In other words, the bending moment due to the external forces from the first step will be balanced by the bending moment due to the bending

strain. This gives the relationship

$$\sum (z_{ci} - \delta)\, w_i t_i \sigma_i - \sum \int_{z_{ci}-t_i/2}^{z_{ci}+t_i/2} w_i E_i \frac{(z-\delta)^2}{R}\, \mathrm{d}z = 0,$$
$$\sum z_{ci} w_i E_i t_i\, (c - \varepsilon_i) - \frac{1}{3R} \sum w_i E_i t_i \left(3z_{ci}^2 + \frac{t_i^2}{4} - 3\delta z_{ci} \right) = 0. \tag{4.8}$$

Note that reducing this boundary condition to the final form of Eq. 4.8 involves eliminating terms in the summations which are known to sum to zero from Eqs. 4.4 and 4.6. The equation for the radius of curvature in terms of known and previously solved for parameters then becomes

$$\frac{1}{R} = \frac{\sum z_{ci} w_i E_i t_i\, (c - \alpha_i \Delta T)}{\sum w_i E_i t_i \left(z_{ci}^2 + \frac{t_i^2}{12} - \delta z_{ci} \right)}. \tag{4.9}$$

For a simple cantilever consisting of two layers of equal widths, the form of Eq. 4.9 simplifies to

$$\frac{1}{R} = \frac{-6 E_\mathrm{d} E_\mathrm{s}\, (t_\mathrm{d} + t_\mathrm{s})\, t_\mathrm{d} t_\mathrm{s} \Delta\alpha \Delta T}{E_\mathrm{d}^2 t_\mathrm{d}^4 + 4 E_\mathrm{d} E_\mathrm{s} t_\mathrm{d}^3 t_\mathrm{s} + 6 E_\mathrm{d} E_\mathrm{s} t_\mathrm{d}^2 t_\mathrm{s}^2 + 4 E_\mathrm{d} E_\mathrm{s} t_\mathrm{d} t_\mathrm{s}^3 + E_\mathrm{s}^2 t_\mathrm{s}^4} \tag{4.10}$$

where $\Delta\alpha = \alpha_\mathrm{s} - \alpha_\mathrm{d}$ and the subscripts d and s indicate the deposited layer and the substrate, respectively [59, 61]. It is sometimes advantageous to group terms and use substitution to reduce this form so that the formula for the deflection, Δz, of the free end of a cantilever of length L can be expressed as [62]

$$\begin{aligned} \Delta z &\approx \frac{L^2}{2R}, \\ &\approx \frac{3 \Delta\alpha \Delta T (n+1) L^2}{t_\mathrm{s} K} \end{aligned} \tag{4.11}$$

where

$$K = 4 + 6n + 4n^2 + \phi n^3 + \frac{1}{\phi n},$$
$$n = \frac{t_\mathrm{d}}{t_\mathrm{s}},$$
$$\phi = \frac{E_\mathrm{d}}{E_\mathrm{s}}.$$

In the case that the width of the deposited layer is not the same as the substrate layer, the modulus of elasticity for the deposited layer is replaced with and effective modulus such that $E_{\mathrm{d}}^{*} \rightarrow \frac{w_{\mathrm{d}}}{w_{\mathrm{s}}} E_{\mathrm{d}}$.

Parameter Choice

The general solution to a composite beam described previously is only valid when the thermally-induced strain is uniform (*i.e.* the temperature gradient across the thickness of the beam is negligible) and the system remains elastic while the curvature is adopted [59]. The solution also only assumed in-plane stresses in the x-direction. A minor modification is made when the other in-plane stresses are considered. For an isotropic in-plane stress, the stress in the x-direction, σ_x, is accompanied by another stress of equal magnitude in a perpendicular direction, in this case the y-direction. The stress σ_y will in turn contribute a Poisson strain in the x-direction. If the stiffness is isotropic and the through-thickness stress σ_z is negligible, the complete stress-strain relationship for an isotropic material can be written as

$$\varepsilon_x = \frac{1}{E}\left(\sigma_x - \nu\sigma_y\right) = \frac{\sigma_x}{E}(1-\nu) \tag{4.12}$$

where ν is the Poisson's ratio. From this relationship a biaxial modulus, $E^{'}$, can be defined as

$$E^{'} = \sigma_x/\varepsilon_x = \frac{E}{(1-\nu)}, \tag{4.13}$$

which is used in place of the uniaxial modulus to find the deflection [63, 64].

The biaxial modulus for anisotropic materials can be more complicated and depends on the orientation of the beam relative to the material axes. Usually this requires looking at the full stress-strain tensor and rotating the tensor appropriately to obtain the the modified modulus along the beam axis. Fortunately, symmetries in the anisotropic material can simplify finding the biaxial modulus. For example, orthotropic materials such as silicon (due to its cubic symmetry) have a stress-strain relationship for in-plane stresses that can be written as

$$\varepsilon_x = \frac{\sigma_x}{E_x} - \frac{\nu_{yx}\sigma_y}{E_y} = \sigma_x\left(\frac{1}{E_x} - \frac{\nu_{yx}}{E_y}\right) \tag{4.14}$$

where ν_{ij} is the Poisson's ratio corresponds to a contraction in the j-direction when an extension is applied in i-direction. Again the modified Young's modulus is defined as $E_x^{'} = \sigma_x/\varepsilon_x$. For microcantilevers with surfaces in the (100) plane and edges along the $[110]$ direction, the symmetry of silicon is such that the relevant elastic parameters are $E_x = E_y = 169$ GPa and $\nu_{xy} = 0.064$. Using Eq. 4.14 and the relationship $\nu_{yx} = (E_y/E_x)\,\nu_{xy}$ gives a biaxial elastic modulus $E_x^{'} = 180.6$ GPa for the microcantilever [63].

While it is common practice to use the modified Young's modulus for the silicon substrate of most microcantilevers, it is not common to use the same approach when considering the thin gold or gold/chromium films. This is usually justified by stating that the films are thin (20-40 nm) in comparison to the substrate thickness (1 μm). When applying the analysis to my microcantilevers, and using the dimensions for the composite beam given in Table 4.1, I found that including the contribution of the gold film in fact had a significant effect on the thermal sensitivity of the microcantilevers, contrary to stated assumptions in Refs. [12,65]. Using the unmodified elastic modulus of 81 GPa for gold gives a thermal sensitivity of 95.9 nm/K. However, if the gold film is treated as an isotropic material with a Poisson's ratio of 0.42 and a resulting modified modulus of 140 GPa, the thermal sensitivity increases to 156.1 nm/K. This is an increase of roughly 63%! While this effect is dependent on the relative thicknesses of the silicon and gold layers, it should not be automatically assumed that the contribution of the perpendicular in-plane stress in the thin gold layer is negligible. The calculated values of the thermal sensitivity so far have neglected the contribution of the chromium layer (typically 5-10 nm thick), which is another common practice in the literature on microcantilevers. Including the contribution of a 5 nm chromium interlayer in the thermal sensitivity calculated from Eq. 4.9 increases the sensitivity to 160.1 nm/K, only a 2.5% increase. Therefore it is a reasonable assumption to treat the structure as a simple bilayer and ignore the thermal sensitivity contribution from the chromium layer.

It is therefore unfortunate that a review of the published literature for microcantilever-based devices, specifically silicon microcantilevers, is inconsistent or vague about the choice of and rational for parameter values. In some cases, such as Refs. [25,37,48,54,70], the maximum values of E and ν are used instead of the values commensurate with the microcantilever orientation. Note that this is most problematic in situations where the biaxial modulus is used either explicitly, as in the previous thermal derivation, or implicitly, as in Stoney's formula where it appears as $E/(1-\nu)$,

Table 4.1: Material properties of microcantilever layers.

	Thermal expansion coefficient (K^{-1})	Young's modulus (GPa)	Poisson's ratio	thickness (nm)	width (μm)
Au	2.6×10^{-6} [66]	81 [67]	0.42 [67]	30	30, 45
Cr	4.9×10^{-6} [68]	140 [69]	0.21	5	30, 45
Si	14.2×10^{-6} [66]	169 [63]	0.064 [63]	650	45

since the maxima of E and ν occur at different orientations. Since the biaxial modulus is invariant in the Si(100) plane, it is possible to neglect the orientation of a microcantilever in the (100) plane and still arrive at the correct stress-to-deflection relationship provided the values used for E and ν correspond to the same orientation [71]. Similarly, although theoretical works discussing the thermomechanical behavior of multilayered microcantilevers (Refs. [58–60]) explicitly use the biaxial modulus of the layers, a majority of experimental works, such as Refs. [25, 37, 48, 54, 70], ignore the two-dimensional nature of the stress and use the uniaxial Young's modulus; Refs. [64, 72] are a few of the exceptions in the literature that I have been able to find.

4.4.2 Measured Thermal Responses of Microcantilevers

The measured deflections as a function of change in temperature as measured by the SEM are shown in Fig. 4.7 along with linear fits to the data points.. Measurements are shown from two different samples, one with microcantilevers 200 μm in length and the other 300 μm in length. Both samples had microcantilevers with full, partial, and no gold coatings.long Coated cantilevers match well with calculated thermal sensitivities. Possible variations could be due to anisotropies of the gold layer and uncertainties in the elastic properties of thin film gold. For both microcantilever lengths, the full gold coating results in larger thermal sensitivities than that of the partial gold coating. Also, due to the longer lever arm, the longer microcantilevers showed a larger deflection than the shorter microcantilevers for the same temperature change. In comparison to the microcantilevers with gold coating, those with no coating had a negligible response to temperature changes. However, the thermal sensitivities of the microcantilevers with no coating are not exactly zero, and slightly vary between the microcantilevers.

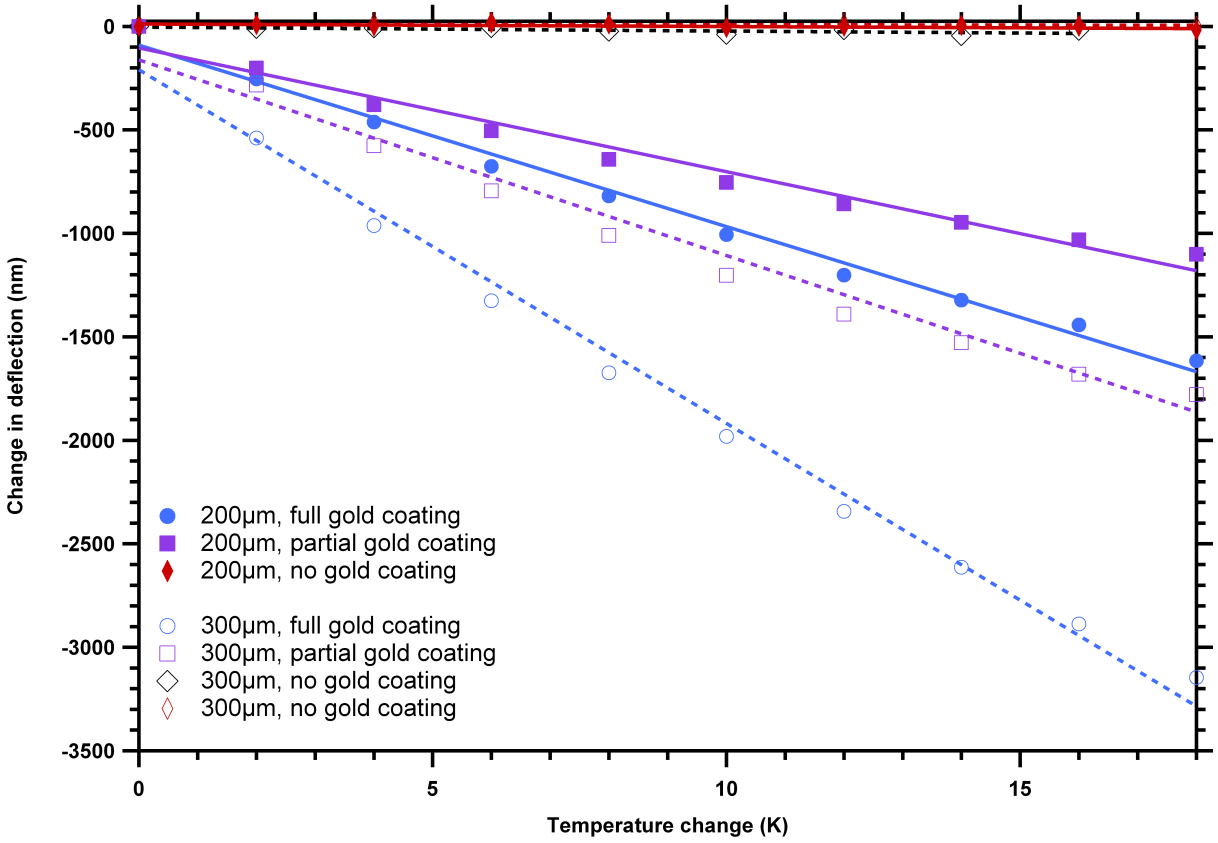

Figure 4.7: Thermally induced deflections of microcantilevers of different lengths, with full, partial, and no gold coating as a function of change in temperature as measured in a scanning electron microscope.

As seen in Table 4.2, the measured sensitivities are within ~5-20% of the calculated values. The calculated values assume film thicknesses and elastic properties given in Table 4.1. Discrepancies between the measured and calculated values could be due to variations in the thicknesses of the deposited metallic layers or the placement of the partial coatings. It should also be noted that research on the elastic properties of metallic thin films is still an active topic, and it is known that the properties can be dependent on thickness and on the conditions during and method of deposition. In the case of the microcantilevers with no coating, the non-zero thermal response and variation would indicate some kind of inhomogeneity in the microcantilever structure or a temperature gradient along the thickness of the microcantilever.

The response of an array of uncoated microcantilevers, as measured by photonic transduction, shows a pattern similar to that of the SEM measured microcantilevers. As seen in Fig. 4.8, the array of microcantilevers 300 μm in length shows a wide variety of thermal sensitivities across

Table 4.2: Thermal sensitivities as measured in the SEM.

MCL Length	Measured Sensitivites (nm/K)			Calculated Sensitivities (nm/K)		
	full Au	partial Au	no Au	full Au	partial Au	no Au
200μm	-87.66	-59.83	-1.24	-71.14	-50.05	~0
300μm	-170.82	-94.51	-0.274, -1.93	-160.06	-112.61	~0

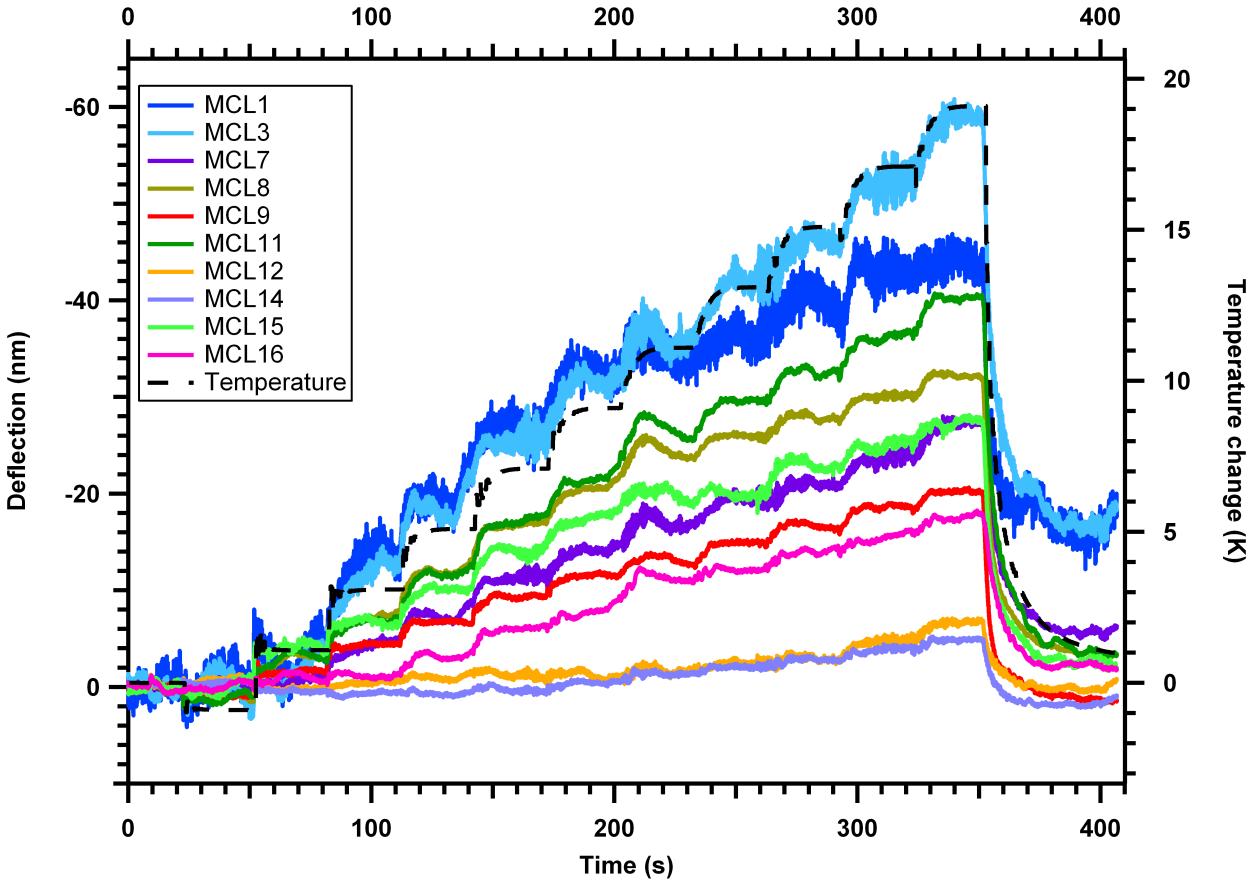

Figure 4.8: Thermal responsive of uncoated microcantilevers as measured by in-plane photonic transduction. Three microcantilevers (MCLs 4, 6, and 10) whose responses were anomalous are not shown.

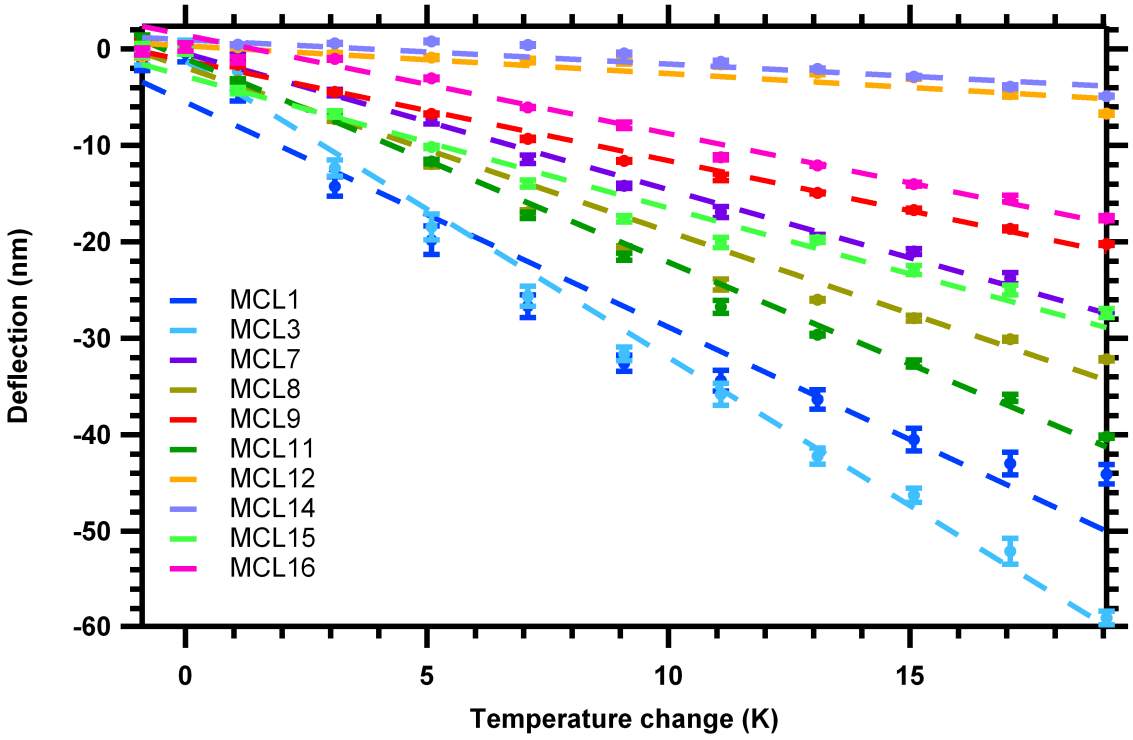

Figure 4.9: Thermal response of microcantilever array and linear fits for average thermal sensitivity.

the range of temperatures. In some cases, microcantilevers that show a similar trend at low temperatures, such as #1 & 3 or #8, 11 & 15, diverge noticeably at higher temperatures. Fig. 4.9 plots the deflections for each temperature step (averaged over the time where the temperature is constant) against the change in temperature. Linear fits to the measured deflections give an average of thermal sensitivity of -1.46$\pm$0.89 nm/K, which is similar to the observed thermal sensitivities measured using the SEM for uncoated microcantilever.

4.5 Conclusion

I have measured the thermal sensitivity of silicon microcantilevers with different gold coating patterns using scanning electron microscope and with the in-plane photonic transduction. The thermal sensitivity of the microcantilevers with gold coating is shown to be at least two orders of magnitude larger than the microcantilevers with no gold coating. Moreover, I show that the measured sensitivities of the gold coated microcantilevers are close to the predicted values when the proper moduli Poisson's ratios are used and when the strain is related to a two dimensional

(biaxial) stress in the calculations. However, the uncoated microcantilevers exhibit a non-zero and variable thermal sensitivity, which would indicate a structural inhomogeneity not accounted for by the theoretical model used. This also sets the limit of detection when the temperature is not stabilized, or conversely, the amount of temperature stabilization to achieve a limit of detection not limited by thermal fluctuations.

CHAPTER 5. TRANSIENT DEFLECTION RESPONSE OF MCL ARRAY INTEGRATED WITH PDMS MICROFLUIDICS

5.1 Motivation

As previously discussed, the use of microfluidics opens up the possibility of total analysis, point of care sensors. Combining microfluidics with an array of label-free sensors, such as microcantilevers, can lead to a versatile multiplexed sensor platform. In such a platform all sensor elements can be exposed to the same environment of interest and queried simultaneously to improve the overall sensor capability, efficiency, and sensitivity [15, 25, 30, 37]. The availability of large arrays of microcantilevers would permit not only multiplexed sensing of multiple target analytes, but also on-chip replicates to improve detection and measurement statistics and the inclusion of calibration standards. Moreover, integration with microfluidics offers improvements in sample handling and response time. This is especially helpful when the available sample volume is small and must be used efficiently. In addition, as is often the case in traditional microcantilever sample containers, longer periods of observation or reduced overall device sensitivities result if transport of target analytes relies on diffusion alone, particularly as the dimensions of each sensor element shrink [38]. An advantage of properly implemented microfluidics is a much higher target analyte flux to the sensor surface through flow-induced advection [39], which reduces sensor response time. Despite the attraction microfluidics, as suggested by Squires *et al*., care must be taken to properly implement microfluidics to optimize the sensitivity and response time of the integrated sensor.

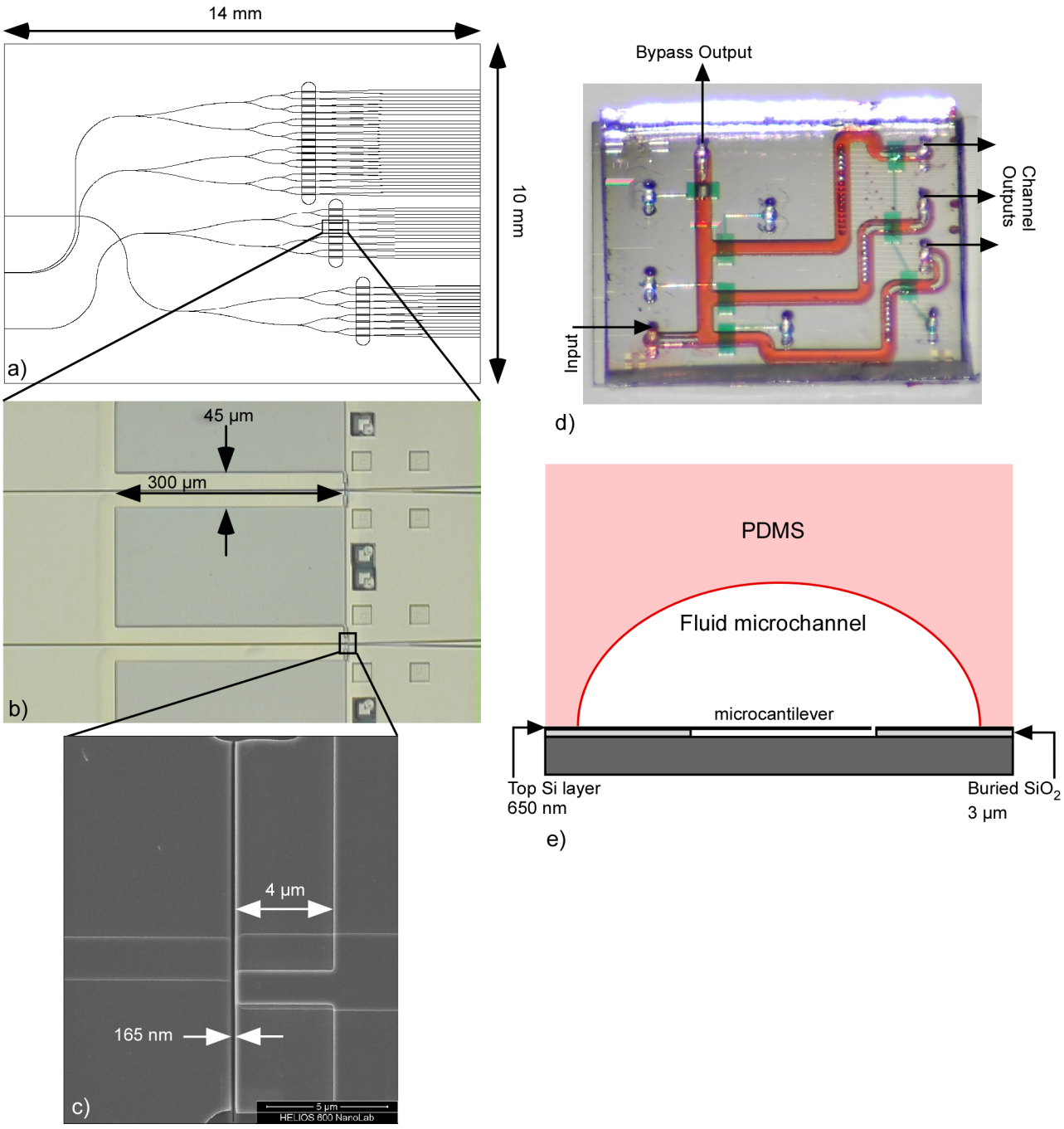

Figure 5.1: (a) Schematic diagram of waveguides and microcantilever array layout on die. (b) Optical image of fabricated microcantilevers and (c) close up SEM image of the unclamped end of microcantilever (left of 165 nm gap) and the differential splitter capture waveguide (right of gap). (d) Photograph of complete integrated device. (e) Schematic of double-layer PDMS microfluidics showing the fluid microchannels (red), control valves (green), hole punches for external tubing attachment (blue), and microcantilever arrays (black). (f) Cross-section of fluid microchannel at a microcantilever array.

5.2 Design

5.2.1 Silicon Device

Silicon microcantilever arrays (Fig. 5.1(a)) are fabricated with differential splitter structures for in-plane all-photonic transduction on silicon-on-insulator (SOI) wafers having a 3 μm buried oxide layer and a 750 nm silicon device layer, as described in previous work [43, 44]. The microcantilevers (Fig. 5.1(b)) are 300 μm long, 45 μm wide, and 650 nm thick. An embedded rib waveguide with a rib height of 100 nm and width of 1.6 μm extends down the center of each microcantilever to form a single mode waveguide at a wavelength of 1550 nm. All other waveguides within the device, with the exception of the differential splitter, have the same dimensions. As shown in Fig. 5.1(a), a fabricated sensor die has three microcantilever arrays, two with 8 microcantilevers and one with 16 microcantilevers. A Y-branch waveguide network directs light from a single input to all microcantilevers in an array. Each array sits in a shallow trench that runs the length of the array that is created during the fabrication process when the buried oxide layer is removed with a hydrofluoric acid etch. The trench forms the lower part of the fluid microchannels for the integrated microfluidic device.

The all-photonic transduction method relies on a differential splitter structure consisting of an asymmetric multimode waveguide (Fig. 5.1(c)) and Y-branch splitter [44]. Light exiting the embedded waveguide in the microcantilever propagates across a 165 nm gap and couples into the asymmetric multimode waveguide of the differential splitter. The multimode waveguide supports two guided modes which roughly correspond to the two outputs, P_1 and P_2, of the Y-branch splitter. Because of the asymmetry of the multimode waveguide, the deflection dependence of the coupling efficiency is different for the two modes [44]. The difference in coupling efficiencies enables me to determine the deflection state of the microcantilever from the optical powers, P_1 and P_2, of the two outputs of the Y-branch splitter by forming a scaled differential signal, η:

$$\eta = \frac{P_2 - \alpha P_1}{P_2 + \alpha P_1} \tag{5.1}$$

where α is a scaling factor related to a reference deflection [45]. Optimization of the differential splitter design has been done to ensure that the scaled differential signal is monotonic and nearly

Table 5.1: Deflection responsivities of microcantilevers (MCLs) in array.

MCL #	Responsivity/μm^{-1}	MCL #	Responsivity/μm^{-1}
1	0.7249	7	0.8928
2	0.8865	8	0.6737
3	0.8416	9	0.6280
4	0.6724	10	0.7183
5	0.8868	11	0.4191
6	1.189	12	0.6397
7	1.247	13	0.5831
8	1.024	14	0.6123

linear over a suitable deflection range and to maximize the deflection responsivity [44]. Prior to integration with PDMS microfluidics, the deflection responsivity of the differential signal is calibrated by physically actuating the microcantilevers using a polished glass edge and piezoactuator as previously described [43, 45]. The measured responsivity values, listed in Table 5.1, are later used to convert the calculated scaled differential signal to actual cantilever deflection for each microcantilever. In the calibration and later experimental measurements, a superluminescent diode (DL-BZ1-CS5403A-FP-00; Denselight) at 1550 nm is the optical source and a linear array camera (SU512LDV-1.7RT-0500/LSE; Sensors Unlimited) is used for simultaneous measurement of the outputs of all microcantilevers in an array.

5.2.2 Microfluidic Device

The microfluidic device used to deliver analyte solution to the microcantilever arrays consists of two bonded layers of polydimethylsiloxane (PDMS), the bottom of which contains fluid microchannels, while the upper layer includes control channels to enable valve actuation to direct solution through the desired fluid microchannel [73, 74]. Master molds for each layer are patterned using photolithography in photoresist on 4 inch silicon wafers with each master mold containing several single-chip patterns. For the fluid microchannel layer, the mold is created with a positive photoresist (AZ 50XT; AZ Electronic Materials). Following photoresist development, the mold undergoes a reflow process on a hot plate at 125 °C for 3 minutes. As a result of the reflow process, the rectangular cross-section of the photoresist patterns becomes semicircular, which is necessary to create pneumatically actuated valves to completely close a microchannel. The cross-section of a

final fluid microchannel is 60 μm center height and 600 μm width. For the control channel layer, the mold is created with a negative photoresist (SU8 25; MicroChem). The control channels on the mold do not require a reflow process and therefore have a rectangular cross-section. At each valve they are 30 μm tall, 600 μm wide, and 1200 μm long.

PDMS prepolymer and curing-agent (Sylgard 184 kit; Dow Corning Corp.) are mixed at a 10:1 ratio for the fluid microchannel layer and at a 4:1 ratio for the control valve layer, and both mixtures are degassed in vacuum for one hour prior to use. The 10:1 ratio PDMS is spun onto the fluid mold at 900 rpm after a silanization treatment of the mold to facilitate later release. The 4:1 ratio PDMS is poured into a cylindrical container with the control valve mold at the base. Both are then heat-cured at 80 °C for one hour in an oven. The PDMS layers are detached from the molds and cut into single chips with a razor blade. Holes for connections between the control valves and a pneumatic solenoid valve manifold, and between the fluid microchannels and external tubing are then punched in the PDMS layers using a generic punch press machine with a dispenser tip (TIP 21GA GP, Nordson EFD). In order to bond the control valve layer with the fluid microchannel layer, the control valve layer is stamped on curing-agent spun onto a 4 inch silicon wafer at 4000 rpm for 30 seconds [75, 76]. Prior to bonding the two PDMS layers, the layers are properly oriented relative to each other so that fluid microchannels and control valves are aligned with the aid of a custom-built alignment stage, and then cured at 80 °C for one hour. Fig. 5.1(d) shows a schematic diagram of the double-layer PDMS microfluidic device in relation to the microcantilever array layout on a die.

After heat curing, the PDMS microfluidic device is bonded to the microcantilever array silicon die. This is done by first stamping the PDMS device on a wafer on which a thin curing agent layer has been spin coated, and then aligning the fluid microchannels in the device with the microcantilever arrays on the silicon die. Fig. 5.1(e) shows a cross-section schematic diagram of the integrated device at one of the fluid microchannels which sits over a microcantilever array. The integrated microfluidic-silicon device is cured at room temperature for ~24 hours [77]. Following curing, a glass piece is placed on top of the PDMS. The glass piece has holes precisely drilled to match holes in the PDMS for tube connections to the microfluidics.

5.2.3 Fluid Introduction and Flow Control

Following assembly, the first fluid introduced into the microchannels is a 1X phosphate buffered saline (PBS) (pH 7.4) solution with 0.2% (w/w) Triton X-100 surfactant. The fluid is introduced at a volumetric flow rate of 10 μL/min, which is then increased to 100 μL/min and flows for a duration of 5 minutes after the microchannel has been filled. The surfactant in the solution prevents air bubbles from forming within the microchannels and under the microcantilevers. Following the initial rinse, a 1X PBS (pH 7) solution is introduced into the microchannels at 30 μL/min and flows for a duration of 30 minutes to allow any fluid-surface interactions to stabilize. The analyte solutions I used are a prepared 70 μM concentration of bovine serum albumin (BSA) in 1X PBS and a set of commercial reference buffers of various pH's, specifically, potassium carbonate buffer at pH 10, phosphate buffer at pH 7, and potassium hydrogen phthalate buffer at pH 4, each with 5 mM ionic concentration.

The microfluidics are designed so that a new fluid analyte can be introduced to an on-chip bypass channel while actuated control valves prevent the analyte solution from traveling down a microchannel to a microcantilever array. Air pressure to the valves is controlled through a manifold of solenoid valves (LFMX0510438BF, LHDA1211111H; The Lee Company) that are actuated using a computer-controlled, digital I/O device (NI USB-6501; National Instruments). At 15 seconds after initiating data acquisition for the experiment, control valves are actuated so as to allow fluid to flow down a microchannel to a desired microcantilever array. At 60 seconds after initiating data acquisition, an automated syringe pump (Harvard 33 Twin Syringe Pump; Harvard Apparatus) begins a pressure driven flow of 5 μL/min.

5.3 Measurement and Analysis

5.3.1 Non-specific Binding of Protein

To understand the temporal response of microcantilevers in the microchannels due to non-specific interaction with analytes in solution, I modeled the flow and diffusion of protein in the microfluidic channel around the microcantilevers using finite-element method (FEM) analysis (COMSOL Mulitphysics 4.0a). For a flow rate of 5 μL/min and an analyte solution with a viscosity and density close to that of water, the Reynolds number, *Re*, for this flow channel geometry is ~0.25,

Table 5.2: Dimensionless parameters for integrated microcantilever array in a microchannel and nonspecific binding of BSA.

Parameter	Above MCL	Below MCL
Pe_H	2100	1.5
Pe_S	7400	N/A
Da	0.013	0.13

which indicates that the flow is laminar. This implies Pouiselle flow with a parabolic flow velocity profile in which the flow velocity is greatest at the center of the channel and nearly zero at the flow channel walls and surfaces of the microcantilever. Because the separation between the microcantilever and the bottom of the microchannel is only 3 μm, the volumetric flow underneath the microcantilever is greatly reduced compared to the flow above the microcantilever. Computational simulation indicates a volumetric flow rate of 1.8 nL/min under the microcantilever for a channel flow rate of 5 μL/min. The reduced flow rate diminishes the contribution of advection-driven mass transport under the microcantilever and results in the average concentration of analyte being different above and below the microcantilever as new analyte solution is first introduced into the microchannel. This is illustrated in Figs. 5.2(a)-(d) where the normalized concentration of analyte is shown in cross section at four different times after an analyte-bearing solution begins to flow down a microchannel containing a microcantilever. In each figure the flow is from left to right. The particular case shown is for BSA, which has a diffusion coefficient of 6.32×10^{-11} m^2/s [78]. The effect is summarized in Fig. 5.2(e) in which the normalized BSA concentration is shown as a function of time following introduction of BSA-containing fluid into the flow channel. I define the normalized concentration, C_n, for both the top and bottom surfaces of the microcantilever as:

$$C_n = \frac{C(t) - C_0}{C_\mathrm{f} - C_0} \tag{5.2}$$

where $C(t)$ is the average surface analyte concentration at time t, and C_0 and C_f are the initial and final analyte concentrations. The differential concentration is the difference between the normalized concentration of the top and bottom surfaces, which is also plotted in Fig. 5.2(e). The full-width, half-maximum (FWHM) time interval during which there is a concentration difference between the top and bottom microcantilever surfaces is 3.3 seconds.

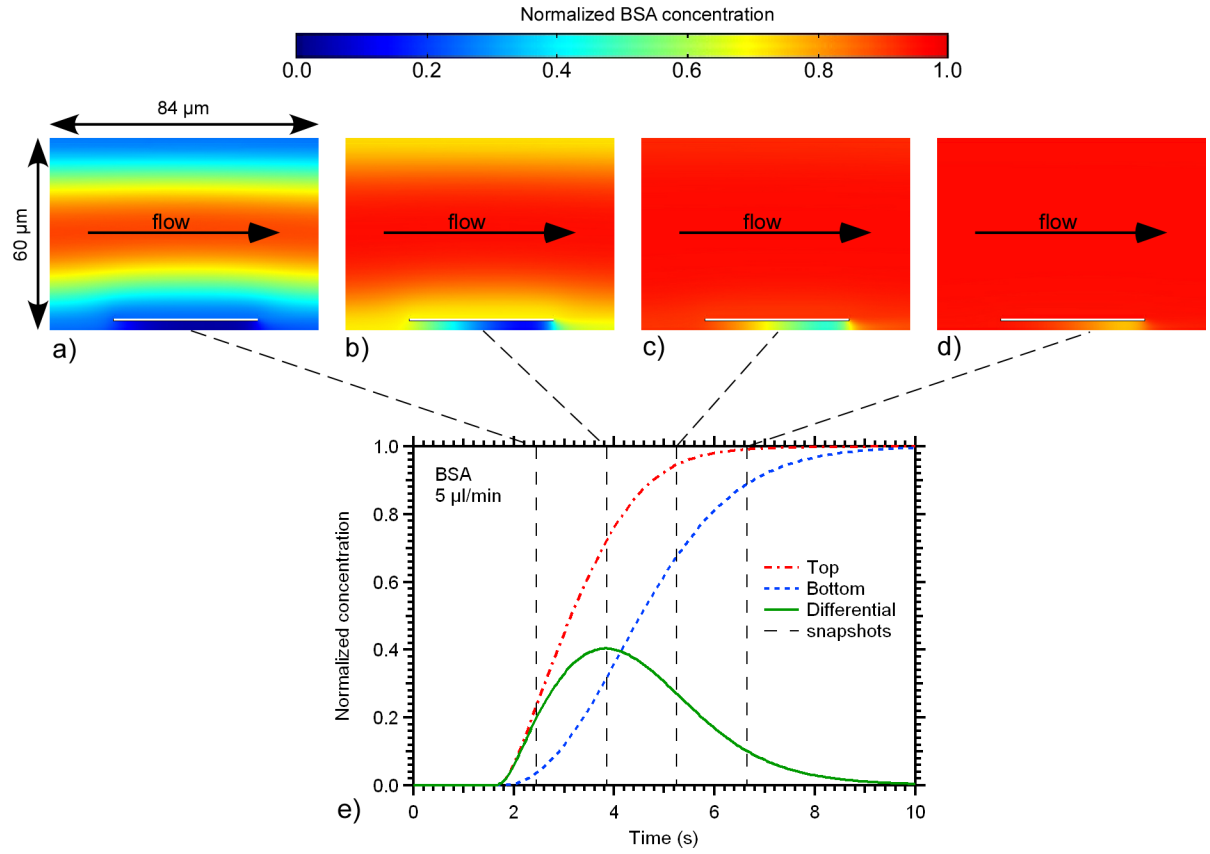

Figure 5.2: (a)-(d) Simulation results for normalized concentration of BSA at four different times (indicated by dashed lines in (e)) around a microcantilever during introduction of a BSA solution. Flow is from left to right and the length of the microcantilever is normal to the image. No BSA is initially in the microchannel. (e) Normalized analyte concentration for top (red) and bottom (blue) surfaces of a microcantilever and differential concentration (green) in a microchannel with a 600 μm$\times$60 μm cross-section.

As described by Squires *et al.* [39], various dimensionless parameters are useful to characterize the operating regime for a sensor that has surface-bound receptors. For example, the relative importance of diffusion and advection to transport of analyte molecules to a sensor surface can be characterized with Peclet numbers. These are given in Table 5.2 for the volume above and below a microcantilever for my flow channel geometry.

In the volume above a microcantilever the Peclet numbers indicate that the depletion region (i.e., the region from within which analyte molecules can reach the sensor surface before flowing past the sensor) is thin compared to the microchannel height ($\mathrm{Pe_H} \gg 1$) and microcantilever width ($\mathrm{Pe_S} \gg 1$). Thus mass transport of analyte molecules to the sensor surface is advection-dominated.

While this results in a large number of molecules contacting the surface per second, not all of the molecules adsorb to the surface. Adsorption depends on the analyte concentration at the surface (C_S), the available binding sites per unit area on the surface for the analyte (Γ_0), and the reaction kinetics of the binding interaction. For non-specific binding of BSA to a native oxide of crystalline silicon, Γ_0 is 1.07×10^4 μm^{-2} and the association and dissociation constants, k_a and k_d, are 1.576×10^4 (M s)$^{-1}$ and 3.152×10^{-3} s^{-1}, respectively [79]. Assuming a first-order Langmuir model, the surface concentration of binding sites filled by target analyte, $\Gamma(t)$, is given by the differential equation

$$\frac{\partial \Gamma}{\partial t} = k_\mathrm{a} C_\mathrm{s} \left[\Gamma_0 - \Gamma\right] - k_d \Gamma. \tag{5.3}$$

The dimensionless Damkohler number, Da, characterizes whether adsorption is transport or reaction limited. As shown in Table 5.2, Da for the top surface of the microcantilever is much less than one so adsorption to the surface is reaction limited, i.e., molecules are transported to the sensor surface faster than they can bind. I can therefore approximate the surface concentration, C_S, as approximately equal to $C(t)$ from my simulation.

In contrast to the flow above the microcantilever, the flow below is characterized by a channel Peclet number, $\mathrm{Pe_H}$, near unity, indicating mass transport that is neither diffusion nor advection dominated. The flow and channel dimensions underneath are such that all BSA molecules that enter the volume have sufficient time to diffuse to the bottom surface of the microcantilever before being swept past. The sensor Peclet number, $\mathrm{Pe_S}$, is largely irrelevant since the microcantilever width (45 μm) is much larger than the separation between the microcantilever and channel floor (3 μm). The Damkohler number indicates that binding to the bottom surface is also reaction limited, but because it is an order of magnitude larger than for the top surface, the approximation $C_\mathrm{S} \approx C(t)$ may not be valid. A better approximation can be made by assuming quasi-steady state binding where the diffusive flux and the reactive flux are equal. In this situation one can derive a modified form of the rate equation,

$$\frac{\partial \Gamma}{\partial t} = \frac{k_\mathrm{a} C_\mathrm{s} \left[\Gamma_0 - \Gamma\right] - k_\mathrm{d} \Gamma}{1 + Da \left[1 - \Gamma/\Gamma_0\right]} \tag{5.4}$$

which reduces to Eq. 5.3 in the limit $Da \ll 1$ with $C_\mathrm{S} \approx C(t)$. Numerical integration of Eqs. 5.3 and 5.4 using concentrations from finite element simulation gives solutions for the filled binding site densities $\Gamma(t)$ for the top and bottom microcantilever surfaces, which are shown in Fig. 5.3(a).

Note that there are small differences in the shape of the curves compared to the concentration in Fig. 5.2(e). The FWHM of the differential fraction of filled surface sites is slightly shorter at 2.9 seconds.

A widely accepted description of microcantilever bending relates the induced surface stress, σ, to the change in Gibbs free surface energy, γ, by the Shuttleworth equation $\sigma = \gamma + \mathrm{d}\gamma/\mathrm{d}\varepsilon$. In most cases, the contribution by the surface strain, $\mathrm{d}\varepsilon$, is taken to be negligible, and the change in surface stress can be assumed to be equal to the change in Gibbs free surface energy due to chemical interactions at the surface [20,65,80]. The change in surface free energy for the chemical reaction at temperature T and with filled binding site concentration Γ can be approximated as

$$\gamma = -\Gamma kT \ln K \tag{5.5}$$

where k is the Boltzman constant and the association constant K is $k_\mathrm{a}/k_\mathrm{d}$. The right axis of Fig. 5.3(a) shows the estimated surface stress on the top and bottom surfaces and the differential surface stress ($\sigma_\mathrm{top} - \sigma_\mathrm{bottom}$) corresponding to the calculated binding dynamics. Note that the maximum differential surface stress is -0.225 mN/m.

Experimental data from exposure of a microcantilever array to a 70 μM BSA solution is shown in Fig. 5.3(b) for each individual microcantilever, and in Fig. 5.3(c) for the average microcantilever response, which has been baseline-corrected [81]. The silicon surface is unmodified and has only been previously exposed to rinsing and stabilization buffer solutions. Note the definite transient downward deflection of all microcantilevers. In the average deflection data this starts at 92 seconds and has a FWHM of 5.3 seconds, which is within a factor of two of the FWHM time response predicted by my binding model. Non-specific adsorption of BSA yields a distinct transient microcantilever deflection that follows the transient differential BSA concentration.

To calculate the equivalent differential surface stress for the observed deflections, it is necessary to know the microcantilever spring constant. Prior to this experiment a similar die was fabricated using the same process, and a spring constant of 5.82 ± 0.0136 mN/m was measured using atomic force microscopy techniques [82]. The calculated differential surface stress is shown on the right axis of Figs. 5.3(b) and 5.3(c). The magnitude of the maximum average downward microcantilever deflection is -1.6 nm, which corresponds to a differential surface stress of -0.23 mN/m.

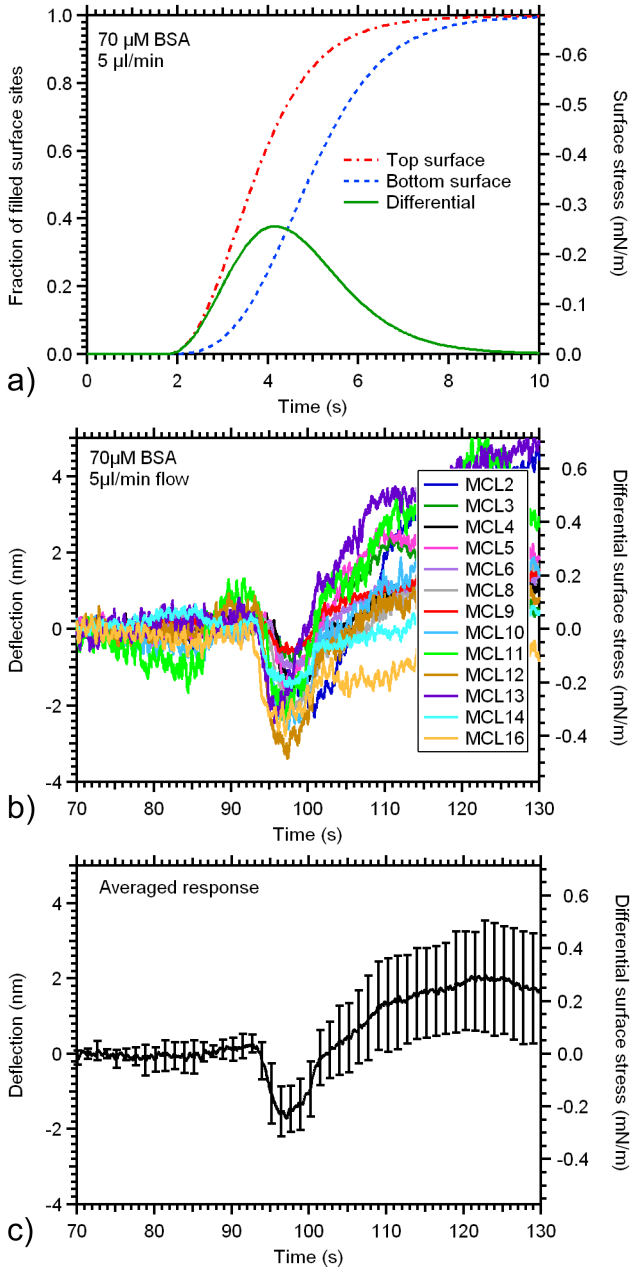

Figure 5.3: (a) Fraction of filled surface sites (left axis) on top and bottom of microcantilever and difference between the two for non-specific adsorption of BSA. (b) Experimental measurement of transient deflection due to non-specific adsorption upon introduction of 70 μM BSA solution. (c) Average microcantilever deflection. Error bars denote standard deviation of deflection. For all figures, right axis shows corresponding surface stress or differential surface stress.

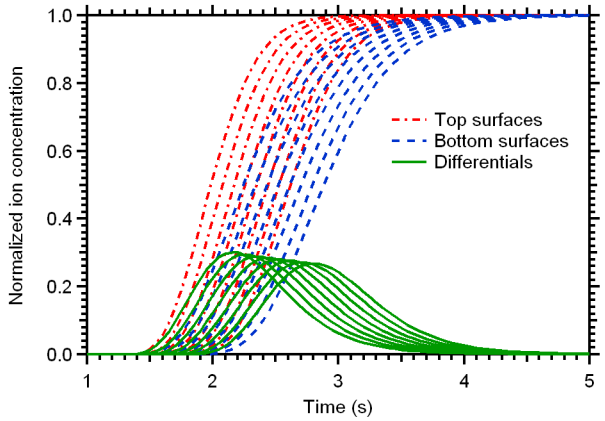

Figure 5.4: Top surface, bottom surface, and differential normalized concentrations for an eight microcantilever array in a microchannel.

Note the excellent agreement with the prediction based on finite element simulation combined with my analysis of the fraction of filled surface sites and the Shuttleworth equation.

There is considerable variation in the drift of individual microcantilever deflection signals after non-specific adsorption of BSA. As has been noted by others [29], this may be due to chemical interaction of the newly-coated microcantilevers with the liquid environment or slow rearrangement of the molecules in the protein layer.

5.3.2 Changes in Solution pH

Following non-specific adsorption of BSA, I expose the microcantilever array to buffer solutions with different pH to further study array transient response. In simulations I treat H^+ as the relevant ion involved in the surface interactions and use a H^+ diffusion coefficient of 8×10^{-10} m^2/s [83]. Simulation results for the concentration above and below the cantilevers for an eight microcantilever array are shown in Fig. 5.4 (16 microcantilevers is beyond the simulation capability of the current computational hardware). Similar to the BSA data, simulation shows a temporary difference of the ion concentration above and below each microcantilever. However, compared to the transient differential BSA concentration, the transient differential ion concentration has a shorter duration with an average FWHM of 0.93 ± 0.05 s. This is attributable to H^+ ions having a larger diffusion coefficient than BSA. I also note that the differential concentration curves for all of the microcantilevers are similar, with a slight decrease in magnitude for microcantilevers

further downstream in the microchannel, and that, as one would expect, there is a uniform time delay between the transient responses of adjacent microcantilevers.

Experimental measurement of transient deflection in response to changes in pH are shown in Figs. 5.5(a)-(d). When a buffer solution with a different bulk pH is introduced, the microcantilevers in the array show a transient deflection similar to the transient differential concentration in Fig. 5.4. A distinct feature of the transient deflection response is that the direction of deflection corresponds to whether the new solution has a higher or lower pH than the solution already occupying the microchannel. Introduction of a solution with a lower bulk pH (higher concentration of H^+) induces a downward transient deflection (Figs. 5.5(a) and 5.5(d)) while a solution with a larger bulk pH induces an upward transient deflection (Figs. 5.5(b) and 5.5(c)). The absolute value of changes in deflection (approximately 20 to 100 nm) correspond to induced differential surface stresses of roughly 2 to 14 mN/m. Also similar to the simulation results, the time delay between transient responses for adjacent microcantilevers is roughly constant with the first transient response occurring for the first microcantilever that the new pH solution encounters. In Fig. 5.5(e) the microcantilever number (left axis) and position in the microchannel (right axis) are shown as a function of the relative time at which the maximum microcantilever deflection occurs for each microcantilever. For each pH change the relationship is linear, as expected. The time delays of the maximum change in deflection can be used to estimate the flow velocity and the volumetric flow rate during each experiment. The time delays correspond to an average flow rate of approximately 5.6 μL/min, which is within $\sim$10% of the flow rate at which the syringe pump is set.

Unlike for non-specific adsorption of BSA, the mechanisms responsible for deflection when introducing solutions of different pH are very complex. For simple bare silicon microcantilevers, induced deflection due to pH change is believed to be primarily caused by protonation and deprotonation of surface silanol sites [8, 65]. The protonation/deprotonation reactions result in a pH-dependent accumulation of surface charge and change in the surface free energy, which produces a surface stress. However, the pH response of a microcantilever changes noticeably when the surface is modified with a pH-sensitive self-assembled monolayer (SAM) since more interactions contribute to the change in surface free energy [8]. For the experimental results shown in Figs. 5.5(a)-(d), it is expected that the non- specifically bound BSA molecules are the main source of the surface stress mechanism, although undoubtedly surface protonation and deprotonation also

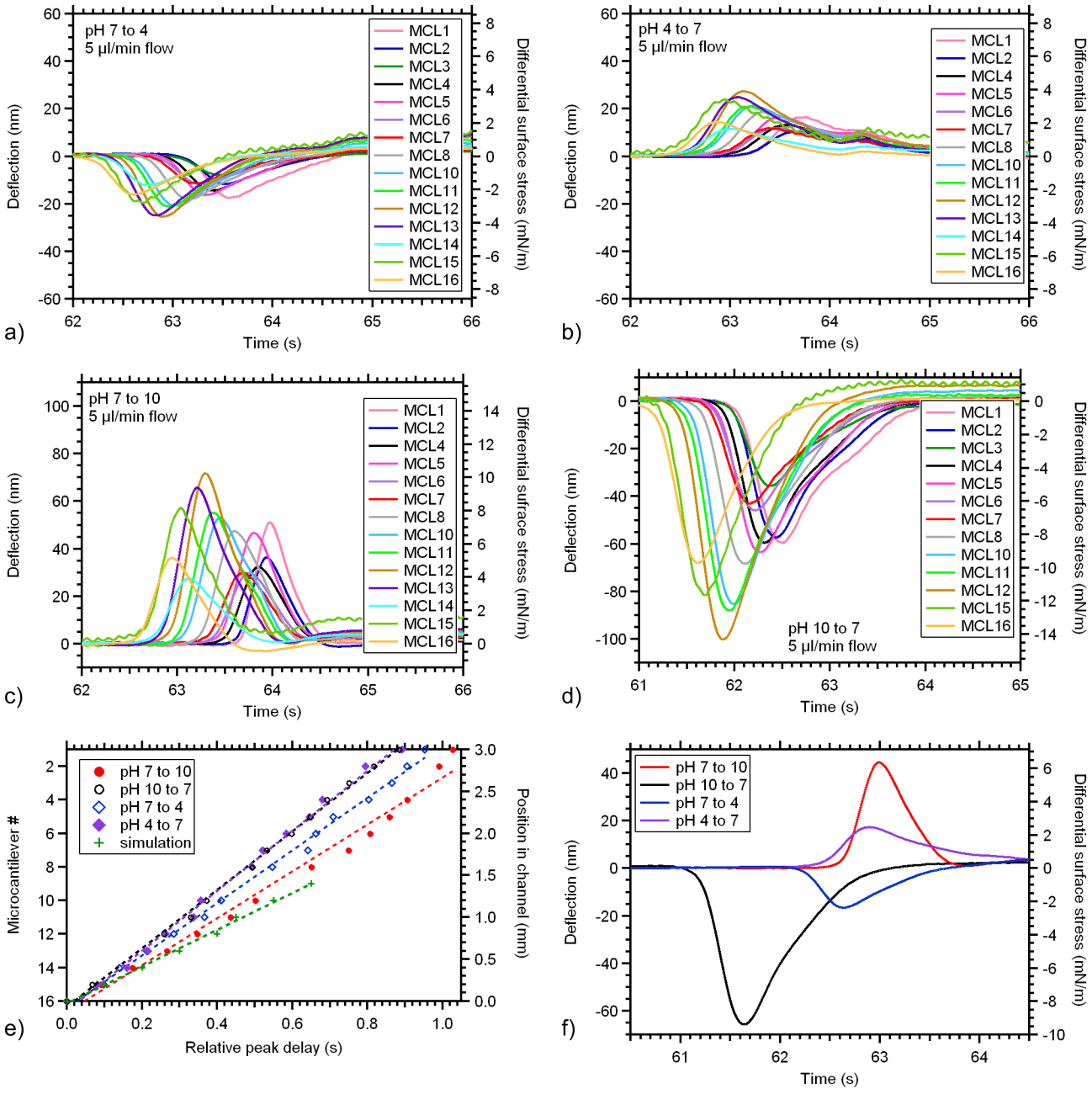

Figure 5.5: Response of a 16 microcantilever array to change in fluid pH going from (a) pH 7 to 4, (b) pH 4 to 7, (c) pH 7 to 10, and (d) pH 10 to 7. (e) Relative time at which the maximum absolute deflection occurs for each microcantilever in the array for different pH changes. A fitted line gives an estimate to the flow velocity at the microcantilevers. (f) Average microcantilever deflection for each pH change. The shift in time at which each response occurs represents variation in when the pH change reaches the microcantilever array for each run.

Table 5.3: Measured average pH responses.

pH change	Maximum Deflection Change (nm)	Temporal Width of Transient Response (s)
7 to 4	-17.5	0.675 ± 0.032
4 to 7	17.2	1.01 ± 0.16
7 to 10	43.9	0.521 ± 0.054
10 to 7	-65.4	0.744 ± 0.049

play a role. The isoelectric point of BSA in solution is 4.7. Moreover, in solution BSA undergoes reversible conformational changes at pHs of 4.3, 8, and 10 [84]. While details of conformational change will be somewhat different when adsorbed to a surface, this may correlate to the transient response for pH changes 4↔7 being weaker than the response for pH changes 7↔10. The former includes a single conformational change and passes through the isoelectric pH, while the latter includes two conformational changes and the protein charge is never neutral over this pH range. As shown in Fig. 5.5(f) and tabulated in Table 5.3, the average microcantilever deflection for pH changes 4↔7 are indeed smaller than for pH changes 7↔10. Moreover, in each case the transient going away from neutral pH (7 to 4 or 7 to 10) is shorter than the corresponding return to neutral pH (4 to 7 or 10 to 7, respectively). This may be due to a difference in the relative rate of BSA unfolding and refolding conformational changes. The overall average FWHM temporal response for all pH changes is 0.74 s, which is within 25% of the simulation prediction (0.93 s). As a further complicating factor, the protein charge of BSA has been shown to be sensitive to the anion species of the solution [85], so the observed transient responses may also be dependent on the change of anion species of the buffers used in my experiments.

5.4 Conclusion

I have successfully integrated PDMS-based microfluidics with an array of silicon microcantilevers that use an in-plane all photonic transduction method. Moreover, I have identified a transient deflection response when the surface stress on the top and bottom of each microcantilever is changed by both non-specific adsorption of BSA and variation in bulk pH. The temporary nature of the deflection response is attributable to a transient difference in analyte concentration between the top and bottom microcantilever surfaces as analyte-bearing fluid is introduced into the

microchannel containing the microcantilever array. As demonstrated by finite element simulation, the brief inhomogeneity in concentration is caused by different volumetric flow rates above and below a given microcantilever owing to its asymmetric vertical placement in the microchannel. Thus, although the concentration at both surfaces ultimately reaches the same equilibrium, the top surface is exposed more quickly to a new fluid as it begins to displace the fluid already in the microchannel.

Non-specific adsorption of BSA results in an average maximum change in microcantilever deflection of -1.6 nm, corresponding to a differential surface stress of 0.23 mN/m, which is in excellent agreement with the prediction of my binding model in conjunction with finite element simulation. Change in bulk pH following BSA non-specific adsorption results in either downward (decreasing pH) or upward (increasing pH) microcantilever deflection corresponding to a differential surface stress change with a magnitude in the range of 2 to 14 mN/m. This is likely related to BSA conformational change as a function of pH as well as change in charge state upon passing through BSA's isoelectric point of pH 4.7.

CHAPTER 6. MCL ARRAY RESPONSE TO PRESSURE DRIVEN FLOWS

6.1 Motivation

As discussed in the previous chapter, volumetric flow rate has a considerable effect on the the response of chemical sensors integrated with microfluidics. Therefore, being able to monitor the flow *in situ* provides a useful tool for understanding sensor behavior. Microfluidic flow sensors have been demonstrated that rely on thermal [86–90], pressure [91, 92], and force [32, 93–95] mechanisms to generate measurable electrical signals. Thermal flow sensors heat fluid and detect heat transfer in the direction flow using sensors downstream of the heat source. Mechanical flow sensors measure the deformation or displacement of structures from flow dependent forces. Recently, microcantilever-based sensors have been demonstrated as mechanical flow sensors for microfluidic sensor platforms [96–98]. These sensors use piezoresistive and strain-gauge sensor elements to transduce drag and lift forces exerted on a microcantilever due to fluid flow around the cantilever beam. Similar to other microcantilever sensors with embedded electrical readouts, the sensors have been demonstrated mainly for gas flow and are inappropriate for sensing in aqueous environments where the fluid is likely to be highly ionic. An alternative to an embedded electrical readout has been demonstrated that uses an optical fiber as the cantilever beam [99]. Deflection due to hydrodynamic drag is determined by measuring the coupling of light from the optical fiber cantilever into a static receiving fiber.

It is conceivable that it would be able adapt the photonic transduction method, which I have previously developed for microcantilever arrays [42–45], to develop a similar flow sensor for integration with a micro-total analysis system. As suggested in the previous chapter, high volumetric flow rates are necessary to improve sensor response time. Therefore, it is advantageous to also determine the flow sensitivity of the microcantilever to characterize the hydrodynamic deflection mechanism so that it can be distinguished from deflection from adsorption of a target analyte. Additionally, as will be discussed in a later chapter, I intend to integrate the microfluidics with on-chip

pump to drive flow which will require an understanding of the microcantilever response to high flow velocities.

6.2 Design

6.2.1 Silicon Device

Chips with photonic microcantilever array sensors are fabricated on a 4-inch silicon-on-insulator (SOI) wafer, with an individual chip having dimensions of 1 cm $\times$ 1.4 cm and two arrays of 16 microcantilevers each. A schematic of the microcantilever array layout on a chip is shown in Fig. 6.1(a). The microcantilevers have dimensions of 300 μm in length, 45 μm in width, and a thickness of 750 nm except for ~2.5 μm on either side of the central embedded waveguide where the surface is etched down 100 nm to define the waveguide. In order to vertically center the microcantilevers in the microfluidic channel, the chip undergo a modified etching process to etch a ~100 μm trench in the underlying silicon substrate beneath the buried oxide layer.

The microcantilevers are patterned using photolithography and defined using an inductively couple plasma reactive-ion etch (ICP-RIE). Following the definition of the microcantilevers, a deep silicon etch (DSE) process is achieved by coating the die in a layer of photoresist polymer SU-8 3005. The SU-8 is applied by a spin process, first at 500 RPM with an acceleration of 125 RPM/s for 5 seconds, then a 2000 RPM spin with 500 RPM/s acceleration for 60 seconds, and finally finishing with a 6000 RPM spin with a 4000 RPM/s acceleration for 2 seconds to help eliminate ridges of SU-8 along the edges. The SU-8 is then soft baked on a hot plate at 65°C for 5 minutes at which time the hot plate is increased to 95°C, and when the set temperature is reached the die is baked for another 5 minutes. Exposure is done on a Karl Suss Mask Aligner MA 150 for 30 seconds using soft contact with a 70 μm gap. Following exposure, a hard bake is conducted identical to the soft bake process described above. After hard baking, the die is developed for 60 seconds in a bath of SU-8 Developer with gentle agitation. The die is then rinsed with IPA and gently dried using compressed N_2.

The developed SU-8 pattern is designed to protect the majority of the die under SU-8, with openings between the adjacent microcantilevers where the Si and the SiO_2 layers will be etched. The openings are smaller the intended regions to be etched by 3 μm on each side to accommodate

etching in the lateral direction. As the etch process requires a lengthy Si etch, the edges of the die must be protected. After the die is attached to a carrier Si wafer using thermal paste, 3M Cleanroom High Temperature ESD Tape is carefully placed around the edges of the die, covering the exposed sides of the die. With the sides covered, the only parts of the die open to etching are from the SU-8, which exposes a layer of 1 μm thick layer of SiO_2. The SiO_2 is anisotropically etched away in a Trion Technology Minilock Phantom III RIE/ICP. The SiO_2 etch process is done for 5 minutes using CF_4 at 50 sccm with an RIE power of 75 watts, an ICP power of 550 watts, and a pressure of 12 mTorr. After etching away the SiO_2 layer, the underlying Si is etched away using a semi-isotropic Si etch process in an STS Multiplex ICP Etch. The process is run for 28 minutes using SF_6 at 130 sccm with a coil power of 700 watts, a platen power of 10 watts, and a pressure of 50 mTorr. This adequately removes all the Si below the microcantilever, while the the microcantilever itself is protected by the SU-8 on the top and sides and the SiO_2 on the bottom.

After the Si is etched, a 12 hour nanostrip bath at 90°C is done to remove all SU-8 and a 2 minute HF etch applied via pipette over the microcantilevers removes the underlying SiO_2. A very gentle rinse in deionized (DI) water and soft N_2 blow removes the HF. A sketch of the DSE trench and the microcantilever array is shown in Fig.6.1(b). Note that because of the isotropy of the Si etch process, the bottom surface of the trench is not flat but rises about 25 μm to a peak beneath each microcantilever. After this step the microcantilevers are still fixed on both ends, so an FEI Helios Nanolab 600 focused beam of Gallium ions is used to release one end of each microcantilever at the differential splitter (Fig. 6.1(c)). The width of gap at the free end of the microcantilever can range between 50 and 200 nm; for the samples used for this investigation, the gap width is ~65 nm. With one end free, the microcantilevers often deflect upward out of the plane due to intrinsic stresses. Low doses from the same gallium ion beam are used to compensate the MCLs so that they lie flat, completing the fabrication process [100].

Before integrating the chip with microfluidics, the responsivity of the microcantilever array is measured as described in Refs. [43, 45]. The scaled differential signals as a function of microcantilever deflection for the array used in the experiment is shown in Fig. 6.2. Microcantilever #1 is not useable due to a waveguide defect occurring during the photolithography when the waveguides were defined. Over a $\pm$500 nm deflection range, the average responsivity of all the microcantilevers in the array is $1.01 \pm 0.07\,\mu\mathrm{m}^{-1}$, comparable to previously achieved respon-

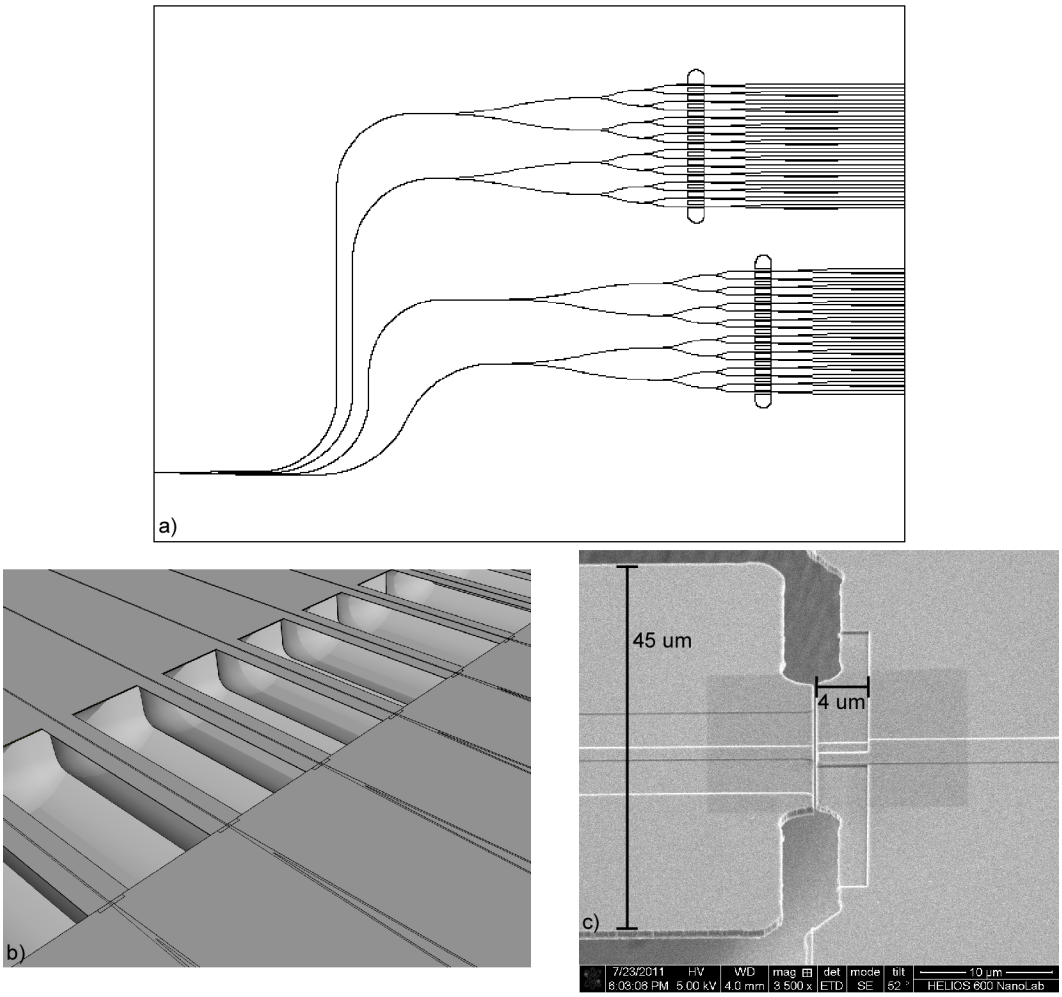

Figure 6.1: a) Schematic of waveguide and microcantilever array layout for a single chip. b) Illustration of microcantilever array following the deep silicon etch. c) Close-up SEM image of microcantilever tip and differential splitter structure.

sivities in magnitude and repeatability between microcantilevers. It should be pointed out that for some of the microcantilevers (notably microcantilevers #5 and #14) the dynamic range, defined as the range over which the scaled differential signal is quasi-linear and monotonic, is smaller than $\pm$500 nm.

6.2.2 Microfluidic Device

The microfluidic device is made of two polydimethylsiloxane (PDMS) layers, a layer containing the fluid microchannel and another layer containing the control valves used to direct fluid

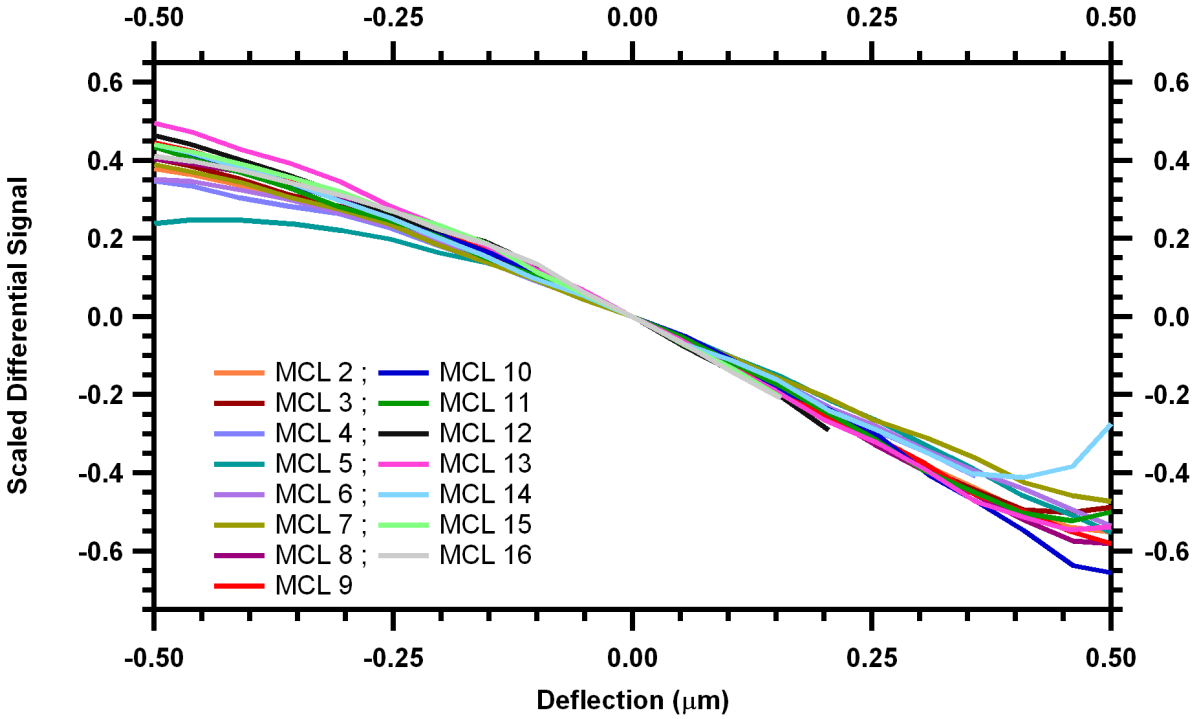

Figure 6.2: Measured responsivities of cantilever array used for flow rate sensing. There is no signal from MCL #1 due to a defect in the waveguide. The average responsivity is $1.01 \pm 0.07\,\mu\text{m}^{-1}$.

to different microchannels. The layers are fabricated and integrated as described in Ref. [77]. The final microfluidic design, shown in Fig. 6.3(a), has individual microchannels for each of the microcantilever arrays on the sample. The cross-section of a fluid microchannel is 60 μm center height and 600 μm width, while the valves in the control layer 30 μm tall, 600 μm wide, and 1200 μm long. The PDMS microfluidic device is then bonded to the microcantilever array silicon die forming a sealed fluid microchannel along the microcantilever array, a cross-section of which is shown in Fig. 6.3(b). Bonding is achieved using PDMS curing agent and letting the integrated microfluidic-silicon device cure at room temperature for $\sim$24 hours as described in Ref. [77]. Following curing, a glass piece is placed on top of the PDMS. The glass piece has holes precisely drilled to match holes in the PDMS for tube connections to the microfluidics. The purpose of the glass piece is to secure the integrated PDMS microfluidic sensor in a clamping holder in the experimental setup and to stabilize the tube connections.

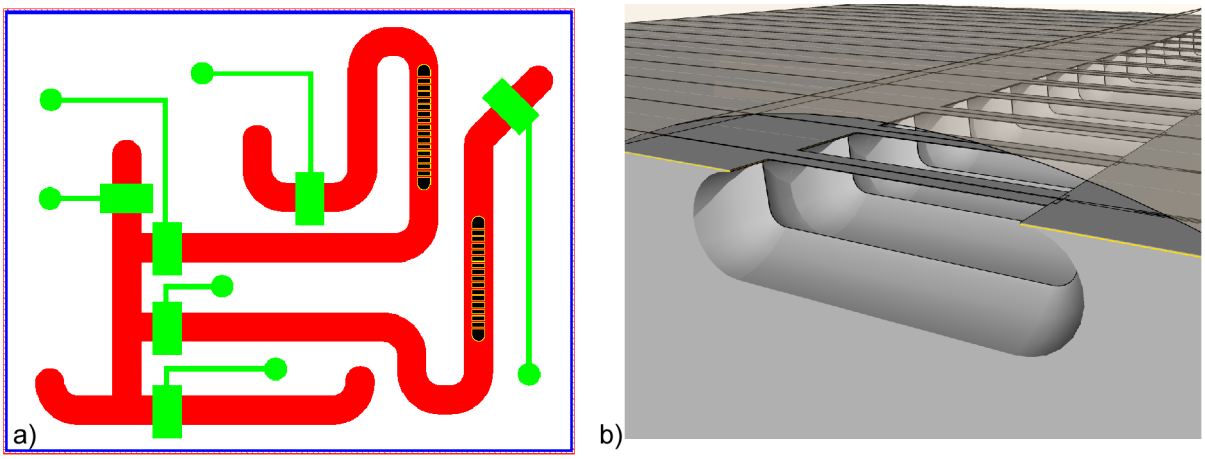

Figure 6.3: a) Layout of microfluidic channels relative to the sample. b) Schematic in cross-section of the PDMS microfluidics attached to the microcantilever array with the deep silicon etch

6.3 Experimental Setup

A schematic of the experimental set-up is shown in Fig.6.4. PDMS control valves are connected to external tubing (Microbore PTFE #24; Cole-palmer, IL, USA) by way of metal pins (0.394" New England Small Tube Corp., NH, USA) which are inserted into previously punched holes in the PDMS to form a tight seal. The external tubing is connected to a computer-controlled solenoid valve manifold to provide 15 psi of pressurized air to actuate the PDMS control valves. The control valves themselves are filled with de-ionized (DI) water to prevent pressurized air traversing the gas-permeable PDMS membrane from an actuated control valves into the fluid microchannel.

The fluid microchannel is connected to a syringe (250 μL Hamilton-Microliter Series Gastight 2.3 mm diameter) filled with a 250mM Tris buffer solution (pH7.5) with 0.2% Triton-X100 mounted in a syringe pump (Harvard 33; Harvard Apparatus, MA, USA). The buffer with surfactant solution reduces the probability of air bubbles becoming trapped in the microchannel around the microcantilevers as fluid is first introduced. Following fluid introduction, the a standard 1X phosphate buffer solution (PBS) is placed in the syringe and introduced in fluid microchannel. For experimental measurements the syringe pump ensures a continuous liquid flow with a set volumetric flow rate specified by the pumping speed and syringe dimensions. An InGaAs line scan camera (SU512LDV; Goodrich) captures simultaneously the output optical signals from the

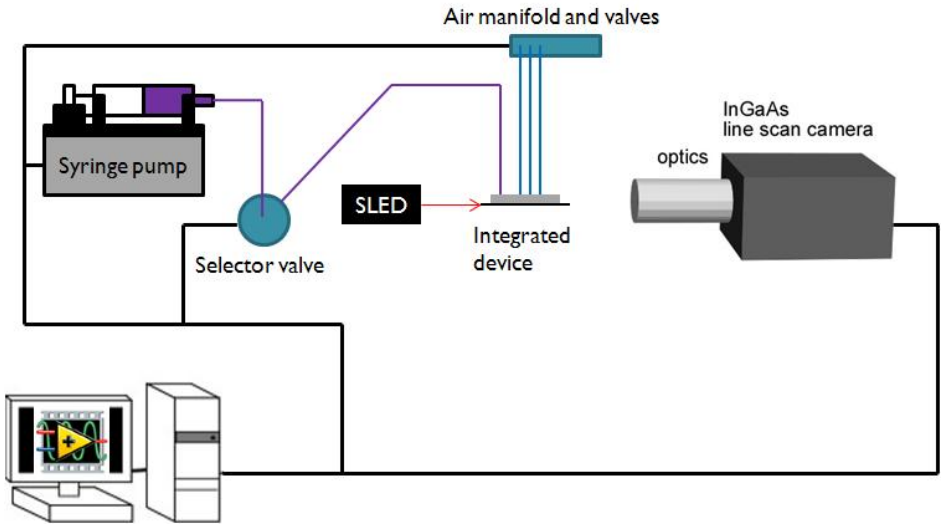

Figure 6.4: Schematic of apparatus setup for measuring microcantilever deflection response to pressure driven flow.

microcantilever array. The syringe pump, solenoid valve manifold, and data acquisition are all controlled via a LabVIEW user interface.

During the experiment, control valves are actuated to direct flow from the syringe to the fluid microchannel for a single microcantilever array, while blocking flow to the other microchannels. While the line scan camera acquires output powers, the syringe pump steps through a preprogrammed set of volumetric flow rates for given durations. Included in the preprogrammed flow rates are durations of no flow where the syringe pump stops for a set period of time inbetween each set flow rate. Two sets of flow rates are investigated, a set of relatively low flow rates and a set of high flow rates. The low flow rates, in the order they are stepped through, are 60, 40, 20, 10, 5, 2 μL/min; the high flow rates are 100, 150, 200, 300, 500, 1000 μL/min. The duration of each flow rate and each no flow period is 60 seconds, with an initial 60 second duration of no flow at the start.

6.4 Measurements and Analysis

6.4.1 Hydrodynamic Simulation

Fluid flow in microfluidics often results in laminar as opposed to turbulent flow where effects from fluid viscosity dominate over inertial effects. This is characterized by the Reynolds

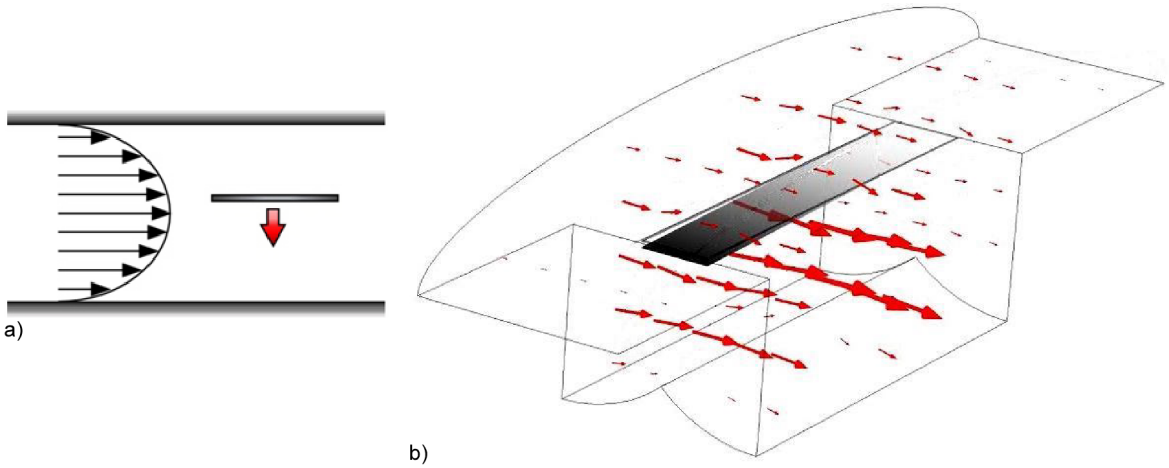

Figure 6.5: (a) Poiseuille flow within the microchannel and the resulting lift force on a thin plate. (b) 3D FEM simulation showing a downward deflection of the microcantilever free end in response to laminar flow. Flow velocity is indicated by the size and direction of the red arrows.

number, *Re*, which is the ratio of inertial to viscous effects. A microcantilever in laminar flow experiences two hydrodynamic forces, a lift force directed perpendicular to the flow and a drag force in the same direction of the flow. Because the flow is laminar and driven by an external pressure source, in this case a syringe pump, the flow has a quadratic Poiseuille flow velocity distribution, as shown in Fig. 6.5(a), so that the flow velocity is zero at the channel walls and maximum at the center of the channel. The hydrodynamic lift force acting on a thin plate in the Poiseuille flow is therefore directed away from the region of lower flow velocity, in accordance with the Bernoulli principle. If the thin plate is a microcantilever clamped at one end, the free end will bend in the direction of the lift force until equilibrium is reached.

I performed finite element method (FEM) simulations using a commercial code (COMSOL Multiphysics; COMSOL, Sweden) to determine the relationship between volumetric flow rate and microcantilever beam deflection for my microfluidics geometry. Fig. 6.5(b) shows a schematic with the geometry of microfluidic channel and the microcantilever deflected to a fluid flow indicated by the red arrows. The simulation indicates that as expected the microcantilever is deflected downwards in response to the flow through the microchannel.

6.4.2 Microcantilever Array Response to Flow

Using the previously measured responsivities the acquired differential signals are converted to deflection. The changes in the deflections of the individual microcantilevers for the set of low flow rates are shown in Fig. 6.6(a). A number of the microcantilevers are not useable as there initial deflection state is close to the extremes of the dynamic range and so gave anomalous responses, either not responding to flow at all or appearing due to the non-monotonic behavior of the responsivity to deflect in the opposite direction as the rest of the array. Likewise the deflections of the individual microcantilevers in response to the set of high flow rates are shown in Fig. 6.7(a). For both set of flow rates, I also average the deflection response of the well-behaved microcantilevers to obtain the average deflection response to the flow rates, shown in Figs. 6.6(b) and 6.7(b) for the low and high flow rates, respectively.

I draw attention to a few notable behaviors seen from the deflection response to the set of low flows. First, the deflection response to flow is not uniform across all of the microcantilevers. This is most likely due to variations arising during the deep silicon etching process resulting in non-uniformities in the oxide etch underneath top silicon layer at the base of the microcantilevers and irregularities in the trench depth beneath the microcantilevers. Such variations result in a varying microchannel cross-section that can cause a non-uniform flow velocity from microcantilever to microcantilever. Second, the deflections of multiple microcantilever appear to drift with an approximate ± 5 nm spread by the end of the 720 second data acquisition period. Both of these anomalies can be corrected in part by using an array of microcantilevers and averaging the deflections across the array, as seen in Figs. 6.6(b) and 6.7(b).

Fig. 6.7 also demonstrates the behavior of the differential signal for large deflections. For flow rates greater than 200 μL/min, the deflection responses of many of the cantilevers no longer appear to follow the previously observed trend of increasing downward deflections with higher volumetric flow rates. That this behavior begins when the deflection approaches and goes beyond -500 nm indicates that the microcantilevers are likely no longer within the dynamic range of the differential signal where the signal is monotonic. Going outside the dynamic range is also indicated by the quick spikes in deflections at the start of the high flow rates before stabilizing at smaller apparent deflections and by the increase measurement noise. In this case, increased noise results from the weak optical powers of P_1 and P_2 of the differential splitter, indicating greater coupling

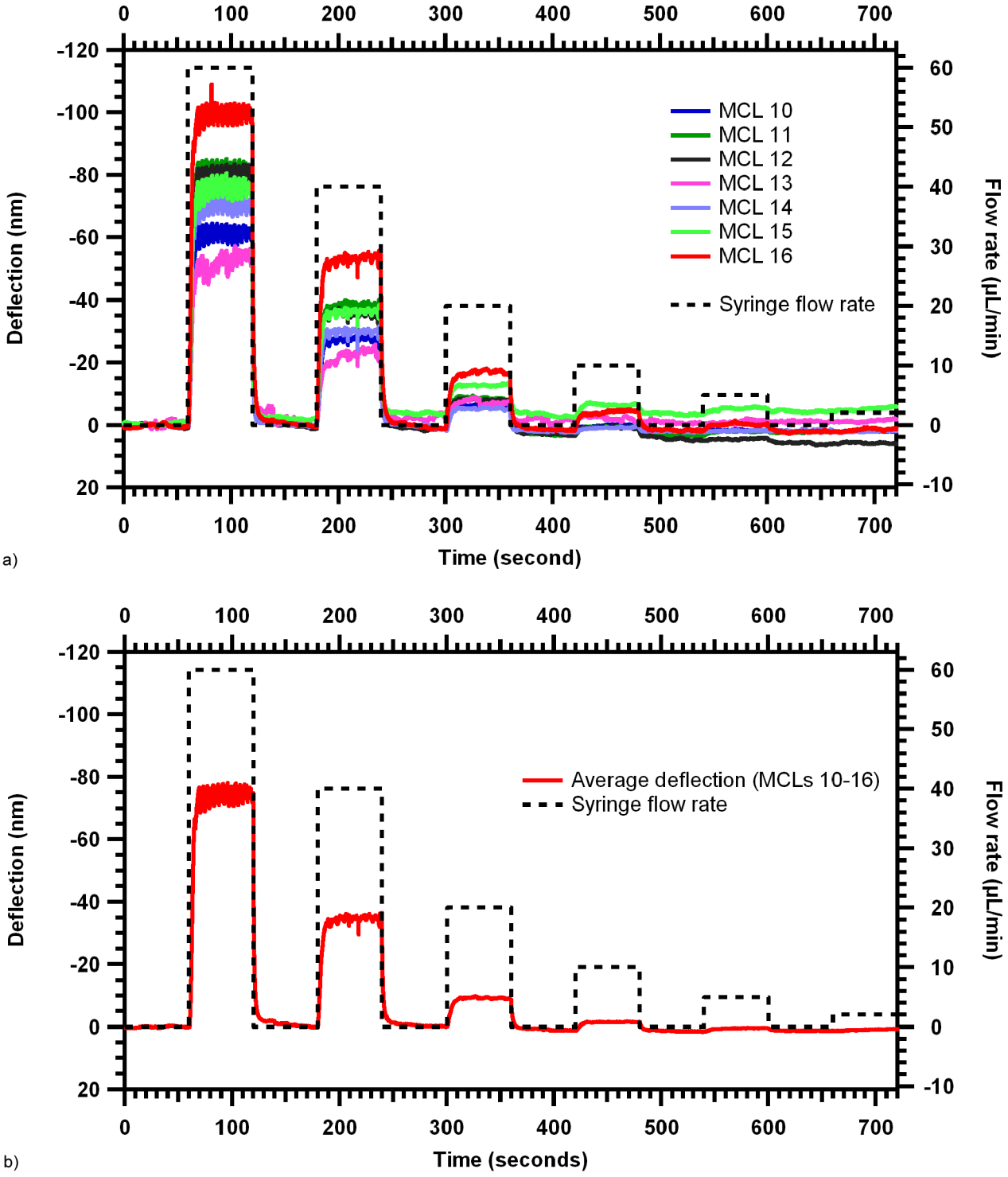

Figure 6.6: Microcantilever array deflection response of (a) individual microcantilevers and (b) average of array. Deflection (left axes) is shown for relatively low flow rates (right axes) with flow returning to zero inbetween each set flow rate.

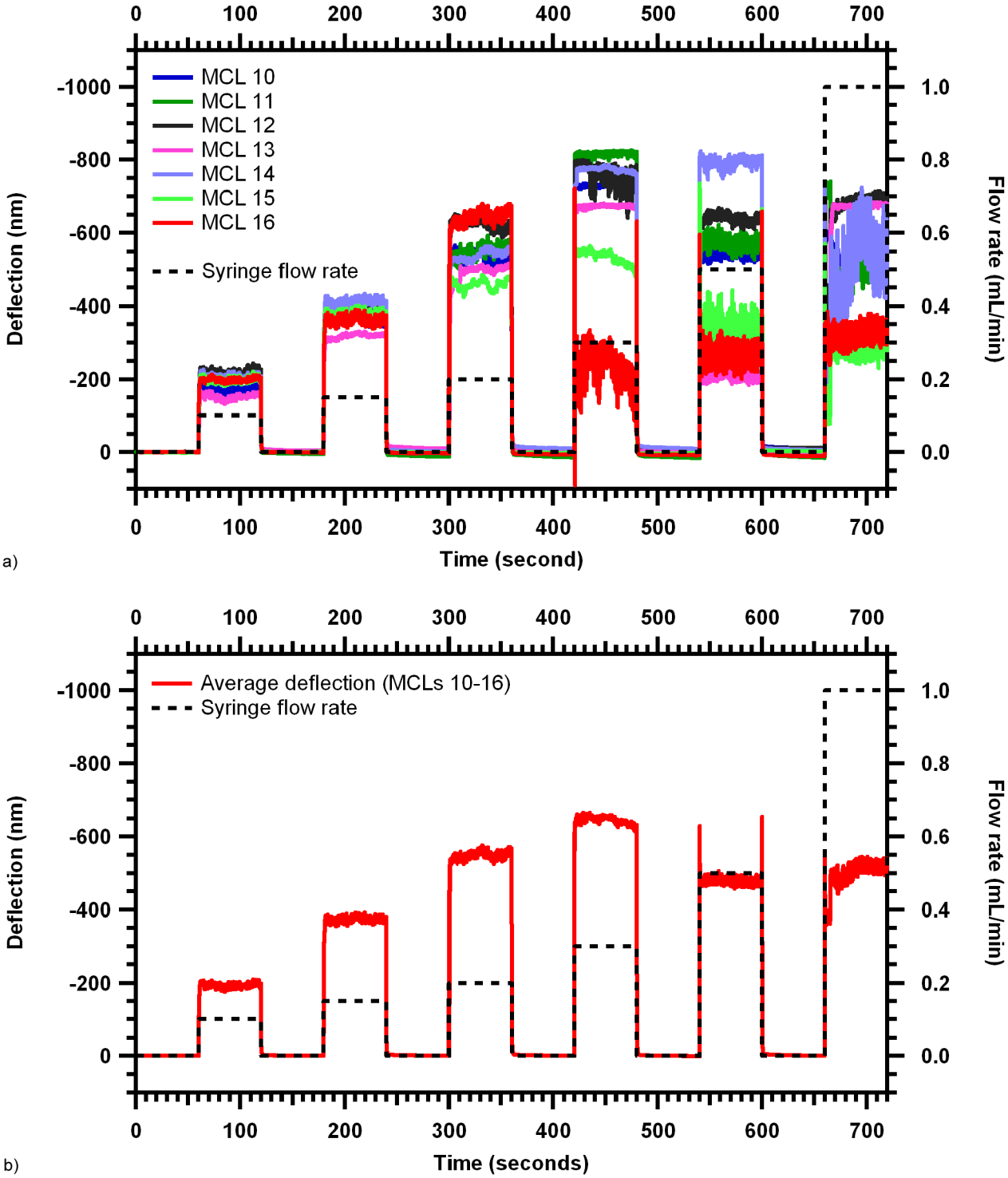

Figure 6.7: Microcantilever array deflection response of (a) individual microcantilevers and (b) average of array. Deflection (left axes) is shown for relatively high flow rates (right axes) with flow returning to zero inbetween each set flow rate.

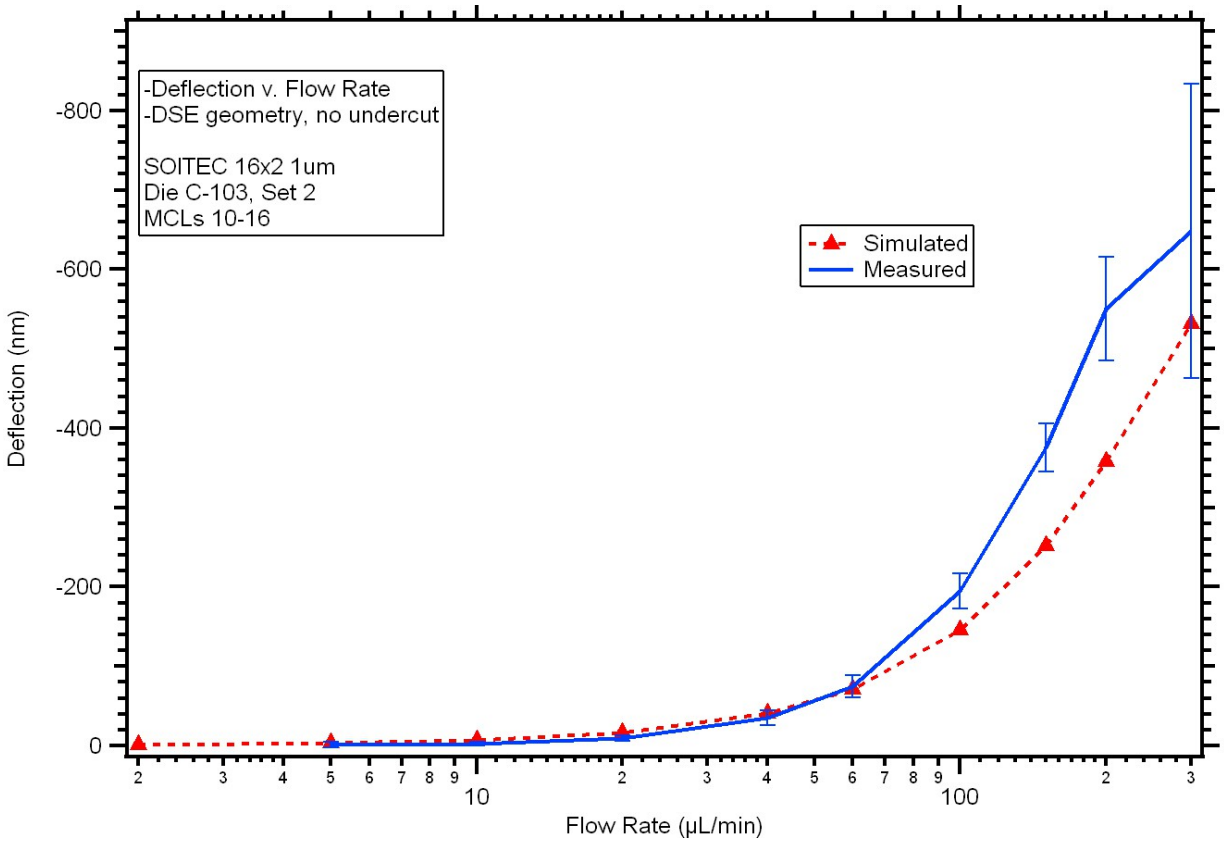

Figure 6.8: Simulated microcantilever deflection in response to flow compared to measured deflection response.

loss from the microcantilever waveguide to the differential splitter waveguide due to deflections greater than ~$\pm$500 nm.

Comparison between the 3D FEM simulation and the average measured deflection response as a function of volumetric flow rate is shown in Fig. 6.8. The measured deflection response agrees well with the simulation for flows below 100 μL/min, however the it diverges from simulation for higher flows. I suggest that this arises from the simulated model underestimating the flow velocity in the microchannel. It has previously been seen, as in Chap. 5, that the actual flow velocity is greater than the the simulated flow velocity, indicating differences between the actual and simulated microchannel cross-sections.

6.5 Conclusion

I demonstrate a microfluidic flow sensing mechanism based on hydrodynamic forces induce by fluid flow in a microchannel across an array of microcantilevers. The average measured deflection is ~1 nm for a volumetric flow rate of 5 μL/min. This is still much larger the estimated minimum detectable deflection (MDD) of the system, therefore I expect the minimum detectable volumetric flow rate to be less than 5 μL/min. Additionally, as the MDD is limited by optical detector noise and not thermomechanical vibrations of the microcantilevers, smaller flows could be detected by utilizing longer microcantilever. The additional flow sensitivity would be at the cost of the dynamic range of flow rates that could be sensed. It is conceivable that an array sensor could be constructed with several microcantilevers of various lengths to give access to a wide dynamic range with the microcantilevers with the narrower dynamic range providing the greater sensitivity. Hence, a photonic microcantilever array sensor for microfluidic flow rate detection can provide high sensitivity and an appropriate dynamic range for large-scale integration with micro-total analysis systems.

CHAPTER 7. INTEGRATION OF RECIPROCATING PUMP IN PDMS MICROFLUIDICS WITH MCL ARRAY

7.1 Motivation

With the advent of lab-on-a-chip microsensors with integrated microfluidics for point-of-care medical diagnoses and detection of environmental chemicals, emphasis has been placed on mechanisms to load small sample volumes into the sensor devices and control flow of the sample solution within the device. Mechanisms for driving flow in microfluidics can be separated into two general classes. through that utilize microfluidics to reduce the sample volume size required and overall device package size are attractive because they have the advantages of high sensitivity and fast response times [101]. However, response time and sensitivity eventually become limited by diffusion and the dimensions of the sensor and microfluidic channels. For laminar flow, diffusion always dominates near the sensor surface while far away convection due to driven flow dominates. The depletion region formed by the analyte molecules being adsorbed and removed from solution at the sensor extends to where the boundary where the dominant transport method transitions from convection to diffusion [39]. To achieve the most rapid sensor response and highest collection rate of analyte to the sensor surface, the depletion region should be kept small to maintain a high concentration gradient, and therefore high diffusive flux, near the sensor. This is typically achieved by using high volumetric flow rates to keep the transition boundary between convective and diffusive transport close to the sensor. While high flow rates result in high collection rates and therefore less time to reach equilibrium between the sensor and solution, the higher flow rates mean that most of the molecules in the sample solution will be swept past the sensor without even coming into contact with the sensor surface. This is a highly inefficient use of the sample volume. In effect this counters the rational for using microfluidics as larger sample volumes are required. One solution to more efficiently use the sample volume while maintaining the advantage of high flow rates is to use microfluidic pathway that continuously recirculates the solution at high flow rates.

Mechanisms for driving flow in microfluidics can be separated into two general classes. Electro-osmotic and the like on one hand, pressure/volume driven on the other. Electro-osmotic can give high flow rates with a uniform flow velocity profile across the channel. But the flow rate is dependent on the ionic nature of the solution. Pressure driven flow does not give a uniform flow, so flow profiles are quadratic with flow highest in the center of the channel and close to zero near the walls of the channel. As PDMS and similar polymers have become widely used to create microfluidic structures, diaphragm-based pumps have been developed.

7.2 Design and Fabrication

7.2.1 Microfluidics and Pump

Similar to the microfluidics previously described, the microfluidics with integrated diaphragm pumps are fabricated in polydimethylsiloxane (PDMS), an elastomeric and visually transparent polymer. Fig. 7.1(a) shows a top-view schematic of the microfluidic PDMS device fabricated which is subsequently integrated with a silicon device which is described later. The microfluidic device consists of two PDMS layers, a fluid channel layer and a control layer, as seen in Fig. 7.1(b) cross-section. Both layers are fabricated using soft lithography techniques by pouring an uncured mixture of PDMS over a mold, baking the PDMS and mold to cure the mixture, and then removing the cured PDMS from the mold. The control layer is then bonded to the top of the fluid layer, which is later bonded to the silicon device.

For the fluid layer, the mold is fabricated using AZ-50XT photoresist polymer, spun at 900 rpm on a wafer to achieve a photoresist thickness of 60 μm. The mold is then soft baked at 60°C for 10 minutes followed by 125°C for 3 minutes. The wafer is exposed in a mask aligner (MA150 Karl Suss) to pattern the mold fluid channels. In order to achieve a curved cross-section for the microfluidic channels, which enables the the valves to fully collapse the channel, after exposure and development the mold undergoes a reflow bake at 125°C for 3 minutes. The resulting dimensions of microfluidic channels in the fluid layer, measured using a profilometer, are 650 μm wide are 64 μm tall. The pump reservoirs, R1 and R2 in Fig. 7.1(a), are 3.5 mm in diameter and the same height, so that the each reservoir has an approximate volume of 620 nL. The total thickness of the fluid layer is 134 μm so that the membrane thickness at the valves and above the reservoirs

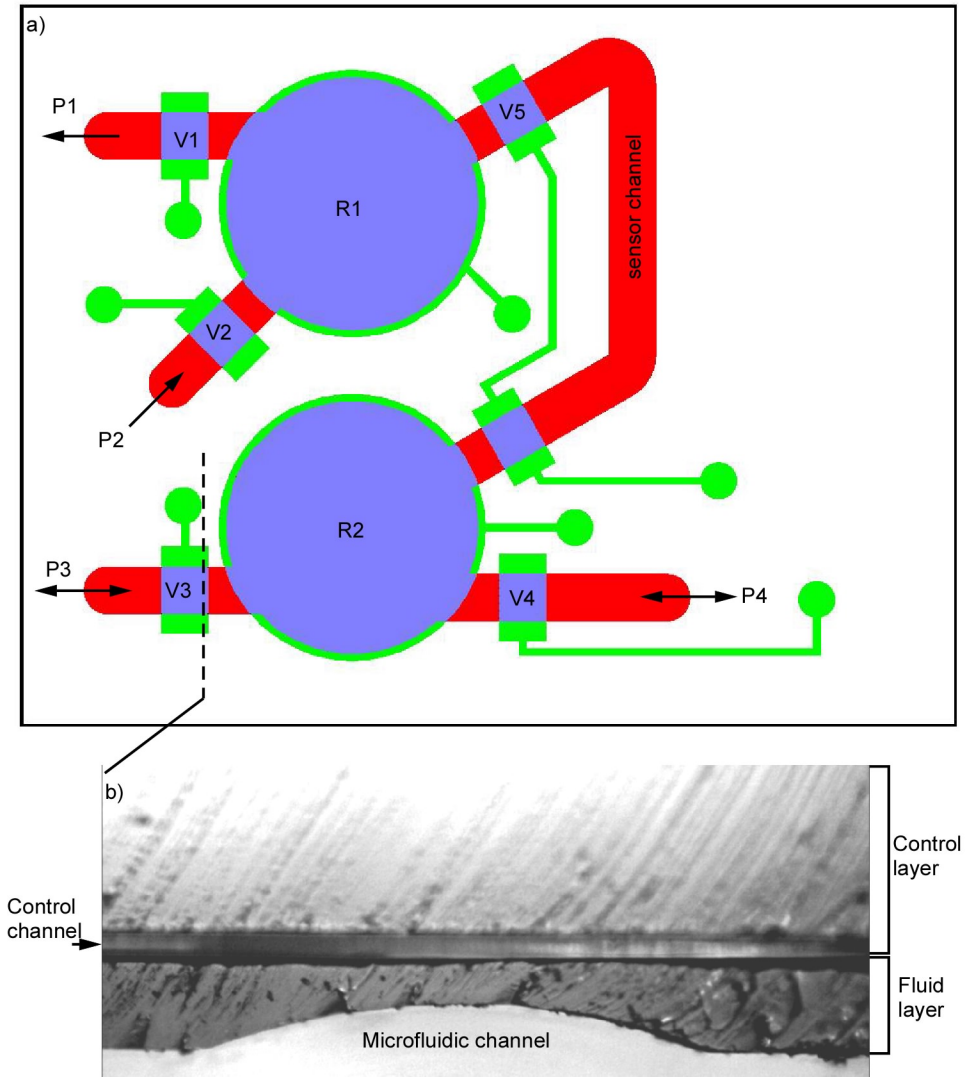

Figure 7.1: (a) PDMS microfluidic device design showing the microfluidic and control channels (red and green, respectively, with overlap in purple) with a reciprocating diaphragm pump. Periodic actuation of reservoirs R1 and R2 drives an alternating pressure driven flow across the sensor channel. Valves V1 through V4 control input and output through the ports, and V5 controls fluid flow into the sensor channel. Ports P1, P3, and P4 are connected to external tubing to allow fluid exchange using a syringe pump. Port P2 has no external tubing to allow small sample volumes to be loaded. (b) Microscope image of cross-section of PDMS device at dashed line.

is 70 μm. The uncured mixture of PDMS for the fluid layer consists of a 10:1 ratio of PDMS prepolymer and curing-agent (Sylgard 184 kit; Dow Corning Corp.) which results in the proper elastomeric properties for the membrane.

A similar process is followed to fabricate the mold for the control layer containing the pneumatically-actuated flow control valves and reservoir actuation chambers. The mold is fab-

ricated using SU8-2025 photoresist polymer, spun at 500 rpm for 6 seconds then 4000 rpm for 30 seconds to achieve a thickness of 24 μm. The control layer mold is then soft baked at 65°C for 3 minutes followed by 95°C for 5 minutes. The wafer is exposed in a mask aligner (MA150 Karl Suss) to pattern the mold control channels, and undergoes a post-exposure bake at 65°C for 1 minutes, then at 95°C for 5 minutes, and finally at 65°C for 1 minute. After development, the mold is hard baked starting at 65°C and ramping up to 150°C for 5 minutes. All control channels are 24 μm tall, the valves are 650 μm by 1200 μm and the reservoir actuation chambers are 3.7 mm in diameter. The total control layer thickness is ~2 mm, and is fabricated using a PDMS mixture with a 4:1 prepolymer to curing-agent ratio.

External tubing (Microbore PTFE #24; Cole-palmer, IL, USA) is connected to the microfluidic and control channels using metal pins (0.394" New England Small Tube Corp., NH, USA) which are inserted into previously punched holes in the PDMS to form a tight seal. For the microfluidic channels, three of the four input/output ports (labeled P1, P3, and P4 in Fig. 7.1(a)) are connected in this way to a syringe for input or a fluid container for output. Port P2 is the small sample volume input and left unconnected without a metal pin. The control channels are connected to two computer-controlled solenoid valve manifolds (H010-H040; Humphrey, LHDA1211111H; The Lee Company) which provide 35 psi of pressurized air to actuate the PDMS control valves and 15 psi to the reservoirs. Because PDMS is gas-permeable, the control channels are filled with water to prevent the pressure differential from forcing air bubbles from an actuated control channel into the microfluidic channel.

7.2.2 Silicon Device

Chips with photonic microcantilever array sensors are fabricated on a 4-inch silicon-on-insulator (SOI) wafer, with an individual chip having dimensions of 1 cm $\times$ 1.4 cm and three arrays, one 16 microcantilever array and two 8 microcantilever arrays. However, for simplicity the microfluidics have been designed to match only the 16 microcantilever array so the other arrays can be ignored. A schematic of the microcantilever array layout on a chip is shown in Fig. 7.2(a). The microcantilevers have dimensions, as seen in Fig. 7.2(b) of 300 μm in length, 45 μm in width, and a thickness of 750 nm except for ~2.5 μm on either side of the central embedded waveguide where the surface is etched down 100 nm to define the waveguide. In order to vertically center the

microcantilevers in the microfluidic channel, the chip undergoes a modified etching process to etch a ~100 μm trench in the underlying silicon substrate beneath the buried oxide layer.

The microcantilevers are patterned using photolithography and defined using an inductively coupled plasma reactive-ion etch (ICP-RIE). Following the definition of the microcantilevers, a deep silicon etch (DSE) process is achieved by coating the die in a layer of the photoresist polymer SU-8 3005. The SU-8 is applied by a spin process, first at 500 RPM with an acceleration of 125 RPM/s for 5 seconds, then a 2000 RPM spin with 500 RPM/s acceleration for 60 seconds, and finally finishing with a 6000 RPM spin with a 4000 RPM/s acceleration for 2 seconds to help eliminate ridges of SU-8 along the edges. The SU-8 is then soft baked on a hot plate at 65°C for 5 minutes at which time the hot plate is increased to 95°C, and when the set temperature is reached the die is baked for another 5 minutes. Exposure is done on a mask aligner (MA150 Karl Suss) for 30 seconds using soft contact with a 70 μm gap. Following exposure, a hard bake is conducted identical to the soft bake process described above. After hard baking, the die is developed for 60 seconds in a bath of SU-8 Developer with gentle agitation. The die is then rinsed with IPA and gently dried using compressed N_2.

The developed SU-8 pattern has a majority of the die protected under SU-8, with openings between the adjacent microcantilevers, with 3 μm covered beyond on each side. As the etch process requires a lengthy Si etch, the edges of the die must be protected. After the die is attached to a carrier Si wafer using thermal paste, 3M Cleanroom High Temperature ESD Tape is carefully placed around the edges of the die, covering the exposed sides of the die. With the sides covered, the only parts of the die open to etching are from the SU-8, which exposes a layer of 1 μm thick layer of SiO_2. The SiO_2 is anisotropically etched away in a Trion Technology Minilock Phantom III RIE/ICP. The SiO_2 etch process is done for 5 minutes using CF_4 at 50 sccm with an RIE power of 75 watts, an ICP power of 350 watts, and a pressure of 12 mTorr. After etching away the SiO_2 layer, the underlying Si is etched away using a semi isotropic Si etch process in an STS Multiplex ICP Etch. The process is run for 28 minutes using SF_6 at 130 sccm with a coil power of 700 watts, a platen power of 12 watts, and a pressure of 50 mTorr. This adequately removes all the Si below the microcantilever, while the the microcantilever itself is protected by the SU-8 on the top and sides and the SiO_2 on the bottom.

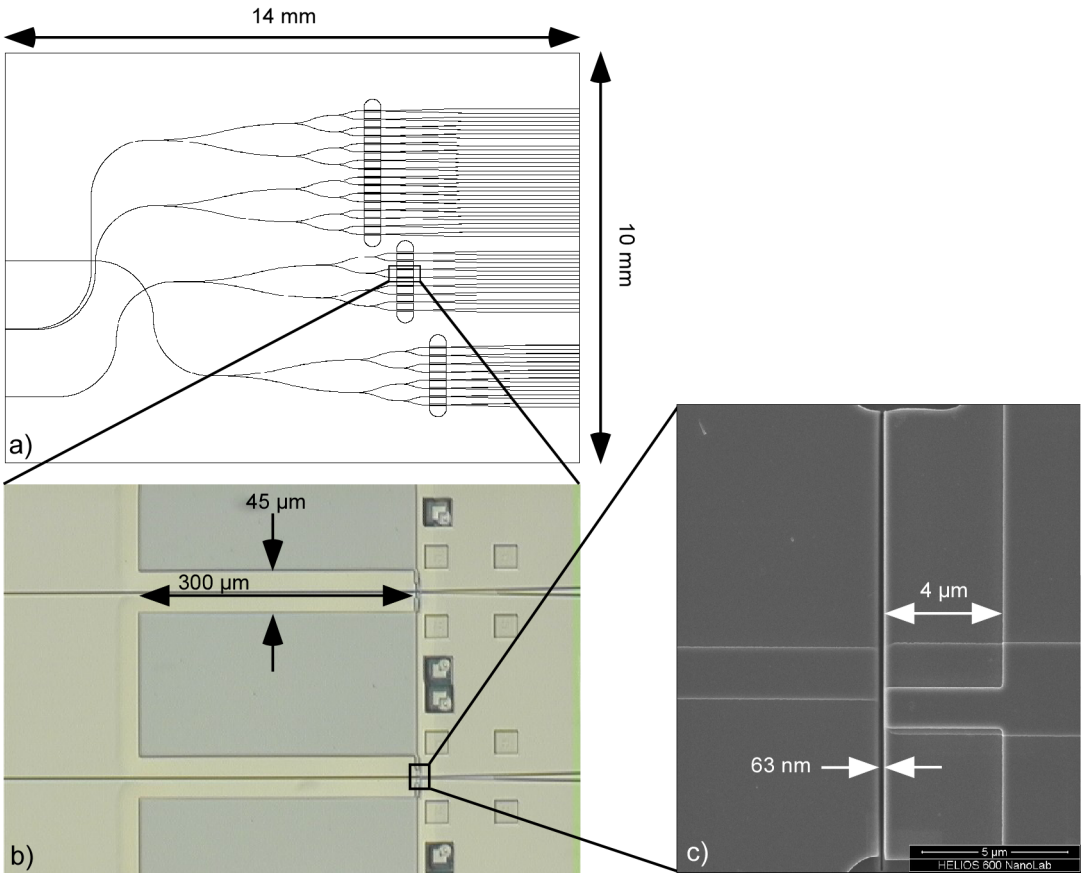

Figure 7.2: Images of silicon device. (a) Schematic of waveguide and microcantilever layout on die. (b) Microscope image of microcantilevers. (c) SEM image of differential splitter and gap at free end of the microcantilever.

After the Si is etched, a 12 hour nanostrip bath at 90°C is done to remove all SU-8 and a 2 minute HF etch applied via pipette over the microcantilevers removes the underlying SiO_2. A very gentle rinse in deionized water and soft N_2 blow removes the HF. A sketch of the DSE trench and the microcantilever array is shown in Fig. 6.1(b). Note that because of the isotropy of the Si etch process, the bottom surface of the trench is not flat but rises about 25 μm to a peak beneath each microcantilever. After this step the microcantilevers are still fixed on both ends, so an FEI Helios Nanolab 600 focused beam of gallium ions is used to release one end of each microcantilever at the differential splitter (Fig.6.1(c)). The width of gap at the free end of the microcantilever can range between 50 and 200 nm; for the samples used for this investigation, the gap width is ~65 nm. With one end free, the microcantilevers often deflect due to intrinsic

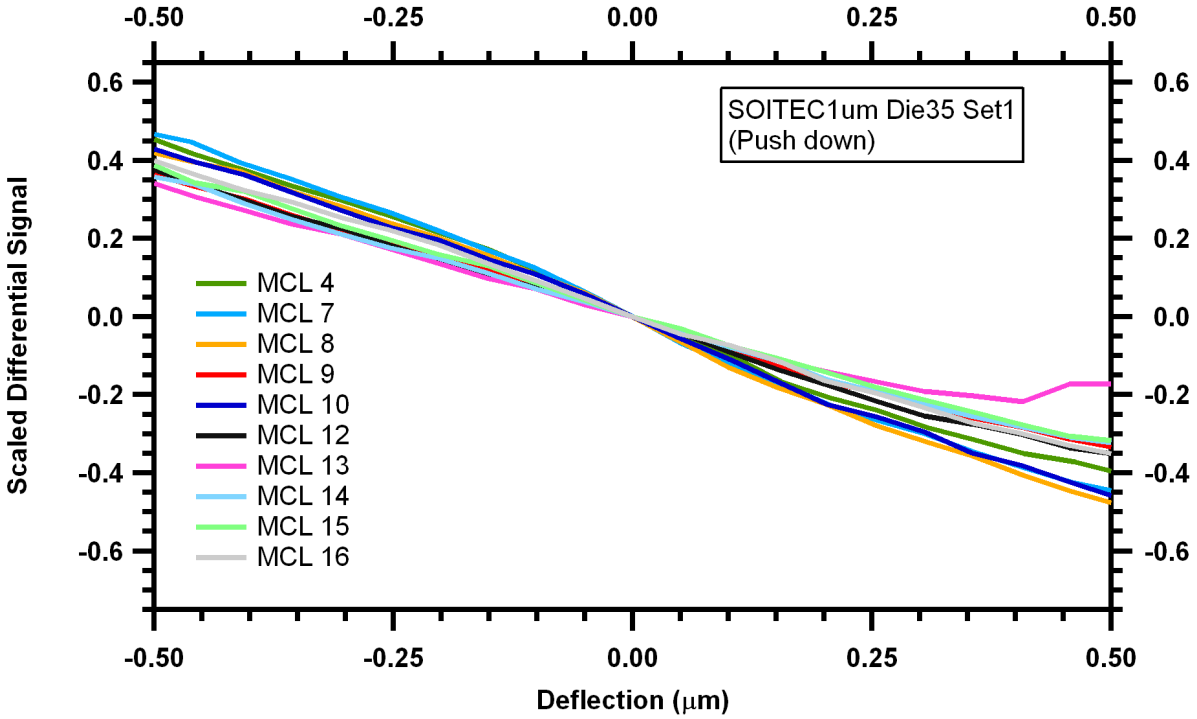

Figure 7.3: Measured responsivities of cantilever array used for testing reciprocating PDMS pumps. There is no signal from MCL #1-3, 5-6 which were broken during fabrication, and #11 which had a defect at the differential splitter. The average responsivity is $0.81 \pm 0.11\ \mu\text{m}^{-1}$.

stresses, and low doses from the same Ga ion beam are used to compensate the MCLs so they lie flat, completing the fabrication process [100].

Once the silicon device is fabricated, the responsivity of the microcantilevers in the sensor array is measured as described in Refs. [43, 45]. The scaled differential signals as a function of microcantilever deflection for the array used in the experiment is shown in Fig. 7.3. Microcantilever #11 is not useable due to a fabrication defect occurring during the focused ion beam etching process to release the free end of the microcantilever. Additionally, microcantilevers #1-3, 5, and 6 broke during the deep silicon etch process. Measurement of the responsivity of the usable microcantilevers over the ± 500 nm deflection range indicates an average responsivity of $0.81 \pm 0.11\ \mu\text{m}^{-1}$, comparable to previously achieved responsivities in magnitude and repeatability between microcantilevers. After the measurement of the responsivity, the PDMS microfluidic device is aligned and bonded to the silicon device to create an integrated sensor package.

7.3 Measurements and Analysis

7.3.1 Small Sample Volume Handling

Similar to unidirectional, single reservoir pumps, periodic actuation of the reservoir can also enable the loading of a small amount of solution into the microfluidics. Reservoir R1, as shown in Fig. 7.1(a), is designed with this in mind, with valves V1 and V2 acting as active check valves. Initially valve V1 is open (unactuated) and valve V2 is closed (actuated), after which the reservoir R1 is also actuated to expel any air or fluid out through port P1, which is connected to a standard syringe pump via external tubing. A droplet of the solution is then placed over the entrance of port P2. Valve V2 is opened and V1 is closed so that when R1 is unactuated, the release of the diaphragm membrane creates a pressure differential which pulls the solution from port P2 into the reservoir. The process is repeated multiple times until a sufficient amount of the solution has been pulled into the reservoir. In order to facilitate the removal of bubbles, a syringe pump connected to port P1 pushes excess fluid (usually from the sample solution itself that has been pulled through the reservoir during the multiple actuations) into the reservoir while V2 is closed, pressurizing the fluid in the reservoir thus maximizing the fluid volume in the reservoir and forces air bubbles out through the gas-permeable PDMS.

7.3.2 Microcantilever Response for Long Period Actuation

To prepare the microcantilever array for the experiment, deionized (DI) water is introduced in all the microfluidic channels. Reservoir R1 is actuated after which valves the channel valve and input/output valves around that reservoir are actuated. DI water is then loaded into R2 via P3 using the syringe pump and, with V4 closed, pressurized to about 4.5 psi to ensure maximum volume capacity for the reservoir, after which V3 is closed. Approximately 15 seconds prior to alternating actuation, the channel valve is opened resulting a small spike in the deflection. The reciprocating diaphragm pump operates by alternately actuating the control chambers above each reservoir with all but valve V5 closed, so that the alternating flow between the reservoirs is driven across the sensor channel. On the first stroke of the pump period, R2 is actuated and the pressure on R1 is released. The deflection response of the microcantilever array is seen Fig. 7.4 for several actuations

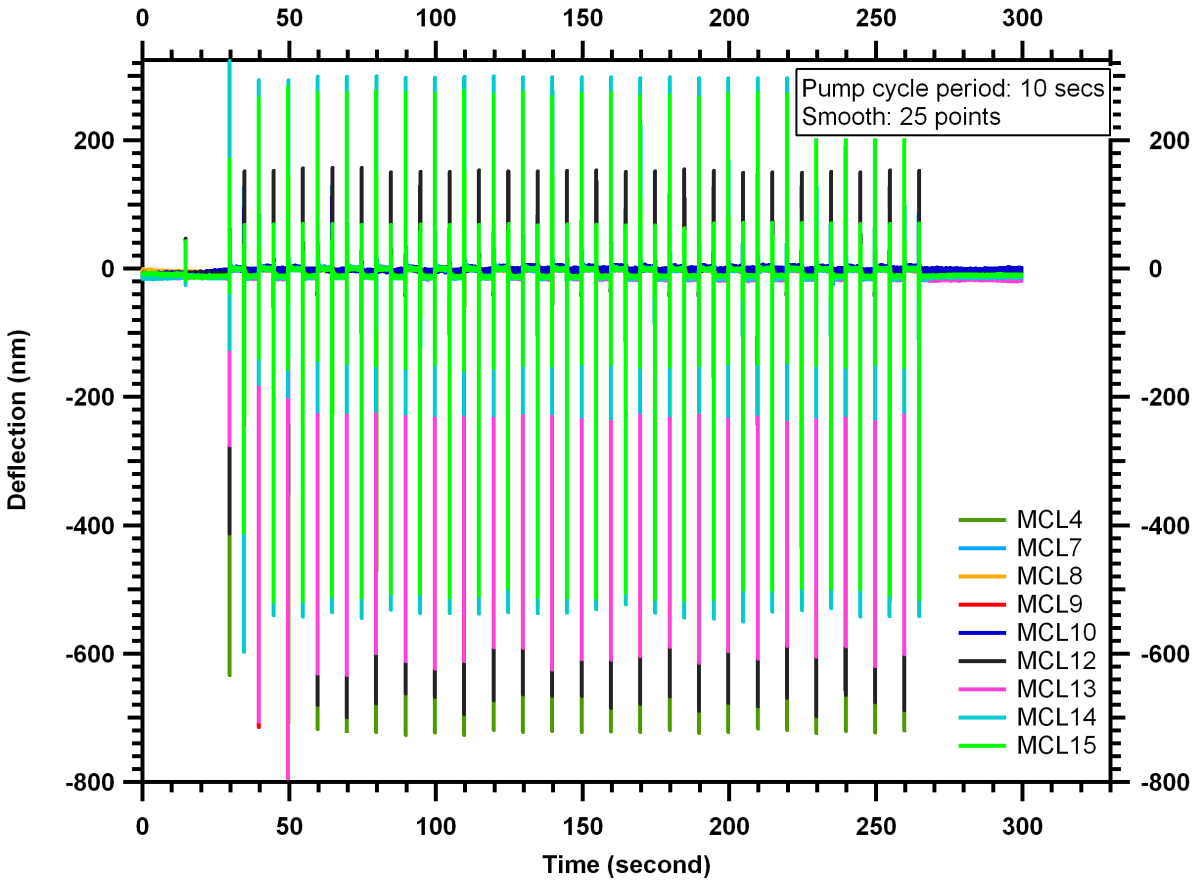

Figure 7.4: Response of microcantilever array to repeated pump actuation. Full cycle period of pump is 10 seconds.

of the pumps over an extended period of time. The deflection spikes due to the short burst of flow vary over the first three pump cycles before becoming more consistent and repeatable.

The response of a single actuation is shown in Fig. 7.5 for both pump actions in a single cycle. I note that as expected the deflection is extremely large. Based on the previously measured responsivities, the average maximum deflection is -417.2$\pm$243 nm for the first pump actuation, and -342.9$\pm$152 nm for the second. However, as discussed in Chap. 6.4.2, the linear relation between scaled differential signal and deflection generally only holds true inside a ~1 μm dynamic range. Outside of the dynamic range, the scaled differential signal as a function of deflection is known to be neither linear nor monotonic. This might explain the anomalous behavior of some of the microcantilevers, such as MCL 15, which appear to reverse direction in the middle of the cycle. As seen in the previous chapter, anomalous bending of the microcantilevers begins to be

apparent for flow rates greater than 200 μL/min. Also using the previously measured relationship between volumetric flow rate and microcantilever deflection, I can estimate maximum flow rates during each actuation to be ~200$\pm$100 μL/min for the first actuation, and ~180$\pm$120 μL/min for the second, although it is likely that these underestimate the actual flow rate due to the anomalous responses.

The full duration of the deflection response is approximately 250 ms, relatively short compared to the period of a full pump cycle. During the first 50 ms, the microcantilevers deflect in the positive direction, most within 100 nm of the initial deflection. This is quickly followed by ~40 ms of large negative deflections, corresponding to a high volumetric flow rate. After this large deflection, the microcantilevers return back near their initial zero deflection, but not before briefly overshooting the zero deflection and slowly settling back. The overshoot into positive deflections during the final interval indicates that the microcantilevers are behaving like harmonic oscillator in a damping viscous solution with $\zeta < 1$ (underdamped). At the present time I am unable to adequately explain the positive deflection during the first 40 ms, as this differs from the negative deflections I've previously observed in response to fluid flow. One possibility is that the type of pressure driven flow, whether it is driven by positive pressure or by negative pressure, results in different flow profiles above and below the microcantilevers causing different hydrodynamic pressures and hence deflections in different directions.

7.3.3 Microcantilever Response for Short Period Actuation

The large deflections induced by the high volumetric flow rate will mask any change in static deflection due to analyte adsorption to the microcantilever surface. The high flow rates are necessary to quickly replenish analyte depletion regions that may form around the microcantilever and improve the response time of the sensors. Measurements of the static deflection can be made in the relatively quiescent intervals between reservoir actuations. Reducing the period of the pump cycle increases the overall average flow rate but decreases the amount of time over which static deflection measurements can be made. The microcantilever response when the full cycle period is 500 ms is seen in Fig. 7.6. Notice that with this short of a cycle period, several of the microcantilevers do not fully return to a steady state deflection prior to the next reservoir actuation. From these observations, the minimum full pump cycle for actual sensing scenarios should at least be

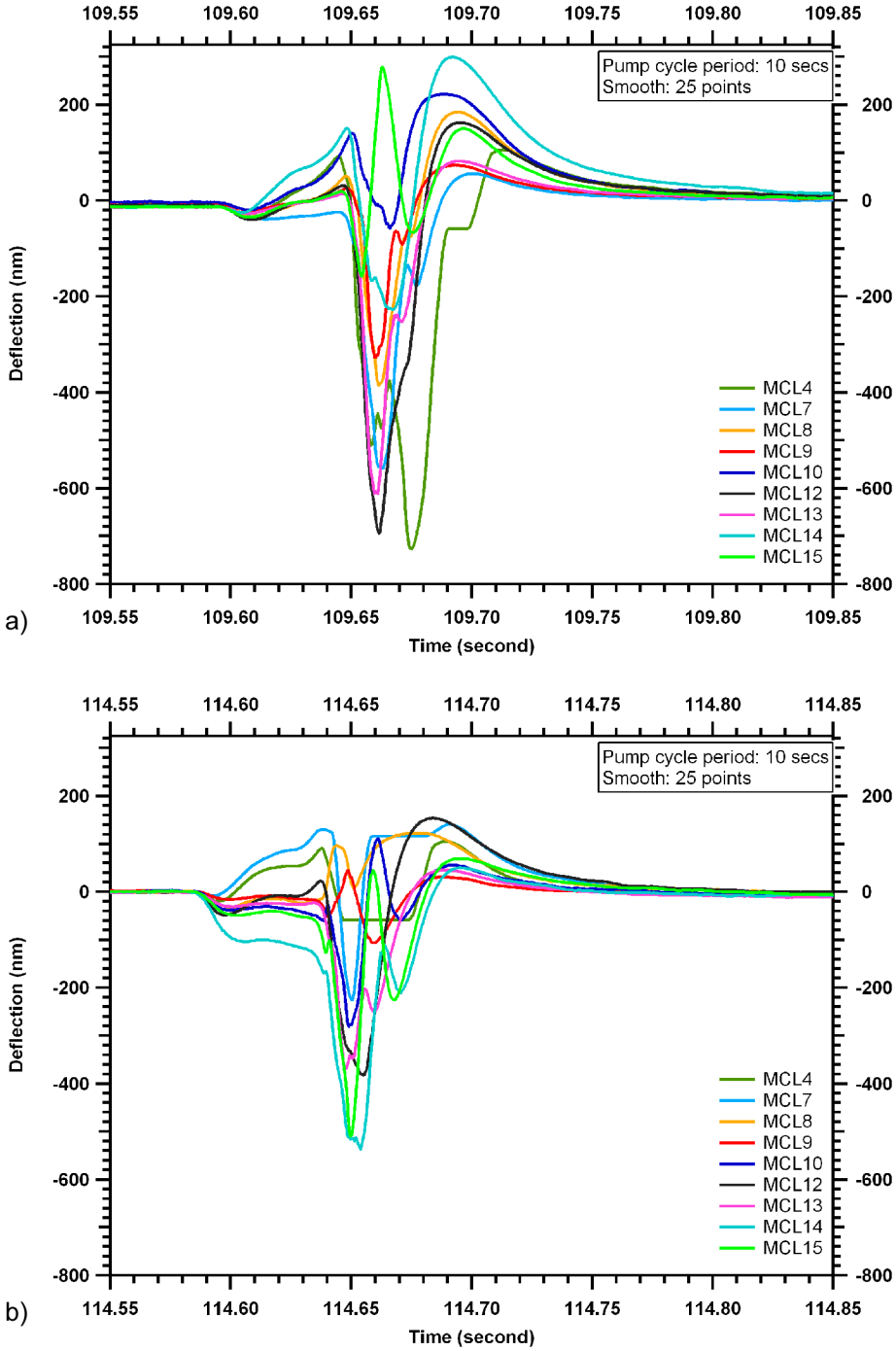

Figure 7.5: Close up of microcantilever responses to single actuation of (a) reservoir 1 and (b) reservoir 2.

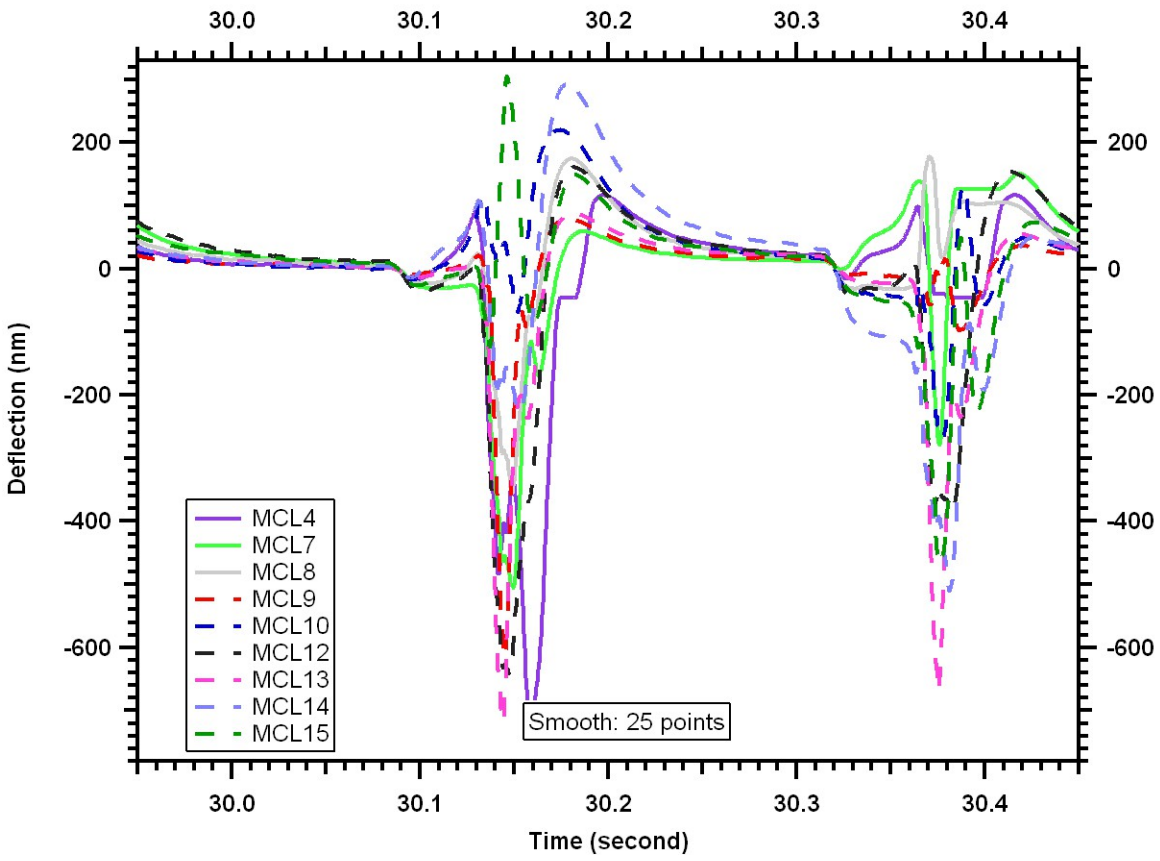

Figure 7.6: Close up of microcantilever responses to multiple pump actuations close together in time. The full pump cycle here is 500 ms.

1 second. Also as the period gets shorter, the effects of the temporal resolution of the internal clock used to time the actuation becomes more apparent making timing of the static deflection measurement more problematic.

7.4 Conclusion

I have successfully integrated PDMS microfluidics with an on-chip reciprocating pump to a microcantilever array sensor. The ability to load small sample volumes with the PDMS microfluidics has also been demonstrated. The microcantilevers respond strongly with average deflections of 417 nm and 342 nm for alternating reservoir actuations. The deflections give estimates for the maximum volumetric flow rate of ~200 μL/min and ~180 μL/min, respectively, when the reservoir is actuated. The microcantilevers are also observed to return to zero-deflection within 250 ms of

the initiation of a reservoir actuation. Returning to a steady state deflection will allow me to interleave static deflection measurements with pump actuations. This will enable me to load a small volume of analyte solution into a reservoir, drive the solution across the microcantilever array with high flow rates, and observe changes in static deflection due to analyte absorption to functionalized microcantilever surfaces.

CHAPTER 8. MEASUREMENT AND CHARACTERIZATION OF MICROCANTILEVER SENSOR NOISE

8.1 Motivation

The main limiting factors for the sensitivity of a microcantilever as a general sensing platform are the responsivity of the sensor to the environmental stimulus of interest, the deflection-to-signal responsivity of the transduction method, and the measurement noise inherent in the transduction method. Because atomic force microscopes (AFM) are widely used and much effort has already been invested into optimizing their performance, AFM microcantilevers provide a standard benchmark for comparison of sensors that employ other methods for deflection transduction. In an AFM the deflection of the microcantilever is measured by reflecting a laser beam from the free end of the microcantilever onto a position sensitive detector (PSD). Typical reported responsivities with this transduction method are typically ~1 μm^{-1}, and a deflection noise density in liquid of ~150 $\text{fm}/\sqrt{\text{Hz}}$ with roughly 1-5 mW incident laser power. As the readout noise is primarily limited by the PSD, the deflection noise could be further improved with greater laser power. However, increasing the optical power increases heating and thermally-driven vibrations due to absorption of a part of the incident laser power.

I have demonstrated the consistent fabrication of silicon microcantilever arrays using the novel in-plane photonic transduction method with responsivities of ~1 μm^{-1}, comparable to the reported responsivities of the optical beam deflection transduction of AFMs. Additionally, the in-plane photonic transduction method operates at a wavelength of 1550 nm, where silicon is transparent so that absorptive heating is negligible, and with optical powers 0.1-1 nW per output. Currently the optical output powers are measured using an InGaAs line scan camera which is, similar to the PSD of the AFM, the limiting noise source. Spectral analysis of the deflection noise density should indicate if the source of the limiting noise is inherent to the photodetector, such as Johnson noise and dark current shot noise, and so would be improved by implementing detectors

in which these noise sources are minimized. Alternatively, if the deflection sensitivity is shot noise limited, which is independent of the type of photodetector, it is sufficient to choose a detector which is shot noise limited for the expected output optical powers.

8.2 Design

8.2.1 Silicon Device Design

In order to measure the inherent noise the in-plane photonic transduction method, chips with photonic microcantilever array sensors are fabricated on a 4-inch silicon-on-insulator (SOI) wafer. Individual chips are 1 cm $\times$ 1.4 cm and contain two arrays of 16 microcantilevers each. A schematic of the microcantilever array layout on a chip is shown in Fig. 8.1(a). The microcantilevers are fabricated with dimensions of 300 μm in length, 45 μm in width, and a thickness of 750 nm except for ~2.5 μm on either side of the central embedded waveguide where the surface is etched down 100 nm to define the waveguide.

After the microcantilevers are defined, the chips are divided into two groups. The fabrication process for one group of chips goes no further than the waveguide and microcantilever definition and left in an unreleased state, seen in Fig. 8.1(b). The chips with unreleased microcantilevers provide a control group to determine how much of the deflection noise of a fully fabricated device is due to vibration of the released microcantilever, due to thermal excitation of the microcantilever itself or coupling of vibration to device from the chip mount and environment.

The microcantilever samples undergo a deep silicon etch (DSE) process to remove the oxide layer to release the microcantilever. The DSE process is achieved by coating the die in a layer of photoresist polymer SU-8 3005. The SU-8 is applied by a spin process, first at 500 RPM with an acceleration of 125 RPM/s for 5 seconds, then a 2000 RPM spin with 500 RPM/s acceleration for 60 seconds, and finally finishing with a 6000 RPM spin with a 4000 RPM/s acceleration for 2 seconds to help eliminate ridges of SU-8 along the edges. The SU-8 is then soft baked on a hot plate at 65°C for 5 minutes at which time the hot plate is increased to 95°C, and when the set temperature is reached the die is baked for another 5 minutes. Exposure is done on a Karl Suss Mask Aligner MA 150 for 30 seconds using soft contact with a 70 μm gap. Following exposure, a hard bake is conducted identical to the soft bake process described above. After hard baking, the

die is developed for 60 seconds in a bath of SU-8 Developer with gentle agitation. The die is then rinsed with IPA and gently dried using compressed N_2.

The developed SU-8 pattern is designed to protect the majority of the die under SU-8, with openings between the adjacent microcantilevers where the Si and the SiO_2 layers will be etched. The openings are smaller the intended regions to be etched by 3 μm on each side to accommodate etching in the lateral direction. As the etch process requires a lengthy Si etch, the edges of the die must be protected. After the die is attached to a carrier Si wafer using thermal paste, 3M Cleanroom High Temperature ESD Tape is carefully placed around the edges of the die, covering the exposed sides of the die. With the sides covered, the only parts of the die open to etching are from the SU-8, which exposes a layer of 1 μm thick layer of SiO_2. The SiO_2 is anisotropically etched away in a Trion Technology Minilock Phantom III RIE/ICP. The SiO_2 etch process is done for 5 minutes using CF_4 at 50 sccm with an RIE power of 75 watts, an ICP power of 550 watts, and a pressure of 12 mTorr. After etching away the SiO_2 layer, the underlying Si is etched away using a semi-isotropic Si etch process in an STS Multiplex ICP Etch. The process is run for 28 minutes using SF_6 at 130 sccm with a coil power of 700 watts, a platen power of 10 watts, and a pressure of 50 mTorr. This adequately removes all the Si below the microcantilever, while the the microcantilever itself is protected by the SU-8 on the top and sides and the SiO_2 on the bottom.

After the Si is etched, a 12 hour nanostrip bath at 90°C is done to remove all SU-8 and a 2 minute HF etch applied via pipette over the microcantilevers removes the underlying SiO_2. A very gentle rinse in deionized (DI) water and soft N_2 blow removes the HF. A sketch of the DSE trench and the microcantilever array is shown in Fig.6.1(b). Note that because of the isotropy of the Si etch process, the bottom surface of the trench is not flat but rises about 25 μm to a peak beneath each microcantilever. After this step the microcantilevers are still fixed on both ends, so an FEI Helios Nanolab 600 focused beam of Gallium ions is used to release one end of each microcantilever at the differential splitter (Fig.6.1(c)). The width of gap at the free end of the microcantilever can range between 50 and 200 nm; for the samples used for this investigation, the gap width is ~65 nm. With one end free, the microcantilevers often deflect upward out of the plane due to intrinsic stresses. Low doses from the same Gallium ion beam are used to compensate the MCLs so that they lie flat, completing the fabrication process [100].

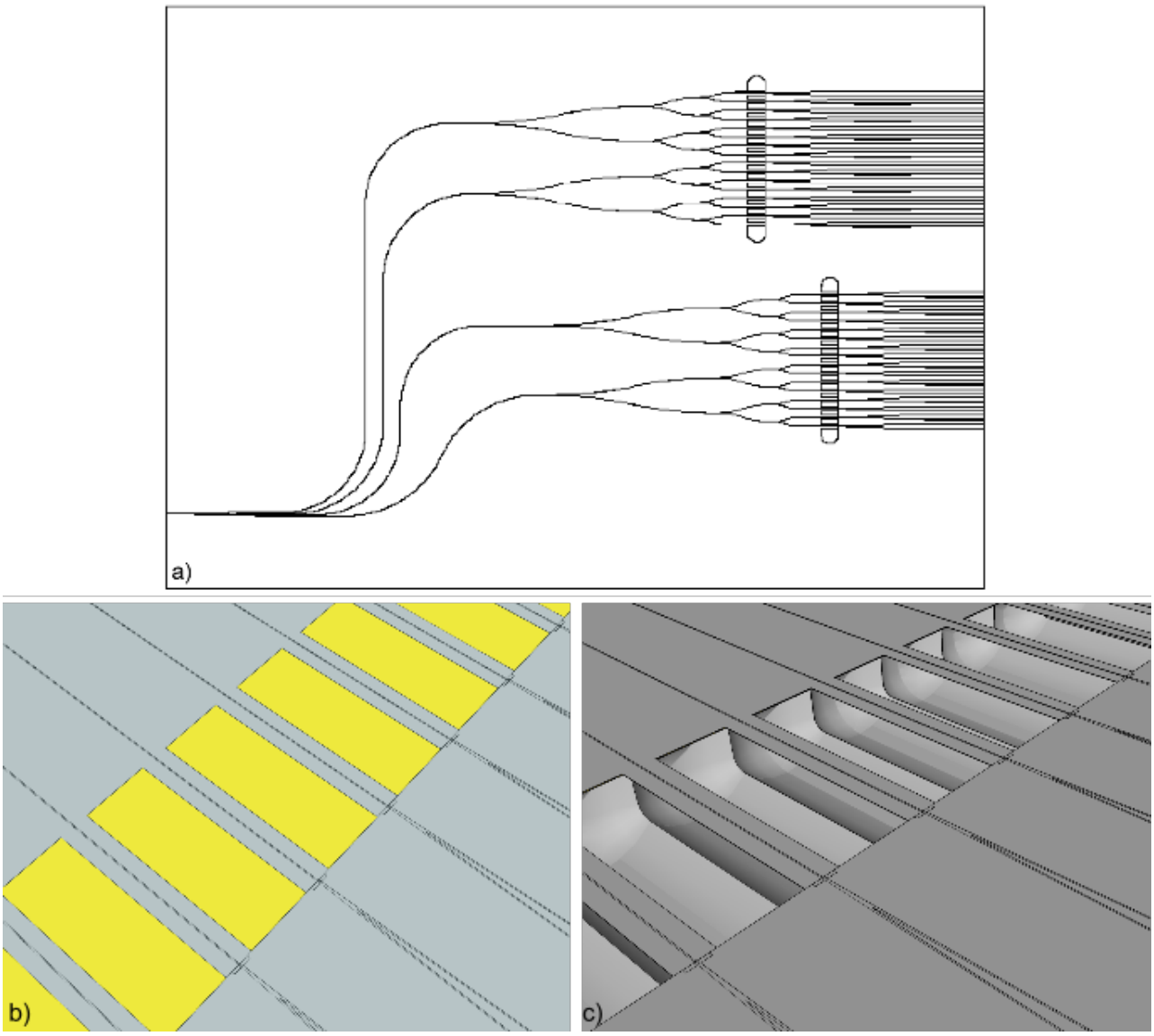

Figure 8.1: a) Schematic of waveguide and microcantilever array layout for a single chip. Illustration of (b) microcantilever array prior to the isotropic deep silicon etch (exposed oxide layer shown in yellow) and (c) microcantilever array after isotropic deep silicon etch.

8.2.2 Experimental Setup

In order to calculate the noise density of the microcantilever sensor, long duration measurements are required. Measurements are made using a similar setup used to determine the deflection responsivity of the scaled differential signal. Optical power is provided by a superluminescent light emitting diode, or SLED (DL-BZ1-CS5403A-FP-00; Denselight), through a butt-coupled optical fiber. The output power of the SLED is controlled by an applied voltage and can vary from 0.3 to 48 mW. The output face of the sample is imaged on 512-element focal plane array, line scan camera (SU512LDV; Goodrich) which enables the outputs to be sampled simultaneously. After the optics are aligned, data is acquired for 500 s and no averaging is done to prevent convolution of the averaging filter with the noise spectrum of the microcantilever signal.

The variance of the power spectrum can be significantly reduced at the cost of frequency resolution by using the Welch method of averaging periodograms [102]. The measured data for each microcantilever is broken up into segments of the 8192 data points with 50% overlap. The number of data points in each segment is chosen to be of the form 2^N to facilitate the computing the discrete Fourier transform (DFT) of each segment. The squared magnitude of the DFT of an individual segment is a periodogram. The periodograms are then time-averaged and divided by the width of the discrete frequency bins to obtain the noise power density.

8.3 Results and Discussion

8.3.1 Basic Principles

Because the scaled differential transduction signal is calculated from measured intensities of each microcantilever's two outputs, the deflection error can be estimated to first order in terms of the powers and the measurement noise of both outputs. The scaled differential signal, η_{sc}, is defined as

$$\eta_{\mathrm{sc}} = \frac{P_2 - \alpha P_1}{P_2 + \alpha P_1} \tag{8.1}$$

where P_1 and P_2 are the measured powers of the two outputs and the ratio α is a scaling factor

$$\alpha = \frac{P_{20}}{P_{10}}$$

defined in terms of the output powers measured at zero deflection, P_{10} and P_{20}. A first-order error estimate of the variance (the noise) of the scaled differential signal, σ_η, is therefore given by

$$\sigma_\eta^2 = \left(\frac{\partial \eta}{\partial P_1}\right)^2 \sigma_1^2 + \left(\frac{\partial \eta}{\partial P_2}\right)^2 \sigma_2^2 \tag{8.2}$$

where σ_1 and σ_2 are the variances of the outputs P_1 and P_2, respectively. Calculating the partial derivatives of the differential signal from Eq. 8.1 with respect to each output yields the following for the differential signal noise:

$$\sigma_\eta = \frac{2\alpha\sqrt{P_2^2\sigma_1^2 + P_1^2\sigma_2^2}}{(P_2 + \alpha P_1)^2}. \tag{8.3}$$

Finally, applying a measured responsivity, R_η, to Eq. 8.3 gives the deflection noise σ_z in terms of the power and noise of the outputs,

$$\sigma_z = \frac{2\alpha\sqrt{P_2^2\sigma_1^2 + P_1^2\sigma_2^2}}{R_\eta\,(P_2 + \alpha P_1)^2}. \tag{8.4}$$

8.3.2 Major Noise Sources

There are multiple possible detection noise sources that will limit the sensitivity of deflection measurements. The sources generally encountered are shot noise from both the generated photocurrent and the detector dark current, Johnson noise from thermal fluctuations in the detector impedance, flicker noise which is inversely proportionate to the measurement frequency, and quantization noise from the analog-to-digital converter. As these noise sources are independent of one another, the total noise is found by summing the individual noises in quadrature. However, devices often operate in a parameter space where a single noise source dominates over the others. For instance, microcantilever deflection measurements using the optical beam deflection, like in AFMs, are typical operating at high frequencies in a high optical power regime where the shot noise of the PSD is the limiting noise.

For photodetectors, shot noise arises from the photocurrent generated by the incident photons as well as from the dark current of the device. Shot noise occurs due to the discrete nature of

the charges that make up the current. The magnitude of the current fluctuations due to shot noise, σ_{shot}, is given by the expression:

$$\sigma_{\text{shot}} = \sqrt{2qI\Delta f} \tag{8.5}$$

where q is the electron charge, I is the current generating the shot noise, and Δf is the measurement bandwidth. Shot noise is therefore frequency independent, also known as "white" noise, and temperature independent. As previously indicated, the generating current can be either the photocurrent or the dark current. In the former case, the photocurrent is related to the incident optical power by the quantum efficiency ϕ of the detector, so that the expression for σ_{shot} takes the form:

$$\sigma_{\text{shot}} = q\sqrt{\frac{2\phi P\lambda\Delta f}{hc}} \tag{8.6}$$

where P is the incident optical power, λ is the wavelength of the incident light, h is Planck's constant, and c is the speed of light. A distinguishing characteristic of photocurrent shot noise is therefore that it is proportional to the square root of the incident power. Combining Eqs. 8.4 and 8.6 then indicates that in the regime where this noise is dominant, the deflection noise is proportional to $P^{-1/2}$. In the latter case, when the shot noise is generated by the detector dark current, the noise is independent of the incident power. Therefore in the regime where dark current shot noise is dominant, the deflection noise is proportional to P^{-1}. When dealing with low-level signals, the dark current shot noise generally greater than the photocurrent shot noise.

Johnson noise, also known as thermal noise, arises from the thermally-driven random motion of the charge carriers within an electric conductor. The random motion results in current fluctuations, σ_{J} even in the absence of an external voltage source. From statistical analysis, the magnitude of the fluctuations σ_{J} is given by

$$\sigma_{\text{J}} = \sqrt{\frac{4k_{\text{B}}T\Delta f}{R}} \tag{8.7}$$

with k_{B} as the Boltzmann constant, T as the detector temperature, and R as the detector impedance. Similar to shot noise, Johnson noise is frequency independent ("white"), however it is also independent of the incident power. Johnson noise can be controlled by reducing and maintaining the

temperature of the detector. Like dark current shot noise, when Johnson noise is the limiting noise, the deflection noise is inversely proportional to the optical power of the outputs.

While shot noise and Johnson noise are typically expected to be the dominant noise source in the low optical power regime, there are other noise candidates that should be considered when determining the sensing limit. Flicker noise is a significant noise source for static deflection measurements of microcantilevers [23, 64, 103–105]. Unlike other noise sources, flicker noise is not "white" noise but is instead inversely proportional to frequency. Depending on the noise levels of the frequency independent noise sources, flicker noise dominates at frequencies below ~1-10 Hz. Another often ignored noise source is quantization noise from analog-to-digital conversions (ADCs). As long as the signal is larger than the least significant bit (LSB) of the ADC, the quantization noise in units of bit depth is $\approx \frac{1}{\sqrt{12}}$LSB. In terms of the equivalent current fluctuations of a photodetector, the quantization noise is given by

$$\sigma_{\mathrm{Q}} = \frac{1}{\sqrt{12}} \frac{Q_{\max}}{\Delta t \, (2^N - 1)} \tag{8.8}$$

where $Q_{\max}$ is the saturation charge of the photodetector and N is the number of bits of the ADC. Finally, the readout integrated circuit connected to the pixel array contributes a noise voltage, called readout noise, that occurs each time the line scan is readout. Readout noise is usually given in units of electrons per root scan. The expression for the equivalent current fluctuations of the readout noise is

$$\sigma_{\mathrm{ro}} = \frac{RO\sqrt{N}}{\Delta t} \tag{8.9}$$

where RO is the readout noise per root scan and N is the number of scans that are being summed together.

The photonic properties of the microcantilever array device and the differential splitter place the sensor within the low optical power regime. Optical losses from the fiber-to-chip coupling, from the ~100 nm gap at the free end of the microcantilever, and from the splitting of the single source into 32 outputs result in output optical powers that are < 10 nW and often sub-nW. Therefore I do not expect photocurrent shot noise to dominate in most situations. Table 8.1 shows the relevant parameters of the InGaAs line scan camera, according to the manufacturer's datasheets, from which can be estimated the contribution of most of the signal independent noise

Table 8.1: Relevant performance characteristics of InGaAs line scan camera per manufacturer documentation.

Parameter	Value
Wavelength	1550 nm
Quantum efficiency	70%
Dark rate (max)	0.5 V/s
Readout noise	800 e/$\sqrt{\text{scan}}$
Gain	400 nV/e , 15.4 nV/e
Saturation charge	0.8 pC , 20.8 pC
ADC bit depth	14 bits
Minimum exposure time	0.02 ms
Maximum line sample rate	4340 Hz

sources. Note that the camera has two operation modes: high sensitivity mode with a high-gain capacitor and hence a smaller saturation charge, and high dynamic range mode with a low-gain capacitor and a larger saturation charge.

8.3.3 Unreleased Microcantilevers

The test samples with unreleased microcantilevers provide a control group for distinguishing detection noise from noise due to physical vibration of the microcantilevers themselves. The lack of a gap between the microcantilever waveguide and the differential splitter causes most of the guided mode to couple into the the mode associated with the P_2 output, such that the ratio of the outputs P_2 to P_1 is approximately 4:1. Additionally, the optical losses are reduced and the output power of the SLED is turned down to prevent saturating the camera pixels. The resulting noise spectra following signal processing are shown in Fig. 8.2 for an exposure time of 24 μs, corresponding to a 4340 Hz line scan sampling rate, with the camera in its high sensitivity mode and with the SLED control voltage at 1.2 V, corresponding to an SLED output power of 29 mW. The corresponding device output powers are measured to be 5-10 μW and 20-40 μW for P_1 and P_2, respectively.

The noise density spectra of the P_1 and P_2, shown in Fig. 8.2(a) and (b), indicate that the noise density floor is flat and frequency independent above 20 Hz. Below 10 Hz, the noise is not frequency independent but dominated by $1/f$ flicker noise. A few narrowband noise sources are

seen at specific frequencies, such as 60 Hz and 120 Hz, as well as a broadband noise between 400 and 500 Hz. The noise density floor is somewhat higher for the P_2 outputs, suggesting at least some significant contribution for the photocurrent shot noise. However, the increase in the noise floor is less than the expected factor two. The noise spectra for the scaled differential signals are also shown in Fig. 8.2(c). The average noise density floor for the scaled differential signal is ~2×10^{-5} $\mathrm{Hz}^{-1/2}$. Assuming an average signal-to-deflection responsivity of 1 $\mu\mathrm{m}^{-1}$, this would result in a deflection noise density of ~20 $\mathrm{pm}/\sqrt{\mathrm{Hz}}$.

Additional power spectra are obtained for different settings of the camera, longer exposure times and the low sensitivity mode, and for different input optical powers. The effect of decreasing the optical power of the SLED is shown in Fig. 8.3. Here the SLED control voltage is set to 0.31 V, corresponding to an output optical power of 2.9 mW. At this low optical power, the noise floor densities for P_1 and P_2 have both converged to the same value indicating that the photocurrent shot noise is negligible at these powers. It should also be noted that the narrowband noise at specific frequencies, specifically 60 Hz and 120 Hz, are diminished relative to the spectra in Fig. 8.2 and are stronger for P_2, which suggests that these noise sources are due to actual fluctuations of the SLED output power. Despite the slight decrease in the noise density floors, the noise density of the scaled differential signal has increased by nearly an order of magnitude. This order of magnitude increase in the scaled differential signal noise density is consistent with the predicted noise increase for an order of magnitude decrease in the optical power assuming a noise source that is signal power independent.

Similar spectra are seen in Fig. 8.4 for which the camera is in its high dynamic range, low sensitivity mode. As before $1/f$ flicker noise dominates below 10 Hz, and the noise floor above that is flat with a few narrowband noise sources. Compared to the saturation optical power, the relative noise floor is lower than the minimum noise floor observed for the low dynamic range, high sensitivity mode. However, converting from gray scale units to NEP reveals that the absolute noise floor density is about an order of magnitude greater. Correspondingly, the noise floor density of the scaled differential signal ~2×10^{-4} $\mathrm{Hz}^{-1/2}$.

As noted previously, the spectra in Figs. 8.2 and 8.3 suggest that, for strong optical signals, the noise is a combination of photocurrent shot noise and power independent noise both which are similar in magnitude. This behavior can also be seen by averaging the noise floor for each mi-

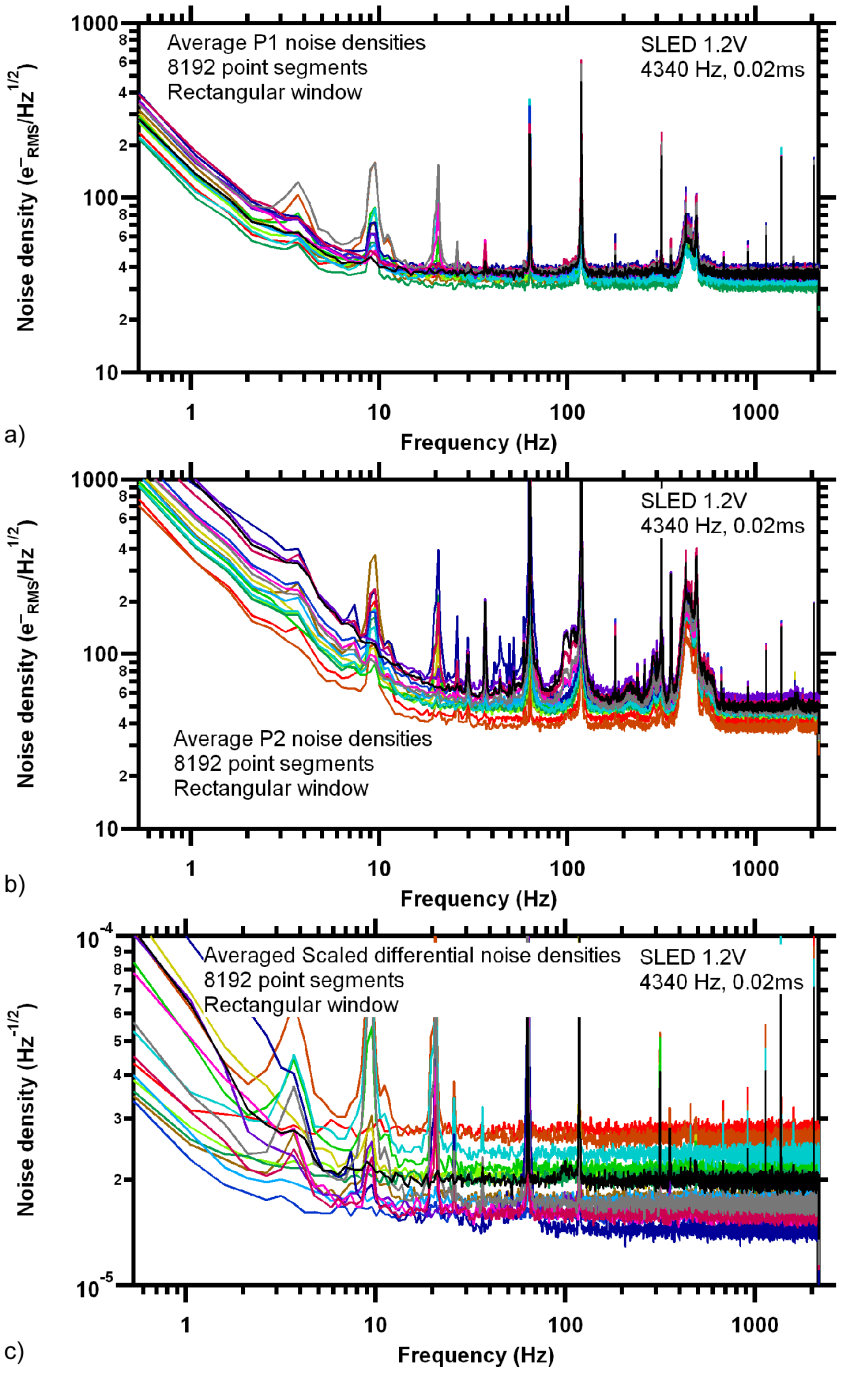

Figure 8.2: Noise density spectra for (a,b) the outputs P_1 and P_2 (in gray scale units), and (c) the scaled differential signal for unreleased microcantilevers. The camera is set to the shortest exposure (24 μs), the fastest sampling rate (4340 Hz), and high sensitivity mode with the SLED control voltage set to 1.2 V.

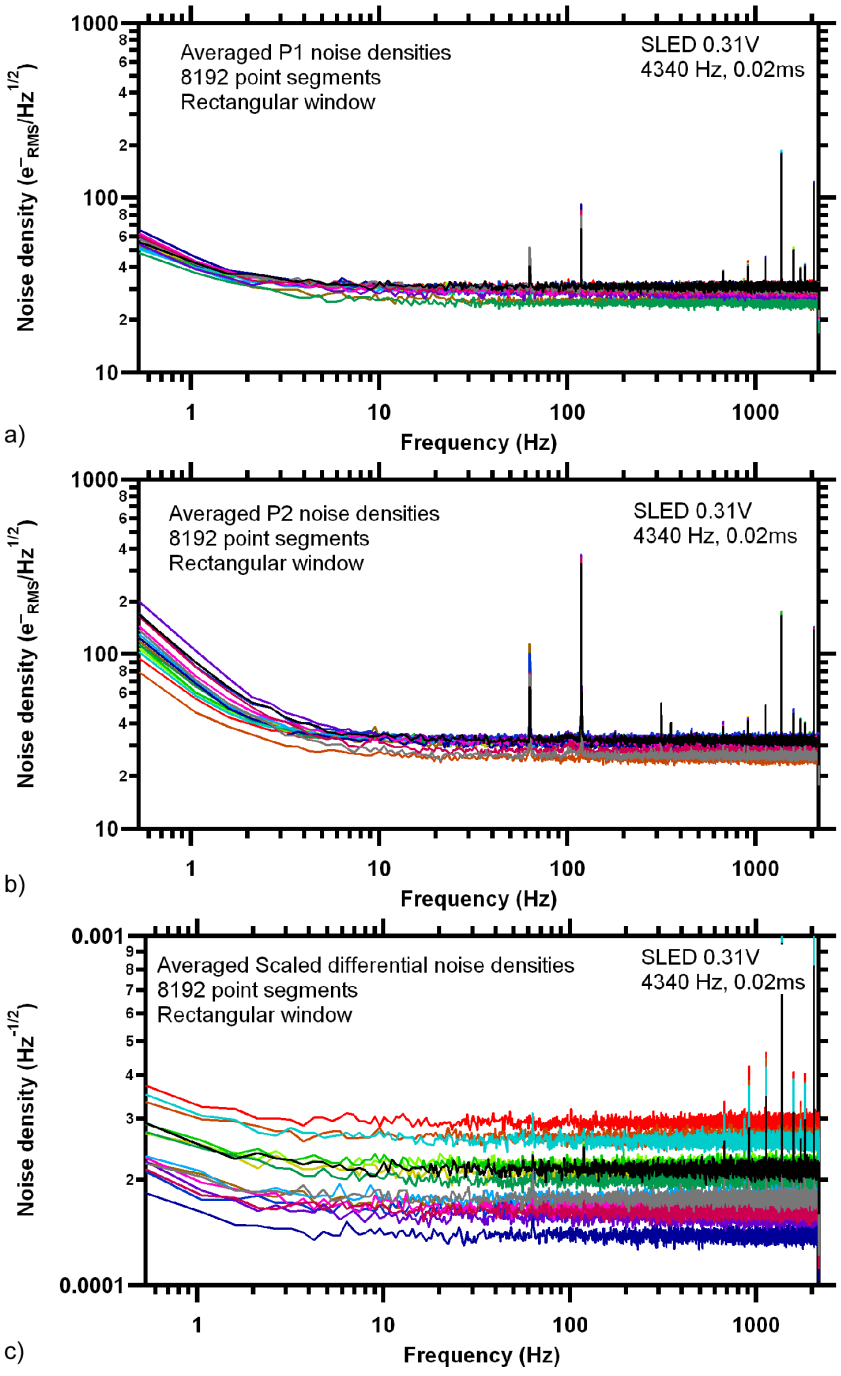

Figure 8.3: Noise density spectra for (a,b) the outputs P_1 and P_2 (in gray scale units), and (c) the scaled differential signal for unreleased microcantilevers. The camera is set to the shortest exposure (24 μs), the fastest sampling rate (4340 Hz), and the high sensitivity mode with the SLED control voltage set to 0.31 V.

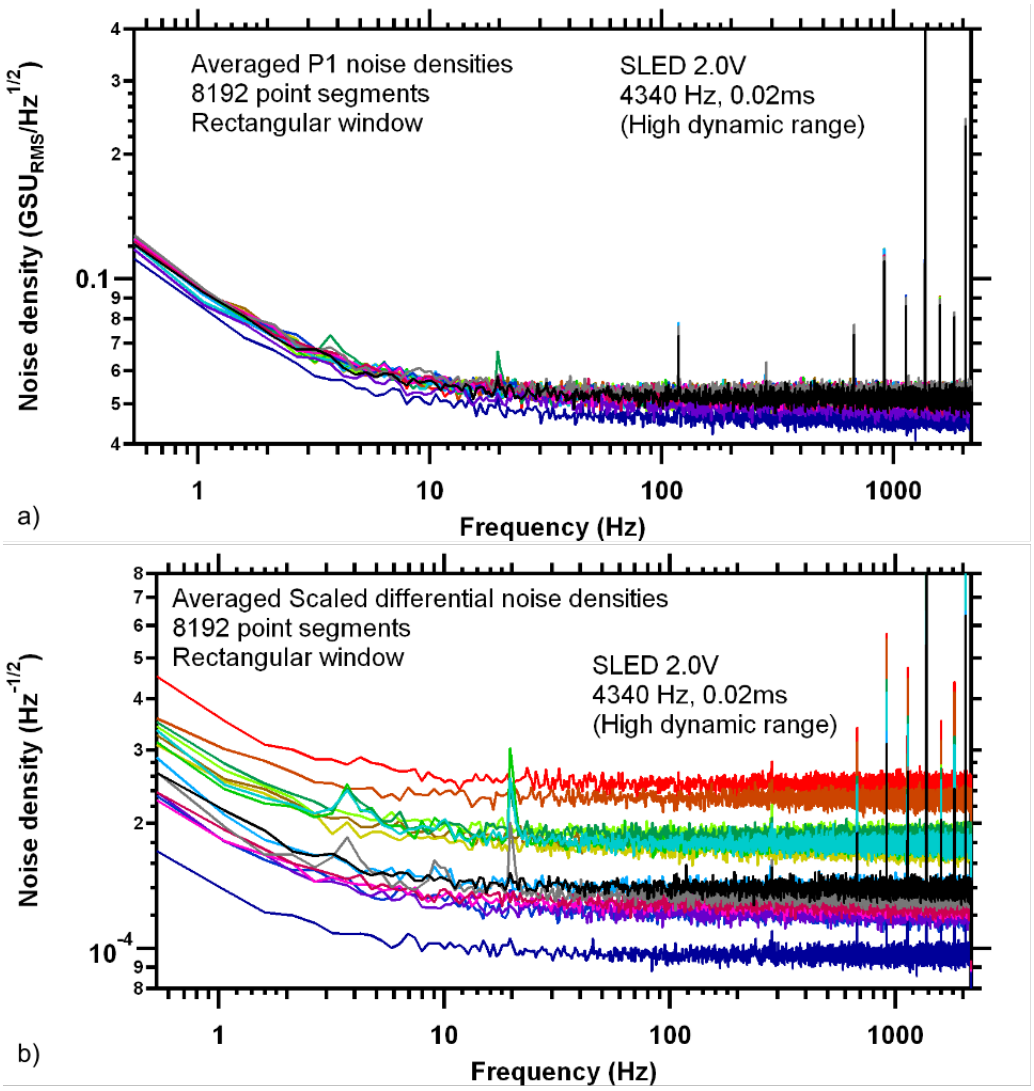

Figure 8.4: Noise density spectra for the (a) outputs and the (b) scaled differential signals with the camera in the low sensitivity, high dynamic range mode.

crocantilever output, not including the $1/f$ flicker noise and narrowband noise contributions, and plotting it as a function of signal strength (Fig. 8.5). Interestingly, as seen in Fig. 8.5, increasing the exposure time decreases the NEP density. From Eqs. 8.5and 8.7, dark current shot noise and Johnson noise are independent of exposure time, hence neither is the dominant noise. On the other hand, the quantization noise and readout noise (Eqs. 8.8 and 8.9, respectively) are dependent on the exposure time. Based on the given characteristics of the camera, the expected NEP densities for quantization noise are 17.3 fW/$\sqrt{\text{Hz}}$ and 2.0 fW/$\sqrt{\text{Hz}}$ for exposure times of 0.02 ms and 0.24 ms, respectively, which are an order of magnitude smaller than the observed noise densities. For read-

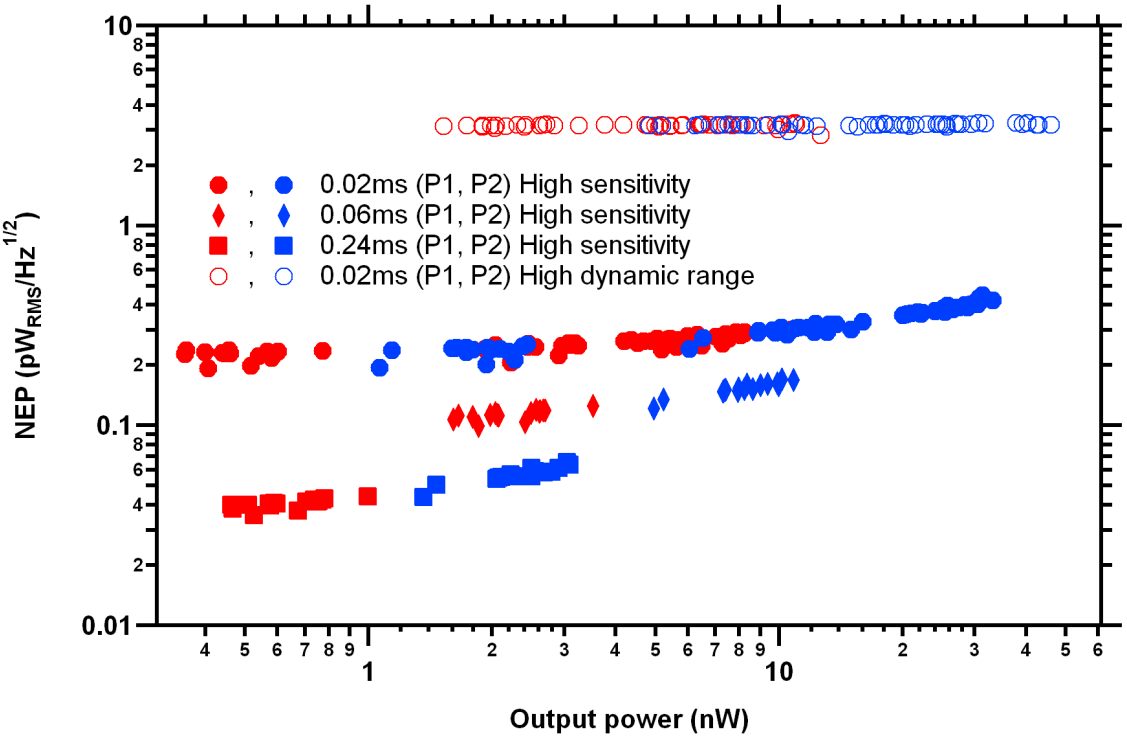

Figure 8.5: Signal noise densities as a function of signal strength for unreleased microcantilevers with camera set for different exposure times and the two sensitivity modes.

out noise, the NEP densities are 131 fW/$\sqrt{\text{Hz}}$ and 18.3 fW/$\sqrt{\text{Hz}}$, which are within a factor of 2 of the observed values. Therefore the readout noise is the most probable dominant noise source for the microcantilever array.

More important than the noise density of the individual camera pixels is the deflection noise density (DND) of a microcantilever. The scaled differential signal noise density and estimated DND, assuming a responsivity of 1 μm^{-1}, are shown in Fig. 8.6 as function of the average of P_1 and P_2. This is represented with the average output signal in GSU (Fig. 8.6(a)) and in units of optical power (Fig. 8.6(b)). Looking at Fig. 8.6(b), it is evident that for a given average output power, the camera operating in the high sensitivity mode and with a longer exposure time results in the lower DND. This ignores the fact, though, that a photodetector can become saturated if the integrated photocurrent exceeds the exceeds Q_{max}. This limit is more clearly seen in Fig. 8.6(a), where the upper limit of the x-axis corresponds to the saturation limit. The figure suggests that the DND for the various camera settings all fall along the same curve inversely proportional to $\bar{P}\Delta t/Q_{\text{max}}$. Extrapolating from the data for signal strengths less than 500 GSU, the high dynamic

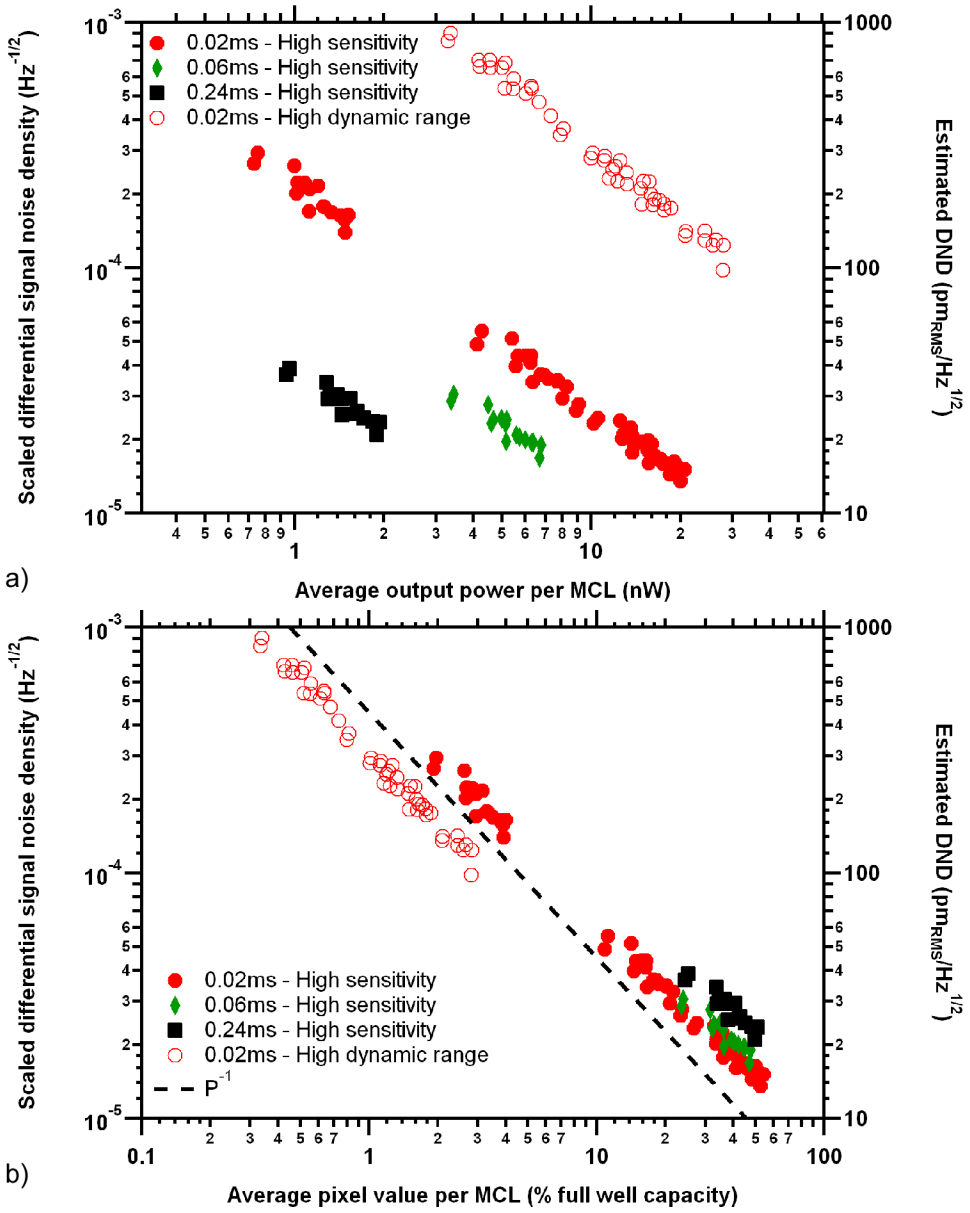

Figure 8.6: Noise densities of the scaled differential signal and of the estimated deflection, assuming a responsivity of 1 μm^{-1}, as a function of signal strength for unreleased microcantilevers with (a) signal in units of GSU, and (b) signal in units of optical power. Data points shown for different exposure times and camera sensitivity modes.

range mode provides a lower DND. However, due to the limitations of the SLED, I am unable to observe the DND with high dynamic range mode at stronger signals.

8.3.4 Released Microcantilevers

A similar experimental procedure is followed for the samples with released microcantilever arrays. With these samples it is possible to calculate real values for the DND as the responsivity for individual microcantilevers has previously been measured. Because of the additional optical losses from the gap between the end of the microcantilever and the differential splitter, the control voltage of the SLED is set to its maximum value of 2.5 V, corresponding to an SLED output power of 48.5 mW. Noise density spectra for the signal and deflection are seen in Fig. 8.7 for the high sensitivity mode and and Fig. 8.8 for the high dynamic range mode of the camera. The noise density floors for microcantilever deflection are 15-30 pm/$\sqrt{\text{Hz}}$ and 150-400 pm/$\sqrt{\text{Hz}}$ for the two camera modes, respectively. The relationship between noise density and average signal power for the released microcantilevers is shown in Figs. 8.9, for the signal noise, and 8.10, for deflection noise. The noise densities seen in these figures are comparable to the estimated deflection noise density floors for the unreleased microcantilevers, consistent with no significant contribution to the deflection noise from actual vibration of the microcantilever. Of particular note, as seen in Fig. 8.10(b) I am able to demonstrate a measured DND of ~40 pm with sub-nW output powers.

8.4 Conclusion

I measured directly the signal noise densities of the outputs of the microcantilever array and the deflection noise densities of the photonic in-plane transduction method. Measured noise densities for both released and unreleased microcantilever are nearly identical, indicating that minimum measurable deflection is not limited by vibrations of free standing microcantilevers. Five different limiting noise sources were considered. The main noise source is frequency independent but exposure time dependent. Of the considered noise sources, the source that best matches this behavior and the observed noise magnitude is readout noise from the readout integrated circuitry in the line scan camera attached to the focal plane array. The readout noise dominates for low optical powers, but the contribution of shot noise from the generated photocurrent is noticeable at optical powers typical of the sensor operation.

The best measured deflection noise density is ~15 pm/$\sqrt{\text{Hz}}$, with an average output power of 18 nW. This is achieved with the camera in its high sensitivity mode and with the shortest ex-

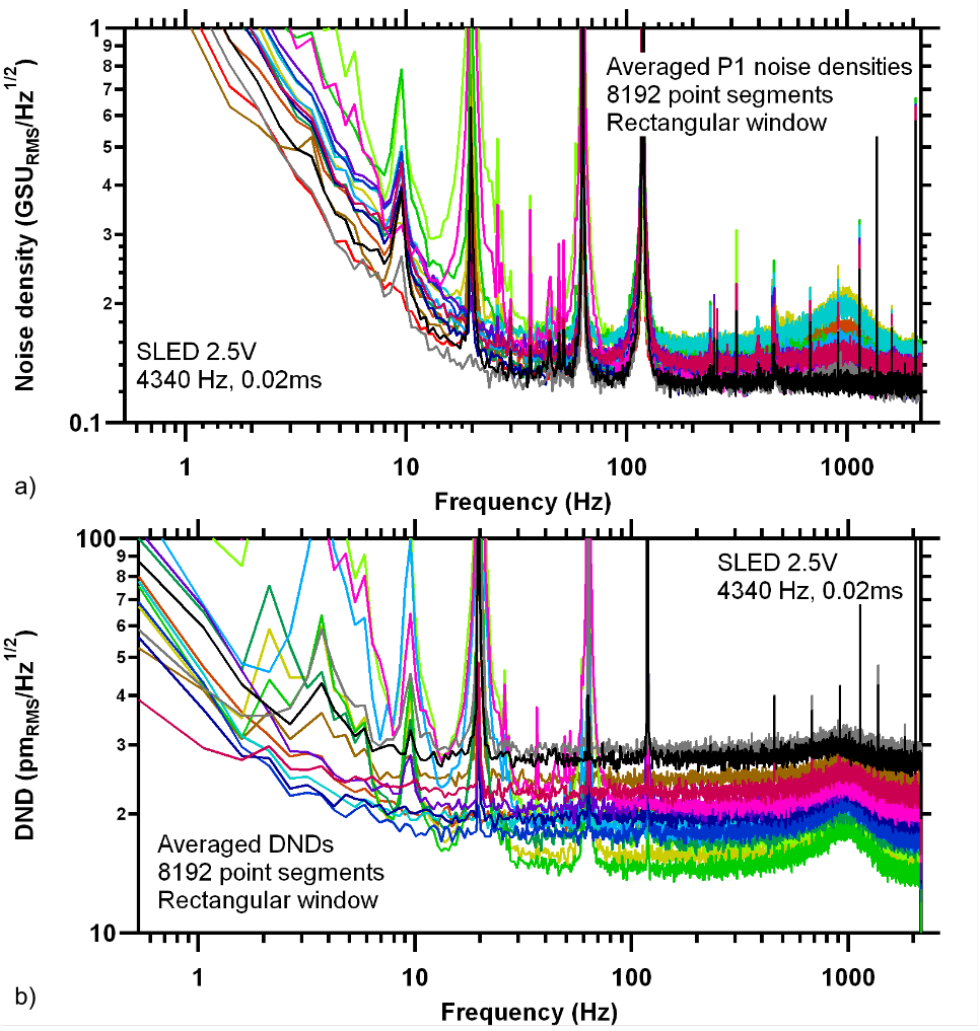

Figure 8.7: Noise density spectra for (a) the P_1 outputs (in gray scale units), and (b) the cantilever deflection for released microcantilevers. The camera is set to the shortest exposure (24 μs), the fastest sampling rate (4340 Hz), and high sensitivity mode with the SLED control voltage set to 2.5 V.

posure time. Longer exposure times give comparable deflection noise densities for weaker signals. Extrapolation from the measurements suggest that longer exposure times or lower gains (higher dynamic ranges) will result in lower deflection noise densities. The former is limited by the saturation charge of the camera's gain capacitors, and the latter is limited by the maximum output power of the SLED optical source. Improvements in the deflection noise density could therefore be achieved with cameras that have lower readout noise and that have larger charge capacity per pixel, and with stronger optical sources.

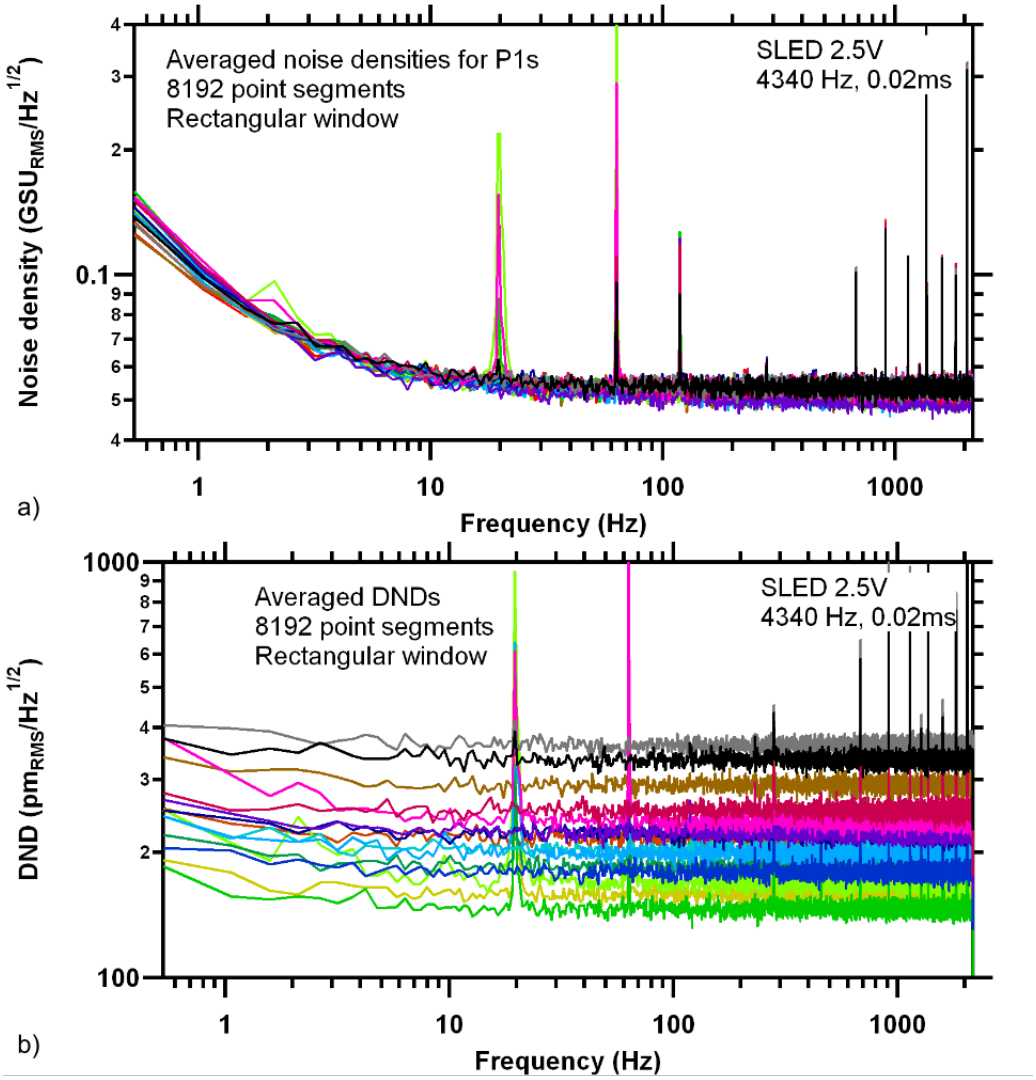

Figure 8.8: Noise density spectra for the (a) outputs and the (b) cantilever deflection with the camera in the low sensitivity, high dynamic range mode.

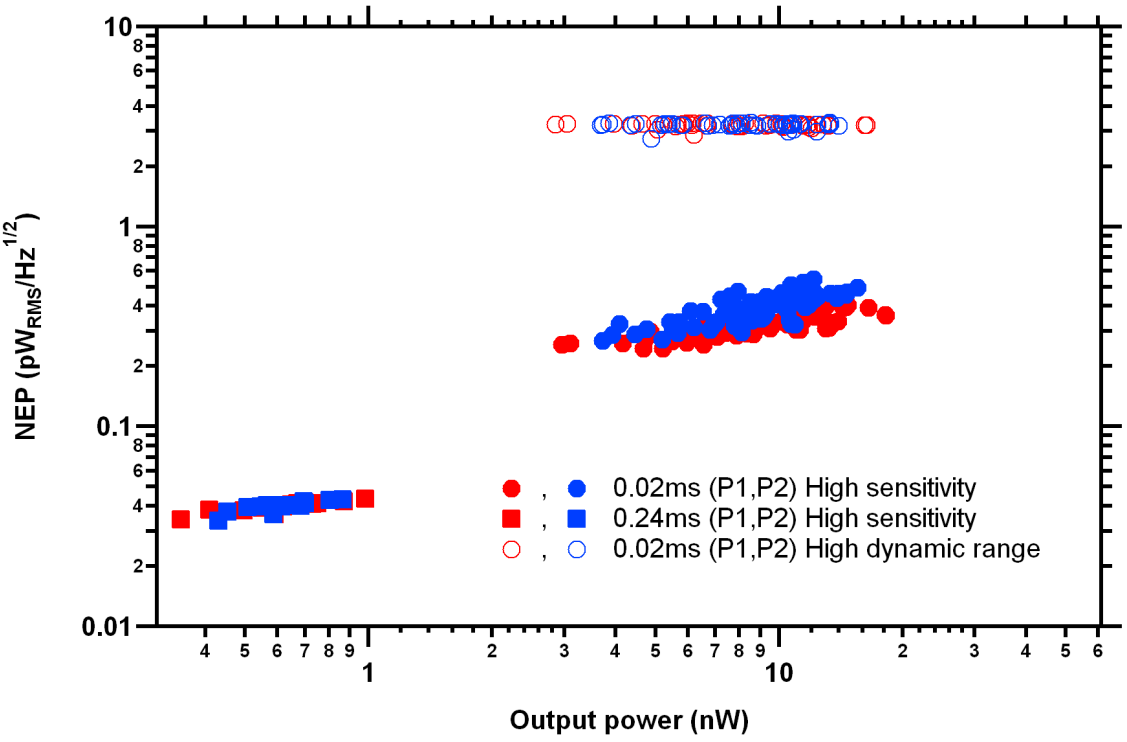

Figure 8.9: Signal noise densities as a function of signal strength for released microcantilevers with camera set for different exposure times and the two sensitivity modes.

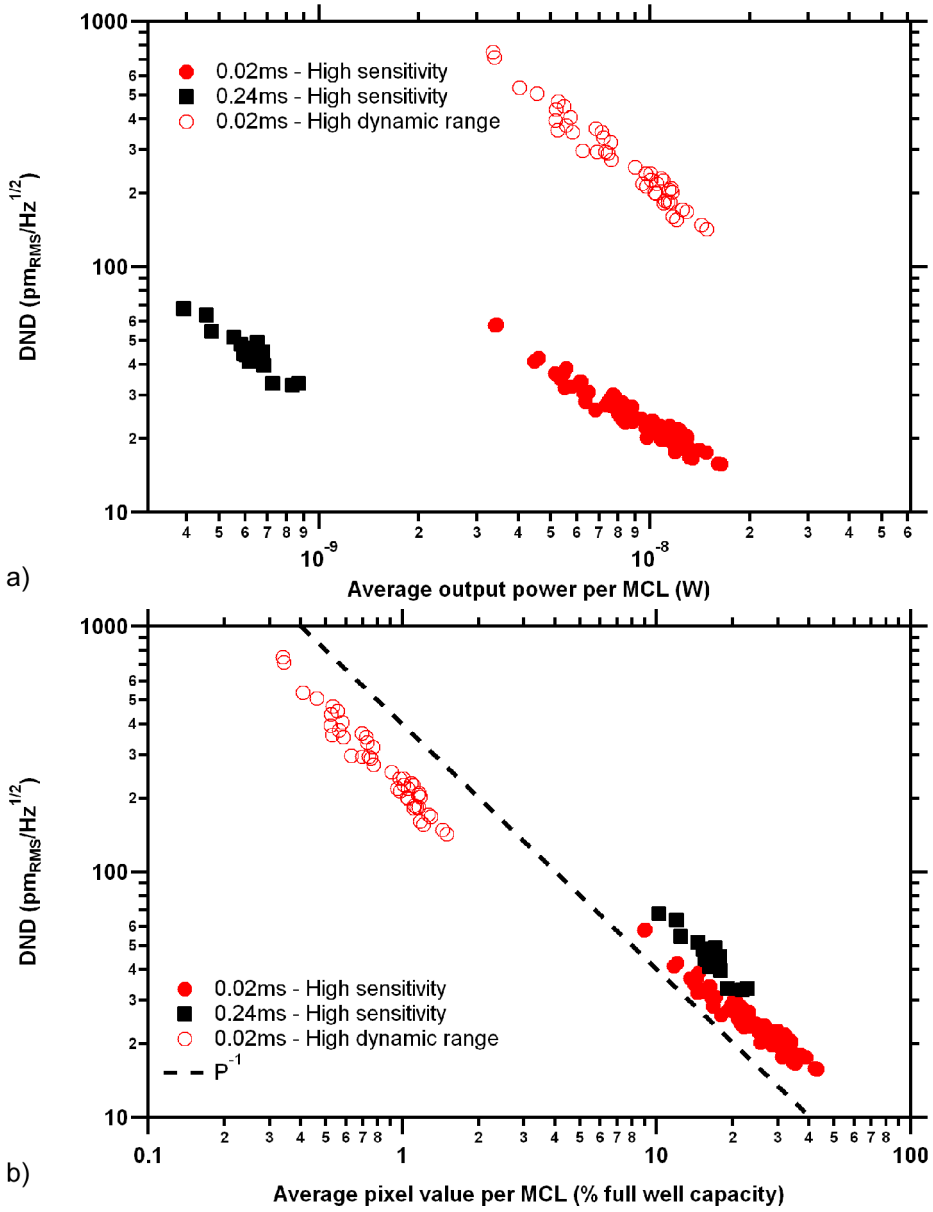

Figure 8.10: Deflection noise densities, using the measured responsivities, as a function of signal strength for released microcantilevers with (a) signal in units of optical power and (b) signal as a percentage of the pixel full well capacity. Data points shown for different exposure times and camera sensitivity modes.

CHAPTER 9. PROPOSED NOISE REDUCTION VIA SELF-LOCKING LOCK-IN AMPLIFIER FOR MCL ARRAY

9.1 Motivation

Microcantilever sensors detect changes in the environment by measuring shifts in the resonant frequency of microcantilevers to detect changes in mass (dynamic mode of operation), or by measuring the static deflection of microcantilevers to detect changes in microcantilever surface stress (static mode) [28]. Measurement of the shift in the resonant frequency are primarily used in gas or vacuum sensing environments, while measurement of static deflection are better suited for liquid sensing environments. Sensors that measure changes in static deflection require the surfaces of the microcantilever to be modified so that the induced surface stress they respond differently to environmental conditions, resulting in a non-zero differential surface stress. The signal-to-noise ratio (SNR) of a microcantilever sensor is often characterized by the minimum detectable deflection (MDD) defined as the amplitude for dynamic mode or the deflection for static mode at which the SNR is unity.

For dynamic mode sensors, the noise is dominated by frequency independent Johnson noise of the detector of the transduction method [104, 105] or by the thermal vibration of the microcantilever [20, 64, 103] over a sufficient bandwidth to observe the resonant frequency of interest. However, for static mode sensors, the noise is usually dominated by $1/f$ noise of either the detector or signal source, such as the light source for optical beam deflection or photonic transduction methods, over a bandwidth determined by the data acquisition sampling rate [23, 64, 103–105]. Because of the different dominant noise, the minimum detectable deflection in static mode sensor is not necessarily the same as the minimum detectable amplitude in dynamic mode even when the sensor and transduction method is the same. It should also be noted that the minimum detectable deflection in static mode is proportional to the detection limit of the sensor, whereas the minimum detectable amplitude in dynamic mode determines which resonant frequency peaks are

observable, but it is the Q-factor of the peaks that is proportional to the actual sensor detection limit. One method to improve the SNR of static and and low-frequency microcantilever deflection measurements is using a lock-in amplifier (LIA) to shift the quasi-static signal away from DC and the dominant $1/f$ noise [70, 106].

9.2 Theory

9.2.1 Lock-in Amplifier

Prior to discussing the proposed self-locking, multiple channel, digital lock-in amplifier, I will review the basic operation of a lock-in amplifier (LIA). The purpose of the LIA is to recover both the amplitude and phase of signal buried in broadband noise. To accomplish this, the source of the signal to be extracted, $n(t)$, is modulated at some carrier frequency, ω_c, with amplitude A such that the new signal $S(t)$ is given by:

$$S(t) = n(t)A\cos(\omega_c t) + \sigma(t) \tag{9.1}$$

where $\sigma(t)$ is the noise from which the signal is to be extracted. In the majority of instances, the noise is independent of the frequency of the original signal and so is not mixed with the source modulation. The modulated signal is then mixed with a reference oscillator signal of frequency ω_r, typically producing both in-phase, $I(t)$, and quadrature, $Q(t)$, signals:

$$\begin{aligned} I(t) &= S(t)\cos(\omega_r t + \theta_r) \\ &= \frac{1}{2}n(t)A\left[\cos((\omega_c - \omega_r)t - \theta_r) + \cos((\omega_c + \omega_r)t + \theta_r)\right] + \sigma(t)\cos(\omega_r t + \theta_r), \end{aligned} \tag{9.2}$$

$$\begin{aligned} Q(t) &= S(t)\sin(\omega_r t + \theta_r) \\ &= \frac{1}{2}n(t)A\left[\sin((\omega_c + \omega_r)t + \theta_r) - \sin((\omega_c - \omega_r)t - \theta_r)\right] + \sigma(t)\sin(\omega_r t + \theta_r) \end{aligned} \tag{9.3}$$

where θ_r is the phase difference between the carrier and reference signals. Typically, the reference signal is obtained by feeding a small signal directly from the source into a phase-locked loop

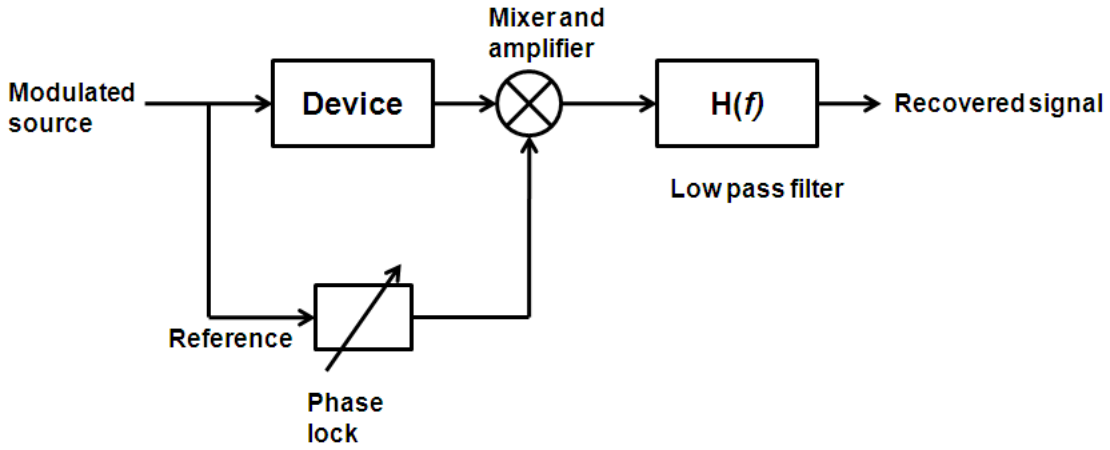

Figure 9.1: Block diagram of lock-in amplifier algorithm

and voltage-controlled oscillator (VCO) to ensure that $\omega_r = \omega_c$. Doing so simplifies the form of Eqs. 9.2 and 9.3.

The mixed signals $I(t)$ and $Q(t)$ are then passed through a low-pass filter to obtain the filtered signals $X(t)$ and $Y(t)$. The bandwidth of the low-pass filter is narrow enough to remove the sidebands of the mixed signals at $2\omega_c$ but broad enough to accommodate the bandwidth of the signal $n(t)$. The resulting filtered signals are then:

$$X(t) = h_L \otimes I(t) \approx \frac{A}{2} n(t) \cos\theta_r, \tag{9.4}$$

$$Y(t) = h_L \otimes Q(t) \approx \frac{A}{2} n(t) \sin\theta_r \tag{9.5}$$

with h_L as the transfer function of the low-pass filter in the time-domain. In most commercial analog LIA, the delay of the phase-locked loop can be adjusted until $\theta_r = 0$ so that only the single signal $X(t)$ is needed to recover $n(t)$. Alternatively, dual-channel LIA recover by summing the two signal in quadrature. A block-diagram of the LIA algorithm is shown in Fig. 9.1.

The lock-in algorithm can also be described in frequency space, as seen in Fig. 9.2. In this representation the modulated source re-centers the original signal about the carrier frequency but leaves the frequency distribution of the the broadband noise unaffected. Mixing with the reference signal shifts the modulated signal back to its original frequency while at the same time shifting the

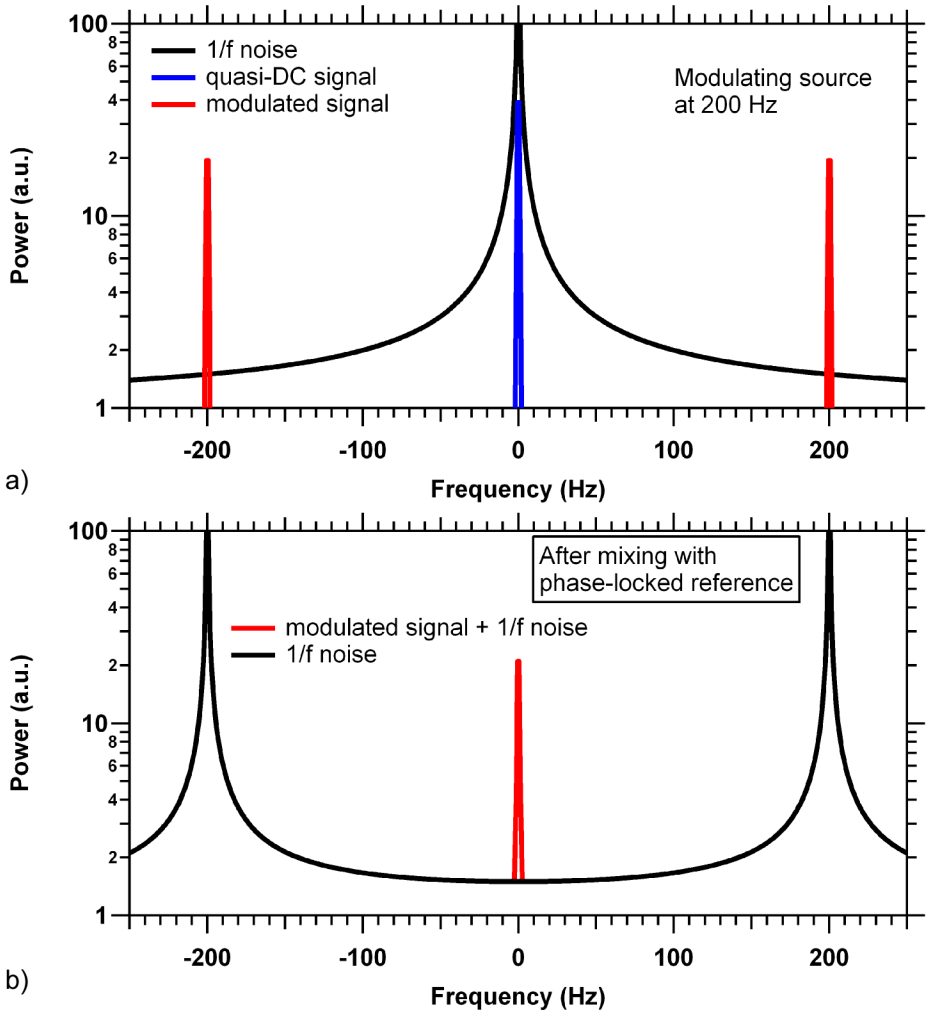

Figure 9.2: Frequency space representation of the theoretical operation of a lock-in amplifier for a narrow band signal about DC and broadband $1/f$ flicker noise. The sidebands at $\omega_c + \omega_r$ (in this case at 400 Hz) following mixing with the reference signal are not shown.

noise spectrum up to the reference frequency. A narrowband low pass filter can then remove both the sidebands due to mixing and the shifted noise spectrum. In frequency space, it is evident that the LIA is only helpful when the noise distribution is not uniform in frequency so that the signal can be shifted to a frequency space where the noise is weaker.

Most commercial LIA use analog circuitry to accomplish the phase-lock of the internal oscillator to the reference signal and mixing of the oscillator with modulated signal. This places limitations on the number of signal channels that can be recovered as each channel requires their own set of analog electronics. Alternatively, the lock-in algorithm can be implemented digitally,

therefore limited only by capability of a digital signal processor. Implementation of a digital LIA (DLIA) requires a digital phase-locked loop (DPLL) and a digitally-controlled oscillator (DCO) to synchronize to the external reference signal and to form the in-phase and quadrature signals. [107] Also, when the measurements of the signals become discrete, additional conditions should be satisfied for the digital LIA to operate properly and to reduce distortion of the recovered signal. One of these conditions is that the sampling frequency ω_s and the modulation frequency ω_c are commensurate. In other words, the ratio ω_c/ω_s has to be equal to a ratio of integers K/N. When this condition is met, there is an integer number of modulation periods K for a data acquisition of N points [108, 109]. Another important condition is $\omega_s > 2\omega_c$ so that the modulated signal is adequately resolved by the sampling.

9.2.2 Digital Phase-lock Loop

The advent of software radio and other modern digital devices have led to the development and implementation of digital phase-locked loops (DPLL) [110]. For a DLIA, the DPLL performs similar to an analog phase-locked loop to provide a control signal feedback to keep the demodulation signal locked with the reference signal and with the input signal in the presence of noise. The reference signal and the demodulation signal generated by the internal oscillator are sinusoidal both with a frequency of ω_r , but with different phases at point n: θ_n for the reference, and ϕ_n for the internal oscillator. The measured phase error, inherently with some noise from the reference signal, is fed into the loop filter of a DPLL. The DPLL returns a control signal, c_n, to the oscillator such that

$$\phi_{n+1} = \phi_n + c_n. \tag{9.6}$$

The closed loop transfer function $H(z)$ for the DPLL is therefore

$$H(z) = \frac{\phi(z)}{\theta(z)} = \frac{F(z)}{(z-1)+F(z)} \tag{9.7}$$

where $F(z)$ is the transfer function for the DPLL's loop filter [107]. A common DPLL in various applications is a type-II DPLL. This type of DPLL is characterized by two loop parameters, K_p and K_i as seen in the phase-domain model for this type of DPLL shown in Fig. 9.3.

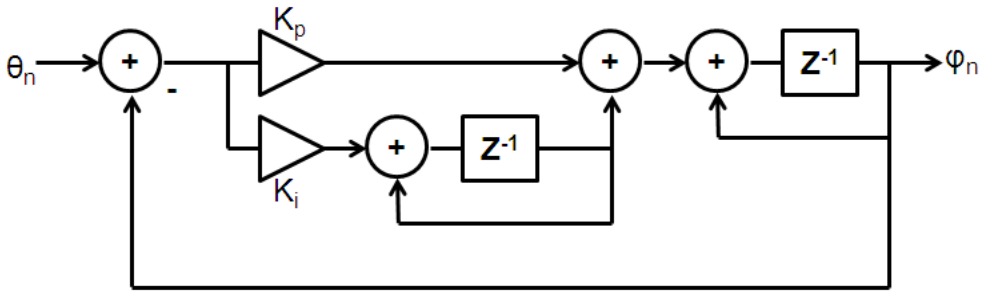

Figure 9.3: Block diagram of discrete phase-lock loop

In addition it is possible to use the DPLL to self-lock a DLIA to an input signal using the input signal itself as a reference signal. Usually operating the DLIA without a reference signal requires precise *a priori* knowledge about the carrier frequency. However, even when the carrier frequency is only known with limited precision, a properly implemented DPLL will compensate for the uncertainty. A frequency mismatch between the carrier frequency and demodulation frequency can be treated as phase difference that increases linearly with time. A DPLL properly compensate in this situation when the error tends asymptotically to zero. For an input phase error that increases linearly with time, this is satisfied as long the transfer function $H(z)$ has at least one pole in $z = 1$ [111]. A pole at $z = 1$ is guaranteed for the type-II DPLL by proper choice of the loop parameters K_p and K_i.

9.3 Simulation

9.3.1 Noise Reduction

The DLIA with the described DPLL is simulated in a LabVIEW environment so that parameters can be easily and quickly adjusted. The simulations are designed to match the capabilities of the data acquisition equipment currently used for the microcantilever array sensors. In most cases, the sampling rate is 4340 Hz (the maximum sampling rate of the line scan camera), the carrier frequency is 2117.07 Hz, and the signal to be recovered has a frequency of 1.5 Hz. The source modulation also has DC offset to correspond to modulation of the SLED optical source about a constant output power. I define the normalized root-mean-squared error (NRMSE) as the root-mean-square error of the recovered signal from the original signal divided by the amplitude

of the original signal, roughly equivalent to $\mathrm{SNR}^{-1/2}$, which will serve as a metric for evaluating the performance of the DLIA. For this initial basic evaluation of the DLIA algorithm I keep the parameters of the DPLL constant and leave the optimization of such for a future study.

A comparison between the performance the DLIA and simple low-pass filter in recovering a signal buried in noise is shown in Fig. 9.4. It is almost impossible to discern the original signal (black curve) in the noisy signal (green curve) because of the presence of a strong $1/f$ noise source. The result of passing the signal through a low-pass filter (red curve) smooths out the signal, but does little to recover the original 1.5 Hz signal. The result from the DLIA (blue curve), seen more clearly in the lower graph of Fig. 9.4, demonstrates successful recovery of the original signal. For both signal recovery attempts the low-pass filter is a centered, moving average filter of 1025 data points with a uniform window. The behavior of the recovered DLIA signal at the beginning and end of the duration are artifacts of padding the ends of the signal to accommodate the moving average filter.

To more particularly characterize the performance, the average NRMSE is measured as a function of the $1/f$ noise density at the signal frequency (Fig. 9.5). For comparison, the NRMSE of the noisy signal prior to recovery and of recovery using just a moving average low-pass filter are shown. The low-pass filter handles little noise before it reaches the limits of its capabilities, with a maximum decrease of a factor of ~2.3 in the NRMSE, corresponding to a factor of 5.4 increase in the SNR. The DLIA reaches the maximum recovery limit at a much higher characteristic noise density, decreasing the NRMSE by a factor of ~78 at this limit. This corresponds roughly to a 6000-fold increase in the SNR! Interestingly, the low-pass filter and the DLIA have an intrinsic noise level such that at very low characteristic noise densities, below 1% of the signal amplitude, it is better to not do any signal recovery attempts.

There are many parameters of the DLIA that can be used to optimize its performance. Two important parameters are the carrier frequency and the amplitude of the source modulation, the effects of which are illustrated in Fig. 9.6. The carrier frequency determines how far from DC and the predominant $1/f$ noise the signal is shifted. Fig. 9.6 shows the NRMSE as a function of the ratio of the carrier frequency to the sampling frequency. As seen in the figure, a K/N ratio greater than 0.3 is sufficient to reach the limits of the capabilities of the DLIA. The abrupt increase of the noise at $K/N = 0.5$ is due to a singularity at this frequency of the low-pass filter. For frequencies

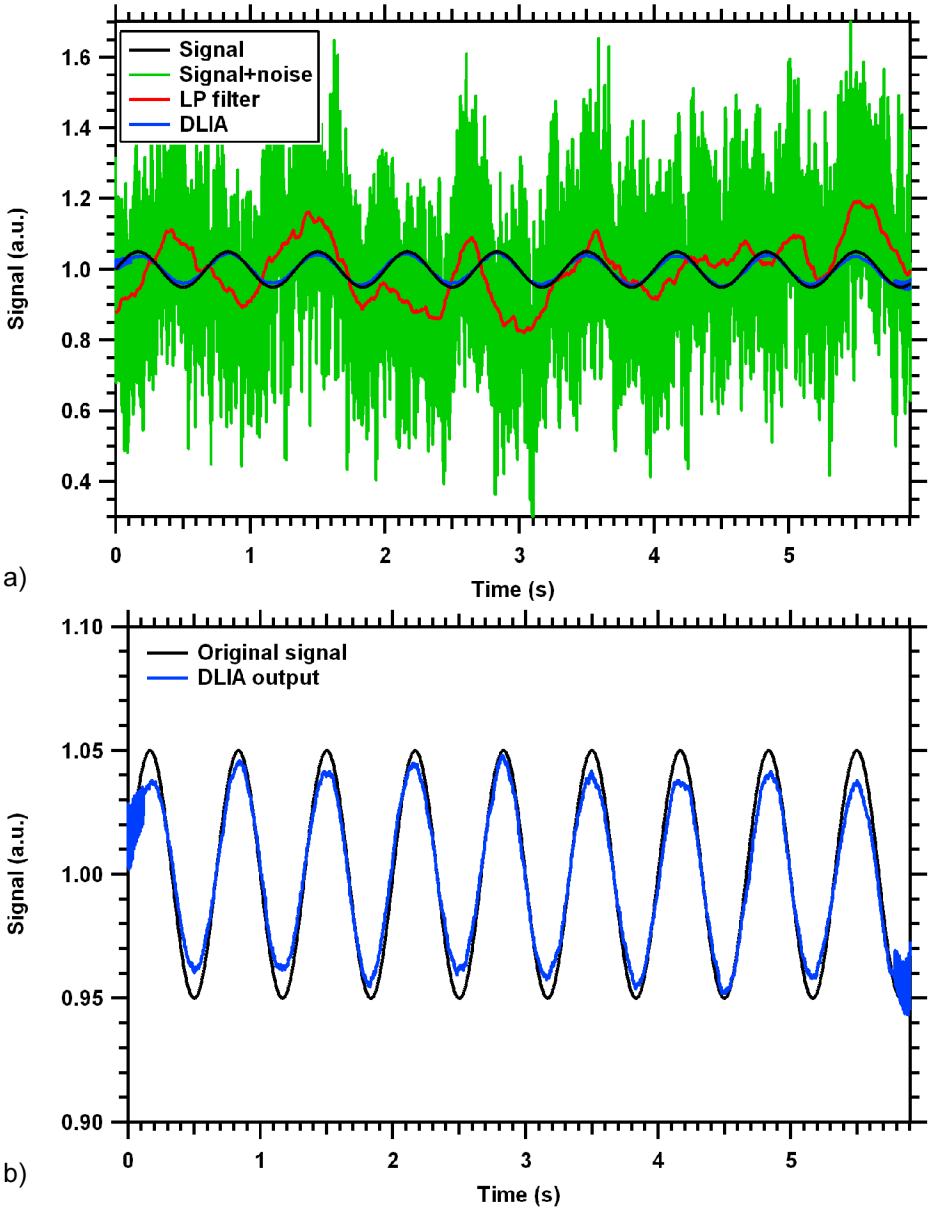

Figure 9.4: Demonstration of noise reduction for a sinusoidal signal with the DLIA shown in the top graph compared to the noisy signal and a simple low-pass filter recovery attempt. For clarity, the same original signal and recovered signal are shown in the bottom graph.

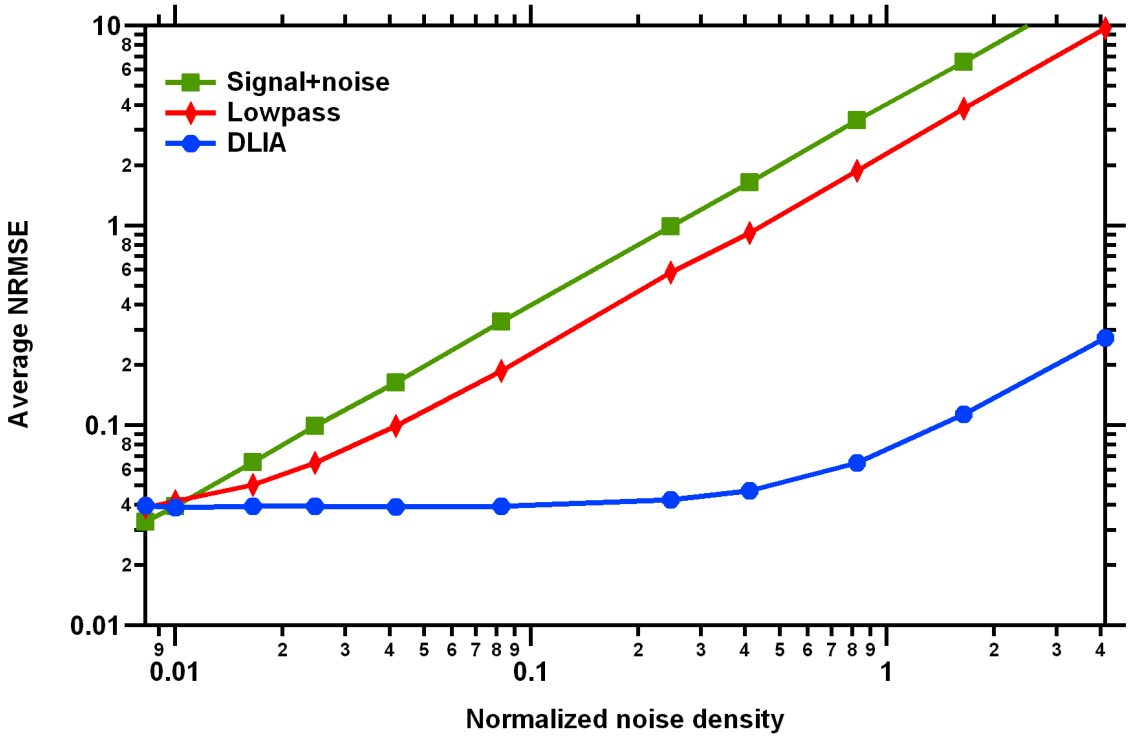

Figure 9.5: NRMSE of the signal for the different recovery methods as a function of the noise density, normalized to the signal amplitude, at the signal frequency.

about the Nyquist limit, defined by $K/N < 0.5$, the DLIA is able to still recover the signal only because the of aliasing of the high carrier and demodulation frequencies to lower frequencies.

As mentioned previously, the intention of implementing the DLIA with a real optical source implies a modulated signal with a DC offset. Therefore the amplitude of the modulation cannot be larger than the DC offset. The source modulation will be accomplished by modulating the control voltage of the SLED. In order to avoid the non-linear response of the SLED at the extremes of the control voltage range, it is advisable to use the maximum allowable modulation amplitude. Therefore I am interested in the behavior of the DLIA for modulation amplitude less than the full scale of the DC offset. Similar to Fig. 9.5, Fig. 9.6(b) shows the average NRMSE of the recovered signal as function of the noise magnitude for varying modulation amplitudes. As expected, decreasing the amplitude also decreases the performance of the DLIA. However, it is promising that an amplitude which is 25% of the DC offset gives an order of magnitude improvement over the low-pass filter recovery process.

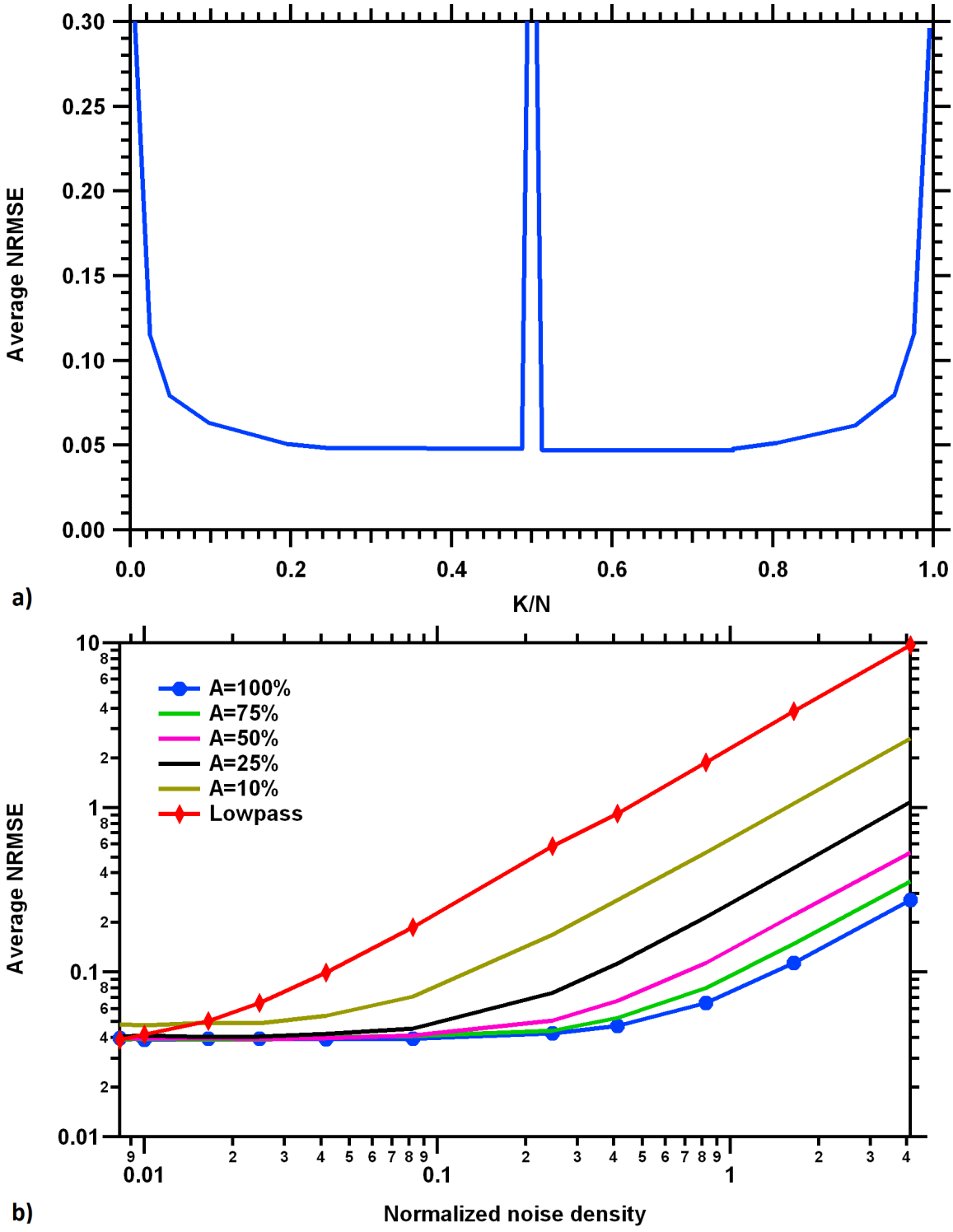

Figure 9.6: Effects of varying the modulation frequency (a) and amplitude (b) on quality of signal recovery.

9.3.2 Phase Mismatch

To obtain Eqs. 9.4 and 9.5 describing the LIA operation, the assumption is made that the carrier and the demodulation frequency are the same. The assumption can be ensured by driving oscillator, which generates the demodulation signal, with an external reference signal from the modulated source. In the case of the line scan camera, a reference signal is difficult to acquire and so the DLIA is designed to operate with an internally driven oscillator. Any error in the actual carrier frequency or the sampling frequency leads to a non-zero value for the $\omega_c - \omega_r$ such that the demodulation step does not shift the signal back to its original frequency. I characterize the phase mismatch by the value

$$\Delta K = K_c - K_r = \frac{N}{\omega_s}(\omega_c - \omega_r) \tag{9.8}$$

where N is the number of points used in the low pass filter.

The effects on the signals recovered from a DLIA without a DPLL and with non-zero amounts of phase mismatch are shown in Fig. 9.7. Increasing the phase mismatch increases the noise of the recovered signal and decreases its DC offset. The effects are attributed to the fact that the frequency of the demodulated signal is no longer within the bandwidth of the low-pass filter. The performance of DLIA with a DPLL are also shown in Fig. 9.7. With a DPLL the DLIA is able to maintain the DC offset of the original signal with only a small increase in the noise of the recovered signal as the phase mismatch increases. The advantages of the DLIA+DPLL combination are also visible in Fig. 9.8 which plots the NRMSE as a function of phase mismatch. When there is no phase mismatch, the simple DLIA and the DLIA+DPLL perform equally well. However, the NRMSE increases quickly, reaching unity NRMSE at a phase mismatch of $\Delta K = \pm 0.25$. In comparison, the DLIA+PLL reaches a NRMSE of 0.32 ($\approx$SNR of 10) for $\Delta K = \pm 0.95$.

9.4 Conclusion

I have been able to successful design and simulate a digital lock-in amplifier (DLIA) with a digital phase-lock loop (DPLL) specifically for improving the SNR of the microcantilever array sensors using the in-plane photonic transduction method. As the implementation of the lock-in amplifier is digital, it is easily scalable to simultaneously handle a number of signal channels. When the dominant noise is flicker $(1/f)$ noise, the DLIA can provide at most a 6000-fold increase in

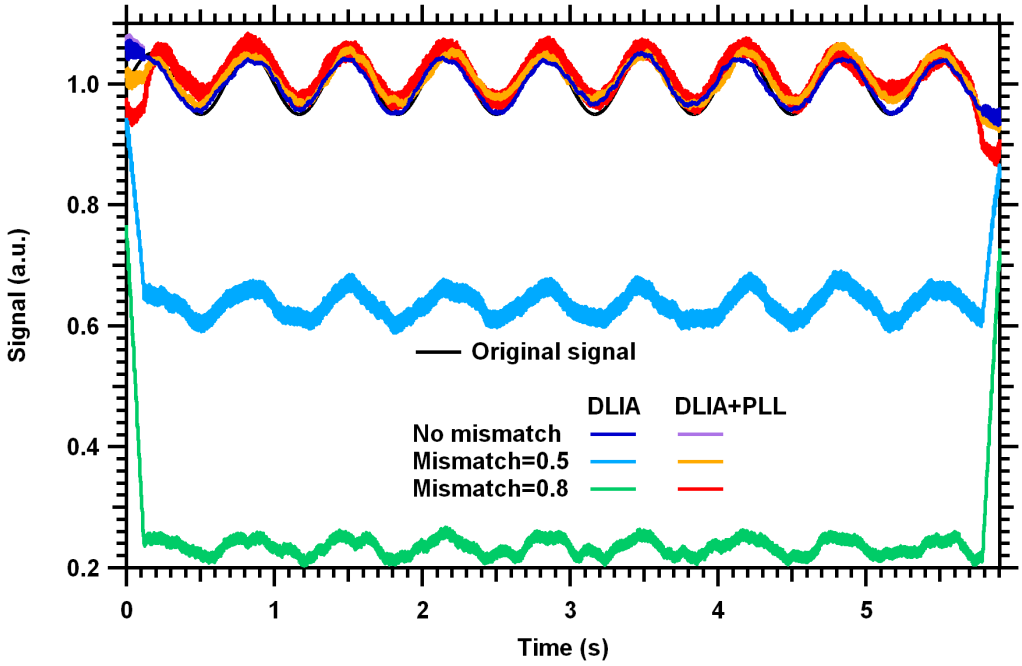

Figure 9.7: Simulation of lock-in amplifier with and without phase-lock loop when there is a frequency mismatch.

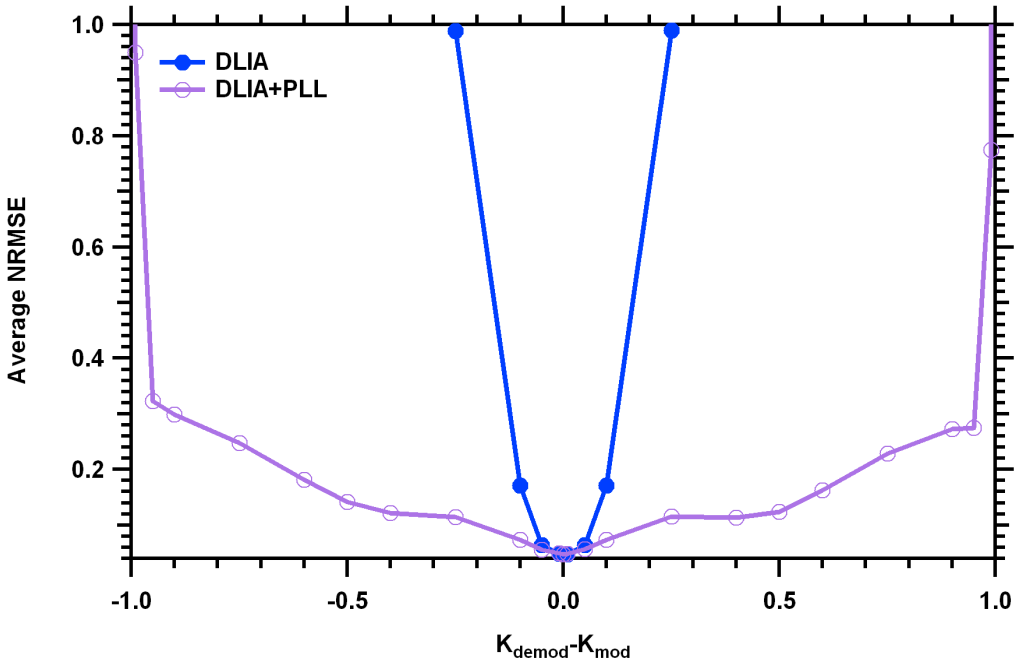

Figure 9.8: NRMSE for lock-in amplifier with and without phase-lock loop as function of frequency mismatch.

the SNR. Certainly including other noise sources besides flicker noise in the analysis will diminish the performance of the DLIA. I have also shown how the frequency and the amplitude of the modulation affect the performance of the DLIA.

Given certain limitations of physically implementing it, the DPLL is included within the DLIA. This allows the DLIA to be self-locking to the carrier frequency without the need of an external reference signal. The DPLL also permits DLIA to compensate for a phase mismatch between the carrier frequency and the initial reference frequency. It does this by passing the phase error through a loop filter and phase integrator to obtain the appropriate phase correction for the demodulation oscillator. The DLIA+DPLL combination shows significant improvement over the DLIA in signal recovery performance in the case of phase mismatch.

The obvious future work with this DLIA is actual implementation with a microcantilever array. There are few parameters that were not varied in this investigation of the DLIA performance, specifically the proportional and integrating constants of the DPLL. Optimization of these parameters may further improve the signal recovery when there is carrier-reference frequency phase mismatch. I also did not consider the effects of a finite integration time comparable to the period of modulation. Future simulations should also include the addition of broadband noise sources like readout noise and shot noise. I believe that elements of the DLIA could also be used as the basis for stroboscopic-type measurements to access microcantilever behavior at frequencies above the sampling rate of the camera.

CHAPTER 10. CONCLUSIONS

10.1 Summary

Microcantilever have attracted significant interest as sensor platform because of their versatility and high sensitivities. Lab-on-a-chip applications using microcantilever-based sensors is limited largely by the need to identify a transduction that is compatible with a wide variety of sensing environments and can be scaled up in number for compact, large arrays of sensors. Each transduction method has its own strengths and weakness. The in-plane photonic transduction method has been developed and demonstrated as a possible alternative solution to these problems. I am currently characterizing the behavior of microcantilever arrays with this transduction method and integrating arrays with polydimethylsiloxane (PDMS) based microfluidics. The performance of the integrated microcantilever arrays in simple sensing scenarios is also investigated.

A large number of microcantilever-based sensors utilize a thin gold film coating to enable the attachment of analyte selective coatings to the microcantilever surface. Doing so creates microcantilever with a bimorph structure that is sensitive to thermal fluctuations. After fabricating several chips with microcantilever arrays, I coat some with different patterns of gold films. Using a scanning electron microscope, I observe the deflection as a function of temperature and measure the temperature sensitivities of 300 μm long microcantilevers to be -170.82 nm/K for a full gold coating, -94.51 nm/K for a partial gold coating, and -0.274 nm/K and -1.93 nm/K for no gold coating. I also use the photonic transduction method to measure the thermal response of a microcantilever array and obtain an average temperature sensitivity of -1.46 nm/K. The measured sensitivities match well with theoretical calculations, but only when the proper parameters and equations are used which I find to not always be the case in the microcantilever literature.

I fabricate PDMS microfluidics and integrate them with a microcantilever array chip. The microfluidics contain active, pneumatically actuated valves that allow me to control the timing and microfluidic pathway of the flow. The microcantilever are exposed to a solution of bovine serum

albumin (BSA) followed by solutions of various pH's. Since the microcantilevers are not prepared with a selective coating, the BSA nonspecifically binds to both the top and bottom surfaces. I do measure a quick but temporary change in deflection of -1.6 nm corresponding to a transient differential surface stress with a maximum value of -0.23 mN/m. Simulations and calculations reveal that the transient response is due to placement of the microcantilevers 3 μm from the lower wall of the microfluidic channels. The closeness to the channel wall causes the concentration increase more rapidly above the microcantilever than below. The higher concentration above results temporarily in more BSA being bound to the top than the bottom until the BSA concentrations above and below become equal. Calculations based on the reaction kinetics of BSA predict a transient surface stress with a maximum value of -0.225 mN/m. Transient deflection responses are also seen when changing the solution pH, the largest giving a maximum average transient deflection of -65.4 nm, and attributed to a similar mechanism with the H^+ion concentration temporarily being unequal above and below the microcantilevers. I hypothesize that the deflection response to pH is due to stress generated by pH-driven conformational changes of the nonspecifically bound BSA.

Using other microcantilever arrays integrated with microfluidics, I look at the response of the microcantilever array to different types of flow. The microcantilever arrays have also undergone a new, additional process to etch out a 100 μm microfluidic trench beneath the microcantilevers. In the first test case, I observe the deflection in response to steady pressure-driven flows generated by an off-chip syringe pump. Simulations of the deflection response match well with experimental results but begin to deviate for higher flow rates. For flow rates greater than 200 μL/min, the deflection responses of many of the cantilevers become erratic and no longer follow the trend observed at lower flow rates. I attribute this to microcantilevers deflecting outside the $\pm$500 nm dynamic range over which the differential signal is known to be monotonic and linear. I am able to successfully observe the ~1 nm deflection from a 5 μL/min flow rate. In a second test case, the microfluidics of the integrated device contain an on-chip reciprocating reservoir pump. When the reservoir pumps are actuated, quick bursts of high flow rate are driven across the microcantilever array and large transient deflection responses are observed. However, the microcantilevers return to a steady state near zero-deflection 250 ms after a reservoir is first actuated. This suggests that it is possible to use the reciprocating pump to achieve high flow rates and efficiently use a small

sample volume by constantly recycle the analyte solution while making deflection measurement inbetween reservoir actuations as long as the half-period of the pump cycle is greater than 250 ms.

Microcantilever arrays with responsivities of ~1 μm^{-1} are regularly fabricated, comparable to the best-reported responsivity of AFM microcantilevers, are reliably fabricated. In Chap. 8 I describe my initial measurements of the noise spectra of the outputs and the deflection noise spectrum for my microcantilever arrays. Noise spectra are acquired for different input powers from the SLED, different exposure times, and the different gain capacitors of the camera. I identify five possible noise sources as the limiting factor for deflection measurements: shot noise, Johnson noise, flicker noise, readout noise, and quantization noise. The noise spectra show that flicker noise typically dominates below ~10 Hz. Above 10 Hz the noise is relatively flat with a few strong, narrowband noise sources. The noise behavior as the exposure time is increased reveals that the dominant noise source is the readout noise at low signal powers, but I do see the onset of the transition to a shot noise limited measurement as the signal gets stronger. Although longer exposure times result in the lower deflection noise densities for a given output power, when the output signals are expressed in terms of fraction of the saturation charge of each pixel, the different exposure times and gain modes perform roughly the same. The minimum deflection noise density floor measured is 15 pW/$\sqrt{\text{Hz}}$ with an average output signal power of 18 nW.

Finally, I suggest a digital lock-in amplifier as a possible tool to increase the signal-to-noise ratio of my data acquisition equipment. The digital lock-in amplifier is simulated and its ability to recover signal buried in flicker noise evaluated. In simulation the digital lock-in amplifier is able to recover signals and achieve a 6000-fold increase in the SNR. I show that this performance is dependent upon both the carrier frequency and the amplitude of the carrier modulation. The lock-in algorithm is also implemented with a digital phase-lock loop. A real possibility for the test equipment is the lack of a good reference signal and uncertainty in the carrier frequency. The digital lock-in amplifier without a digital phase-locked loop shows a narrow tolerance for a frequency mismatch between the carrier and the internal oscillators frequencies. However, with a digital phase-locked loop, the lock-in amplifier is able to compensate for the frequency difference and is able to self-lock to the carrier signal in the presence noise and with the carrier and oscillator frequencies not being equal.

10.2 Future Work

While the responsivity of the in-plane photonic transduction method is comparable to the OBD method of AFMs, the deflection noise density is higher by at least two orders of magnitude. The limiting factors are mainly equipment dependent, *i.e.* the readout noise of the camera electronics, the saturation limit of the focal plane array, and the maximum output power of the SLED. Other equipment options should be investigated as possible means of achieving lower deflection noise densities. Another tool that may help in the endeavor to improve the deflection sensitivity is the digital lock-in amplifier. The algorithm appears to perform well in simulation, but it has yet to be seen if it is possible to implement it with the current data acquisition equipment.

One of the things that I have found is that simple binding events do not generate large amounts of surface stress. This is likely due to the attachment chemistry used, attaching reactive molecules directly to the silicon surface. The more common attachment chemistry utilizes a thin gold coating and thiol-based attachment chemistry. As discussed by Godin *et al.* [51], it is the interaction between an adsorbed target molecule and the electronic structure of the gold surface that generates the most amount of stress. This seems to agree with my own experiments where streptavidin-biotin binding events resulting in at most 15 nm of deflection, equivalent to ~5 mN/m surface stress and other similar experiments by other groups [33].

However, as described in Chap. 5, large amounts of surface stress are generated by changes in pH with a simple coating of non-specifically bound BSA on the microcantilever surface. As described in that chapter, I believe the mechanism for the surface stress to be due to pH-induced conformational changes of the bound protein. This suggests that the ideal sensing events are those involve similar conformational changes in the presence of the target molecule or environment. Certainly this limits the types of sensing scenarios to which this technology can be applied. Testing the hypothesis that conformational changes generate significant stress and identifying reactions with practical applications is one of the next steps in research with the microcantilever array sensors with integrated microfluidics

One intriguing possibility within this scope involves the development of new drugs for treating flu viruses. Until recently, the most common drug for treating flu viruses was amantadine. Rhodamine catalyzes the tetramerization of M2 peptide chains on the virus surface. As the monomer M2 chains are necessary for the virus to interact with cell walls, tetramerization of the

chains effectively prevents the virus from infecting healthy cells. Beginning in 2005, strains of the H1N2 flu virus began to exhibit mutations in the M2 peptide chains which remained functional but no longer tetramerized in the presence of amantadine. By 2008, all flu virus strains express the same mutations and are immune to amantadine. Therefore, there is interest in other drugs that may behave similar to amantadine by inactivating the now mutated M2 peptide chains. A microcantilever array sensor with various strains of M2 peptide chains immobilized on one side of the microcantilevers could act as a quick and highly parallel testbed for identifying new drugs. It is likely that the tetramerization of the immobilized peptide chains would generate significant amounts of surface stress similar to the pH response of the immobilized BSA.

REFERENCES

[1] G. G. Stoney, "The tension of metallic films deposited by electrolysis," *Proc. R. Soc. London, Ser. A*, vol. 82, no. 553, pp. 172–175, 1909.

[2] G. Binnig, C. F. Quate, and C. Gerber, "Atomic force microscope," *Phys. Rev. Lett.*, vol. 56, pp. 930–933, Mar 1986.

[3] J. R. Barnes, R. J. Stephenson, C. N. Woodburn, S. J. O'Shea, M. E. Welland, T. Rayment, J. K. Gimzewski, and C. Gerber, "A femtojoule calorimeter using micromechanical sensors," *Rev. Sci. Instrum.*, vol. 65, no. 12, pp. 3793–3798, 1994.

[4] R. Berger, E. Delamarche, H. Lang, C. Gerber, J. Gimzewski, E. Meyer, and H. Güntherodt, "Surface stress in the self-assembly of alkanethiols on gold probed by a force microscopy technique," *Appl. Phys. A: Mater. Sci. Process.*, vol. 66, pp. S55–S59, 1998. 10.1007/s003390051099.

[5] G. G. Yaralioglu, A. Atalar, S. R. Manalis, and C. F. Quate, "Analysis and design of an interdigital cantilever as a displacement sensor," *J. Appl. Phys.*, vol. 83, no. 12, pp. 7405–7415, 1998.

[6] T. Thundat, E. A. Wachter, S. L. Sharp, and R. J. Warmack, "Detection of mercury vapor using resonating microcantilevers," *Appl. Phys. Lett.*, vol. 66, no. 13, pp. 1695–1697, 1995.

[7] H. P. Lang, R. Berger, F. Battiston, J. P. Ramseyer, E. Meyer, C. Andreoli, J. Brugger, P. Vettiger, M. Despont, T. Mezzacasa, L. Scandella, H. J. Güntherodt, C. Gerber, and J. K. Gimzewski, "A chemical sensor based on a micromechanical cantilever array for the identification of gases and vapors," *Appl. Phys. A: Mater. Sci. Process.*, vol. 66, pp. S61–S64, 1998.

[8] H. Ji, K. M. Hansen, Z. Hu, and T. Thundat, "Detection of ph variation using modified microcantilever sensors," *Sens. Actuators, B: Chem.*, vol. 72, no. 3, pp. 233 – 238, 2001.

[9] H. P. Lang, M. Hegner, E. Meyer, and C. Gerber, "Nanomechanics from atomic resolution to molecular recognition based on atomic force microscopy technology," *Nanotechnology*, vol. 13, no. 5, pp. R29–R36, 2002.

[10] J. D. Adams, G. Parrott, C. Bauer, T. Sant, L. Manning, M. Jones, B. Rogers, D. McCorkle, and T. L. Ferrell, "Nanowatt chemical vapor detection with a self-sensing, piezoelectric microcantilever array," *Appl. Phys. Lett.*, vol. 83, no. 16, pp. 3428–3430, 2003.

[11] L. Fadel, F. Lochon, I. Dufour, and O. Francais, "Chemical sensing: millimeter size resonant microcantilever performance," *J. Micromech. Microeng.*, vol. 14, no. 9, pp. S23–S30, 2004.

[12] V. Tabard-Cossa, M. Godin, L. Beaulieu, and P. Grütter, "A differential microcantilever-based system for measuring surface stress changes induced by electrochemical reactions," *Sens. Actuators, B: Chem.*, vol. 107, no. 1, pp. 233 – 241, 2005. Proceedings of the 7th European Conference on Optical Chemical Sensors and Biosensors - EUROPT(R)ODE VII.

[13] K. Goeders, J. Colton, and L.A.Bottomley, "Microcantilevers: Sensing chemical interactions via mechanical motion," *Chem. Rev.*, vol. 108, no. 2, pp. 522–542, 2008.

[14] J. Amírola, A. Rodríguez, L. Castañer, J. P. Santos, J. Gutiérrez, and M. C. Horrillo, "Micromachined silicon microcantilevers for gas sensing applications with capacitive read-out," *Sens. Actuators, B: Chem.*, vol. 111-112, pp. 247 – 253, 2005. Eurosensors XVIII 2004 - The 18th European Conference on Solid-State Transducers.

[15] J. Fritz, M. K. Baller, H. P. Lang, H. Rothuizen, P. Vettiger, E. Meyer, H. J. Güntherodt, C. Gerber, and J. K. Gimzewski, "Translating biomolecular recognition into nanomechanics," *Science*, vol. 288, no. 5464, pp. 316–318, 2000.

[16] A. M. Moulin, S. J. O'Shea, and M. E. Welland, "Microcantilever-based biosensors," *Ultramicroscopy*, vol. 82, no. 1-4, pp. 23 – 31, 2000.

[17] R. Raiteri, M. Grattarola, and R. Berger, "Micromechanics senses biomolecules," *Materials Today*, vol. 5, no. 1, pp. 22 – 29, 2002.

[18] G. Wu, R. H. Datar, K. M. Hansen, T. Thundat, R. J. Cote, and A. Majumdar, "Bioassay of prostate-specific antigen (psa) using microcantilevers," *Nat. Biotechnol.*, vol. 19, pp. 856–860, 2001.

[19] P. A. Rasmussen, J. Thaysen, O. Hansen, S. C. Eriksen, and A. Boisen, "Optimised cantilever biosensor with piezoresistive read-out," *Ultramicroscopy*, vol. 97, no. 1-4, pp. 371 – 376, 2003. Proceedings of the Fourth International Conference on Scanning Probe Microscopy, Sensors and Nanostructures.

[20] N. Lavrik, M. Sepaniak, and P. Datskos, "Cantilever transducers as a platform for chemical and biological sensors," *Rev. Sci. Instrum.*, vol. 75, no. 7, pp. 2229–2253, 2004.

[21] K. M. Hansen and T. Thundat, "Microcantilever biosensors," *Methods*, vol. 37, no. 1, pp. 57 – 64, 2005. Biosensors.

[22] L. Carrascosa, M. Moreno, M. Álvarez, and L. Lechuga, "Nanomechanical biosensors: a new sensing tool," *Trends Analyt. Chem.*, vol. 25, no. 3, pp. 196 – 206, 2006.

[23] G. Shekhawat, S.Tark, and V. Dravid, "Mosfet-embedded microcantilevers for measuring deflection in biomolecular sensors," *Science*, vol. 311, no. 5767, pp. 1592–1595, 2006.

[24] J. Zhang, H. P. Lang, F. Huber, A. Bietsch, W. Grange, U. Certa, R. Mckendry, H. J. Güntherodt, M. Hegner, and C. Gerber, "Rapid and label-free nanomechanical detection of biomarker transcripts in human rna," *Nat. Nanotechnol.*, vol. 1, pp. 214–220, 2006.

[25] R. Zhang, A. Best, R. Berger, S. Cherian, S. Lorenzoni, E. Macis, R. Raiteri, and R. Cain, "Multiwell micromechanical cantilever array reader for biotechnology," *Rev. Sci. Instrum.*, vol. 78, no. 8, p. 084103, 2007.

[26] Y. Zhang, H. Ji, D. Snow, R. Sterling, and G. M. Brown, "A ph sensor based on a microcantilever coated with intelligent hydrogel.," *Instrumentation Science & Technology*, vol. 32, no. 4, pp. 361 – 369, 2004.

[27] A. Boisen, J. Thaysen, H. Jensenius, and O. Hansen, "Environmental sensors based on micromachined cantilevers with integrated read-out," *Ultramicroscopy*, vol. 82, no. 1-4, pp. 11 – 16, 2000.

[28] P. Waggoner and H. Craighead, "Micro- and nanomechanical sensors for environmental, chemical, and biological detection," *Lab Chip*, vol. 7, pp. 1238–1255, 2007.

[29] N. Backmann, C. Zahnd, F. Huber, A. Bietsch, A. Plückthun, H. P. Lang, H. J. Güntherodt, M. Hegner, and C. Gerber, "A label-free immunosensor array using single-chain antibody fragments," *Proc. Natl. Acad. Sci. U. S. A.*, vol. 102, no. 41, pp. 14587–14592, 2005.

[30] R. McKendry, J. Zhang, Y. Arntz, T. Strunz, M. Hegner, H. Lang, M. Baller, U. Certa, E. Meyer, H. Güntherodt, and C. Gerber, "Multiple label-free biodetection and quantitative dna-binding assays on a nanomechanical cantilever array," *Proc. Natl. Acad. Sci. U. S. A.*, vol. 99, no. 15, pp. 9783–9788, 2002.

[31] M. Yue, A. Majumdar, and T. Thundat, "Cantilever arrays: A universal platform for multiplexed label-free bioassays," in *BioMEMS and Biomedical Nanotechnology* (M. Ferrari, R. Bashir, and S. Wereley, eds.), pp. 21–33, Springer US, 2007. 10.1007/978-0-387-25845-42.

[32] D. Czaplewski, B. Ilic, M. Zalalutdinov, W. Olbricht, A. Zehnder, H. Craighead, and T. Michalske, "A micromechanical flow sensor for microfluidic applications," *Microelectromechanical Systems, Journal of*, vol. 13, pp. 576 – 585, aug. 2004.

[33] G. Oliviero, P. Bergese, G. Canavese, M. Chiari, P. Colombi, M. Cretich, F. Damin, S. Fiorilli, S. Marasso, C. Ricciardi, P. Rivolo, and L. Depero, "A biofunctional polymeric coating for microcantilever molecular recognition," *Anal. Chim. Acta*, vol. 630, no. 2, pp. 161 – 167, 2008.

[34] M. Sepaniak, P. Datskos, N. Lavrik, and C. Tipple, "Peer reviewed: Microcantilever transducers: A new approach in sensor technology," *Anal. Chem.*, vol. 74, no. 21, pp. 568 A–575 A, 2002.

[35] J. Adams, B. Rogers, M. Manning, Z. Hu, T. Thundat, H. Cavazos, and S. Minne, "Piezoelectric self-sensing of adsorption-induced microcantilever bending," *Sens. Actuators, A: Phys.*, vol. 121, no. 2, pp. 457 – 461, 2005.

[36] M. Nordström, D. A. Zauner, M. Calleja, J. Hübner, and A. Boisen, "Integrated optical readout for miniaturization of cantilever-based sensor system," *Appl. Phys. Lett.*, vol. 91, no. 10, p. 103512, 2007.

[37] M. Yue, H. Lin, D. Dedrick, S. Satyanarayana, A. Majumdar, A. Bedekar, J. Jenkins, and S. Sundaram, "A 2-d microcantilever array for multiplexed biomolecular analysis," *J. Microelectromech. Syst.*, vol. 13, pp. 290–299, April 2004.

[38] P. Sheehan and L. Whitman, "Detection limits for nanoscale biosensors," *Nano Lett.*, vol. 5, no. 4, pp. 803–807, 2005.

[39] T. Squires, R. Messinger, and S. Manalis, "Making it stick: convection, reaction and diffusion in surface-based biosensors," *Nat. Biotechnol.*, vol. 26, pp. 417–426, 2008.

[40] S. Wu and H. J. Frankena, "Integrated optical sensors using micromechanical bridges and cantilevers," in *Integrated Optics and Microstructures* (M. Tabib-Azar and D. L. Polla, eds.), vol. 1793, pp. 83–89, SPIE, 1993.

[41] K. E. Burcham, G. N. D. Brabander, and J. T. Boyd, "Micromachined silicon cantilever beam accelerometer incorporating an integrated optical waveguide," in *Integrated Optics and Microstructures* (M. Tabib-Azar and D. L. Polla, eds.), vol. 1793, pp. 12–18, SPIE, 1993.

[42] J. W. Noh, R. Anderson, S. Kim, J. Cardenas, and G. P. Nordin, "In-plane photonic transduction of silicon-on-insulator microcantilevers," *Opt. Express*, vol. 16, no. 16, pp. 12114–12123, 2008.

[43] J. W. Noh, R. R. Anderson, S. Kim, W. Hu, and G. P. Nordin, "In-plane all-photonic transduction with differential splitter using double-step rib waveguide for photonic microcantilever arrays," *Opt. Express*, vol. 17, no. 22, pp. 20012–20020, 2009.

[44] J. W. Noh, R. R. Anderson, S. Kim, W. Hu, and G. P. Nordin, "Sensitivity enhancement of differential splitter-based transduction for photonic microcantilever arrays," *Nanotechnology*, vol. 21, no. 15, p. 155501, 2010.

[45] W. Hu, R. Anderson, Y. Qian, J. Song, J. W. Noh, S. Kim, and G. P. Nordin, "Demonstration of microcantilever array with simultaneous readout using an in-plane photonic transduction method," *Rev. Sci. Instrum.*, vol. 80, no. 8, p. 085101, 2009.

[46] H. P. Lang, M. Hegner, and C. Gerber, "Cantilever array sensors," *Materials Today*, vol. 8, no. 4, pp. 30 – 36, 2005.

[47] M. Alvarez and L. M. Lechuga, "Microcantilever-based platforms as biosensing tools," *Analyst*, vol. 135, no. 5, pp. 827–836, 2010.

[48] S. L. Biswal, D. Raorane, A. Chaiken, H. Birecki, and A. Majumdar, "Nanomechanical detection of dna melting on microcantilever surfaces," *Anal. Chem.*, vol. 78, no. 20, pp. 7104–7109, 2006.

[49] C. L. Britton, R. L. Jones, P. I. Oden, Z. Hu, R. J. Warmack, S. F. Smith, W. L. Bryan, and J. M. Rochelle, "Multiple-input microcantilever sensors," *Ultramicroscopy*, vol. 82, no. 1-4, pp. 17 – 21, 2000.

[50] P. G. Datskos and I. Sauers, "Detection of 2-mercaptoethanol using gold-coated micromachined cantilevers," *Sens. Actuators, B: Chem.*, vol. 61, pp. 75–82, Dec 1999.

[51] M. Godin, V. Tabard-Cossa, Y. Miyahara, T. Monga, P. J. Williams, L. Y. Beaulieu, R. B. Lennox, and P. Grutter, "Cantilever-based sensing: the origin of surface stress and optimization strategies," *Nanotechnol.*, vol. 21, no. 7, p. 075501, 2010.

[52] P. G. Datskos, P. I. Oden, T. Thundat, E. A. Wachter, R. J. Warmack, and S. R. Hunter, "Remote infrared radiation detection using piezoresistive microcantilevers," *Appl. Phys. Lett.*, vol. 69, no. 20, pp. 2986–2988, 1996.

[53] N. Backmann, N. Kappeler, T. Braun, F. Huber, H. P. Lang, C. Gerber, and R. Y. H. Lim, "Sensing surface pegylation with microcantilevers," *Beilstein J. Nanotechnol.*, vol. 1, pp. 3–13, 2010.

[54] D. Raorane, S. Lim, and A. Majumdar, "Nanomechanical assay to investigate the selectivity of binding interactions between volatile benzene derivatives," *Nano Lett.*, vol. 8, no. 8, pp. 2229–2235, 2008.

[55] D. Filenko, T. Ivanov, B. E. Volland, K. Ivanova, I. W. Rangelow, N. Nikolov, T. Gotszalk, and J. Mielczarski, "Experimental setup for characterization of self-actuated microcantilevers with piezoresistive readout for chemical recognition of volatile substances," *Rev. Sci. Instrum.*, vol. 79, no. 9, p. 094101, 2008.

[56] J. W. Ndieyira, M. Watari, A. D. Barrera, D. Zhou, M. Vogtli, M. Batchelor, M. A. Cooper, T. Strunz, M. A. Horton, C. Abell, T. Rayment, G. Aeppli, and R. A. McKendry, "Nanomechanical detection of antibiotic-mucopeptide binding in a model for superbug drug resistance," *Nat. Nanotechnol.*, vol. 3, pp. 691–696, 2008.

[57] J. Mertens, M. Calleja, D. Ramos, A. Tarýn, and J. Tamayo, "Role of the gold film nanostructure on the nanomechanical response of microcantilever sensors," *Journal of Applied Physics*, vol. 101, no. 3, p. 034904, 2007.

[58] T. Clyne, "Residual stresses in surface coatings and their effects on interfacial debonding," *Key Eng. Mater.*, vol. 116-117, pp. 307–330, 1996.

[59] T. Clyne, "Residual stresses in coated and layered systems," in *Encyclopedia of Materials: Science and Technology (Second Edition)* (K. H. J. Buschow, R. W. Cahn, M. C. Flemings, B. Ilschner, E. J. Kramer, S. Mahajan, and P. Veyssière, eds.), pp. 8126–8134, Oxford: Elsevier, 2001.

[60] C. Hsueh, "Thermal stresses in elastic multilayer systems," *Thin Solid Films*, vol. 418, pp. 182–188, Oct 2002.

[61] B. T. Comella and M. R. Scanlon, "The determination of the elastic modulus of microcantilever beams using atomic force microscopy," *J. Mater. Sci.*, vol. 35, pp. 567–572, 2000. 10.1023/A:1004712007729.

[62] J. Lai, T. Perazzo, Z. Shi, and A. Majumdar, "Optimization and performance of high-resolution micro-optomechanical thermal sensors," *Sens. Actuators, A: Phys.*, vol. 58, no. 2, pp. 113 – 119, 1997.

[63] M. A. Hopcroft, W. D. Nix, and T. W. Kenny, "What is the young's modulus of silicon," *J. Microelectromech. Syst.*, vol. 19, pp. 229–238, April 2010.

[64] R. Katragadda, Z. Wang, W. Khalid, Y. Li, and Y. Xu, "Parylene cantilevers integrated with polycrystalline silicon piezoresistors for surface stress sensing," *Appl. Phys. Lett.*, vol. 91, no. 8, p. 083505, 2007.

[65] H. J. Butt, "A sensitive method to measure changes in the surface stress of solids," *Journal of Colloid and Interface Science*, vol. 180, no. 1, pp. 251 – 260, 1996.

[66] T. Braun, M. K. Ghatkesar, V. Barwich, N. Backmann, F. Huber, W. Grange, N. Nugaeva, H. P. Lang, J. P. Ramseyer, C. Gerber, and M. Hegner, "Digital processing of multi-mode nano-mechanical cantilever data," *J. Phys. Conf. Ser.*, vol. 61, no. 1, p. 341, 2007.

[67] A. Pageler, T. Blum, K. Kosbi, U. Scheer, and S. Boseck, "Determination of bonding properties in layered metal silicon systems using sezawa wave modes," in *Acoustical Imaging* (H. Lee, ed.), vol. 24 of *Acoustical Imaging*, pp. 229–235, Springer US, 2002.

[68] C. W. Tan and J. Miao, "Optimization of sputtered cr/au thin film for diaphragm-based mems applications," *Thin Solid Films*, vol. 517, pp. 4921–4925, July 2009.

[69] B. Halg, "On a nonvolatile memory cell based on micro-electro-mechanics," in *Micro Electro Mechanical Systems, 1990. Proceedings, An Investigation of Micro Structures, Sensors, Actuators, Machines and Robots. IEEE*, pp. 172–176, Feb 1990.

[70] Y. Lin, M. McConney, M. LeMieux, S. Peleshanko, C. Jiang, S. Singamaneni, and V. Tsukruk, "Trilayered ceramic-metal-polymer microcantilevers with dramatically enhanced thermal sensitivity," *Adv. Mater. Weinheim*, vol. 18, no. 9, pp. 1157–1161, 2006.

[71] G. C. A. M. Janssen, M. M. Abdalla, F. van Keulen, B. R. Pujada, and B. van Venrooy, "Celebrating the 100th anniversary of the stoney equation for film stress: Developments from polycrystalline steel strips to single crystal silicon wafers," *Thin Solid Films*, vol. 517, no. 6, pp. 1858 – 1867, 2009.

[72] N. F. Martínez, P. M. Kosaka, J. Tamayo, J. Ramírez, O. Ahumada, J. Mertens, T. D. Hien, C. V. Rijn, and M. Calleja, "High throughput optical readout of dense arrays of nanomechanical systems for sensing applications," *Review of Scientific Instruments*, vol. 81, no. 12, p. 125109, 2010.

[73] M. A. Unger, H. Chou, T. Thorsen, A. Scherer, and S. R. Quake, "Monolithic microfabricated valves and pumps by multilayer soft lithography," *Science*, vol. 288, no. 5463, pp. 113–116, 2000.

[74] C. Lee, G. Sui, A. Elizarov, C. J. Shu, Y. Shin, A. N. Dooley, J. Huang, A. Daridon, P. Wyatt, D. Stout, H. C. Kolb, O. N. Witte, N. Satyamurthy, J. R. Heath, M. E. Phelps, S. R. Quake, and H. Tseng, "Multistep synthesis of a radiolabeled imaging probe using integrated microfluidics," *Science*, vol. 310, no. 5755, pp. 1793–1796, 2005.

[75] S. Satyanarayana, R. Karnik, and A. Majumdar, "Stamp-and-stick room-temperature bonding technique for microdevices," *J. Microelectromech. Syst.*, vol. 14, pp. 392 – 399, apr. 2005.

[76] B. Samel, M. K. Chowdhury, and G. Stemme, "The fabrication of microfluidic structures by means of full-wafer adhesive bonding using a poly(dimethylsiloxane) catalyst," *J. Micromech. Microeng.*, vol. 17, no. 8, p. 1710, 2007.

[77] L. Tsai, W. C. Dahlquist, S. Kim, and G. P. Nordin, "Bonding of polydimethylsiloxane (pdms) microfluidics to silicon-based sensors," *J. Micro/Nanolithogr. MEMS MOEMS*, vol. 10, no. 4, p. 043009, 2011.

[78] A. K. Gaigalas, J. B. Hubbard, M. McCurley, and S. Woo, "Diffusion of bovine serum albumin in aqueous solutions," *The Journal of Physical Chemistry*, vol. 96, no. 5, pp. 2355–2359, 1992.

[79] T. A. Ruzgas, V. J. Razumas, and J. J. Kulys, "Sequential adsorption of γ-interferon and bovine serum albumin on hydrophobic silicon surfaces," *J. Colloid Interface Sci.*, vol. 151, pp. 136–143, Jun 1992.

[80] P. G. Datskos, N. V. Lavrik, and M. J. Sepaniak, *Smart Sensors and MEMS*, vol. 181, ch. 11, pp. 331–379. Kluwer Academic Publishers, 2004.

[81] T. Braun, F. Huber, M. K. Ghatkesar, N. Backmann, H. P. Lang, C. Gerber, and M. Hegner, "Processing of kinetic microarray signals," *Sens. Actuators, B: Chem.*, vol. 128, no. 1, pp. 75 – 82, 2007.

[82] C. T. Gibson, G. S. Watson, and S. Myhra, "Determination of the spring constants of probes for force microscopy/spectroscopy," *Nanotechnology*, vol. 7, no. 3, p. 259, 1996.

[83] N. F. al Baldawi and R. F. Abercrombie, "Cytoplasmic hydrogen ion diffusion coefficient," *Biophys. J.*, vol. 61, pp. 1470–1479, June 1992.

[84] J. F. Foster, *Albumin structure, function and uses*. Pergamon Press, 1977.

[85] M. K. Menon and A. L. Zydney, "Measurement of protein charge and ion binding using capillary electrophoresis," *Anal. Chem.*, vol. 70, no. 8, pp. 1581–1584, 1998.

[86] S. Wu, Q. Lin, Y. Yuen, and Y. Tai, "Mems flow sensors for nano-fluidic applications," in *Micro Electro Mechanical Systems, 2000. MEMS 2000. The Thirteenth Annual International Conference on*, pp. 745–750, 2000.

[87] R. Buchner, C. Sosna, M. Maiwald, W. Benecke, and W. Lang, "A high-temperature thermopile fabrication process for thermal flow sensors," *Sens. Actuators, A: Phys.*, vol. 130-131, pp. 262–266, Aug 2006.

[88] W. C. Shin and R. S. Besser, "A micromachined thin-film gas flow sensor for microchemical reactors," *J. Micromech. Microeng.*, vol. 16, no. 4, p. 731, 2006.

[89] W. Shu, E. D. Laue, and A. A. Seshia, "Investigation of biotin-streptavidin binding interactions using microcantilever sensors," *Biosens. Bioelectron.*, vol. 22, no. 9-10, pp. 2003 – 2009, 2007. Selected Papers from the Ninth World Congress On Biosensors. Toronto, Canada 10 - 12 May 2006, Alice X. J . Tang.

[90] L. Zhu, D. Meier, Z. Boger, C. Montgomery, S. Semancik, and D. DeVoe, "Integrated microfluidic gas sensor for detection of volatile organic compounds in water," *Sens. Actuators, B: Chem.*, vol. 121, pp. 679–688, Feb 2007.

[91] R. Oosterbroek, T. Lammerink, J. Berenschot, G. Krijnen, M. Elwenspoek, and A. van den Berg, "A micromachined pressure/flow-sensor," *Sens. Actuators, A: Phys.*, vol. 77, no. 3, pp. 167–177, 1999.

[92] O. Berberig, K. Nottmeyer, J. Mizuno, Y. Kanai, and T. Kobayashi, "The prandtl micro flow sensor (pmfs): a novel silicon diaphragm capacitive sensor for flow velocity measurement," in *Solid State Sensors and Actuators, 1997. TRANSDUCERS '97 Chicago., 1997 International Conference on*, vol. 1, pp. 155 –158 vol.1, Jun 1997.

[93] N. Svedin, E. Kalvesten, E. Stemme, and G. Stemme, "A new silicon gas-flow sensor based on lift force," *Microelectromechanical Systems, Journal of*, vol. 7, pp. 303 –308, sep 1998.

[94] N. Svedin, E. Kälvesten, and G. Stemme, "A lift force sensor with integrated hot-chips for wide range flow measurements," *Sens. Actuators, A: Phys.*, vol. 109, no. 1-2, pp. 120 – 130, 2003.

[95] R. Attia, D. C. Pregibon, P. S. Doyle, J. L. Viovy, and D. Bartolo, "Soft microflow sensors," *Lab Chip*, vol. 9, no. 9, pp. 1213–1218, 2009.

[96] Y. Wang, C. Lee, and C. Chiang, "A mems-based air flow sensor with a free-standing microcantilever structure," *Sensors*, vol. 7, no. 10, pp. 2389–2401, 2007.

[97] Y. Wang, C. Chen, C. Chang, C. Lin, C. Lin, L. Fu, and C. Lee, "Mems-based gas flow sensors," *Microfluid. Nanofluid.*, vol. 6, no. 3, pp. 333–346, 2009.

[98] A. Jana, A. Raman, B. Dhayai, S. L. Tripp, and R. G. Reifenberger, "Microcantilever mechanics in flowing viscous fluids," *Appl. Phys. Lett.*, vol. 90, p. 114110, 2007.

[99] V. Lien and F. Vollmer, "Microfluidic flow rate detection based on integrated optical fiber cantilever," *Lab Chip*, vol. 7, no. 10, pp. 1352–1356, 2007.

[100] S. Kim, T. Gustafson, D. C. Richards, W. Hu, and G. P. Nordin, "Microcantilever deflection compensation with focused ion beam exposure," *Journal of Micromechanics and Microengineering*, vol. 21, no. 8, p. 085007, 2011.

[101] G. M. Whitesides, "The origins and the future of microfluidics," *Nature*, vol. 442, pp. 368–373, Jul 2006.

[102] J. Proakis and D. Manolakis, *Digital signal processing*. Pearson Prentice Hall, 2007.

[103] A. García-Valenzuela and J. Villatoro, "Noise in optical measurements of cantilever deflections," *J. Appl. Phys.*, vol. 84, pp. 58–63, Jul 1998.

[104] J. Gonska, C. Schelling, and G. Urban, "Application of hydrogel-coated microcantilevers as sensing elements for ph," *J. Micromech. Microeng.*, vol. 19, no. 12, p. 127002, 2009.

[105] J. Harley and T. Kenny, "1/f noise considerations for the design and process optimization of piezoresistive cantilevers," *J. Microelectromech. Syst.*, vol. 9, pp. 226–235, Jun 2000.

[106] A. Dorrington and R. Kunnemeyer, "A simple microcontroller based digital lock-in amplifier for the detection of low level optical signals," in *Electronic Design, Test and Applications, 2002. Proceedings. The First IEEE International Workshop on*, pp. 486–488, 2002.

[107] J. Gaspar, S. F. Chen, A. Gordillo, M. Hepp, P. Ferreyra, and C. Marqués, "Digital lock in amplifier: study, design and development with a digital signal processor," *Microprocess. Microsyst.*, vol. 28, no. 4, pp. 157 – 162, 2004.

[108] P. K. Dixon and L. Wu, "Broadband digital lock-in amplifier techniques," *Rev. Sci. Instrum.*, vol. 60, no. 10, pp. 3329–3336, 1989.

[109] J. Masciotti, J. Lasker, and A. Hielscher, "Digital lock-in algorithm for biomedical spectroscopy and imaging instruments with multiple modulated sources," in *Engineering in Medicine and Biology Society, 2006. EMBS '06. 28th Annual International Conference of the IEEE*, pp. 3198–3201, 30 2006-Sept. 3 2006.

[110] J. Wilson, A. Nelson, and B. Farhang-Boroujeny, "Parameter derivation of type-2 discrete-time phase-locked loops containing feedback delays," *IEEE Trans. Circuits Syst. II*, vol. 56, pp. 886 –890, dec. 2009.

[111] F. Barone, E. Calloni, L. DiFiore, A. Grado, L. Milano, and G. Russo, "High-performance modular digital lock-in amplifier," *Rev. Sci. Instrum.*, vol. 66, no. 6, pp. 3697–3702, 1995.

APPENDIX A. MODIFIED SOLUTION TO LANGMUIR BINDING

The Langmuir rate equation,

$$\frac{d\sigma}{dt} = k_{\text{on}} c_{\text{s}} (1 - \sigma) - k_{\text{off}} \sigma, \tag{A.1}$$

relates the fraction of filled binding sites, σ, to the on and off reaction rates, k_{on} and k_{off} respectively, and the time-dependent concentration, c_s, at the sensor surface. Adsorption to the surface creates a depletion region in the solution above the sensor across which transport is diffusion dominated. The mass-transport flux J_{D} through the depletion region can be approximated as

$$J_{\text{D}} \sim D(c_0 - c_{\text{s}}) W_{\text{s}} \mathscr{F} \tag{A.2}$$

where D is the diffusion coefficient of the binding molecule in solution, c_0 is the bulk concentration outside of the depletion region, W_{s} is the sensor width, and $\mathscr{F}$ is the dimensionless flux. The reaction flux J_{R} at the surface is

$$J_{\text{R}} = L W_{\text{s}} \frac{d\sigma}{dt} \Gamma_{\max} \tag{A.3}$$

where L is the length of the sensor and Γ_{max} is the density of surface receptor sites. In the quasi-steady approximation, these two fluxes must be balanced

$$D(c_0 - c_{\text{s}}) \mathscr{F} = L \Gamma_{\max} \dot{\sigma}. \tag{A.4}$$

At this point it is common to introduce a dimensionless number, the Damkohler number (Da), defined as

$$Da = \frac{k_{\text{on}} \Gamma_{\max} L}{D \mathscr{F}}. \tag{A.5}$$

The concentration difference across the depletion can be expressed in terms of Da,

$$c_0 - c_\mathrm{s} = \frac{Da\dot{\sigma}}{k_\mathrm{on}}, \tag{A.6}$$

which gives an expression for c_s

$$c_\mathrm{s} = c_0 - \frac{Da\dot{\sigma}}{k_\mathrm{on}} \tag{A.7}$$

in terms of the bulk concentration. Substituting this into the Langmuir rate equation, the binding rate $\dot{\sigma}$ is given by a modified Langmuir rate equation in terms the bulk solution concentration rather than the surface concentration:

$$\dot{\sigma} = k_\mathrm{on}\left(c_0 - \frac{Da\dot{\sigma}}{k_\mathrm{on}}\right)(1-\sigma) - k_\mathrm{off}\sigma = k_\mathrm{on}c_0(1-\sigma) - k_\mathrm{off}\sigma - Da\dot{\sigma}(1-\sigma), \tag{A.8}$$

$$\dot{\sigma} = \frac{k_\mathrm{on}c_0(1-\sigma) - k_\mathrm{off}\sigma}{1 + Da(1-\sigma)}. \tag{A.9}$$

A reasonable question is whether or not I can assume a quasi-steady binding rate. One argument to check this is to assume the binding reaction reaches an equilibrium, and use the equilibrium time scale to determine a quasi-steady binding or not. If however I am analyzing the reaction prior to reaching an equilibrium and the bulk concentration is treated as dynamic, it is not evident that this line of reasoning can be used to check the quasi-steady state assumption. It might be possible to make use of numerical values at discrete time steps obtained from finite-element method (FEM) simulations of the concentration. The total number of molecules bound to the surface at time t_n is

$$N_\mathrm{n} = \Gamma_\mathrm{max}\sigma_\mathrm{n} = \sum_{\mathrm{m}=1}^{\mathrm{n}} h_\mathrm{m}c_\mathrm{m}, \tag{A.10}$$

which can be rewritten as

$$\Gamma_\mathrm{max}\left(\sigma_\mathrm{n} - \sigma_{\mathrm{n}-1}\right) = h_\mathrm{n}c_\mathrm{n} \tag{A.11}$$

where c_n is value of the bulk solution concentration c_0 at t_n and h_n is the minimum distance into the solution needed to go to account for all the molecules bound to the surface in one time step Δt. Here I am assuming that the bulk concentration is a uniform c_n close to the sensor and that the advective flow is sufficient to significantly repopulate the depleted region, that is the depletion is

small in comparison to the sensor dimensions. For this to be quasi-steady, all the particles within h_n need sufficient time to diffuse to the surface, that is $h_{\mathrm{n}} < \sqrt{D\Delta t}$, or

$$\frac{\Gamma_{\max}\left(\sigma_{\mathrm{n}} - \sigma_{\mathrm{n}-1}\right)}{c_{\mathrm{n}}\sqrt{D\Delta t}} \ll 1. \tag{A.12}$$

Using the values from the FEM simulations for out microfluidics as shown in Chap. 5 indicate that this condition is always met except briefly at the initial times when the bulk solution concentration is negligible. This is likely an artifact of the discrete nature of the analysis as $c_{\mathrm{n}} \sim 0$ can cause the fraction on the left of Eq. A.12 to be nearly undefined when $\sigma_{\mathrm{n}} - \sigma_{\mathrm{n}-1} \sim 0$.

APPENDIX B. LABVIEW CODE

B.1 Calibration Measurements

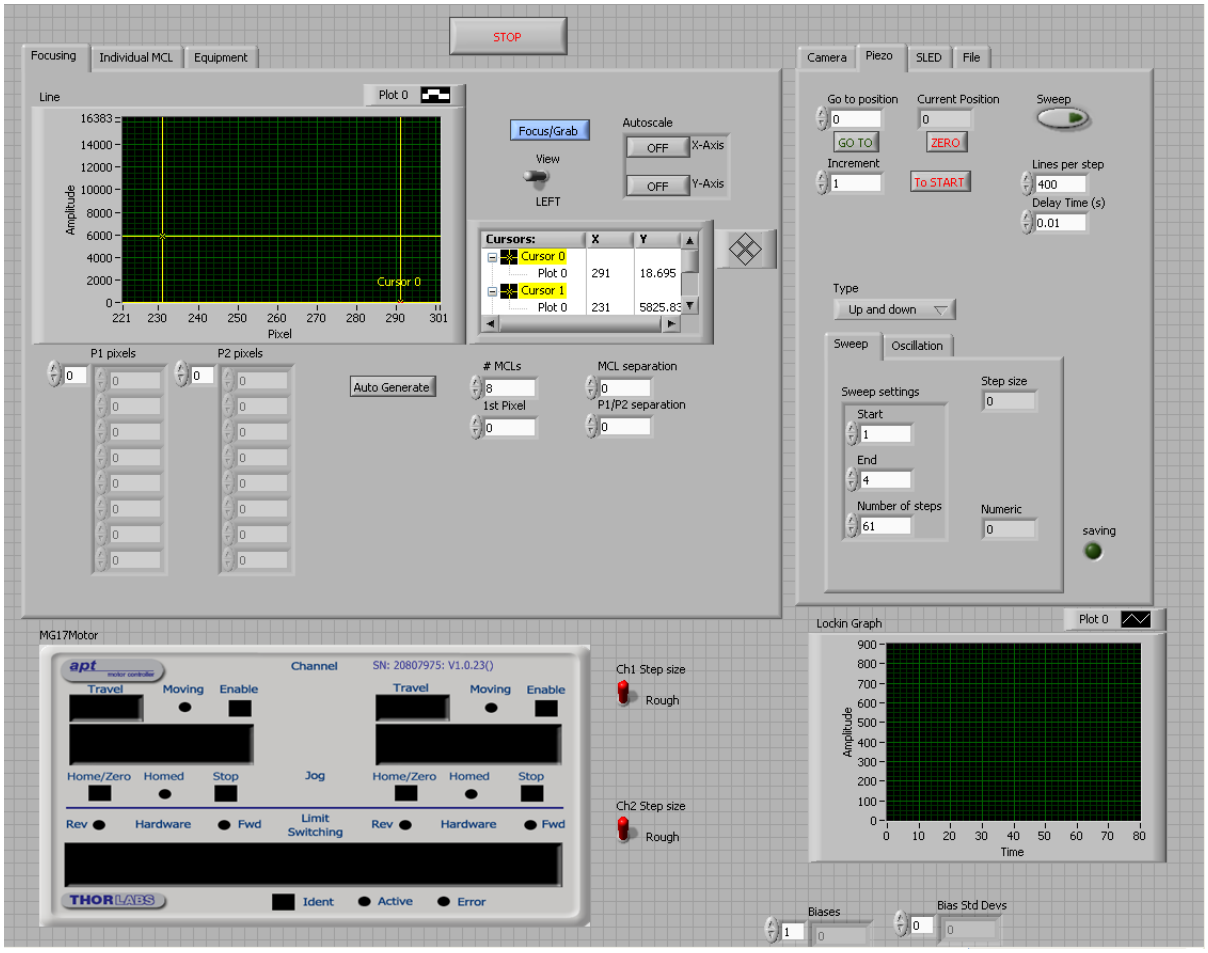

Figure B.1: GUI for responsivity measurements.

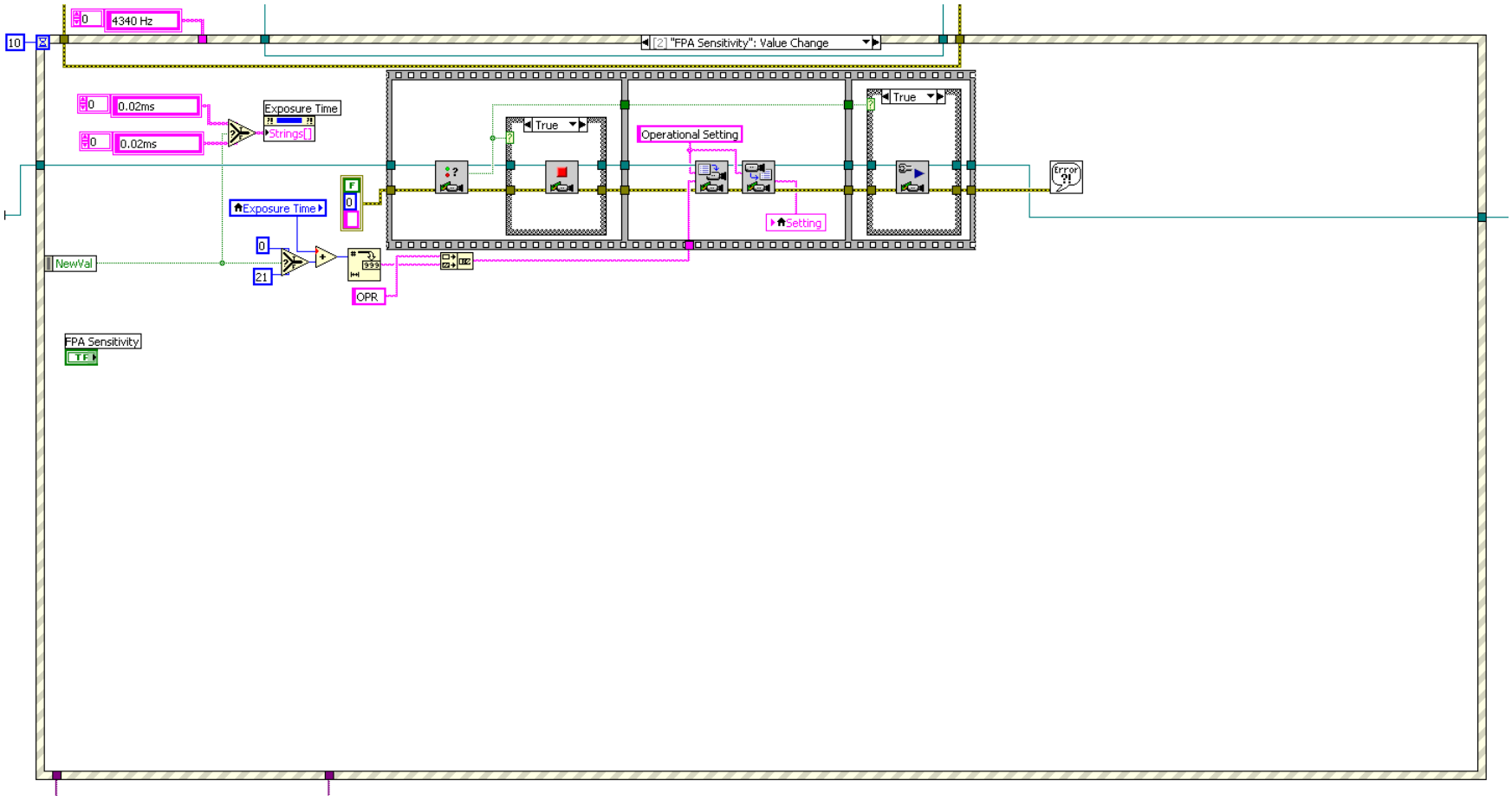

Figure B.2: Block diagram for changing the operational mode of the line scan camera.

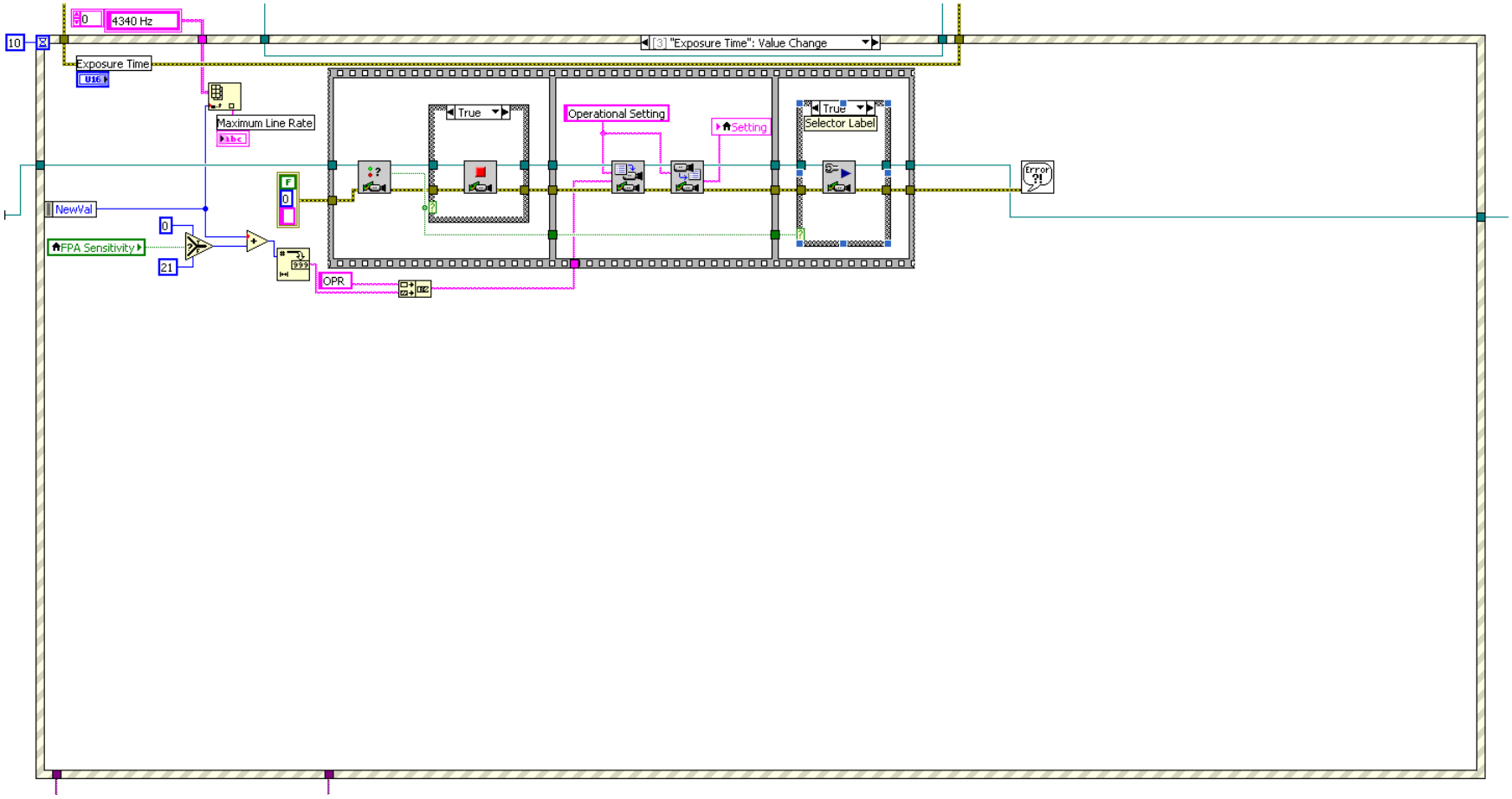

Figure B.3: Block diagram for changing the exposure time of the line scan camera.

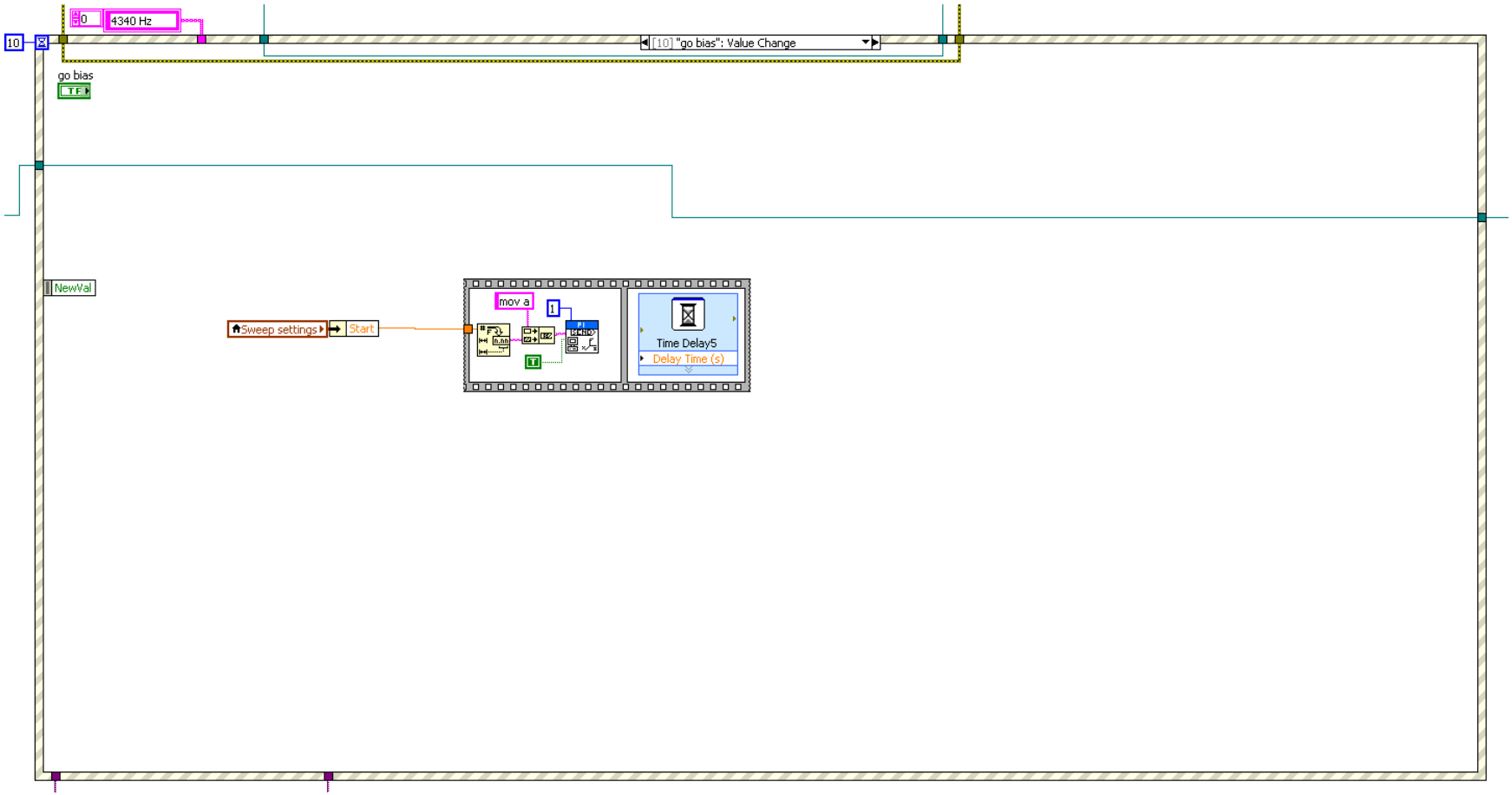

Figure B.4: Block diagram for moving the piezotranslator to the initial position of a calibration sweep.

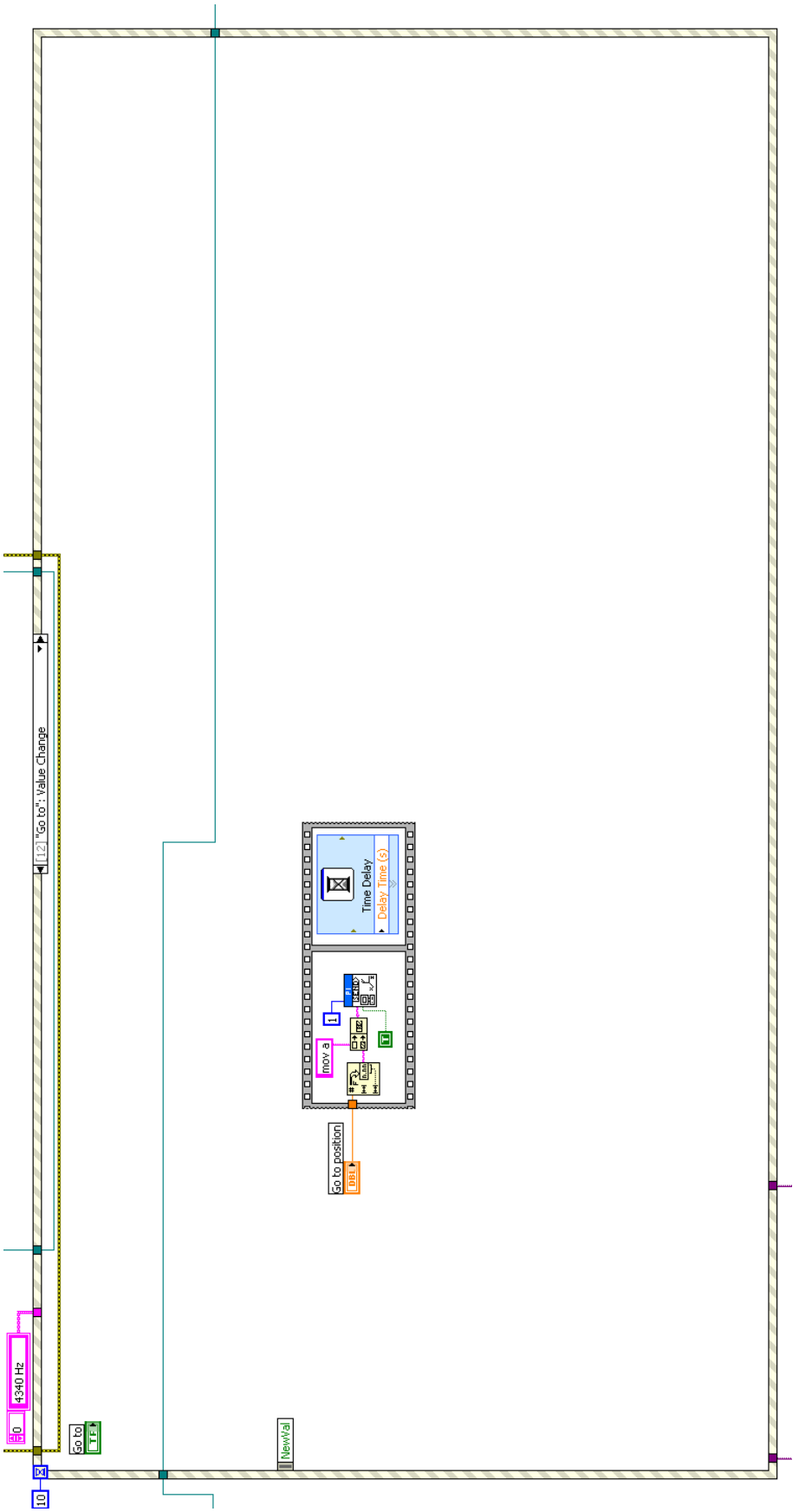

Figure B.5: Block diagram for moving the piezotranslator to its zero position.

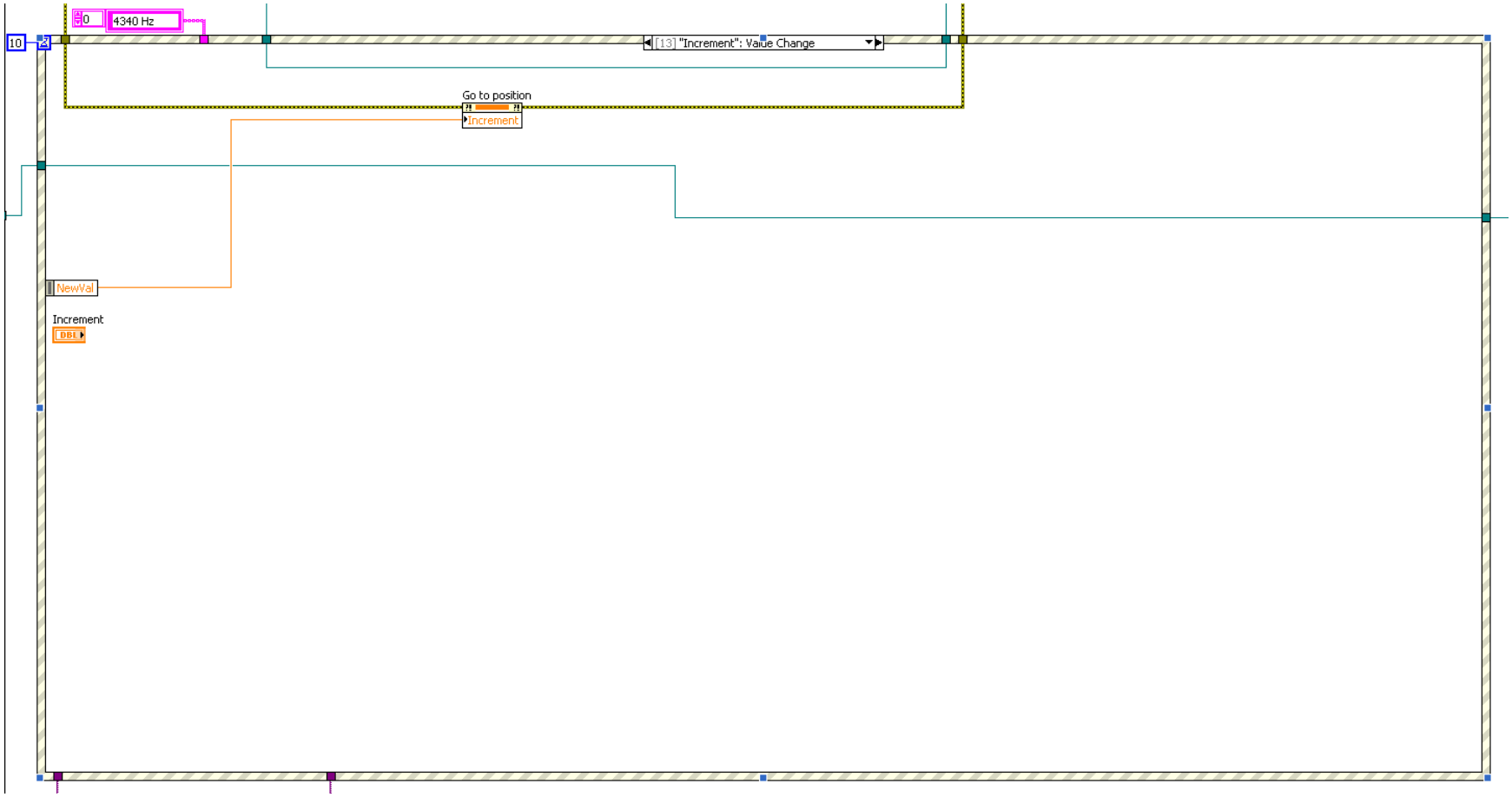

Figure B.6: Block diagram for change the increment/decrement step size for the piezotranslator position control.

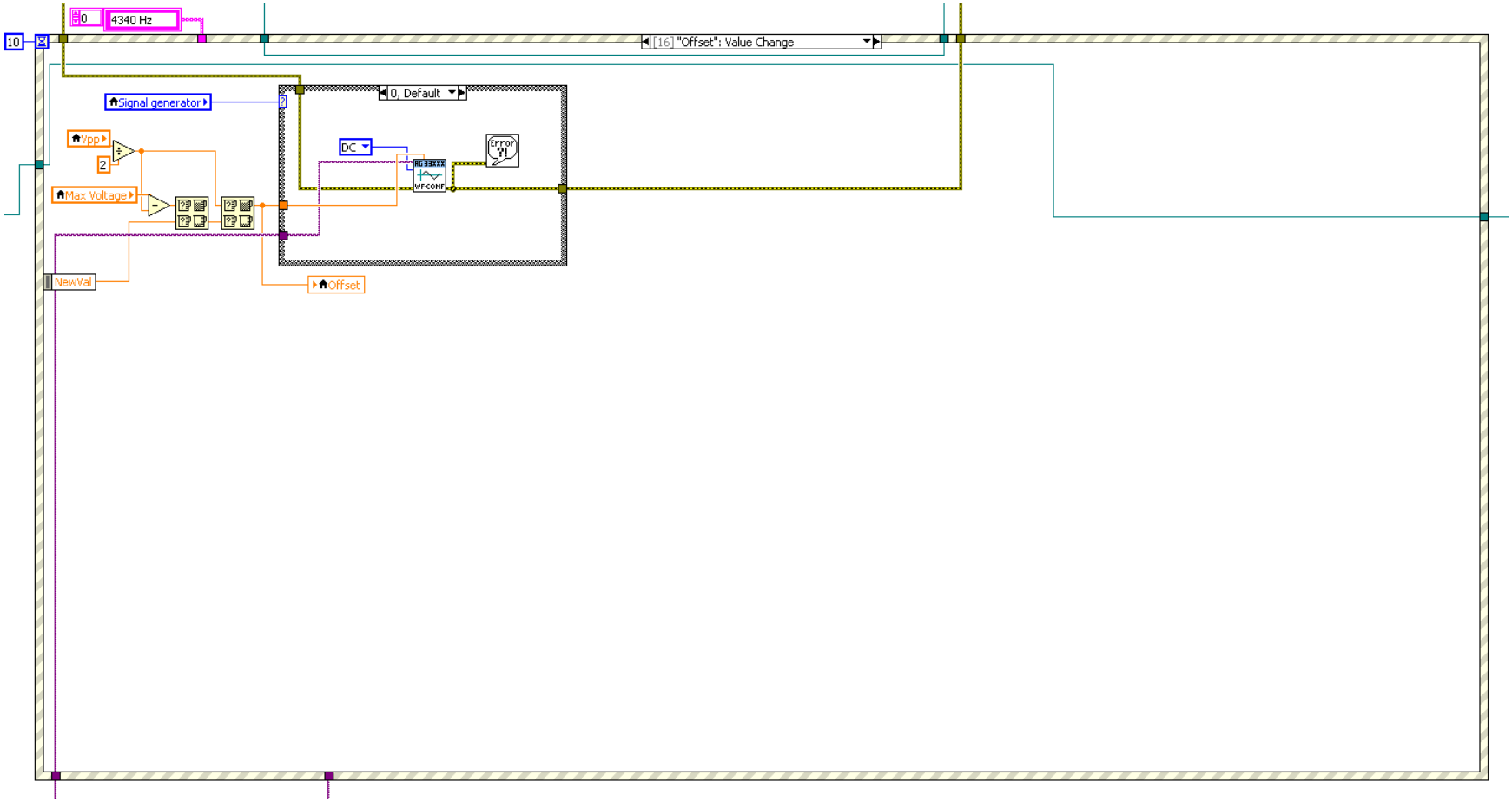

Figure B.7: Block diagram for setting the DC control voltage sent to the SLED.

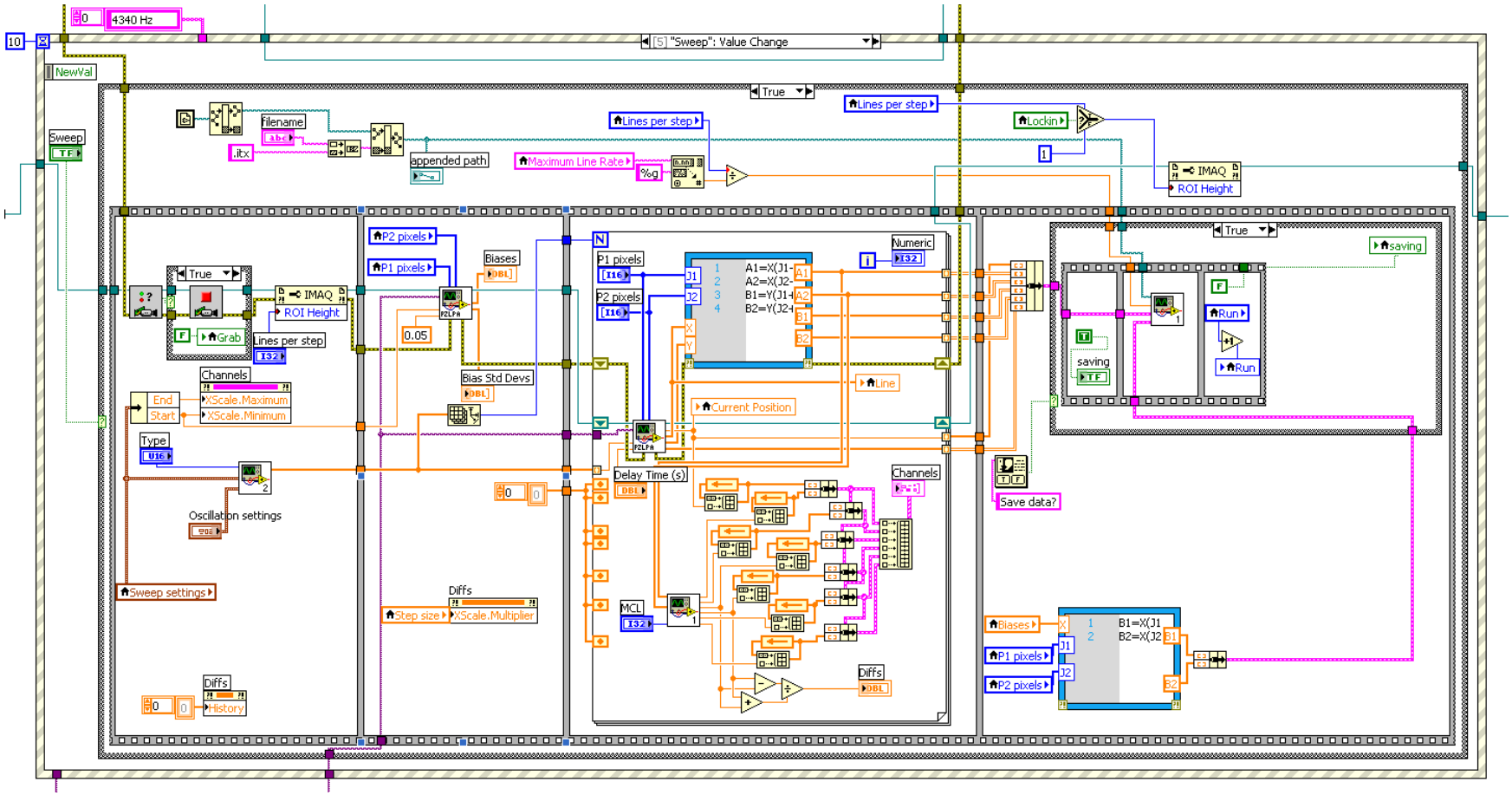

Figure B.8: Block diagram for doing a full calibration measurement sending commands to the piezotranslator, querying its position, and grabbing images from the camera.

B.2 Experiments Requiring Microfluidics and Syringe Control

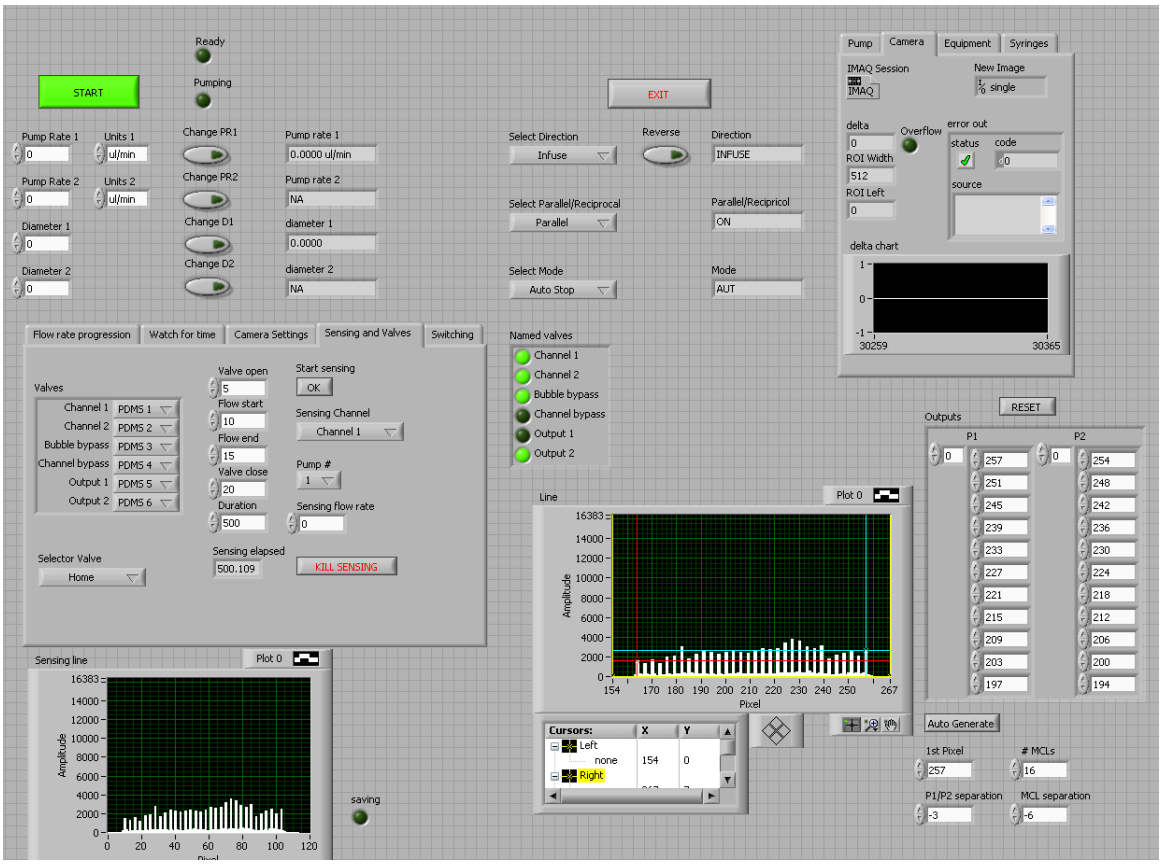

Figure B.9: GUI for responsivity measurements.

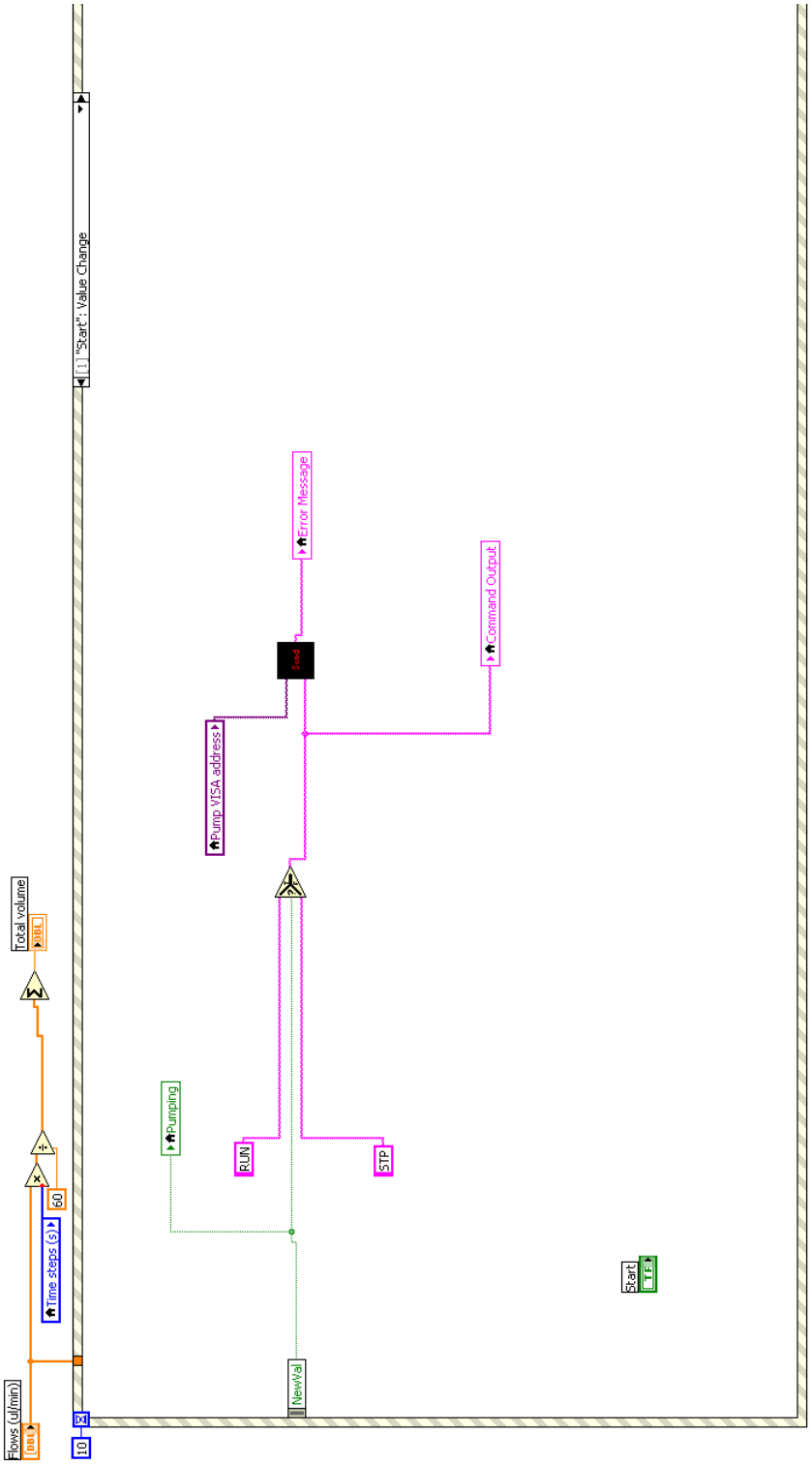

Figure B.10: Block diagram sending the command to start or stop the syringe pump.

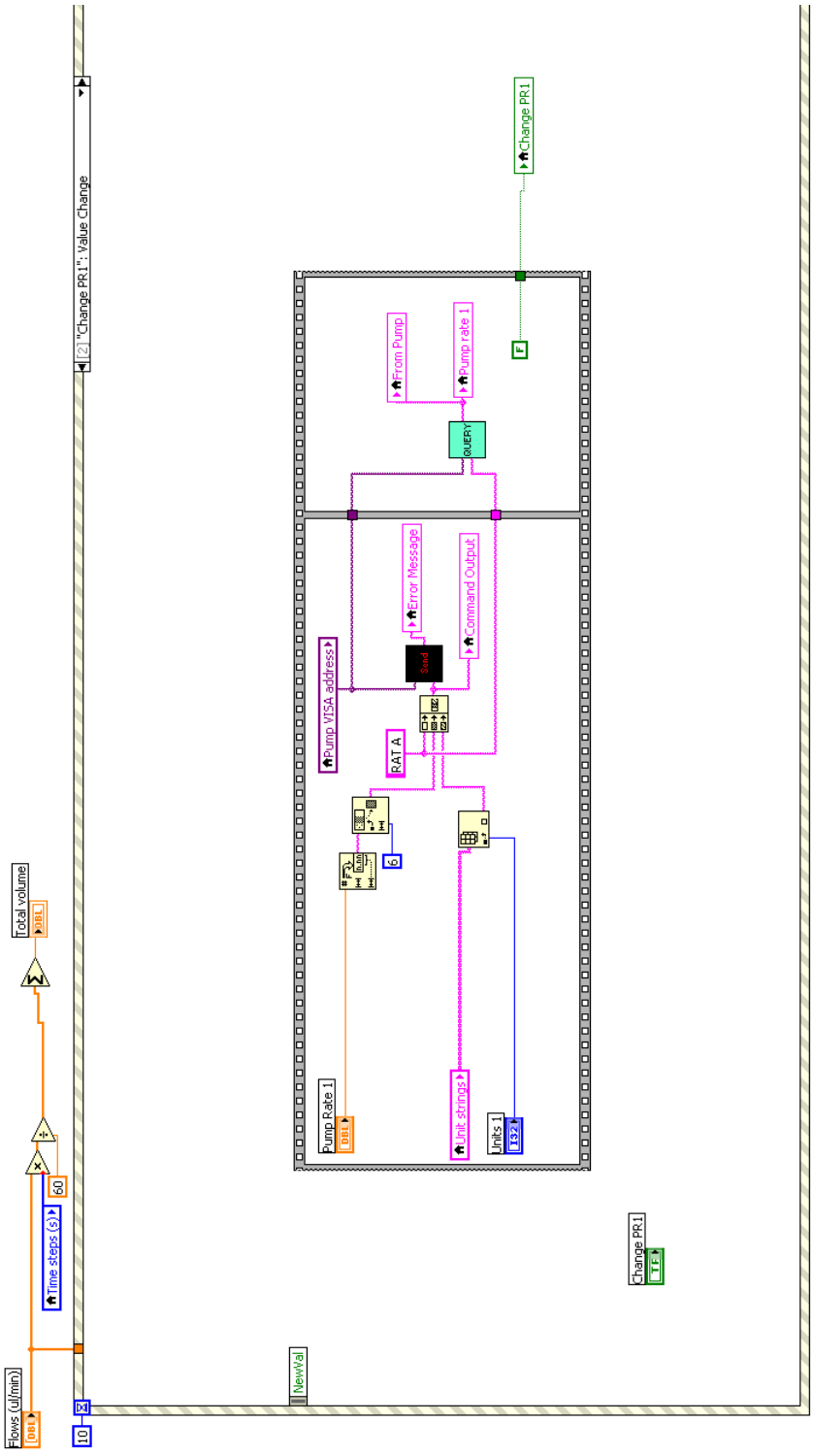

Figure B.11: Block diagram to change to volumetric flow rate for one of the syringes in the pump.

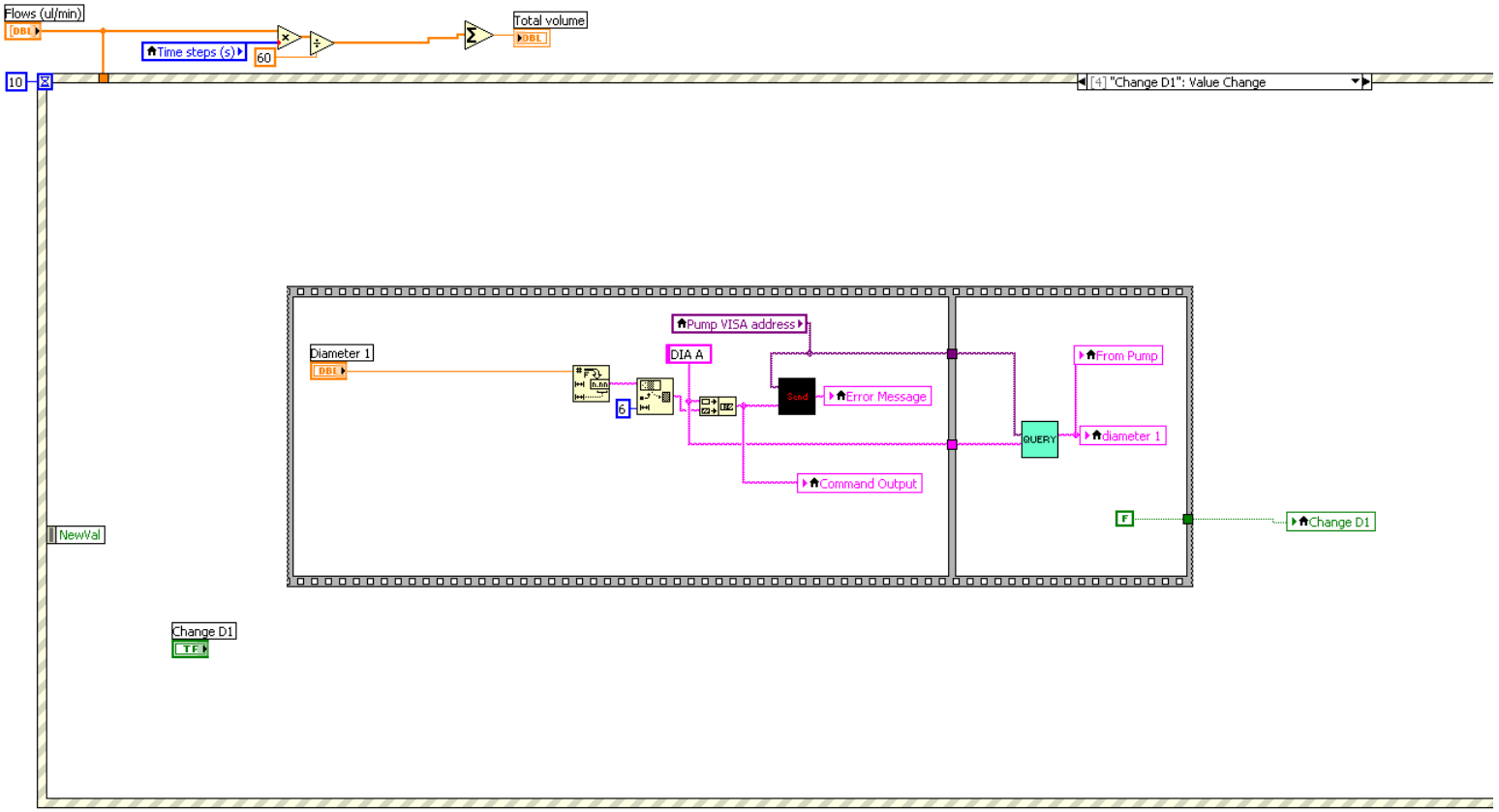

Figure B.12: Block diagram to change the programmed diameter for one of the syringes in the pump.

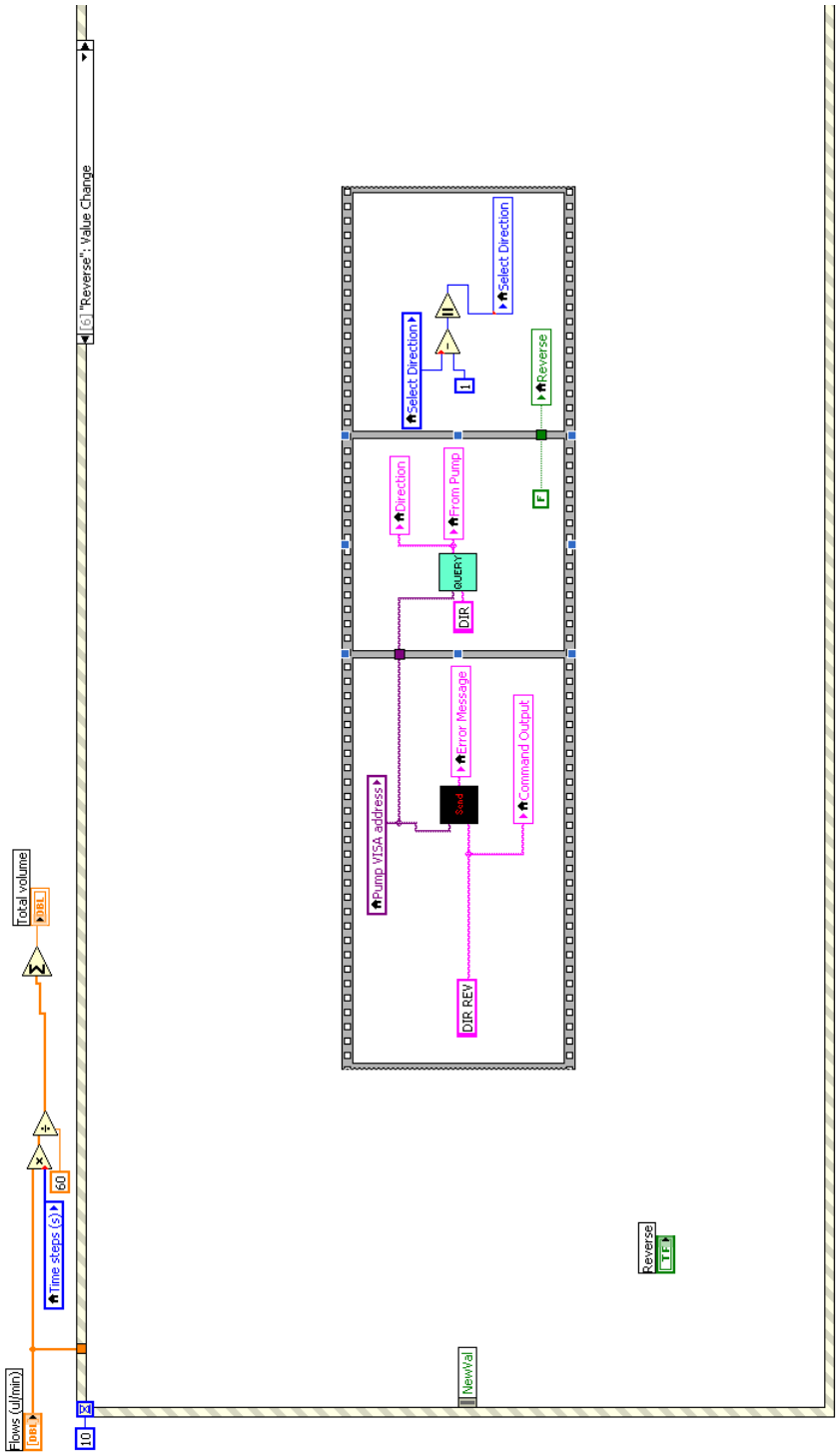

Figure B.13: Block diagram to change the direction of flow for the syringe pump.

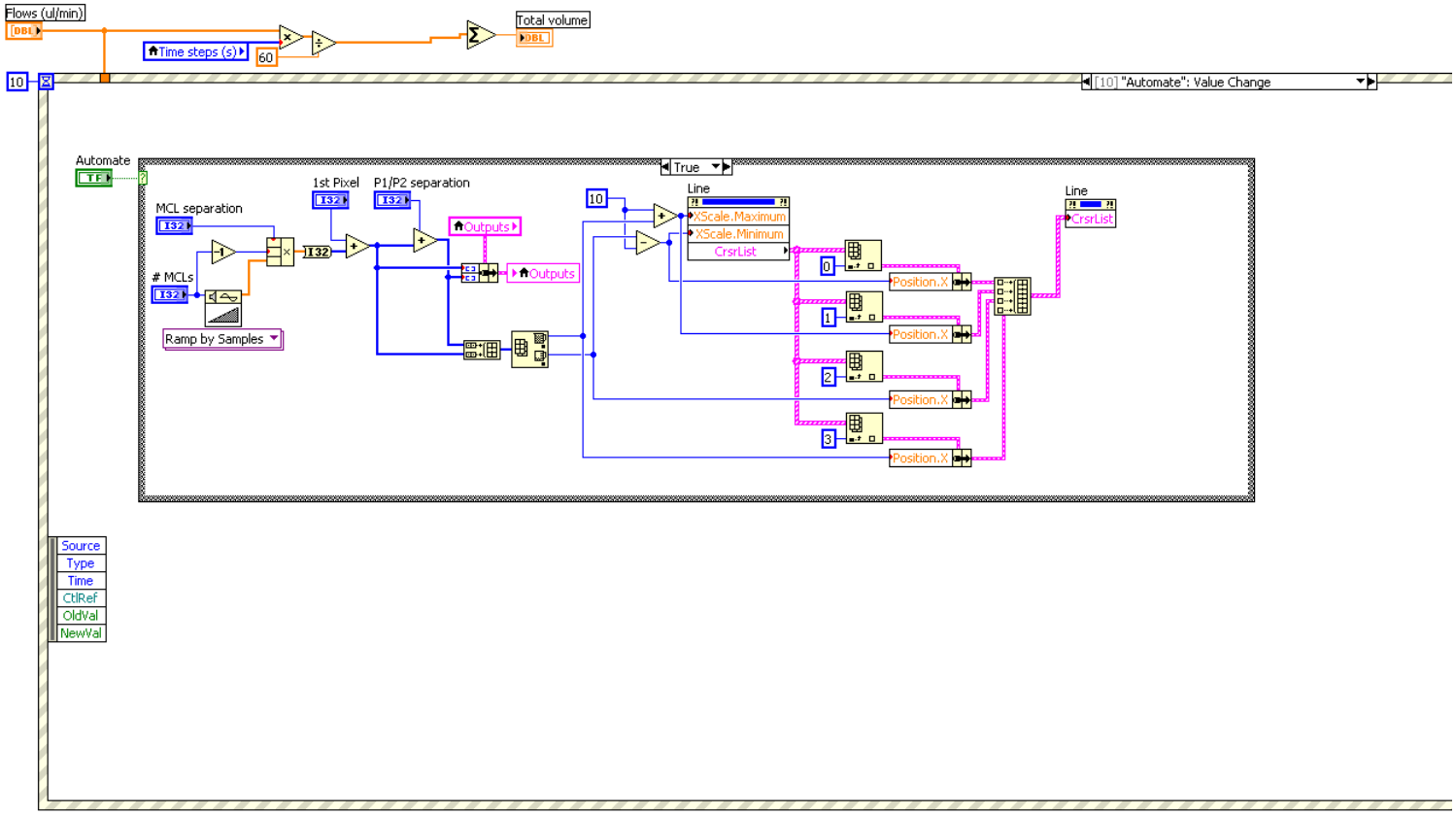

Figure B.14: Block diagram to generate an array containing the pixel positions corresponding to microcantilever outputs.

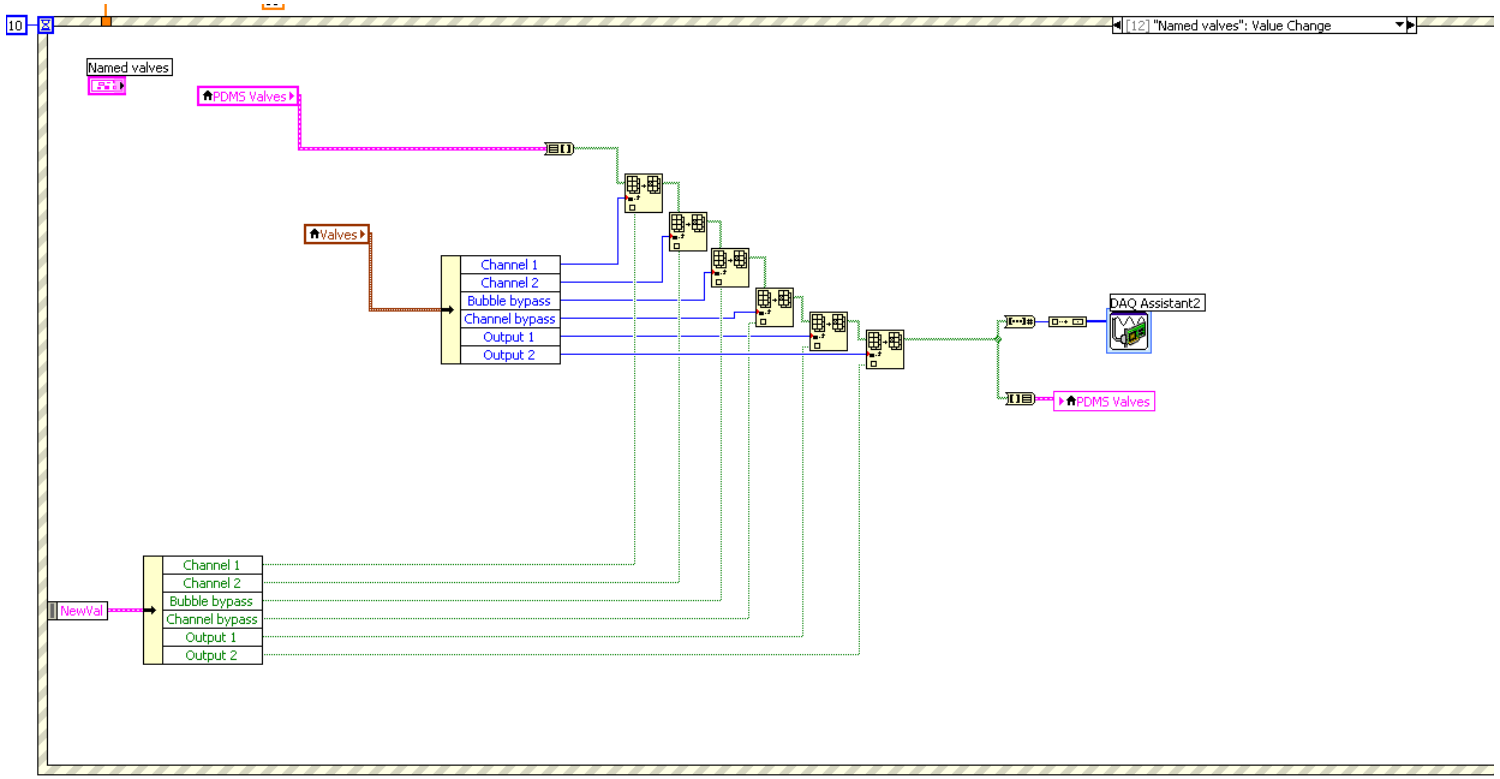

Figure B.15: Block diagram to send command to digital I/O to open and close PDMS valves.

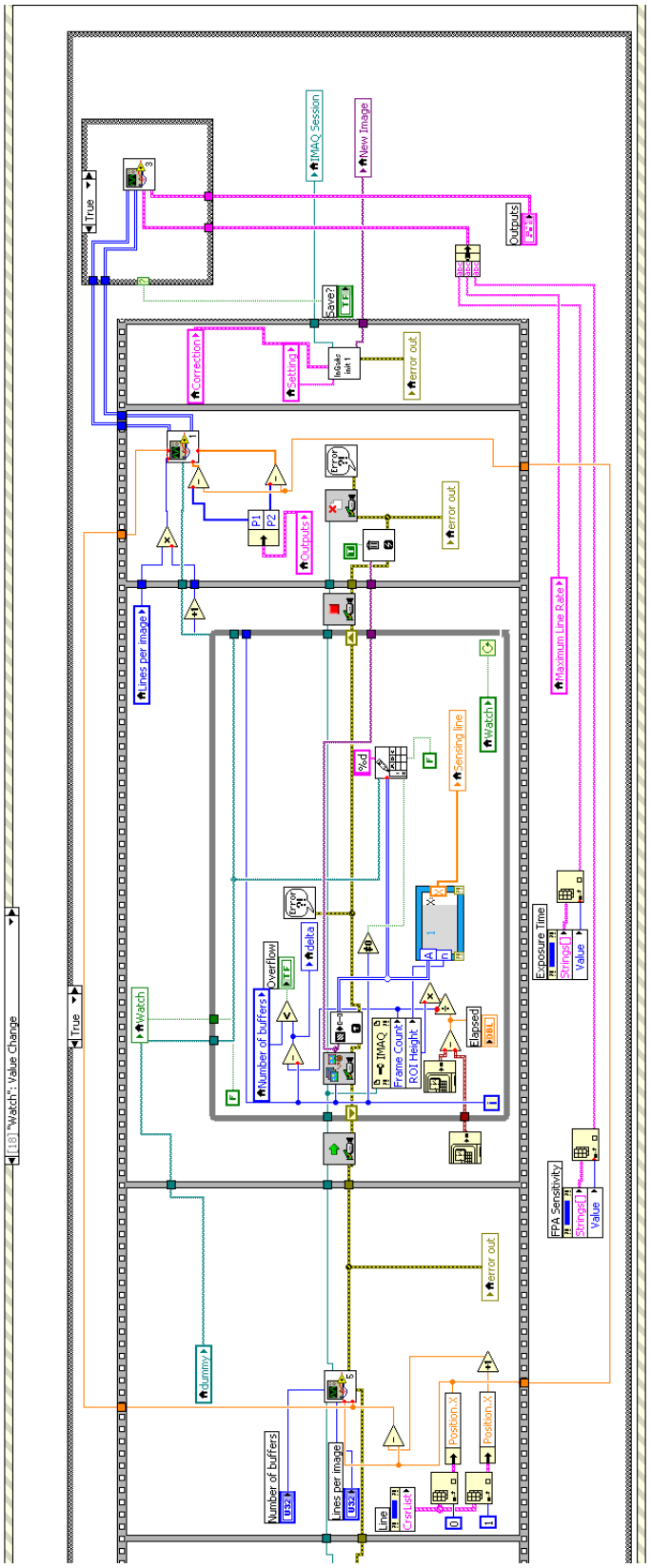

Figure B.16: Block diagram to continuously grab and display images from the line scan camera.

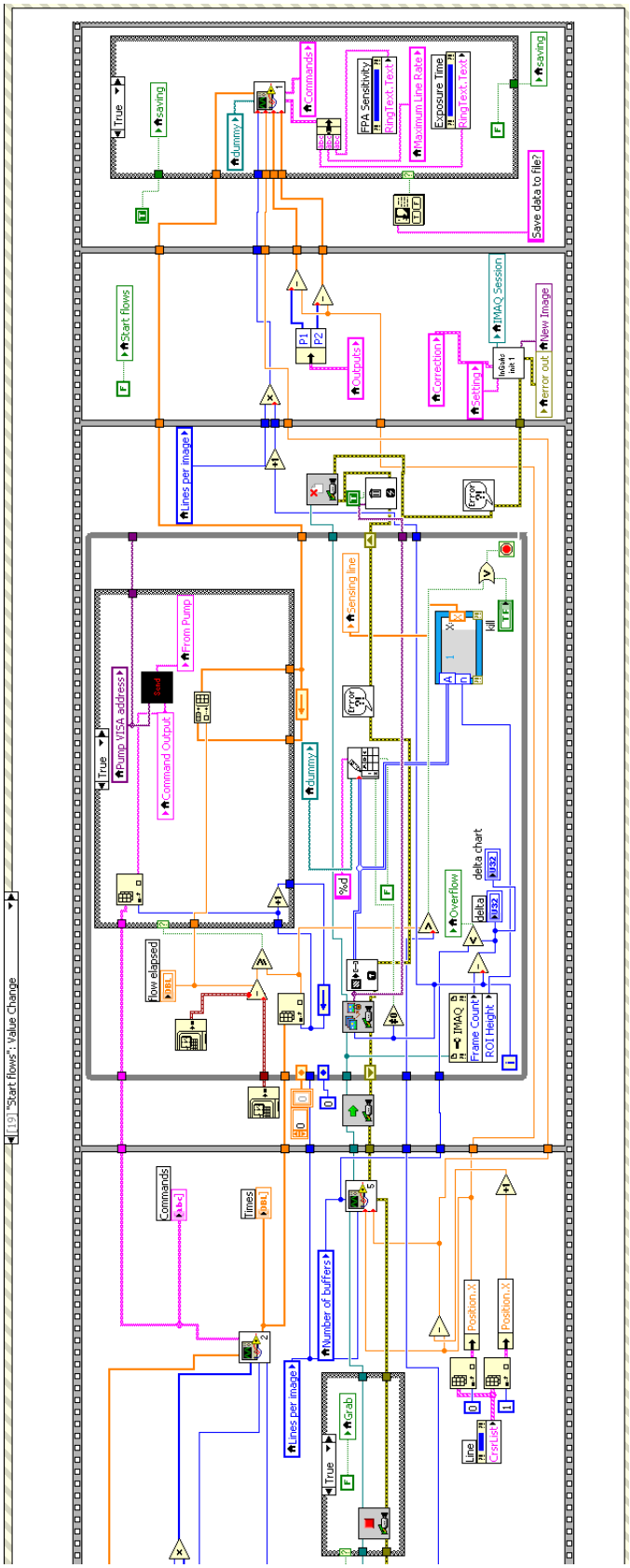

Figure B.17: Block diagram for driving a series of volumetric flow rates and observing the microcantilever response.

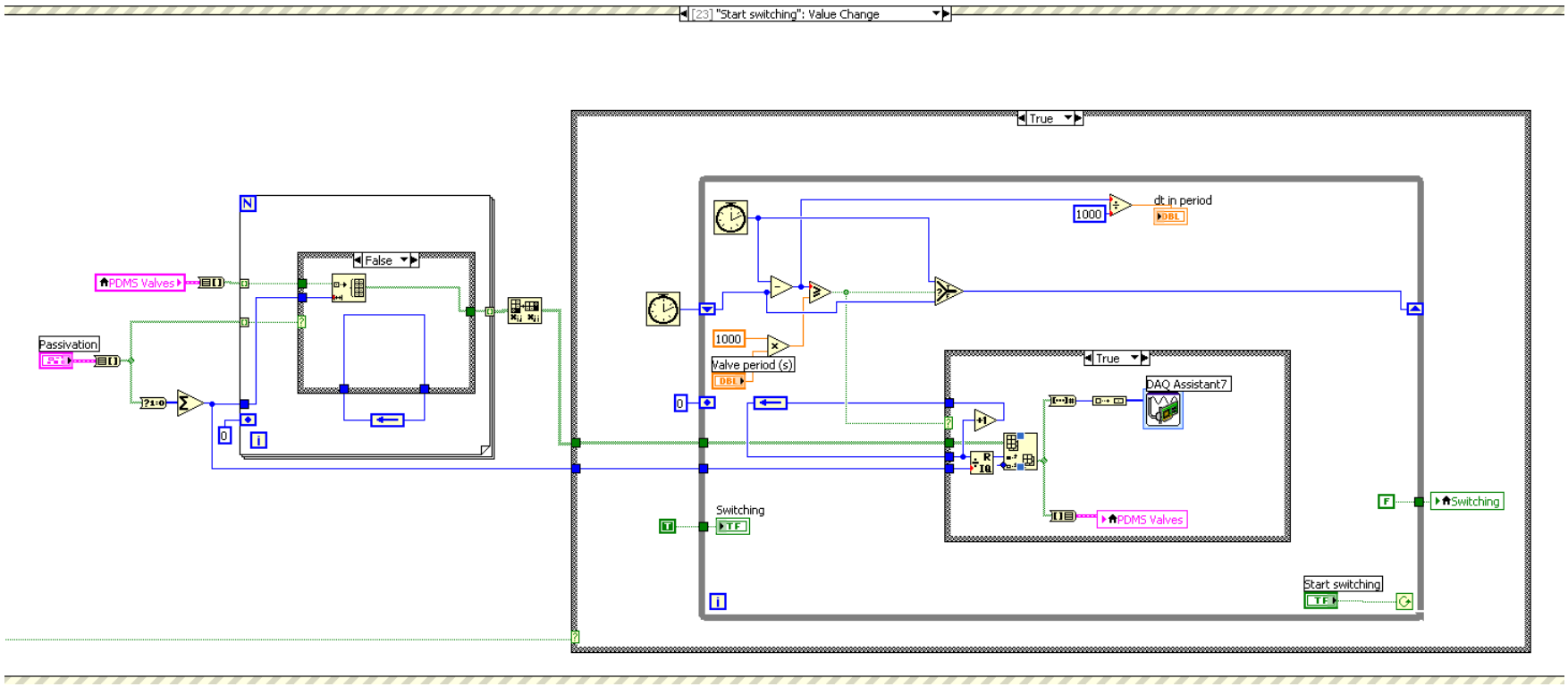

Figure B.18: Block diagram to alternate actuation of several PDMS valves during the passivation process.

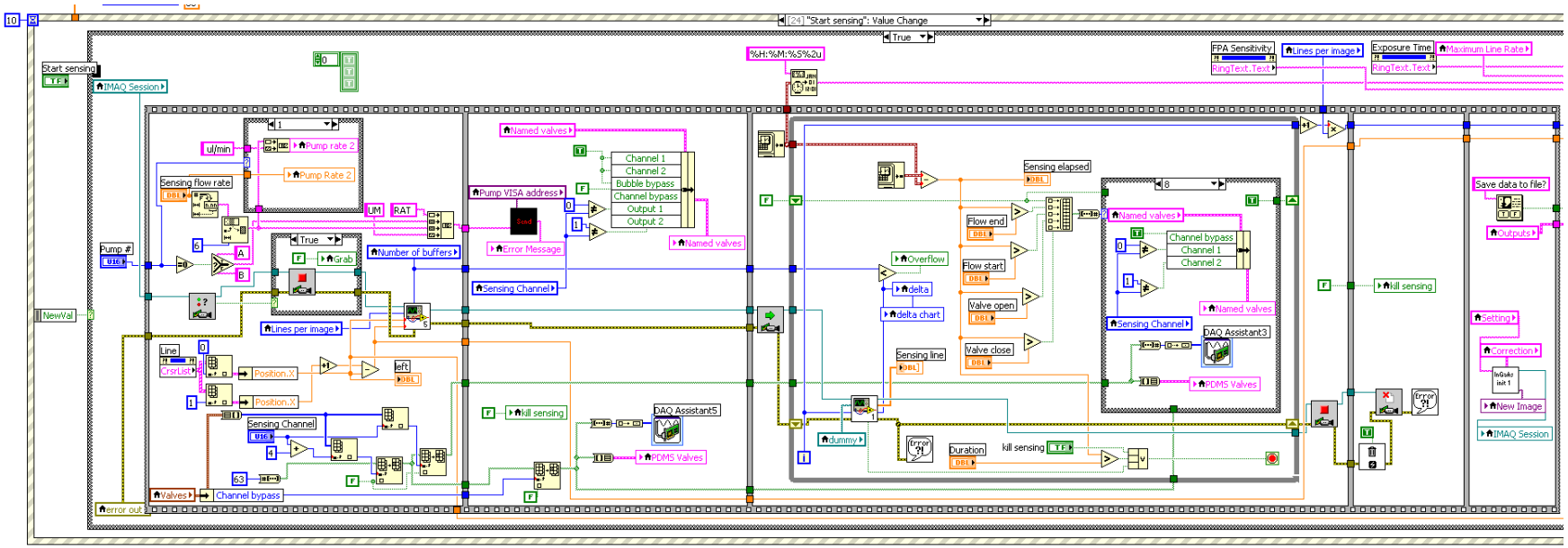

Figure B.19: Block diagram to run a full sensing experiment by starting and stopping flows, opening and closing valves, and acquiring line scan images throughout.

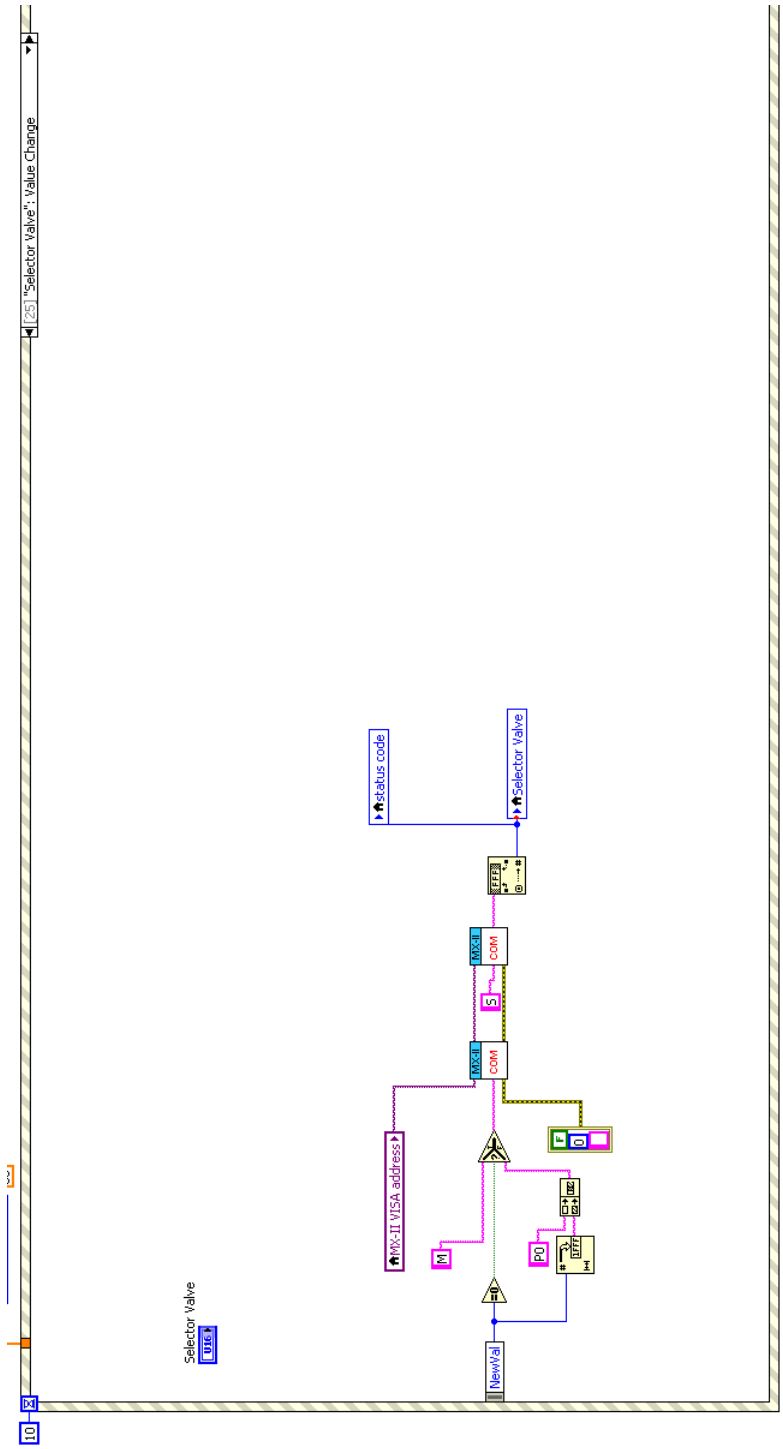

Figure B.20: Block diagram to control which port of the selector valve is connected to the common port.